

SHORT WAVE INFRARED MULTI-COLORED NANOPROBE BASED
DIAGNOSTICS FOR DISTAL SITE METASTATIC SURVEILLANCE AND
MOLECULAR PHENOTYPING

By

HARINI KANTAMNENI

A dissertation submitted to the

School of Graduate Studies

Rutgers, The State University of New Jersey

In partial fulfillment of the requirements

For the degree of

Doctor of Philosophy

Graduate program in Chemical and Biochemical Engineering

Written under the direction of

Prabhas V. Moghe, Charles M. Roth

And approved by

New Brunswick, New Jersey

May 2019

ABSTRACT OF THE DISSERTATION

Short Wave Infrared Multi-Colored Nanoprobe Based Diagnostics for Distal
Site Metastatic Surveillance and Molecular Phenotyping

By HARINI KANTAMNENI

Dissertation Directors:

Prabhas V. Moghe, Ph.D. and Charles M. Roth, Ph.D.

Current clinical imaging modalities are lacking in their ability to quantify parameters that are critical for the early detection of cancer metastases and heterogeneity. Early identification of micro lesions and tracking the growth of cancerous lesions in real time are vital to realize the complete potential of precision medicine. In addition to uncontrolled growth of cells, the dynamic nature of cancer leads to the presence of different sub-populations of cell types among patients or within a single tumor. These variable molecular phenotypes may have different growth and metastases patterns along with variations in response to therapy. It is therefore imperative to evaluate the presence of biomarkers specific to cancer phenotypes, stage of progression and metastatic potential for development of more effective personalized treatment courses. Current clinical diagnostic imaging modalities like MRI, CT and X-ray possess the ability to determine anatomical details; however, they lack the sensitivity and specificity for molecular phenotyping of lesions. Optical imaging, on the other hand, uses non-ionizing radiation to potentially visualize and

characterize both anatomical and molecular details of the disease state. Although the ability to develop optical contrast agents targeted to a diverse range of biological targets is attractive for preclinical and clinical applications, imaging in the visible wavelength region yields poor depth of penetration caused by tissue absorbance and scattering. The near-infrared (NIR) and short-wave infrared (SWIR) regions are more amenable for biological imaging due to minimal attenuation and low tissue auto-fluorescence in these regions.

Rare earth nanoparticles (RENPs) when excited with NIR light (980 nm) emit in the SWIR region (1000 - 1700 nm), allowing for deeper tissue illumination and detection depth. Additionally, RENPs can produce upconversion emissions in the visible region (450-800 nm), when excited with NIR radiation. The ability to emit in the SWIR region (for deep-tissue imaging-preclinical studies) and visible region (for validation of *in-vitro* and *ex-vivo* samples) is attractive for the use of RENPs as optical contrast agents. Furthermore, RENPs possess tunable optical properties with varying emission wavelengths based on dopant chemistry, allowing for generation of a library of multi-colored nanoparticles. RENPs can be rendered biocompatible for *in vivo* imaging by encapsulation in human serum albumin to form rare earth albumin nanocomposites (ReANCs). Additionally, the albumin shell facilitates biofunctionalization and fabrication of cancer-biomarker targeted probes for precision targeting of lesions.

The focus of this dissertation is to use the multi-colored and biomarker-specific targeting properties of ReANCs to create an *in vivo* imaging platform capable of discerning early stage multi-organ metastases with the goal of molecular mapping of tumors at distinct metastatic sites. In this thesis dissertation, it is shown that ReANCs modified with a targeting moiety can detect lung micro lesions in an *in vivo* metastatic breast cancer model. Furthermore, the potential of ReANCs to differentially localize to distinct metastatic sites, including the adrenal glands, lungs and bone marrow, was evaluated in *in vivo* models using orthotopic tumors and spontaneous metastases. Notably, passively accumulated ReANCs could be imaged to the bone space prior to

detection with conventional imaging modalities and preferential localization of actively targeted ReANCs to organs including the lungs and adrenals. Owing to the proficiency of the ReANC imaging system to detect micro lesions, *in vivo*, multi-colored nanoparticles were then used to discern specific molecular phenotypes in a bilateral tumor model. Additionally, the biocompatibility and *in vivo* localization of RENPs modified with an alternate polymer coating, polyethylenimine (PEI), was evaluated as an imaging contrast agent and gene delivery vehicle. The resulting nanophotonic formulation demonstrated superior resolution with increased signal-to-noise ratio in a lung tumor model. Furthermore, the surface charge was modified to reduce toxicity even at concentrations as high as 625 $\mu\text{g/mL}$. The RENPs@PEI formulation was also used to deliver genetic cargo (FILIP1L oligo) to FILIP1L overexpressing cells more efficiently than FILIP1L oligo alone. In summary, a precision-targeted, SWIR-emitting ReANCs has been advanced to detect ~ 1 cm deep tissue micro-lesions in multi-organ metastatic *in vivo* mouse models.

ACKNOWLEDGEMENTS

A lot of people are responsible for me getting here. Over the past 5 years, you have helped me grow into a focused, organized and meticulous researcher. In these years that I have been here, my love for science and passion for research has only grown and for this I am grateful.

Dr. Prabhas Moghe and Dr. Charles Roth, my PIs; two very sharp, focused and visionary professors; under your leadership and guidance I have learned to think critically, be structured and articulate my ideas well. Thank you! Dr. Richard Riman and Dr. Mark Pierce, your expertise and insights into imaging and materials have broadened my horizons and have helped me become a well-rounded researcher. Thank you!

Dr. Vidya Ganapathy, boss, leader, mentor, and a friend whenever I needed one. Through every project, every animal experiment, every paper and every discussion we have had, your contagious love for science has rubbed off on me. I will forever cherish my time here with you. Thank you!

Dr. Margot Zevon, a great friend and the big sister I never had. You have left big shoes here, and I have done the best I could to fill them. Your advice professionally and personally has helped me get through many a tough time. Thank you!

Dr M.C.Tan, all those batches of nano particles, those international phone calls and discussions, they have made my time as a doctoral fellow a little bit easier. Thank you!

Dear Mice, I am so very sorry for the pain and suffering you go through on the name of science. You are our true heroes. Thank you!

My lab support system, Dr. Nicola Francis, Dan Martin, Dr. Rebecca Chmielowski, thank you for helping me find my way through research and cheering me on through some difficult times.

Nanxia Zhao and Prakhar Mishra, my fellow graduate students, I am truly grateful for the lunches, the dinners, the ping-pong games and for company in getting through some tough times. There truly is light at the end of the tunnel.

Karthik Iyer, Srinivas Mushnoori and Noopur Gosavi, Thank you for the late night philosophical discussions and getting me through my existential phases. May each of you be a “Doctor” soon!

My friends from Bits Pilani, thank you very much for the strength and courage you people have shown in your lives. It made me push forward relentlessly. You truly are an inspiration.

Akhila Gollakota, my dearest, from the undergraduate days of last minute exam preparation to this day of my thesis defense, thank you for always being there! What would I have done without you?

Goutam Chalasani, best friend, boy friend and now husband, thank you for your unwavering support and confidence in me all these years. You are my strength.

Sai, my brother, I hope to be an inspiration to you. Love you!

Rajani Sabbineni and Prasad Kantamneni, mom and dad, thank you for all the unconditional love. Through every sacrifice, you have made for us; you have taught us kindness and compassion. I hope I made you guys proud. I miss you!

To anyone I have not mentioned and have been through with me in my journey I am incredibly grateful for everything I have learned from you. I am a better researcher and person because of your love and support.

DEDICATION

I dedicate this dissertation to my family. My parents, Prasad Kantamneni and Rajani Sabbineni who have constantly supported and encouraged me through this process. My brother, Sai, who helped me push through some tough times. And my husband, Goutam, who has shown his unwavering support and confidence in my ability to complete this PhD. I would not have made it without your constant faith and encouragement.

PRIOR PUBLICATIONS

Sections of chapters in this dissertations were previously published or being prepared for publication and are listed as below

- Chapter 2 has been published in its entirety:

Zevon M, Ganapathy V, Kantamneni H, Mingozi M, Kim P, Adler D, Sheng Y, Tan MC, Pierce M, Riman RE, Roth CM, Moghe PV. CXCR-4 Targeted, Short Wave Infrared (SWIR) Emitting Nanoprobes for Enhanced Deep Tissue Imaging and Micrometastatic Cancer Lesion Detection. *Small*. 2015;11(47):6347-57. Doi: 10.1002/sml.201502202. PubMed PMID: 26514367; PMCID: PMC4763715.

The work and text in this chapter was produced in close collaboration with the first and second authors- Dr. Margot Zevon and Dr. Vidya Ganapathy. This author's primary contribution to this body of work were collaboration on the fabrication of targeted and untargeted nanoparticles, longitudinal *in vivo* SWIR imaging of lung tumors and *ex vivo* SWIR imaging and validation of presence of tumors.

- Chapter 3 has been published in its entirety:

Kantamneni H, Zevon M, Donzanti MJ, Zhao X, Sheng Y, Barkund SR, McCabe LH, Banach-Petrosky W, Higgins LM, Ganesan S, Riman RE, Roth CM, Tan M-C, Pierce MC, Ganapathy V, Moghe PV. Surveillance nanotechnology for multi-organ cancer metastases. *Nature Biomedical Engineering*. 2017;1(12):993-1003. doi: 10.1038/s41551-017-0167-9.

- Sections of Chapter 4 are being prepared for publication with the following citation

Kantamneni H, Donzanti MJ, Martin D, Barkund SR, Zhao X, Sheng Y, Tan MC, Riman RE, Pierce MC, Roth CM, Ganapathy V, Moghe PV. Cancer-specific short-wave infrared emitting multi-colored nanoprobes for in-vivo imaging

- Chapter 5 is published in its entirety:

Zhao Z, Kantamneni H, He S, Pelka S, Venkataraman AS, Kwon M, Libutti SK, Pierce M, Moghe PV, Ganapathy V, Tan MC. Surface-Modified Shortwave-Infrared-Emitting Nanophotonic Reporters for Gene-Therapy Applications. *ACS Biomaterial Sci Eng.* 2018;4(7):2305-63. Doi: 10.1021/acsbiomaterials.8b00378. PubMed PMID: 30417087; PMCID: PMC6226244. - **Co-first author.** This author's primary contribution to this work is towards evaluating the RE@PEI nanoparticles *in vitro* cellular uptake and toxicity, *in vivo* bio-distribution studies and RE@PEI mediated gene delivery.

TABLE OF CONTENTS

ABSTRACT OF THE DISSERTATION.....	ii
ACKNOWLEDGEMENTS	v
DEDICATION	vii
PRIOR PUBLICATIONS.....	viii
TABLE OF CONTENTS.....	x
LIST OF FIGURES	xvi
CHAPTER 1.....	1
INTRODUCTION	1
1.1. Cancer	2
1.1.1. Cancer Metastasis.....	3
1.1.2. Tumor Heterogeneity	5
1.1.3. Breast Cancer.....	6
1.1.4. Clinical Diagnostics Tools for Cancer	9
1.2. Optical Imaging	10
1.2.1. Optical Contrast Agents.....	11
1.2.2. Wavelengths for Biomedical Imaging.....	13
1.3. Short Wave Infrared (SWIR) imaging	15
1.4. Nanoparticles as Biological Agents	17
1.4.1. Nanoparticle size	18
1.4.2. Nanoparticle surface properties.....	19
1.4.3. Actively Targeted Nanoparticles.....	20
1.4.4. Barriers for <i>in vivo</i> use of nanoparticles.....	23
1.5. Rare earths nanoparticles as optical imaging agents.....	24
1.5.1. Synthesis of Rare Earth nanoparticles.....	26
1.6. Albumin based nanoparticles.....	27
1.6.1. Albumin for biomedical applications.....	27
1.6.2. Albumin based formulations in the clinical path.....	28
1.7. Dissertation overview	29
CHAPTER 2.....	31

CXCR-4 TARGETED, SHORT WAVE INFRARED (SWIR) EMITTING NANOPROBES FOR ENHANCED DEEP TISSUE IMAGING AND MICROMETASTATIC CANCER LESION DETECTION.....	31
2.1 . Abstract	32
2.2. Introduction	32
2.3. Results.....	35
2.3.1. Synthesis and characterization of nanoparticles	35
2.3.2. Cancer-Targeting Probes: AMD3100 Functionalized ReANCs (fReANCs)	35
2.2.4 <i>In vivo</i> SWIR imaging.....	39
2.2.5 Histopathological analysis of Nanoparticle Biocompatibility	43
2.2.6. <i>Ex vivo</i> SWIR imaging	44
2.2.7 <i>In vivo</i> detection of tumors in internal organs with SWIR imaging	45
2.4. Discussion.....	49
2.5. Conclusion.....	52
2.6. Experimental Methods	53
2.6.1 Reagents:.....	53
2.6.2 Cell Culture:.....	53
2.6.3 ReANC Fabrication	53
2.6.4 Preparation of functionalized nanoparticles (fReANCs):	53
2.6.5 Quantification of loading:	54
2.6.6 <i>In vitro</i> cellular uptake of fReANCs:	54
2.6.7 Cell uptake and confocal imaging	54
2.6.8 Cell viability assay:	55
2.6.9 <i>In vivo</i> imaging:	55
2.6.10 SWIR-imaging:.....	55
2.6.11 MRI Imaging:	56
2.6.12 Detection of subcutaneous cancer lesions:	56
2.6.13 <i>Ex vivo</i> analysis of subcutaneous tumors:	56
2.6.14 Detection of lung metastatic lesions:	57
2.6.15 <i>Ex vivo</i> analysis of metastatic tumors:	57
2.7 Supplemental Figures	58
CHAPTER 3.....	64
SURVEILLANCE NANOTECHNOLOGY FOR MULTI-ORGAN CANCER METASTASES	64

3.1. Abstract.....	65
3.2. Introduction	65
3.3. Results.....	68
3.3.1 Design and characterization of C-X-C chemokine receptor type4 (CXCR4)-targeted photonic nanoparticles:	68
3.3.2. SWIR imaging of photonic nanoparticles discerns bone lesions <i>in vivo</i> that are undetectable by MRI and CT.....	69
3.3.3. Distal bone lesions can be detected with SWIR imaging earlier than MRI in a biomimetic basal-like breast cancer metastasis model	72
3.3.4. Differential niche-based accumulation of ReANC and fReANC formulations leads to multi-organ detection of metastases in a luminal breast cancer model.	75
3.3.5. Superior resolution with SWIR imaging compared with contrast-enhanced MRI for bone lesion detection in a biomimetic mouse metastatic model.....	80
3.3.6. Distinct metastatic lesions originating from a common cell line exhibit niche-dependent molecular signatures.....	83
3.4. Discussion.....	86
3.5. Methods.....	89
3.5.1. Fabrication of rare-earth nanoparticles.....	89
3.5.2. <i>In vivo</i> imaging.	90
3.5.3. Whole-animal SWIR imaging.....	90
3.5.4. MRI and CT imaging.	90
3.5.5. Cell lines.	91
3.5.6. Orthotopic model of bone metastasis.	91
3.5.7. Biomimetic model of bone metastasis.	92
3.5.8. Biomimetic model of multi-organ distal metastases.	92
3.5.9. <i>Ex vivo</i> analysis of bone microlesions.	93
3.5.10. <i>Ex vivo</i> analysis of adrenal lesions.	93
3.5.11. SWIR image analysis.....	93
3.5.12. MRI image analysis.....	94
3.5.13. Human soluble receptor array and human oncology array for molecular phenotyping. 94	
3.5.14. Quantitative biodistribution, clearance and toxicology studies.	95
3.5.15. Competitive inhibition of CXCR4 as a measure of passive targeting.	95

3.5.16. <i>In vitro</i> optimization of nanoprobes.	95
3.6.17. Statistical analysis.	96
3.6. Supplementary Figures	97
CHAPTER 4.....	112
CANCER-SPECIFIC SHORT-WAVE INFRARED EMITTING MULTI-COLORED NANOPROBES FOR <i>IN-VIVO</i> IMAGING	112
4.1 Abstract.....	113
4.2. Introduction	114
4.3. Results.....	116
4.3.1. Synthesis and characterization of multi-colored nanoprobes:.....	116
4.3.2. Synthesis of biomarker-specific nanoprobes:.....	117
4.3.3. <i>In vitro</i> target validation of functionalized multi-color probes:	118
4.3.4. <i>In vivo</i> target validation of multi-color nanoprobes:	120
4.3.5. Biomarker level based preferential accumulation of multi-color nanoprobes:	123
4.4. Discussion.....	125
4.5. Methods.....	127
4.5.1. Cell lines	127
4.5.2. Rare-earth nanoprobe synthesis and modification:	127
4.5.3. Synthesis of functionalized nanoprobes (fReANCs):.....	128
4.5.4. <i>In vitro</i> uptake of functionalized ReANCs:	129
4.5.5. <i>In vivo</i> imaging	130
4.5.6. Whole body SWIR imaging:.....	130
4.5.7. <i>In vivo</i> MCF7 subcutaneous model:	130
4.5.8. <i>In vivo</i> 4175 subcutaneous model:	131
4.5.9. <i>In vivo</i> SKOV3 subcutaneous model:.....	131
4.5.10. <i>In vivo</i> bilateral subcutaneous model:	132
4.5.11. SWIR image analysis:.....	132
4.5.12. <i>Ex vivo</i> tumor imaging:.....	133
4.5.13. <i>Ex vivo</i> confocal imaging:	133
4.5.14. Statistical analysis:	133
4.6. Future studies:	134
4.6.1. Bilateral tumor model with varied time point of erbium and holmium injections	134

4.6.2. In vivo imaging of multi-color nanoparticle in a single mass.....	135
4.7. Supplementary Figures	138
CHAPTER 5.....	145
SURFACE-MODIFIED SHORTWAVE-INFRARED-EMITTING NANOPHOTONIC REPORTERS FOR GENE-THERAPY APPLICATIONS	145
5.1 Abstract.....	146
5.2. Introduction	146
5.3. Results.....	150
5.3.1. Size, Morphology, and Crystal Structure of Surface-Modified RENPs.....	150
5.3.2. Surface Characteristics and Charges of Surface-Modified RENPs.....	153
5.3.3. Optical Properties of the RENPs.....	162
5.3.4. Cellular Uptake and Toxicity of the RENPs.....	165
5.3.5. <i>In vivo</i> SWIR Imaging for the Monitoring of RENPs@PEI Biodistribution and Bioavailability	168
5.3.6. RENPs@PEI-Mediated Gene Targeting as Evidenced by the in Situ Hybridization of Genetic Probes to Genes of Interest.....	170
5.4. Summary	172
5.5. Methods.....	173
5.5.1. Chemicals	173
5.5.2. Trifluoroacetate Precursor Preparation.....	174
5.5.3. Synthesis of Rare-Earth-Doped Nanoparticles.....	174
5.5.4. Synthesis of PEI-Coated RENPs	175
5.5.5. Synthesis of Yb ³⁺ Impregnated RENPs	175
5.5.6. Material Characterization	176
5.5.7. Cellular Toxicity and Intracellular Distribution Studies.....	178
5.5.8. Biodistribution and Toxicity of RENPs <i>in vivo</i>	179
5.5.9. Biodistribution, Clearance, and Toxicology Studies.....	180
5.5.10. Resolution of Tumor lesions Using RENPs <i>in vivo</i>	181
5.5.11. Gene-Therapy Applications of RENPs: In Situ Hybridization of Oligonucleotides Conjugated to RENPs@PEI.....	181
5.6. Supplementary Figures	183
CHAPTER 6.....	190
CONCLUSIONS AND FUTURE DIRECTIONS	190

6.1 Conclusions	190
6.1.1. CXCR-4 targeted, Short Wave Infrared (SWIR) emitting nanoprobes for enhanced deep tissue imaging and micro metastatic cancer lesion detection.....	190
6.1.2. Surveillance nanotechnology for multi-organ cancer metastases	191
6.1.3. Cancer-specific Short-wave infrared emitting multi-colored nanoprobes for <i>in vivo</i> imaging.....	192
6.1.4. Surface-Modified Shortwave-Infrared-Emitting Nanophotonic Reporters for Gene-Therapy Applications	192
6.2. Future Directions	193
6.2.2. Theranostic particles.....	193
6.2.3. Nanoparticle guided immune surveillance	194
APPENDIX	197
CHAPTER 7.....	200
REFERENCES	200

LIST OF FIGURES

Figure 1.2-Process of metastasis from primary tumor site	4
Figure 1.3-Metastasis of Breast cancer.....	6
Figure 1.4- Molecular subtypes of BC.....	8
Figure 1.5- Tissue auto-fluorescence in different wavelength ranges	14
Figure 1.6- Effective attenuation coefficient of biological components as a function of wavelength.....	16
Figure 1.7- Effect of size and surface properties of NPs on biodistribution.....	20
Figure 1.8- Emission spectra of rare earth nanoparticles.....	25
Figure 1.9- Three-dimensional structure of albumin.....	28
Figure 2.10- Design, fabrication, and preclinical efficacy of rare earth nanoprobe.....	37
Figure 11.2-Characterization of functionalized Rare Earth Nanoprobe:.....	38
Figure 2.12- Active Cancer Targeting of Rare Earth Nanoprobe.....	40
Figure 2.13- Functionalized nanoprobe are capable of molecular discrimination of tumors in vivo.....	42
Figure 2.14- Rare-Earth nanoprobe proved safe for long-term use with no significant impact on animals' weight or damage to organs of accumulation	44
Figure 2.6- Targeted fReANCs allow for detection of microscale lung lesions.....	47
Figure 2.7- Longitudinal tracking of internal lesions with SWIR imaging	48
Supplementary Figure 2.1- Size distribution histograms of ReANC and fReANC showing nanoscale, monodisperse populations:.....	58
Supplementary Figure 2.2- Effect of various concentrations of AMD3100 on cellular uptake of fReANC, showing that uptake is largely independent of loading concentration:.....	59
Supplementary Figure 2.3- Quantification of receptor expression of relevant cell lines:.....	60
Supplementary Figure 2.4- <i>Ex vivo</i> analysis of organs showing punctate pattern of fluorescence associated with visible metastatic tumors.....	61
Supplementary Figure 2.5- <i>Ex vivo</i> analysis of excised subcutaneous tumors:.....	62
Supplementary Figure 2.6- flow chart detailing the matlab scripts used to process videos:.....	63
Figure 3.15- Design and workflow of photonic nanotechnology for cancer-metastasis detection and profiling.....	67
Figure 3.16- SWIR imaging of photonic nanoparticles discerns bone lesions in vivo that are undetectable by conventional MRI and CT.....	72
Figure 3.17- Distal bone lesions can be detected with SWIR imaging earlier than by MRI and CT in a biomimetic metastasis model.....	75
Figure 3.18- Differential niche-based accumulation of ReANC and fReANC formulations leads to multi-organ detection of metastases in a luminal breast cancer model.....	77
Figure 3.19- Passive accumulation of ReANCs, via the discontinuous fenestration architecture of bone tissue, in a metastatic luminal breast cancer model	78
Figure 3.20- Differential accumulation of ReANCs in leg lesions and fReANCs in lung lesions in a multi-organ metastatic model	80

Figure 3.21- Distal bone lesions can be detected with SWIR imaging earlier than by contrast-enhanced MRI in a biomimetic metastasis model.....	83
Table 3.1: Distinct metastatic lesions originating from a common cell line exhibit niche-dependent molecular signatures	85
Supplementary Figure 3.7- Encapsulation of rare earth cores in albumin using a solvent induced controlled coacervation process forming rare earth albumin nanocomposites (ReANCs):	97
Supplementary Figure 3.8- Validation of the active targeting mechanism of fReANCs vis-à-vis ReANCs.....	98
Supplementary Figure 3.9-Functional validation of molecular targeting features of fReANCs	99
Supplementary Figure 3.10- Histopathological analysis of organs of clearance over time.....	100
Supplementary Figure 3.11- Histopathological evaluation of organs of clearance for toxicity with repeated nanoparticle administration.....	101
Supplementary Figure 3.12- Quantitative clearance studies highlight effective clearance of nanoprobe.....	102
Supplementary Figure 3.13- <i>Ex vivo</i> validation of ReANCs in bones	103
Supplementary Figure 3.14- Expression levels of CXCR4 in breast cancer cell lines	104
Supplementary Figure 3.15- MRI and In situ white light images indicate the presence of adrenal tumors.....	105
Supplementary Figure 3.16- Ex-vivo images showing presence of SWIR signal in adrenal glands of tumor bearing mice	106
Supplementary Figure 3.17- Histopathological validation of ER-positive tumor cells in adrenal.....	107
Supplementary Figure 3.18- H and E staining of adrenal metastases	108
Supplementary Figure 3.19- Validation of contrast uptake by tumor bearing and healthy animals	109
Supplementary Figure 3.20- Variations in molecular signatures based on metastatic niche	110
Figure 4.1: Multi-color nanoparticles for biomarker specific <i>in vivo</i> imaging	116
Figure 4.2- <i>In vitro</i> analysis of functionalized multi-color probes	119
Figure 4.3: <i>In vivo</i> targeting validation of multi-color nanoprobe in subcutaneous tumors	121
Figure 4.4: <i>Ex vivo</i> analysis of multi-color probes localization	123
Figure 4.4: <i>In vivo</i> specificity of FITC-fErANCs and Rh-fHoANCs in a bilateral tumor model.....	124
Figure 4.5: Schematic of heterogeneous 3D tumor spheroids	136
Supplementary figure 4.1: SWIR emission spectra.....	138
Supplementary figure 4.2: Size characterization of untargeted and targeted multi-colored nanoparticles	139
Supplementary figure 4.3: Spectra of visible fluorophore loaded ReANC	140
Supplementary Figure 4.4: Flow cytometry to determine optimal concentration of targeting ligand.....	141
Supplementary figure 4.5: Validation of targeted probes to corresponding receptor positive cell lines.....	142
Supplementary figure 4.6: <i>Ex vivo</i> MsFxPro imaging of tumor samples	143
Supplementary figure 4.7: Bilateral tumor bearing animal show increased localization of targeted nanoprobe to corresponding receptor positive tumor	144
Figure 5.22- Size and crystal structure characteristics of as-synthesized and surface modified core-shell RENPs.....	152

Scheme 5.1: Schematic Representation of the Molecular Conformation and Interactions within the Organic PEI Coating	155
Figure 5.23- Surface characteristics of as-synthesized and surface-modified core–shell RENPs	155
Table 5.1: Estimated Thickness of Each Surfactant (Or Polymer) from the TGA Weight-Loss Measurements, Assuming That a Uniform Layer Is Coated around the Inorganic RENPa	157
Scheme 5.2: Schematic Illustration of the Resultant Key Differences between Extended and Collapsed-Chain Conformations of PEI Coating around the Inorganic RENPs ^a	160
Figure 5.24- Optical characteristics of as-synthesized and surface-modified core–shell RENPs, evaluated to determine the effects of surface modification.....	163
Table 5.2: Estimated Average Lifetime of Each As-Synthesized or Surface-Modified RENC from Time-Resolved Spectroscopy Measurements Made Using a Pulse-Modulated 975 nm Source, Assuming Double-Exponential Decay Behaviora	165
Figure 5.25- Effect of surface modification of core–shell RENPs on cell proliferation, viability, and intracellular distribution	168
Figure 5.26- SWIR imaging showing enhanced signal-to-noise ratio with RENPs@PEI localization in lung lesions	170
Figure 5.27- Delivery of genetic cargo enhanced by RE-PEI. ES2 cells were induced to over-express the FILIP1L gene by the addition of doxycycline (DOX):.....	171
Supplementary Figure 5.1 - Inflection points calculated from the first derivative weight loss of the TGA measurement data.....	183
Supplementary Figure 5.2 - Time resolved lifetime measurements of the IR emission.....	184
Supplementary Figure 5.3 - Hydrodynamic diameter of PEI coated particles.....	185
Supplementary Figure 5.4 - RENC@PEI show increased resolution of smaller cell clusters	186
Supplementary Figure 5.5 - <i>Ex vivo</i> SWIR imaging of organs of accumulation and clearance....	187
Supplementary Table 5.1 - Assignment of the FTIR absorption peaks	189
Figure 6.1- PD1-targeted RENCs illuminate T-cells <i>in vivo</i> and <i>ex vivo</i>	195
Figure 6.2: Workflow for the use of Rare earth probes for immune response monitoring	196

CHAPTER 1

INTRODUCTION

1.1. Cancer

Cancer is the second leading cause of death globally, with 18 million new diagnoses and 9.55 million deaths worldwide in 2018 ¹. In the United States alone, there are 1.7 million new cases with 609,640 deaths annually ². While lung cancer has the highest rate of incidence, it is followed closely by breast cancer (BC) as the second most common malignancy worldwide ¹. Several factors have been shown to contribute to the development of solid tumor cancers. The use of tobacco is associated with up to 22% of cancer related deaths¹, while alcohol^{3,4}, unhealthy diet, and physical inactivity^{5,6} together contribute to about 10% of cases. While these correlations are well known, further progress in the fight against cancer requires identifying other factors that contribute to the development of complex malignancies.

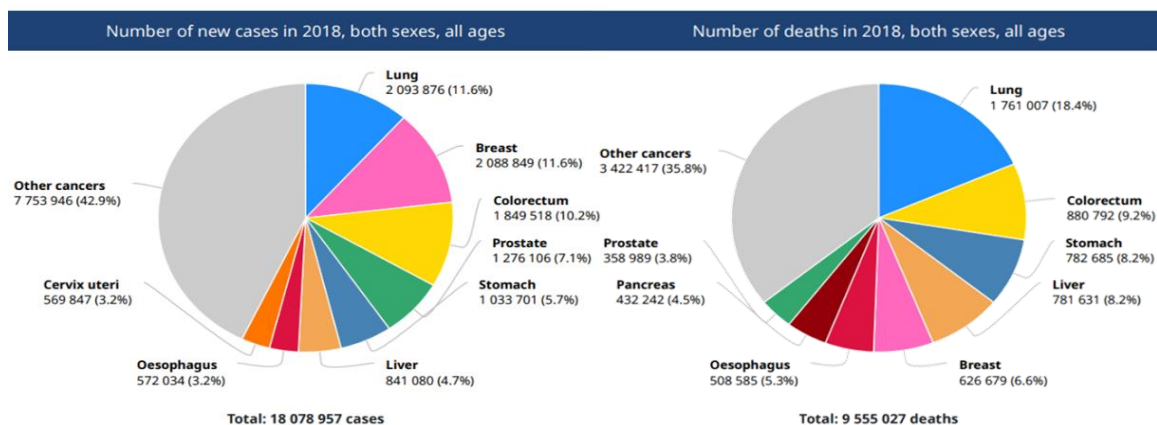


Figure 1.1- Rate of occurrence and mortality in cancers

Worldwide analysis showing number of new cases diagnosed and resulting deaths in 2018 categorized by type of cancer (Source: All cancers; Globocan 2018, World Health Organization)

Cancer is a collection of diseases caused by the uncontrolled division of abnormal cells, leading to the invasion of surrounding healthy tissue. The uncontrollable growth of cancerous cells can be attributed to genetic changes in one of three “drivers” of cancer: the proto-oncogenes contributing

to normal cell growth, tumor suppressor genes responsible for growth control in cells, and DNA suppressor genes involved in fixing damaged DNA⁷. Mutations in any one of these classes of genes can lead to development of a cancerous cell. The cancerous cells eventually invade surrounding healthy tissue, disrupting normal function and leading to metastases.

1.1.1. Cancer Metastasis

The abnormal and aggressive division of cells characterizes solid tumor cancers. Such malignant tumors can spread from the organ of origin to invade other parts of the body, a process called cancer metastasis⁷. The local invasion of tumor cells into surrounding healthy environment follows a sequence of steps called the metastasis cascade, ultimately leading to tumor development in distant organs. Any inhibition of the intermediate steps in the cascade can arrest the process of cancer advancement and improve patient prognosis⁸.

The metastasis cascade involves the infiltration of primary tumor cells into the epithelial lining of surrounding healthy tissue and migration into neighboring blood vessels and lymphatic tissue. The cancer cells dispersed through the lymphatic system reach distant organs, where they seed and begin to develop new malignancies, becoming macro-metastatic lesions⁹. The organs of metastasis vary for each type of primary tumor, which can be explained best by Stephen Paget's seed and soil hypothesis. The seed and soil theory, published in 1889 and based on a study of 735 women with metastatic BC, states that the distal organ's microenvironment (the soil) facilitates the growth of the disseminated cancer cells (the seed)^{10,11}. Metastasis is used by clinicians to stage disease progression, which further dictates patient prognosis and treatment plan. Treatment of cancer metastasis is mainly aimed at stalling the further spread and growth of lesions. Metastasis is the major cause of mortality in cancer, damaging normal bodily functions, and hence there is an urgent need for early diagnostic and screening methods.

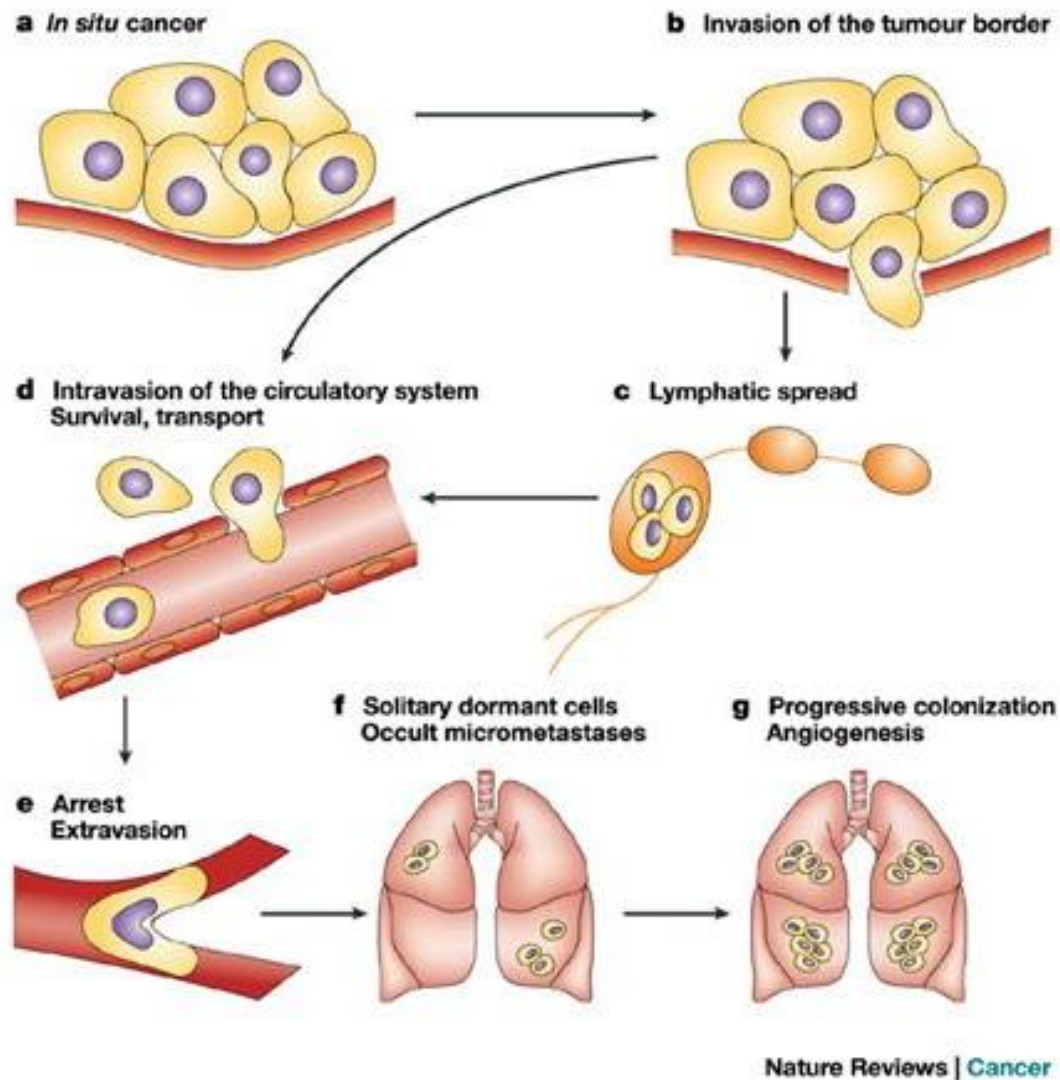


Figure 1.2-Process of metastasis from primary tumor site

Schematic showing the progression of cancer cells from (a) primary tumor site to metastatic site through (b) local invasion of epithelial cells at the tumor border followed by (c, d) intravasation via neighboring blood vessels and lymphatic vessels. The disseminated cancer cells eventually reach distant organs by (e) extravasation leading to (f) micro-metastases eventually progressing to angiogenic (g) macro metastases. Figure reproduced with permission from Steeg *et. al.* Metastasis suppressors alter the signal transduction of cancer cells. *Nature Reviews Cancer* 3, pages 55–63 (2003) (License number: 4494920517164)

1.1.2. Tumor Heterogeneity

Another aspect of cancer that plays a major role in determining patient prognosis and treatment strategy is cancer heterogeneity. Cancer, being a dynamic disease, is composed of various subsets of cells with different phenotypes, morphologies, genotypes and molecular signatures¹²⁻¹⁴. These sub-populations of cells may have different growth rate and patterns with varied levels of sensitivity and resistance to therapeutics. This variation in tumor signature can partially explain the difference in outcomes between patients who receive the same treatment. Over the years, histology-based techniques have been developed to identify cancer subtype to create more precisely tailored treatment regimens leading to better outcomes¹². There can exist multiple sub-populations of malignant cells within a single bulk of tumor (called “intra-tumor heterogeneity”), confounding treatment and providing a plausible explanation for why some patients relapse after initially responding to therapy¹⁵. This heterogeneity may arise due to genetic changes in subpopulations of an individual’s cancer across primary and metastatic sites (called spatial heterogeneity) or distinct molecular signatures of cells (called temporal heterogeneity)¹⁴.

Accurate identification of tumor heterogeneity is needed in order to develop a therapeutic strategy to address the total disease state. Techniques like needle biopsy, where only a small fraction of cells are extracted and examined, often fail to capture the entire tumor mass. Emerging diagnostic technologies like longitudinal liquid biopsy^{16,17}, single cell sequencing using RNA-seq¹⁸ of extracted cancerous lesions, and multi-region sequencing^{19,20} are all contributing towards improved understanding of the complex nature of heterogeneity. Tumor heterogeneity is evident in all cancer types, but is particularly salient in leukemias and malignancies of the breast, prostate, colon, and brain. In the era of personalized medicine, it is vital to have a non-invasive tool for identifying the various molecular phenotypes in a single tumor, to create a tailored adaptive therapy regimen.

1.1.3. Breast Cancer

Breast cancer (BC) is the second most common cancer with about 1 in 8 American women developing it over the course of their lifetime²¹. An estimated 2.08 million new cases were diagnosed in 2018 worldwide, with ~626,000 related deaths¹. BC is generally caused by genetic abnormalities of which 5-10% are inherited from either parent and 85-90% are caused by mutations developed through the aging process combined with hormonal changes²². BC is classified by the point of cancer origin, with occurrence either in the milk producing glands/lobules (lobular carcinoma), in the passages to the nipples/ducts (ductal carcinoma) or in rare cases in the connective tissue (phyllodes tumor and angiosarcoma)²³.

BC is staged according to the extent of tissue infiltration beyond the primary tumor location. Stages I and II are generally characterized by primary tumor size about 2-5 cm with no metastasis or limited infiltration to lymph nodes with a five-year survival rate of 96%. Stage III is indicative of tumor spread to the axillary lymph nodes and other adjacent structures like skin of breast or chest wall, resulting in a five-year survival of 46%. Stage IV BC involves metastasis to other organs with a

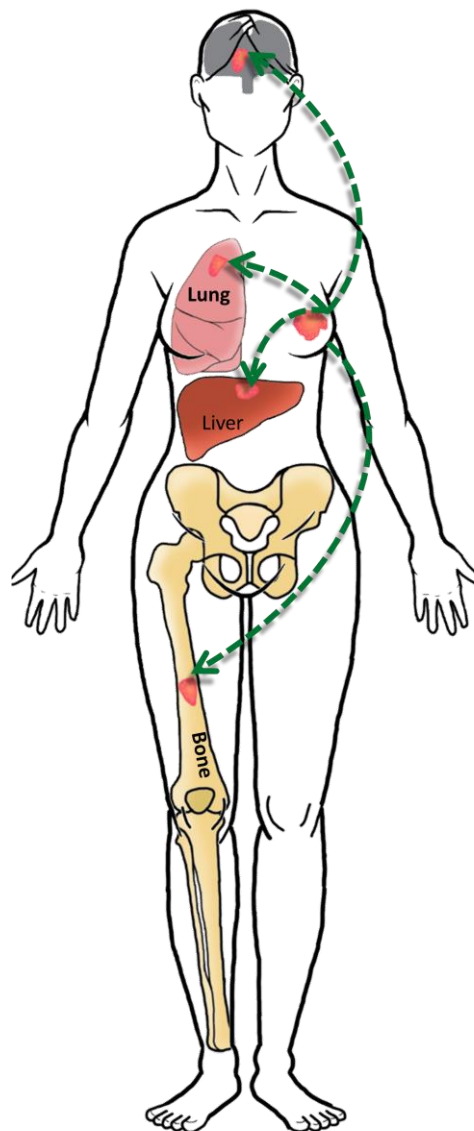


Figure 1.3-Metastasis of Breast cancer

70% of breast cancer metastasis is found in the lungs, liver, brain and.

survival rate of 24%^{24,25}. The stage of cancer detection plays a major role in patient prognosis, as is evident from the survival rates. Metastasis in BC, similar to that in other cancers, spreads via the axillary lymph nodes to the lung, liver, adrenal glands, and bone. About 6-10% of all diagnosed BC cases present with distal metastasis, while about 20-30% of women diagnosed with non-metastatic disease develop metastasis within 5 years of diagnosis^{26,27}. Of these sites, bone represents a significant portion of metastatic disease, with 70% of patients with advanced disease presenting with bone lesions^{28,29}.

In addition to disease stage, the molecular signature of a tumor also plays a big role in determining treatment plan and prognosis. BC is a highly heterogeneous disease with a great deal of cellular and molecular diversity within individual tumors as well as among patients. BC can be categorized into basal and luminal subtypes based on the variations in genetic expression. Expression array analysis has led to further classification of BC into four intrinsic molecular subtypes: basal-like BC, human epidermal growth factor receptor (HER2) positive, luminal A, and luminal B³⁰⁻³². Normal breast tissue commonly expresses estrogen and progesterone hormone receptors, whereas malignant cells of luminal A and B subtypes of BC tend to overexpress one or both of these hormone receptors. In addition to hormone receptors, luminal B BC subtype presents with amplified HER2 expression. Tumor receptor expression is determined by pathological analysis of biopsy samples, which help formulate tailored a treatment plan for each patient^{33,34}. BC tumors that overexpress the estrogen hormone receptor (ER) are classified as ER positive, whereas progesterone receptor (PR) overexpression leads to development of PR positive type tumors. Approximately 66% of BC cases are hormone receptor-positive for either of these two receptors³⁵. The treatment course of ER+ and PR+ tumors varies with cancer stage, but the most common course of action is surgery followed by hormone therapy. Hormone therapy is based on depriving the tumor of estrogen, stalling the growth and spread of the lesions, and is often used after or before surgery to reduce the risk of relapse. These hormone positive tumors are most commonly treated

with chemotherapeutic drugs in combination with agents such as tamoxifen^{36,37} and fulvestrant (Faslodex)^{38,39}. HER2 positive tumors represent 20-30% of diagnosed BC cases and do not respond to hormone therapy. HER2 overexpressing tumors often present as aggressive disease with low survival rate and higher rate of recurrence⁴⁰. The current clinical standard for HER2 positive tumors is a combination of chemotherapy and targeted therapy. The current gold standard of targeted HER2 therapy is trastuzumab (Herceptin), a humanized monoclonal antibody that has been shown to be very effective as part of combination therapy in patients with early stage and metastatic BC⁴¹.

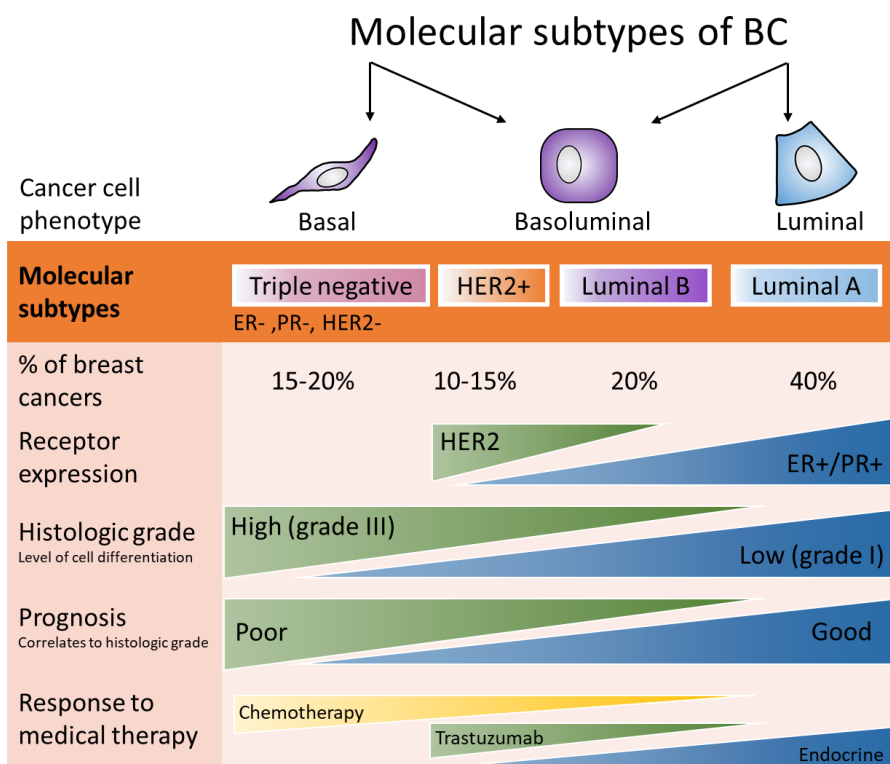


Figure 1.4- Molecular subtypes of BC

There exists a co-relation among the phenotype of BC and molecular subtypes, receptor expression, and percentages of occurrence and patient prognosis. Adapted from Eric Wong *et al*, Breast cancer pathogenesis and histologic vs. molecular subtypes, McMaster Pathophysiology review, (2012)

Triple negative breast cancer (TNBC), which occurs when a tumor does not overexpress any of these three (ER, PR and HER2) receptors, accounts for 10-30% of all diagnosed BC cases. Here, the lack of specific molecular signatures limits the availability of targeted therapies. Due to the variation in molecular phenotypes in BC within a solid tumor as well as between primary and metastatic populations, it is vital to identify the molecular signatures of cancer in a patient to inform the most effective course of clinical action.

1.1.4. Clinical Diagnostics Tools for Cancer

The first step in determining a course of action for any malignancy is diagnostics, which confirms the presence of tumor and provides insight into tumor location, molecular phenotype, and stage. Most clinical imaging modalities are aimed at determining the size and anatomical location of the primary tumor. Techniques such as magnetic resonance imaging (MRI), positron emission tomography (PET), single-photon emission computed tomography (SPECT), X-ray computed tomography (CT) and ultrasound could all provide vital information about a primary tumor⁴²⁻⁴⁴. Of these modalities, MRI and CT provide anatomical and spatial information with unlimited depth of penetration, whereas PET, CT and SPECT provide further molecular information about the lesions. The sensitivity and specificity of MRI can be improved through the use of magnetic contrast agents (contrast-enhanced MRI), providing earlier detection and improved delineation of tumor margins.

An ideal imaging modality should have the potential to give insight in to both the anatomical location and molecular phenotype of tumor lesion. A prospective diagnostic regimen in cancer should involve screening of cancer using specific diagnostic markers, following the tumor through treatment in real time and forming a feedback loop for therapy guidance⁴⁵. Another aspect of lesion detection involves identification of biomarkers specific to cancer phenotypes, tumor stage, metastatic potential, and response to therapy^{46,47}. Although great strides have been facilitated by

these modalities, conventional modalities fail to provide information regarding the molecular phenotypes and lack sensitivity to detect early stage micro lesions.

1.2. Optical Imaging

Optical imaging uses non-ionizing radiation to visualize and characterize the anatomical and/or molecular features of a particular disease state. Optical imaging is non-invasive, low-cost and portable, with a wide range of applications in the microscopic and macroscopic imaging. Optical imaging in visible, infrared (IR) and near infrared (NIR) regions can provide detailed images at levels spanning from organs and tissues to smaller structures at the cellular and molecular levels. Optical imaging confers several advantages over conventional clinical imaging modalities, notably that it avoids exposing patients to harmful ionizing radiation. The use of non-harmful radiation sources over shorter periods makes them safer for performing repeated longitudinal procedures, which can be used to monitor disease progression or create an adaptive therapeutic regimen. Additionally, physicians can be aided by optical imaging deployed in combination with clinical techniques like MRI, CT or X-rays, to provide a multi-modal approach to disease monitoring and detection.

Optical imaging can be broadly classified into planar or tomographic imaging approaches. Planar imaging involves capturing emitted light from biological components (molecules, cells and tissues) or exogenous contrast agents. Planar imaging in mouse models involves exposing the animal to broad beam or excitation light and capturing the emission using a charge-coupled device (CCD) camera. Whole body fluorescence imaging is a major application of this technique called fluorescence reflectance imaging (FRI). Bioluminescence is another example of planar imaging where signal can be detected in the absence of an excitation source, through the incorporation of a luciferase reporter gene. This imaging technique is a highly attractive, easy to implement tool for high throughput imaging⁴⁸⁻⁵⁰. Tomographic biological imaging uses the intrinsic tissue absorption

and scattering to study the image at different depths⁵¹. In biomedical applications, different points of the tissue boundary are illuminated, and the light patterns are collected at the boundary using a CCD camera. Fluorescence acquisition in combination with the tomographic scheme led to the development of fluorescence molecular tomography (FMT).

One of the most successful clinical translation of optical imaging is endoscopy, in which a flexible tube with a light source is inserted to illuminate the organ of interest. Endoscopy is a procedure usually performed for visualization and exploration of the digestive track based on the patient's symptoms^{51,52}. It is also used in minimally invasive surgery, providing visualization to the surgeons. Optical coherence tomography (OCT) is another low cost method, typically using NIR for sub-surface visualization with various applications in ophthalmology and recently in cardiology and dermatology⁵³. Other commercially available methods include photoacoustic imaging, Raman spectroscopy, and diffuse optical tomography (DOT). Hence, optical imaging is a low-cost, non-invasive, fast and efficient technique used by clinicians and scientists alike in disease diagnosis, treatment and research.

1.2.1. Optical Contrast Agents

Biomedical optical imaging can be a non-invasive, non-ionizing tool for real time probing of structural and functional changes in disease states^{54,55}. Optical imaging techniques exploit photo-physical effects including absorption, scattering and emission of light caused by innate interactions between light and tissue via endogenous contrast agents or detect the emission caused by exciting exogenous contrast agents targeted to a disease location. Most biomedical optical applications depend on exogenous contrast agents, whose chemical and spectral properties can be selected, based on the need of the application, ranging from cellular mechanism studies to cancer diagnostics. Exogenous contrast agents with excitation and emission in the visible region are mainly used for cellular and microns-deep sub-surface imaging. Based on chemical and spectral properties, contrast

agents can be divided into families of non-specific dyes and probes with molecular targeting capability. Non-specific fluorophores like fluorescein (FITC), methylene blue, toluidine blue, crystal violet and indocyanine green (ICG) have been used in a range of cellular and select surgical imaging applications⁵⁶. However, photo bleaching and lack of specificity to disease limit their efficacy in generating viable signal to noise ratio. Targeted optical contrast agents like bioluminescent proteins and fluorescent probes are widely used in cellular level and *in vivo* applications⁵⁷⁻⁵⁹. A typical molecularly targeted probe consists of the fluorophore, a ligand and in some cases, a linker based on the application⁶⁰. The ligand is used to recognize a biomarker typically either overexpressed or activated on the diseased cells caused by underlying biological pathways. Targeted organic probes such as antibodies and peptides modified with optical reporters can have high specificity to disease lesion. Antibody conjugated probes targeted to receptors as EGFR, HER2 and VEGF have been explored and optimized *in vitro* and in preclinical applications^{59,61,62}. Anti-EGFR antibody, cetuximab, was fluorescent labelled and approved by FDA for imaging head and neck cancers⁶³. Antibody conjugated probes are highly effective in labelling fresh biopsies, resulting in better signal to noise ratio, but are unfavorable due to faster clearance and concerns of invoking an immune response from the host⁶⁴. Peptides have been used as ligands to specifically bind to overexpressed receptors on cancer cells. For example, EGF has been labelled with Alexa 647 to show increased fluorescence signal in excised human oral tissue from in epithelial cancers⁶⁵, and RGD-targeting peptides have been conjugated with Cy5.5 dye to show increased tumor targeting abilities in subcutaneous xenograft models⁶⁶. Although the use of peptides as ligands has better biodistribution compared to larger molecular weight antibodies, there is sub-optimal control and scope for structural modification while retaining initial targeting abilities⁵⁶. Inorganic optical reporters have also been developed, including the use of nanoparticles (NPs) possessing physical and optical properties including spectra in favorable wavelength windows for application in biomedical imaging. Semiconductor quantum dots have improved photo stability compared to organic fluorophores, and their size dependent optical properties allow for

imaging of multiple biomarkers. First generation quantum dots, i.e., CdSe or CdS nanoparticles, have been tested in *in vivo* models but have limited translation due to toxicity⁶⁷.

1.2.2. Wavelengths for Biomedical Imaging

Conventional contrast agents use excitation wavelengths in the ultraviolet (UV) (e.g., quantum dots) or visible region (E.g. Alexa dyes, Cy5.5, FITC, etc.) that are suitable for *in vitro* and microscopic imaging purposes. However, these wavelength regions are inadequate for macroscopic and large-scale imaging. The carcinogenic nature of excitation UV rays and visible light presenting with low imaging penetration depth (< 1 cm) limits their applications. For tissue imaging either in animal models or patients, a wavelength range with higher sensitivity and deeper penetration capabilities is vital.

Use of NIR light in biological imaging offers several advantages over other wavelength ranges due to less attenuation and tissue auto-fluorescence in this region. Total attenuation, owing to the cumulative effect of scattering and absorbance in tissue, determines the effectiveness of a contrast agent. Most biomolecules have low absorbance in the NIR range, limiting the interaction of excitation light with healthy non-diseased tissue. This enables efficient transmission of light to the target region, possibly containing the exogenous contrast agents. Any medium will absorb a fraction of incident light per incremental path length traveled within the medium. Absorption coefficient, μ_a , is defined as shown in equation 1 where T is the transmitted fraction of incident light and L represent the path length⁶⁸.

$$\mu_a = -\frac{1}{T} \frac{\partial T}{\partial L} \quad \text{Equation 1}$$

The absorption coefficient of biological tissue containing strongly absorbing components such as melanin, oxygenated blood containing hemoglobin, and water drops drastically at wavelengths above 650 nm. Water absorption increases in the infrared region at wavelengths greater than 900 nm, with significantly higher absorption coefficient above 3000 nm^{69,70}. The low absorption of

biological components thereby causes minimal auto-fluorescence generated by tissue, resulting in lower interference of signal and hence improved sensitivity to image contrast agents.

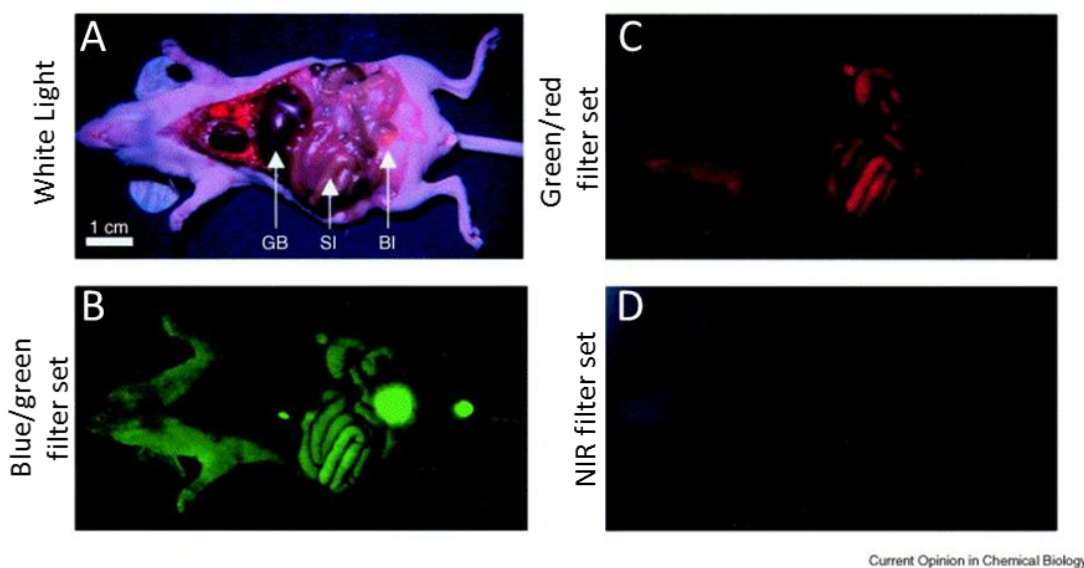


Figure 1.5- Tissue auto-fluorescence in different wavelength ranges

Athymic nude mouse dissected to expose healthy organs was imaged in (A) white light followed by exposure to (B) blue/green and (C) green/red wavelength range depicting high tissue auto-fluorescence with almost negligible levels in the (D) NIR range. Figure reproduced with permission from Frangioni *et al*, In vivo near-infrared fluorescence imaging *Cur. Opin. in Chem. Bio*, 7, 626 (2003). (License number: 4494961248938)

Scattering of light is the deviation of the path of incident rays due to the presence of a medium; in the case of biomedical imaging, this would be due to cell and tissue structural components. Rayleigh and Mie scattering are commonly used terms while calculating scattering effects in biomedical applications. Rayleigh scattering occurs in cases when light interacts with particles or elements with size considerably smaller than the wavelength of light. Mie scattering plays a role in cases where medium size is comparable to the wavelength. Both Rayleigh and Mie scattering

dictate an inverse relationship between wavelength and scattering coefficient. In the case of Rayleigh scattering, scattering of light is proportional to λ^{-4} meaning higher scattering at lower wavelength (UV, blue green) and lower scattering at comparatively higher wavelengths (red, IR)⁶⁸.

Cumulatively, the low-attenuation and auto-fluorescence enable penetration of NIR light to depths greater than one cm. Imaging in the NIR region is considered safe with minimal risk to biological tissues with enhanced depth and sensitivity as compared to imaging in the visible.

1.3. Short Wave Infrared (SWIR) imaging

One of the main limitations for clinical and pre-clinical applications of optical imaging is the lack of sensitivity, resolution and deep tissue penetration capabilities of conventional contrast agents. However, with the NIR and further wavelengths possessing the optical advantages of greater total attenuation coefficient and deeper penetration, there is a possibility for clinical translation of biomedical optics. Various biological windows for imaging have been defined based on optical properties of normal tissue including absorbance, scattering and depth of penetration. The NIR region (700-1000 nm) is called the “tissue transparent window” with deeper imaging capabilities than the visible and UV counterparts. Further into the infrared, the second ‘tissue transparent window’ using SWIR (1000 nm-1700 nm) has comparably lower absorbance than in the first window (700 nm- 1000 nm) but greater reduction in scattering, opening an avenue for imaging at unprecedented depths⁷¹.

One of the major obstacles to imaging in the SWIR region has been the lack of sensitive detectors to capture light of such wavelengths. Detectors in this range are challenging to develop since commonly used silicon (Si) detectors are inefficient beyond 1100 nm, as the Si material becomes transparent to the photons⁷². Other detectors like germanium (Ge) or indium antimonide (InSb) are more sensitive to SWIR but have low quantum efficiency⁷³. The indium gallium arsenide (InGaAs)

detectors are more efficient in detecting SWIR emission and are used in most current SWIR cameras.

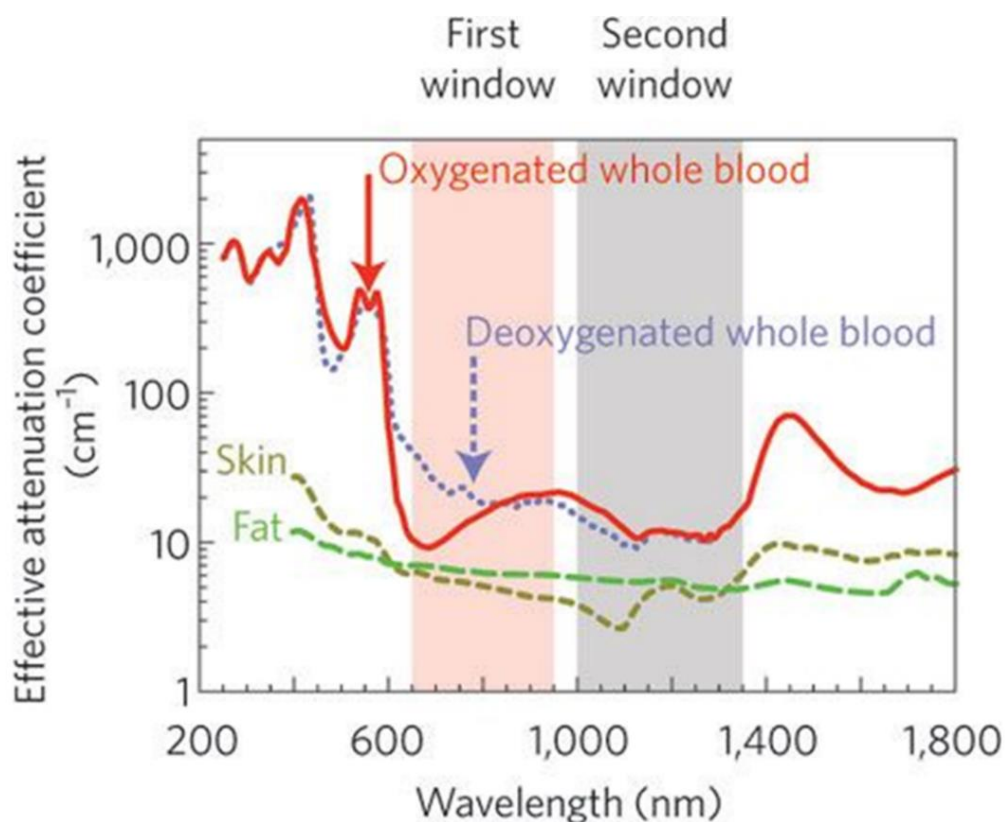


Figure 1.6- Effective attenuation coefficient of biological components as a function of wavelength

Oxygenated blood containing hemoglobin and melanin, which are major contributors to absorption, shows significant reduction in attenuation at wavelengths $>650\text{nm}$. While both the first and second biological windows possess significantly reduced attenuation coefficients in comparison to visible region, the SWIR region (1000nm-1700nm) is considered optimal for *in vivo* imaging with the lowest attenuation caused by biological components. Figure reproduced with permission from Smith et. al. Second Window for *In Vivo* Imaging. *Nature Nanotechnology* 4(11): 710-711 (2009) (License number: 4494971426337)

1.4. Nanoparticles as Biological Agents

Nanotechnology is an emerging field with a wide range of applications in the electronics industry, optics, medical imaging, disease diagnosis, delivery, and therapeutics. Nanoparticles (NPs) are defined as particles within the size range of 1-1000 nm, which mimics the range of many biological assemblies and presents a large surface area that can be tailored biochemically for desired cellular and tissue interactions. NPs are currently in the forefront of research as delivery vehicles for medical imaging and therapy. While there is a plethora of novel therapeutics and contrast agents emerging that capitalize on our increasing understanding of molecular cancer biology, there is a vital need to develop efficient delivery approaches that will enable clinical applications.^{74,75} The inadequate translation of these agents to date is mainly due to the lack of an effective way to deliver therapeutic moieties or contrast agents to the lesion site with minimal side effects and negligible damage to the healthy tissue. An ideal delivery vehicle in cancer should be able to: (1) increase selectivity of drug/contrast agent to malignant cells with improved pharmacodynamics (PD), pharmacokinetics, (PK) and active targeting^{76,77}; and (2) evade biological barriers and reach lesion sites efficiently⁷⁸. The key advantages of NPs include their unique biological interactions based on their physical and chemical properties including charge, size, shape and surface chemistry. Their high surface area to volume ratio also allows for loading therapeutics at a high concentration and display of targeting ligands, which can increase localized effect by controlled release of drug at targeted cancer cells⁷⁹. Additionally, integrating the diagnostic and therapeutic cargo in NPs holds promise for multimodal theranostic particles. Consequently, nanotechnology when combined with cancer biology research could hold enormous potential to overcome current challenges in cancer diagnostics and therapy.

Among the key attributes of nanoparticles that can be manipulated for prolonged circulation and improved delivery to lesion are their size, surface properties and presence of active targeting moieties.

1.4.1. Nanoparticle size

Size plays a major role in determining the *in vivo* biodistribution and clearance of NPs. These effects have been extensively studied in the case of spherical geometry of NPs. The ideal range for cancer applications is estimated to be within the range of ~10 nm - 200 nm⁸⁰. Ideally, the NPs should have good circulation half-life while being able to clear out of the body to avoid toxicity by prolonged retention. While circulation half-life depends on an interplay of size, charge and surface chemistry, nanoparticles with smaller sizes ~10 nm tend to show better half-life with the kidneys being the primary organ of clearance⁸¹. The reticulo-endothelial system (RES), specifically the liver and spleen, becomes the primary source of clearance for particles in the range of 20 nm-200 nm⁸².

During the development of a tumor, angiogenesis occurs to form a supply of blood vessels to the cluster of cells responsible for delivering oxygen and necessary nutrition. Vascular endothelial growth factor (VEGF-A) present on cancerous cells drives rapid angiogenesis, the uncontrolled nature of which causes the leakiness and abnormal flow of the blood vessels in tumors^{83,84}. The 'leaky' vasculature allows for higher accumulation of NPs in tumor due to the enhanced penetration and retention (EPR) effect⁸⁵. However, the permeability of the solid tumor is inversely related to nanoparticle size⁸⁶. The pore size of the tumor and vasculature also varies based on location of the tumor. In addition, the endothelial and basal membrane properties of the host organ can also influence the selective localization of NPs. For instance, the bone space consists of a discontinuous basal membrane and large gaps between the endothelial cells, facilitating greater accumulation of particles caused by EPR effect, whereas endocrine glands such as adrenals, which have a continuous basal membrane with slightly fenestrated endothelial cells, have lower accumulation of similarly size particles compared to spaces like the bone marrow. The cumulative effect of tumor and endothelial pore size dictates the localization of NPs based on size.

1.4.2. Nanoparticle surface properties

Although size plays a major role in delivery of NPs, the high surface to volume ratio compared to larger moieties dictates that controlling the surface characteristic plays a crucial role in their *in vivo* delivery and clinical translation. Properties including charge and the presence and density of functional groups on the nanoparticle surface are defining factors for solubility and nanoparticle-cell interactions, which are major determinants of the effectiveness of drug delivery. Charge is a key determinant of cellular localization, where highly positively charged NPs tend to show higher cell uptake compared to neutral or negatively charged particles⁸⁷. However, this high rate of accumulation also leads to increased non-specific binding to normal cells, and to cytotoxicity combined with short half-life. In contrast, negatively charged NPs have limited uptake in cells⁸⁸. Moreover, the walls of blood vessels are negatively charged, which may cause repulsion with high negative charge-bearing particles. In addition to having an effect on cellular localization, NP surface charge can also vary the overall biodistribution. For example, positively charged particles show enhanced penetration of the otherwise protected blood brain barrier (BBB)⁸⁹, which overshadows the need to reduce non-specific interactions. The key is to find a balance for a particular application between effective cellular interaction and minimal non-specific binding. To this end, particles engineered with low negative or low positive charge have been shown to be optimal for most common applications. Since non-specific interactions cannot be eliminated, some particle loss in circulation is inevitable. The objective then is to engineer a nanoparticle system to minimize these non-specific losses.

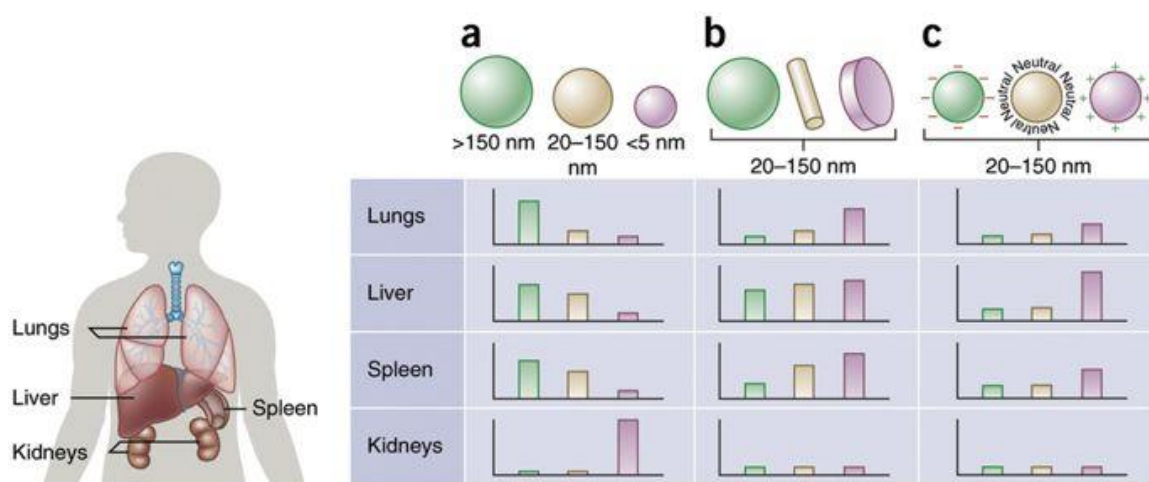


Figure 1.7- Effect of size and surface properties of NPs on biodistribution.

A schematic representing the level of accumulation of NPs based on physical properties. (a) For spherical particles, the major organ of localization of NPs with size <5 nm is kidneys, whereas NPs >20 nm tend to accumulate in the RES organs of liver, spleen, and lungs. (b) For NPs within the 20-150 nm size range, non-spherical shape tends to result in increased localization to RES organs. (c) Electrostatic interactions also influence organ distribution, with positively charged NPs showing increased levels in the RES organs. Figure reproduced with permission from Blanco *et al*, Principles of nanoparticle design for overcoming biological barriers to drug delivery. *Nature biotechnology* 33.9 (2015): 941. (License number: 4494980531342)

1.4.3. Actively Targeted Nanoparticles

Even though passively targeted NPs have innate tumor localization properties via EPR, these are not optimal for clinical translation due to limited specificity and off-target binding behaviors. Active targeting is a design strategy employed in current NP development to overcome barriers at a cellular level and ensure higher specificity to cancer cells. The most common mode of active targeting utilizes receptor-mediated uptake, thereby increasing the specific uptake NPs when

present in the diseased cell vicinity. The specificity leading to reduced off-target interaction with healthy tissue is highly beneficial in therapeutics and contrast agents, in delivering effective dosages and reducing toxic side effects.

The first step in developing targeted NPs is the identification of surface receptors, molecules and biomarkers that are upregulated in the disease microenvironment, cells or tissue, which helps formulate efficient ligands for conjugation with NPs. Ligands, can range from small molecules, peptides, carbohydrates, antibodies and aptamers^{79,90}. Various factors contribute to the design consideration for an effective targeted NP system including ligand concentration⁹¹, binding affinity, NP size and shape⁹². The density of ligand on NP surface is a major determinant in targeting affinity both *in vitro* and *in vivo*. The increase of ligand density results in ligands being in close proximity to each other, such that one ligand binding to the receptor will facilitate the binding of its neighbors⁹³. These multiple interactions induce the receptors to cluster, leading to folding of the cell membrane and eventual internalization⁹⁴. Thus, increasing the ligand density is an excellent strategy for low binding affinity ligands to increase the multivalent binding or avidity, a better approach than monovalent binding. The correlation between ligand density and cellular internalization *in vitro* usually follows a non-linear pattern. With the increase in density beyond a certain “saturation point”, there can be reduction in cell binding caused by either steric hindrance or non-optimal orientation of the ligand^{91,95}. On the other hand, ligand affinity is also a vital determining factor, usually proportional to cellular uptake. However, use of high binding affinity NPs in solid tumors could be detrimental as a consequence of the “binding-site barrier” observed in studies with highly selective antibodies⁹⁶. This is a result of high affinity moieties binding to the surface of solid tumors so strongly that they do not penetrate into the tumor interior⁷⁷. External factors such as route of administration and interactions of NPs with proteins in circulation also affect active targeting ability *in vivo*. Although ligand conjugated NPs can have high selectivity, the cancer cell receptors can only recognize and interact with targeted NPs in their vicinity, the

extent of which is governed mainly by the biodistribution. Therefore, varying NP architectural properties can be used to manipulate distribution via the EPR, while active targeting can ensure enhanced retention favorable for imaging agents and selective internalization in cancer cells. Various cancer markers have been widely explored for active targeting via NPs including transferrin receptor⁹⁷, folate receptor⁹⁸ and certain cell surface integrins⁹⁹.

Ligand functionalization strategies are key for developing competent NP systems, as the ligand-NP bond must withstand and overcome biological barriers to effectively reach the target site. Additionally, as ligand density is directly correlated to NP avidity, control over the surface concentration through conjugation also plays an important role. Attachment can be achieved broadly either via physical adsorption, via binding/affinity complexes, or using covalent bonds, in some cases with a cross-linker. The conjugation of ligand can be done either to the components of NPs pre-formulation or directly on to the surface of completely formed NP. Non-covalent conjugation methods include adsorption to the drug binding sites on surface or via streptavidin-biotin interactions between streptavidin-NPs and biotinylated ligand complexes⁹². Covalent conjugation involves crosslinking the reactive groups present on NPs and ligand, mainly carboxyl, amine, sulfhydryl or aldehyde groups. Additionally, a mechanism called 'click chemistry,' featuring a reaction between azide and alkyne or phosphine groups to form a high yield, stable covalent bond, has been used¹⁰⁰.

Active targeting can be potentially extremely beneficial for clinical oncology applications. Nonetheless, there is currently a lack of knowledge regarding the behavior of targeted NPs in uncontrolled disease environment in humans, relative to that in pre-clinical studies structured to evaluate individual components meticulously. With select-targeted NPs in the clinical development stage, there is a widening avenue to realize the benefits of the molecular cancer biology through more effective NP designs.

1.4.4. Barriers for *in vivo* use of nanoparticles

The efficacy of NPs in a pre-clinical or clinical setting is dependent on the ability of NPs to cross biological barriers to reach the target lesion site. Barriers are present at the systemic, organ and cellular levels, and the design of NPs needs to be tailored to overcome these in a manner that is based on tumor location and type.

The route of administration determines the initial distribution of NPs in the tumor. Nanoparticles can be formulated for various routes of administration including intravenous, inhalation, oral or intraperitoneal administration. Various design characteristics also dictate the circulation of the NPs. In the case of tumor in the lungs, which experiences first pass circulation, inhalation or intravenous administration are optimal with particles $>100\text{ nm}^{101}$. Whereas for delivery via systemic circulation, the size modulation should be to avoid rapid clearance by the RES system and to attain sufficient concentration of nanoparticle in tumor required for imaging or therapeutic purposes. With oral administration, the nanoparticle surface properties need to be altered to maintain stability in the acidic conditions of the gastrointestinal track and to adhere to and cross its mucosal linings^{102,103}. Intraperitoneal administration is used more extensively in the preclinical than in the clinical setting. It can be effective in cases where intravenous administration is impractical or if the tumor is located near the peritoneal cavity, e.g. ovarian cancer. Yet, it is likely to meet with varied results based on the precise site of injection and clearance via local lymph node system.

For intravenous administration, there is a high chance of multi-organ clearance, mainly by the RES. The primary method for minimizing RES clearance is to create a hydrophilic coating on the nanoparticle. Many polymeric NPs are coated with polyethylene glycol (PEG) to increase circulation, which has been the most widely used method for both organic and inorganic particles

^{104,105}.

On a cellular level, any engineered NPs should be able to bypass the endocytic pathway leading to the lysosome. The two main mechanisms of cellular endocytosis are clathrin and caveolin-mediated pathways. Clathrin-mediated endocytosis eventually leads to degradation in the lysosome, whereas the caveolin-mediated pathway does not explicitly involve the lysosome; nonetheless caveolar vesicles can merge with late endosomes and thus their cargoes may be degraded in lysosomes. Therefore, in both cases endosomal escape of NPs must occur prior to the lysosome stage¹⁰⁶. The size of the nanoparticle controls the cell intake pathway to a certain extent. Internalization of particles with size < 200 nm involves clathrin-mediated mechanism, whereas with an increase in size there is a tendency towards caveolin-mediated pathways; however, there is not a clear size distinction¹⁰⁷. Ligand conjugation via adsorption or covalent bonding can influence the process of cellular-internalization. Albumin and folic acid are examples of ligands, which can facilitate caveolin-mediated uptake of NPs¹⁰⁶. Actively- targeted NPs to tumor biomarker may also enable receptor-mediated cellular internalization without degradation by lysosomal compartment.

1.5. Rare earths nanoparticles as optical imaging agents

Nanoparticles with the ability to be tracked using light in the optical imaging space will present interesting translational opportunities in the area of molecular imaging. Various NPs have been developed for *in vivo* optical imaging applications including single walled carbon nanotubes (SWNTs)^{108,109}, gold NPs, and quantum dots. The major drawbacks to these technologies are toxicity due the presence of harmful elements¹¹⁰ or low quantum yield¹⁰⁸. Factors influencing the selection of an efficient imaging agent includes quantum yield, depth of imaging in tissue, biocompatibility and biodistribution.

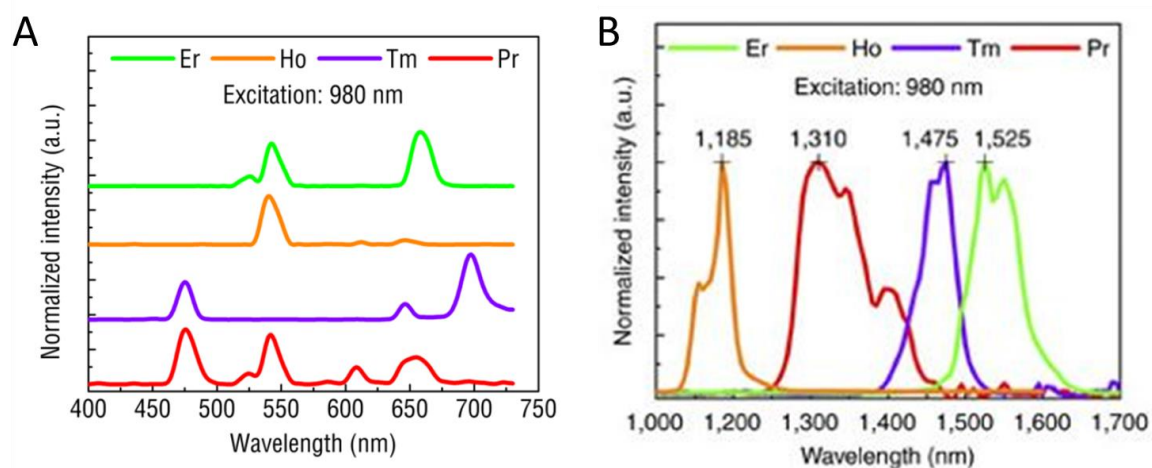


Figure 1.8- Emission spectra of rare earth nanoparticles

(A) Up-conversion of RENPs when excited with NIR light varies with core dopant. (B)

Similarly with downconversion, when excited with 980 nm varying core dopants results in

distinct narrow emission spectra. Figure reproduced with permission from Naczynski *et al* -

Rare-earth-doped biological composites as in vivo shortwave infrared reporters- *Nature*

Communications volume 4, Article number: 2199 (2013). (License number: 4494991303177)

The rare earth nanoprob (RENPs) are crystalline structures possessing pristine optical properties highly favorable for biological imaging. RENPs are inorganic nanocomposites with NaYF_4 as host materials generally synthesized in a core-shell structure, wherein the core consists of the host and RE elements as dopants with an undoped shell comprising just the host material¹¹¹. The function of the shell is to protect the core crystal structure and increase optical efficiency. The REs are excited with NIR wavelength (980 nm) in the ‘first transparent window’ and emit in the SWIR (1000-1700 nm) ‘second transparent window’ range, which allows for higher transmittance of both excitation and emission light to and from biological structures of interest. Additionally, RE probes when excited with NIR wavelength emit light in both the SWIR and visible region via upconversion and

downconversion mechanisms, respectively. While the SWIR emission can be used for *in vivo* deep tissue imaging, visible emission is effective in validating *in vitro* phenomena. RENPs also have tunable optical properties, as the emission wavelength of the RENPs varies with the dopant of the core of the nanoparticles. It is thus possible to generate a library of multispectral nanoparticles, which enables imaging of multiple biological structures or phenomena by capturing the emissions across discrete wavelengths, while being excited by the same NIR wavelength.

1.5.1. Synthesis of Rare Earth nanoparticles

RENPs are synthesized typically via a solvothermal decomposition process, which is a liquid based reaction wherein the compounds dissolved in an organic or aqueous solution are allowed to react under specific temperature and pressure conditions^{112,113}. Specifically, for the synthesis of RENPs, the core and shell RE trifluoroacetates precursors are dissolved in oleylamine or oleic acid separately. The precursor solution with the core components is heated under inert conditions to a high temperature of 340°C, facilitating interactions between precursor components and formation of core particles via burst nucleation. The shell precursor solution is then added to form the core-shell structured NPs. The modulation of factors like temperature, time and type of solvent and precursors can control the size, shape and crystalline morphology of the RENPs¹¹²⁻¹¹⁴. The size and the crystalline structure dictate the optical properties of the NPs to a certain extent, where a hexagonal structure is shown to exhibit higher upconversion efficiencies versus a cubic phase, and a decrease in size to nanoscale reduces the emissions in both visible and SWIR range. Nevertheless, since the nano size range is far more viable for biological applications, the smaller size range is opted for such purposes.

The RENPs have a unique set of features, which can be used to create a versatile *in vivo* imaging platform for disease tracking. However, the ceramic nature of the particles causes high cytotoxicity,

and the high hydrophobicity leads to poor biodistribution making it challenging for biological applications.

1.6. Albumin based nanoparticles

1.6.1. Albumin for biomedical applications

The fate of a biological agent as it journeys through the body is described by its absorption, distribution, metabolism and elimination along with toxicological issues (ADMET). The delivery of drug moiety to diseased cells dictated by absorption and distribution is as important as the clearance of drug from the body, largely controlled by metabolism and elimination. Most drugs do not have desirable distribution qualities, which calls for modification of the surface chemistry or loading the drug in a vehicle possessing optimal ADMET properties. While designing a delivery vehicle, it is important to consider the binding affinity of the cargo and possibly targeting ligands. With the presence of multiple ligand binding pockets, high circulation time and interaction with cellular receptors¹¹⁵, albumin is a beneficial choice as the basis of a delivery vehicle. Human serum albumin (HSA) is the most abundant protein present in the plasma at a concentration of ~600 μM ensuring minimal immunogenic reaction and biocompatibility¹¹⁶. The 3-dimensional structure of albumin is heart shaped with multiple hydrophobic binding pockets, naturally used for transport of various fatty acids and steroids¹¹⁷, which can be used for non-covalent binding of hydrophobic or amphiphilic cargo like drugs or ligands. Albumin also has carboxyl and amine groups, which can be used for covalent binding using bioconjugation techniques. The long circulation time of albumin-based systems is mainly due to recycling via the Fc receptor (FcRn) present on most endothelial cells. Gp60 is another receptor that, when bound to proteins like albumin, triggers a caveolin-mediated internalization eventually leading to cellular transcytosis, protecting albumin from lysosomal degradation^{118,119}. Additionally, albumin has an overall surface negative charge

leading to better water solubility¹¹⁶. Hence, albumin is an attractive choice for developing novel drug or contrast agent delivery mechanisms.

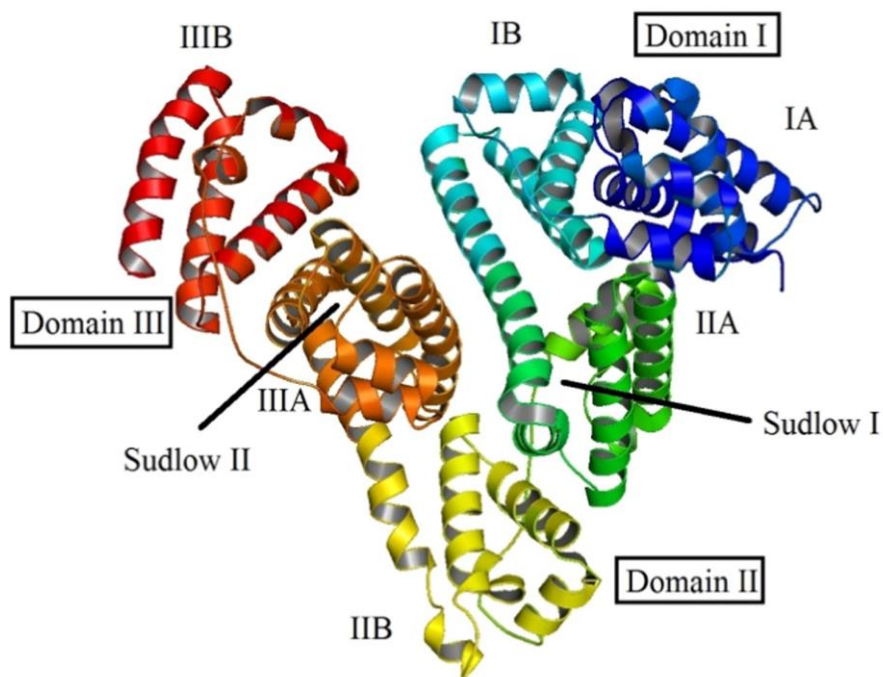


Figure 1.9- Three-dimensional structure of albumin

Schematic representing tertiary structure of human serum albumin in a stearic acid solution, depicting the three domains. Figure reproduced with permission from Moradi *et al* - Spectroscopic study of drug-binding characteristics of unmodified and pNPA-based acetylated human serum albumin: Does esterase activity affect microenvironment of drug binding sites on the protein?- Journal of Luminescence -Volume 160, 351-361 (2015). (License number: 4501051414330)

1.6.2. Albumin based formulations in the clinical path

Owing to the biocompatibility and other advantages, the FDA for clinical use has approved various albumin-based formulations. Albumin modified moieties have been used for therapeutic application in type-2 diabetes¹²⁰, emphysema, other cancers including leukemia and melanoma,

viral infections, and multiple sclerosis, along with the use of radiolabeled albumin in various diagnostic modalities. Abraxane represents one of the most successful clinical applications of albumin nanomedicine, with use in metastatic BC, non-small cell lung cancer and pancreatic cancer¹²⁰. Abraxane is a nanoparticle-based system employed for increasing efficacy of paclitaxel, one of the most effective chemotherapeutic drugs. The NPs with size ~130 nm consist of the outer layer of albumin encapsulating paclitaxel. The low solubility and severe side effects caused by Taxol (an organic solvent-based formulation of paclitaxel) rendered the need for further modification. In comparison with Taxol, Abraxane exhibits increased circulation and preferential localization to tumor site via EPR¹²¹. Furthermore, the presence of secreted protein, acidic and rich in cysteine (SPARC) on tumors has shown to promote increased uptake of Abraxane due to interactions between albumin and SPARC¹²². It is hypothesized that SPARC and Gp60 mediated accumulation of albumin in combination supports enhanced tumor uptake. Other chemotherapeutic drugs like doxorubicin (DOX), when modified by covalently binding to albumin, have also shown to exhibit better selectivity and anti-tumor activity while avoiding side effects caused by free drug¹²³. The validation and successful application of albumin-based formulations in various pre-clinical and clinical studies proves the promise of albumin as a biological delivery agent.

1.7. Dissertation overview

With the increasing need for personalized medicine in every disease, it is imperative that the understanding of disease biology is translated to a clinical setting. Cancer, in particular, is a disease space where diagnostics and therapy require high precision levels due to its vast variability among patients and considerable heterogeneity within individual lesions. Current diagnostic imaging modalities either lack the sensitivity to make accurate predictions or are very expensive for detection and molecular labelling of micro-lesions. There is an acute need for a versatile imaging tool for sensitive prediction of the disease state and non-invasive molecular phenotyping. Optical imaging is a highly adaptable biomedical technology to track specific molecular events at a low

cost with good resolution without the harmful effect of ionization. However, several challenges, such as poor penetration depth due to tissue absorbance and scattering, must be overcome for optical imaging to realize its clinical potential.

We have designed optical contrast agents based on rare earth (RE) nanoproboscopes, which absorb near infrared (NIR) radiation (980 nm) and emit in the short wave infrared (SWIR) region (1000- 1700 nm), allowing for improved tissue penetration and detection depth. RE probes are optically stable (no photo bleaching or quenching effects) and, when encapsulated in albumin, form a biocompatible system that can detect and monitor cancerous lesions *in-vivo*.

The vision for this dissertation is to leverage the biocompatible and disease targeting features of RE nanoparticles to develop an *in vivo* imaging platform for RE imaging probes capable of tracking multi-organ, metastatic cancer lesions with varied molecular signature. Chapter 2 details the effectiveness of actively targeted ReANCs in detecting micro-lesions in a lung metastatic model of BC. Chapter 3 focuses on the ability of ReANCs to localize differentially to distinct metastatic sites like adrenal glands, lungs, and bone marrow tested in various biomimetic BC murine models. Here, we show the potential of ReANCs for non-invasive optical imaging of micro-lesions prior to conventional diagnostic modalities. Chapter 4 investigates the potential of tunable wavelengths of ReANCs by using multiple ‘colors’ to target specific molecular signatures. This capability can unleash the potential of the ReANCs to molecularly profile in a non-invasive ‘optical biopsy’. Chapter 5 explores the potential use of an alternative formulation based on polyethylenimine (PEI) as an encapsulation method for RENPs, with potential applications in the gene delivery.

CHAPTER 2

CXCR-4 TARGETED, SHORT WAVE INFRARED (SWIR)

EMITTING NANOPROBES FOR ENHANCED DEEP TISSUE

IMAGING AND MICROMETASTATIC CANCER LESION

DETECTION

Note: This chapter has been reproduced with permission from the following publication under license 4436001376470

Zevon M, Ganapathy V, Kantamneni H, Mingozi M, Kim P, Adler D, Sheng Y, Tan MC, Pierce M, Riman RE, Roth CM, Moghe PV. CXCR-4 Targeted, Short Wave Infrared (SWIR) Emitting Nanoprobes for Enhanced Deep Tissue Imaging and Micrometastatic Cancer Lesion Detection. *Small*. 2015;11(47):6347-57. doi: 10.1002/sml.201502202. PubMed PMID: 26514367; PMCID: PMC4763715

2.1. Abstract

Realizing the promise of precision medicine in cancer therapy depends on identifying and tracking of cancerous growths in order to maximize treatment options and improve patient outcomes. However, this goal of early detection remains unfulfilled by current clinical imaging techniques that fail to detect diseased lesions, due to their small size and sub-organ localization. With proper probes, optical imaging techniques can overcome this limitation by identifying the molecular phenotype of tumors at both macroscopic and microscopic scales. In this study, we propose the first use of Nanophotonic short wave infrared technology to molecularly phenotype small sub-surface lesions for more sensitive detection and improved patient outcomes. To this end, we designed human serum albumin encapsulated rare-earth (RE) nanoparticles (ReANCs)^{124,125} with ligands for targeted lesion imaging. AMD3100, an antagonist to CXCR4 (a chemokine receptor involved in cell motility and a classic marker of cancer metastasis) was adsorbed onto ReANCs to form functionalized ReANCs (fReANCs). Functionalized nanoparticles were able to discriminate and preferentially accumulate in receptor positive lesions when injected intraperitoneally in a subcutaneous tumor model. Additionally, fReANCs, administered intravenously, were able to target sub-tissue tumor micro-lesions, at a maximum depth of 10.5 mm, in a lung metastatic model of breast cancer. Internal lesions identified with fReANCs were 2.25 times smaller than those detected with unfunctionalized ReANCs ($p < .01$) with the smallest tumor being 18.9 mm³. Thus, we present an integrated nanoprobe detection platform that allows target-specific identification of sub-tissue cancerous lesions.

2.2. Introduction

Breast cancer, the most common form of cancer among women, is a heterogeneous disease with substantial inter-individual variability in the molecular phenotypic expression.¹²⁶ Despite recent advances in treatment, 40% of breast cancer patients die as a result of distant site metastasis, commonly disseminated from the breast tissue to the patient's lungs, bones or liver.¹²⁷ Early

detection of small metastatic populations in these organs is critical to reducing the burden of metastatic disease. Development of sensitive and specific methods for non-invasively identifying these cancerous lesions can aid in determining optimal treatment regimens and improving patient outcomes. Unfortunately, current diagnostic methods lack the sensitivity and specificity to provide actionable biological readouts during cancer therapy.^{128,129} Techniques such as MRI, ultrasound and PET/SPECT, though capable of anatomical imaging and detection of breast tumors, are limited by their high cost, lack of targeted contrast agents (MRI) and use of radionuclides (PET/SPECT). Hence, these techniques are unable to provide molecular information about lesions in a low cost, high-resolution platform, which is pivotal to determining treatment regimen and patient response to therapy.

Optical imaging is a promising technique for high-resolution detection that can facilitate molecular classification of disease lesions and avoid the hazard of radionuclides used in PET/SPECT imaging. Novel optical imaging tools have the potential to aid clinicians in detecting small metastatic tumors and tracking pharmacological agents, facilitating selection of appropriate therapeutic agents for nascent lesions and monitoring of molecular responses to therapy. However, current optical imaging modalities are faced with several limitations. One important limitation is the small number of clinically approved contrast agents. An additional limitation of widely used fluorescent organic dyes is their poor photostability and low quantum efficiency,¹³⁰⁻¹³² and their excitation and emission in visible light wavelengths. These wavelengths are absorbed and scattered by tissues and thus are limited in their ability to penetrate biological materials. Signal from these fluorophores is further attenuated by tissue absorption and autofluorescence in this visible wavelength range, limiting the utility and translational potential of the fluorophores. While the visible and near infrared wavelengths of light often used in biomedical optical imaging suffer from endogenous tissue autofluorescence, the short wave infrared range (1500-1700 nm) has less associated interference. This allows for improved detection of fluorescent moieties, greater

sensitivity and improved penetration through biological tissue.¹³³ Additionally, contrast agents with emissions in this range are frequently excited using NIR photons. Therefore, their excitation wavelength reduces associated tissue autofluorescence and scattering (as compared to UV and visible excitation wavelengths) leading to improved imaging.¹³⁴ Stable near-infrared emitting agents such as quantum dots and carbon nanotubes have shown promise for *in vivo* imaging, but do not achieve appreciable tissue penetration *in vivo* at biologically safe doses, limiting their clinical applicability.

To address limitations of existing technologies, in our previous work we have engineered optical nanoprobes as a new approach for detection of small sub-tissue cancerous lesions. These probes are based on ceramic nanoparticles doped with rare-earth (RE) cations that absorb near infrared (NIR) radiation to luminesce in the shortwave infrared (SWIR) spectrum (1000-3000 nm),^{135,136} emitting in the overlooked second “tissue transparent short-wave infrared window” of biological imaging.¹³⁷ Rare-Earth Albumin Nanocomposites (ReANCs), fabricated by encapsulating the RE nanoparticles within a human recombinant albumin shell, can be functionalized with ligands that complement cancer receptor markers. This functionalization results in imaging probes with selectivity to specific tumor molecular receptors.¹²⁴ Additionally, because of the hydrophobic nature of several binding pockets within the albumin shell, these probes exhibit high adsorptive capacity for small molecules pharmacologic drugs, and can be used for lesion-targeted delivery of antagonist molecules to cancers.¹³⁸

In this study, we investigated whether such functionalized nanoprobes could detect small cancerous lesions based on the combination of three key design features: the relative tissue transparency afforded by SWIR emitting nanoprobes, deeper tissue illumination potential of SWIR probes, and molecular targeting to cancerous lesion markers. Cancer targeting nanoprobes were generated by passive adsorption on albumin shells of AMD3100^{139,140} a hydrophobic small molecule inhibitor of the chemokine receptor CXCR4.¹⁴¹⁻¹⁴³ CXCR4 is strongly expressed on

highly motile cancer cells, and has been previously used to target a PET imaging agent that localizes to metastatic lesions in the lungs.¹⁴⁴ CXCR4-targeted, AMD3100 functionalized nanoprobe preferentially accumulate within receptor positive cells and tumors allowing for more sensitive detection of small-scale lung lesions in an *in vivo* metastatic breast cancer model (**Figure 2.1**). This is of particular clinical relevance as CXCR4 has previously been indicated in the site specific invasion and metastasis of breast cancer cells to the lungs, and is correlated to decreased survival time and poor prognosis.¹⁴² Strikingly, the cancer targeted probes enabled imaging of microlesions ($\sim 25 \text{ mm}^3$) in the lungs at a depth of approximately 1 cm while allowing for simultaneous molecular identification of the tumor population phenotype.

2.3. Results

2.3.1. Synthesis and characterization of nanoparticles

Rare earth nanoparticles were synthesized via burst nucleation as previously described. Nanoparticle structure consisted of a NaYF_4 core doped with ytterbium (Yb) and erbium (Er) coated in an undoped shell. Dopants were found to comprise 30% of the total nanoparticle atomic weight. Lifetime emissions scans revealed that the calculated delay time for the particles 1530 emissions was found to be 3.55 ms (**Supplementary Figure 2.1**). Rare earths were incorporated into albumin nanocomposites (ReANCs) by solvent induced controlled coacervation of albumin.^{124,138} Hydrodynamic diameters of ReANCs were determined using dynamic light scattering (DLS) (**Figure 2A**), which revealed monodisperse particle populations. The yield of ReANCs was found to be approximately 70% by BCA protein assay.

2.3.2. Cancer-Targeting Probes: AMD3100 Functionalized ReANCs (fReANCs)

Functionalized ReANCs (fReANCs), namely, ReANCs targeting the CXCR4 receptor over-expressed on motile cancer cells, were generated by adsorbing AMD3100, a small molecule antagonist of CXCR4, onto the ReANC surface (**Figure 2.1A**) by exploiting the native drug binding

pockets on human serum albumin.¹⁴⁵ The particles were characterized to determine the effect of functionalization on the physical properties of the probes. fReANCs were somewhat larger than unmodified ReANCs (5-35 nm increase in diameter depending on loading concentration), with marginally but not statistically significant greater polydispersity (**Figure 2.2A**). Emission spectra for albumin coated ReANCs have been previously reported, showing that albumin encapsulated rare earth particles exhibit detectable SWIR emissions.¹²⁴ The adsorption of AMD3100 onto the albumin surface had a slight dampening effect on SWIR emissions; nonetheless, fluorescence was strong enough to be resolved via the current imaging prototype (**supplemental figure 2.1**).

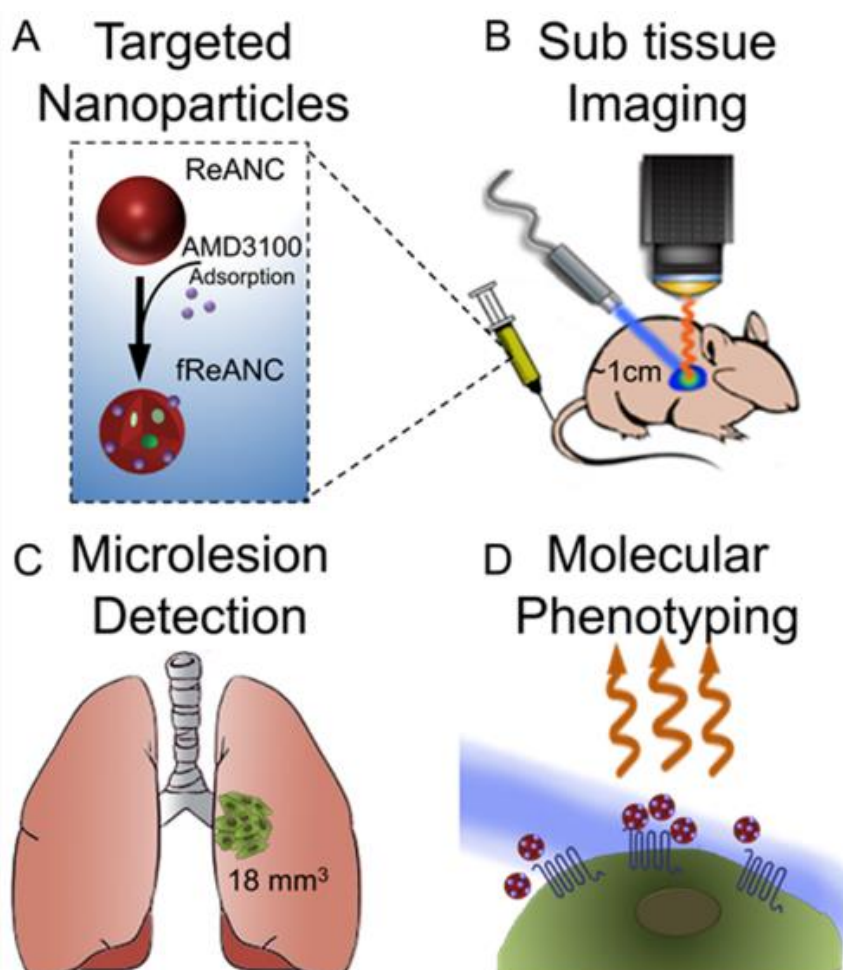


Figure 2.10- Design, fabrication, and preclinical efficacy of rare earth nanoprob

ReANCs were synthesized by controlled coacervation of albumin monomers in solution and REs dissolved in a solvent. (A) AMD3100 was adsorbed onto the surface of fully formed ReANCs to generate AMD3100 functionalized ReANCs, or fReANCs. (B) Athymic nude mice were inoculated with human breast cancer cells through the tail vein. Animals were treated with either ReANCs or fReANCs and SWIR imaging performed to determine nanoprobe-tumor localization. fReANCs were imaged in tumors up to 1 cm into the animal (B). Microlesions as small as 18 mm³ were detected with targeted probes (C). Probe localization to receptor positive tumors enabled optical molecular phenotyping (D).

Scanning electron microscopy (SEM) of ReANCs and fReANCs revealed spherical populations indicating successful adsorption, as evidenced by a change in surface texture with varying concentrations of AMD3100 (**Figure 2.2B-E; Supplementary Figure 2.1**). Loading efficiency was validated by HPLC and was determined to be dependent on the amount of AMD3100 introduced, ranging up to 70% (**Figure 2.2A**). Scatchard analysis of the loading data revealed a binding affinity of $K_d=1.8 \times 10^{-7}$ M. This value is comparable with binding of drug moieties such as paclitaxel to albumin indicating that drug binding activity is retained by albumin in a nanoshell form.¹⁴⁶ Additionally, AMD3100 loading of ReANCs had no significant effect on the viability of MDA-MB-231 breast cancer cells (**Figure 2.2F**).

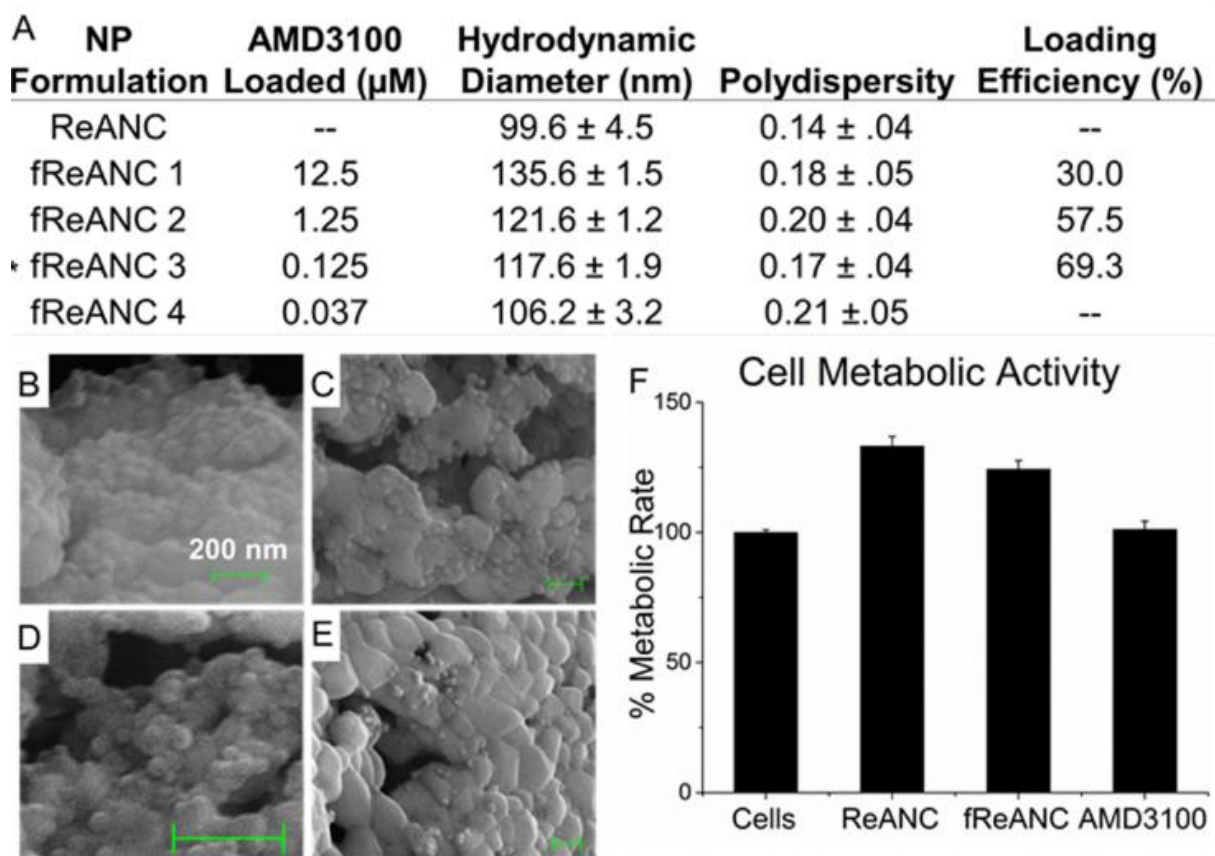


Figure 11.2-Characterization of functionalized Rare Earth Nanoprobes:

(A) fReANCs were synthesized by adsorbing AMD3100 onto fully formed ReANCs. Both populations had narrow size distributions and low polydispersity index. The formulation used for in vivo studies is as indicated with asterisk. (B) Scanning electron microscopy (SEM) of fReANCs revealed spherical particles. The addition of AMD3100 at concentrations of 12.5 μM (B), 1.25 μM (C), 125 nM (D) and 37.5 nM (E) yielded an increase in granulated surface texture directly proportional to the loading concentration. Drug loading efficiency (last column) was determined using HPLC as described in methods section. Cellular treatment with REANCs, fReANCs or free drug did not have an effect on cell metabolic activity (F), suggesting that the nanoprobes are non-cytotoxic. (F) Error bars denote standard deviation ($n = 3$), $p < .05$ metabolic activity (F), suggesting that the nanoprobes are non-cytotoxic.

2.2.3. Active receptor targeting of fReANCs

Effective targeting of fReANCs was determined by cellular association of AMD3100 functionalized probes using three breast cancer cell lines with varying levels of CXCR4 expression: 1) 4175-TR (a highly aggressive, lung-tropic subpopulation of the MDA-MB-231 cancer cell line¹⁴⁷) with low CXCR4 expression, 2) MDA-MB-231, with moderate levels of CXCR4 expression, and 3) MCF-7, with relatively high levels of CXCR4 expression,¹⁴⁸. We observed a 3-fold increase in cellular association of fReANCs when compared to ReANCs by both receptor positive cell lines as determined by flow cytometry, with no significant change in association with receptor negative 4175-TR cells (**Supplementary Figure 2.2 and Figure 2.3A, 2.3B, and 2.3E**). Based on cell surface binding and cytotoxicity studies, the optimal concentration for loading REANCs was determined to be 125 nM. Confocal microscopy showed that nanoprobe internalization of both ReANCs and fReANCs occurred within 24 hours, with nanoprobe distributed in a punctate pattern throughout the cell cytoplasm and the increased intracellular fluorescence signal leading to overall increased signal in each individual cell. (**Figure 2.3C and 2.3D; Supplementary Figure 2.3**).

2.2.4 *In vivo* SWIR imaging

Tumor-Specificity of Targeted Nanoprobes:

The ability of the functionalized probes to discriminate between receptor-positive (MDA-MB-231) and receptor-negative (4175-TR) lesions *in vivo* was assessed using nude mice bearing palpable bilateral subcutaneous tumors. Animals were treated with a bolus dose of 200 μ L (10 mg kg^{-1}) of either unfunctionalized ReANCs or fReANCs into the intraperitoneal cavity (i.p. administration). Immediately following injection of the particles, SWIR emissions were visualized in the abdominal cavity around the site of injection. The fReANCs cleared much more rapidly from the site of injection than the ReANCs, which were retained in the peritoneal cavity up to 48 hours post administration (data not shown).

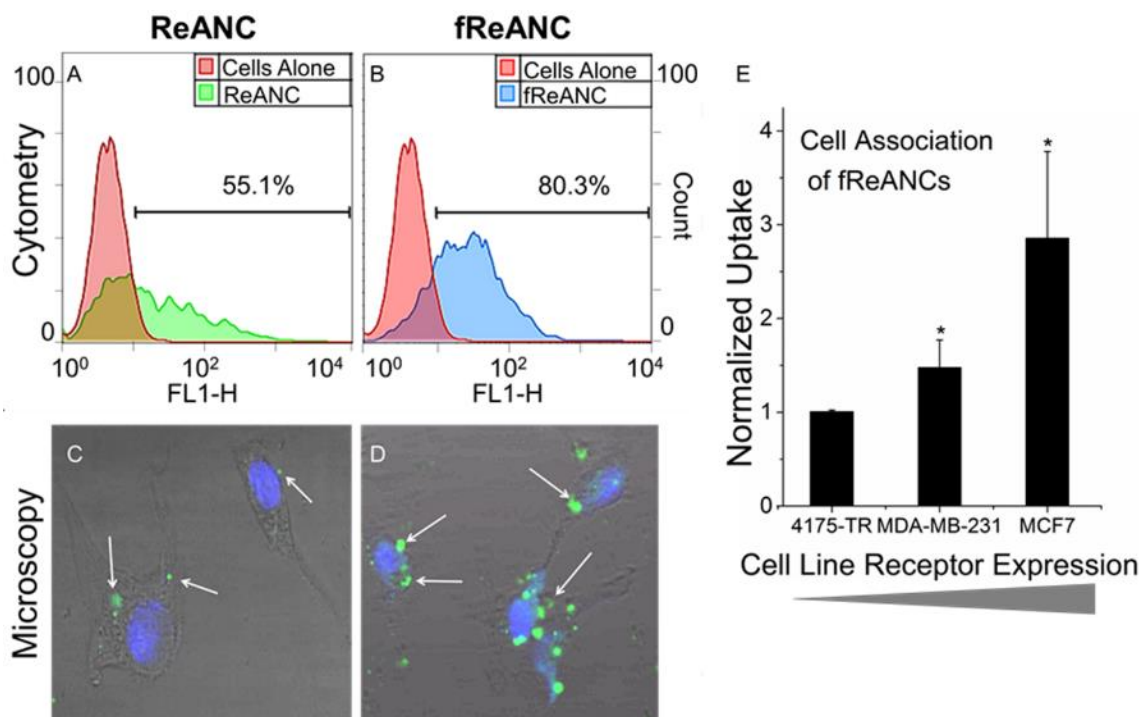


Figure 2.12- Active Cancer Targeting of Rare Earth Nanoprobes

Cellular uptake and association between ReANCs (A) and fReANCs (B) by MDA-MB-231 breast cancer cells was analyzed by flow cytometry for up to 24 hours. Functionalization increased particle uptake as determined by FACS. This was confirmed with confocal imaging of receptor positive cells treated with ReANCs (C) or fReANCs (D) for 24 hours. White arrows indicate nanoparticle fluorescence. While ReANCs showed some cellular association, the degree of nanoprobe association was greater with the functionalized constructs. Quantitative flow cytometry analysis revealed that nanoprobe association increased with greater expression of the targeted CXCR4 receptor (E). Error bars denote standard deviation for $n = 3$. * $p < .05$ (t test, comparing between ReANC and fReANCs groups)

SWIR fluorescence was detected 24 h after fReANCs administration at the receptor-positive, left dorsal tumor (**Figure 2.4B and C**). This was in contrast to little or no SWIR signal seen with ReANC administration (**Figure 2.4A**). Additionally, little SWIR signal was observed with

fReANC administration from the receptor-negative (4175-TR derived) right dorsal tumor (**Figure 2.4B and C**). Ex-vivo SWIR imaging also revealed irregular fluorescence patterns surrounding the receptor positive tumor validating tumor-specificity of our nanoprobes *in vivo*, indicated by white arrows (**Figure 2.4E**). There was no fluorescence associated with the receptor negative tumors excised from the animals' right flank (**Figure 2.4F and 2.4G**) or the receptor positive tumors treated with ReANCs (**Figure 2.4D**).

Strikingly, the receptor-positive tumors were 4X smaller than the receptor-negative tumors (**Figure 2.4D-G insets**). This indicated that fReANCs possess the ability to detect and target small, poorly vascularized tumor microlesions. The maximum SWIR signal elicited with fReANCs was observed at 1-2 weeks of tumor growth and then declined, which may correlate with a decrease in CXCR4 expression as the metastasis develops into a mature tumor. These results validated the ability of targeted fReANCs to molecularly phenotype tumors *in vivo*.

Additionally, there was no overt toxicity from injection of the particles, and the particles were cleared 72-96 h post injection to non-detectable levels in the mouse (data not shown). Repeated injections of REANCs and fReANCs over time did not lead to toxicity as evidenced by uniform body weight over the course of the 11 week study (**Figure 2.5A**) and by lack of distress signals exhibited by the animals, as determined by the IACUC monitoring.

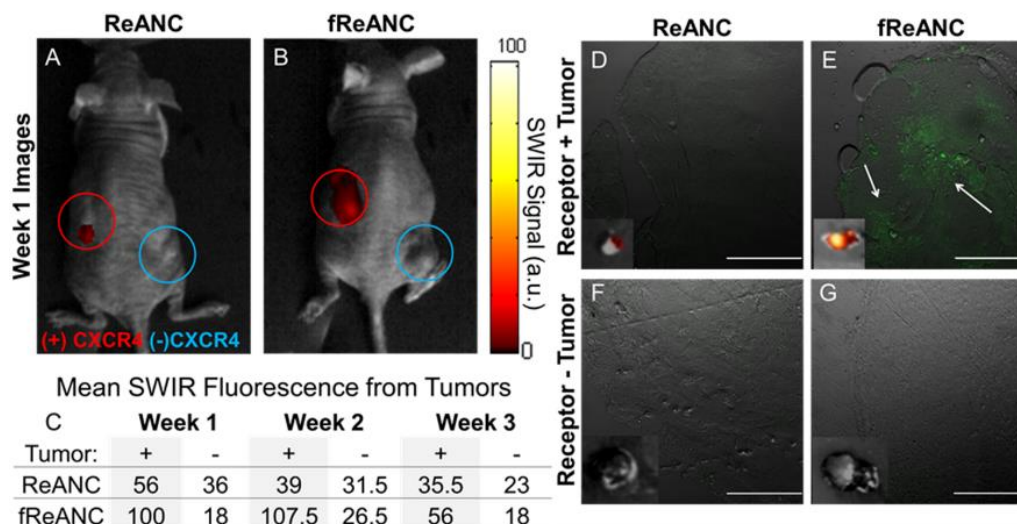


Figure 2.13- Functionalized nanoprobes are capable of molecular discrimination of tumors in vivo

The ability of targeted constructs to molecularly target *in vivo* lesions was evaluated using nude mice bearing bilateral, subcutaneous, dorsal tumors derived from human breast cancer cells. Receptor positive MDA-MB-231 cells (Red open circle) were injected into the left dorsal flank, while receptor negative 4175-TR cells (Blue Open circle) were injected on the right. Unfunctionalized ReANCs (A) showed little associated red SWIR fluorescence at either lesion sites, while fReANCs (B) had red SWIR fluorescence associated with only the receptor positive tumor. The maximum SWIR values for each region of interest (C) show that fReANCs accumulated preferentially to the receptor positive left tumor. $n = 2$. (D-G insets) *Ex vivo* SWIR imaging revealed SWIR fluorescence associated with the receptor positive tumor treated with fReANCs. Excised tumors treated with (D, F) ReANC and (E, G) fReANC were sectioned and imaged to determine nanoprobe localization (green fluorescence) within the tumor mass. Scale bars represent 500 μm . Representative images from week 1.

2.2.5 Histopathological analysis of Nanoparticle Biocompatibility

At experimental endpoints, animals were sacrificed and organs of clearance (liver and spleen) were analyzed for toxicity due to the administered ReANCs. Analysis of H&E sections revealed no alterations suggestive of toxicity when compared to untreated controls (**Figure 2.5B and C**). Lung sections, obtained from lesions from the lung tumor model described in later sections, revealed a high degree of tumor burden (**Figure 2.5E**). Notably, administration of ReANCs to control animals did not show overt toxicity or changes in lung architecture on H&E staining (**Figure 2.5D**). Taken together these results support the biocompatibility of the targeted-nanoprobes and their utility to detect microlesions and enable real-time imaging of tumors.

Animal's body weight was recorded weekly over the course of the experiment (A) and animals were closely monitored for any signs of distress. Repeated injections were well tolerated by animals. Animals' livers were excised and examined to determine changes in the organ's structure with no (B) and fReANC (C) treatment. Analysis showed no change in the liver's integrity with dosing. Lung sections, from fREANC treated animals showed tumor infiltration in tumor bearing animals (E) and no morphological change in the control healthy animals (D) confirming the safety of the nanoprobes. $n = 6$.

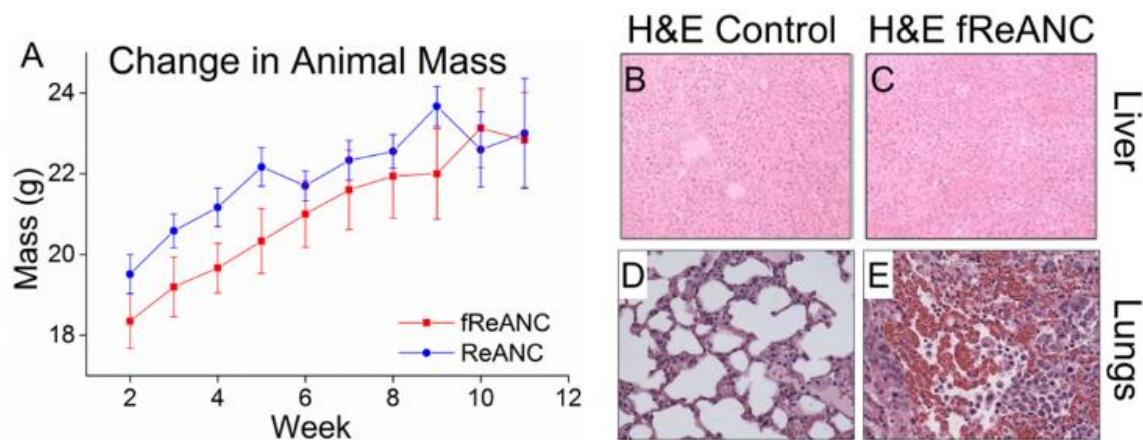


Figure 2.14- Rare-Earth nanoprobes proved safe for long-term use with no significant impact on animals' weight or damage to organs of accumulation:

Animal's body weight was recorded weekly over the course of the experiment (A) and animals were closely monitored for any signs of distress. Repeated injections were well tolerated by animals. Animals' livers were excised and examined to determine changes in the organ's structure with no (B) and fReANC (C) treatment. Analysis showed no change in the liver's integrity with dosing. Lung sections, from fReANC treated animals showed tumor infiltration in tumor bearing animals (E) and no morphological change in the control healthy animals (D) confirming the safety of the nanoprobes. $n = 6$.

2.2.6. *Ex vivo* SWIR imaging

Following necropsy, *ex vivo* SWIR imaging of tumors and organs revealed SWIR fluorescence associated with the livers of animals given i.v. injections of both ReANCs and fReANCs. *Ex vivo*, analysis of animals that received intra-peritoneal injections of the particles showed SWIR fluorescence in the major organs of clearance (spleen and liver) for both ReANC and fReANC treatment groups (**Supplementary Figure 2.4**).

Excised tumors were sectioned and imaged with confocal fluorescence microscopy to determine the localization of the nanoprobe within the tumor interstitium. Analysis of receptor positive tumors treated with fReANCs revealed a punctate pattern of nanoparticles distributed throughout the tumor mass (**Figure 2.4E and Supplementary Figure 2.5**). *Ex vivo* results thus far confirmed that the targeted fReANCs are able to molecularly phenotype lesions *in vivo*.

2.2.7 *In vivo* detection of tumors in internal organs with SWIR imaging

We assessed the ability of the SWIR nanoprobe imaging approach to locate tumors in sub-tissue organs using female athymic nude mice bearing lung tumors in an established model of metastatic breast cancer.¹⁴⁹⁻¹⁵¹ One of the most significant observations was that the nanoprobe-related SWIR signal was detectable up to 10.5 mm into the animal. Animals were treated with 200 μ L of unfunctionalized ReANCs or fReANCs (10 mg kg⁻¹) via i.v. administration and imaged up to 24h post-injection and yet no toxicity was associated with repeated use of probes. SWIR fluorescence was distinguishable in animal's livers immediately after injection. Notably, we obtained discernible SWIR signal using fReANCs in the lungs as early as three weeks following the inoculation of tumor cells (**Figure 2.6D**), compared to unfunctionalized ReANCs (**Figure 2.6B and 2.6C**) where signal was observed approximately 7 weeks post-inoculation. Preferential accumulation of fReANCs in tumors within lungs is indicated by the combination of enhanced lung-related and depressed liver-related signal in fReANC treated animals as compared to unfunctionalized, ReANC treated animals (**Figure 2.6D and 2.6E**). In particular, as shown in **Figure 2.6D**, fReANC accumulation in lungs increased significantly from week 2 after inoculation to week 4 after inoculation, which was in correlation with the increase in tumor volume.

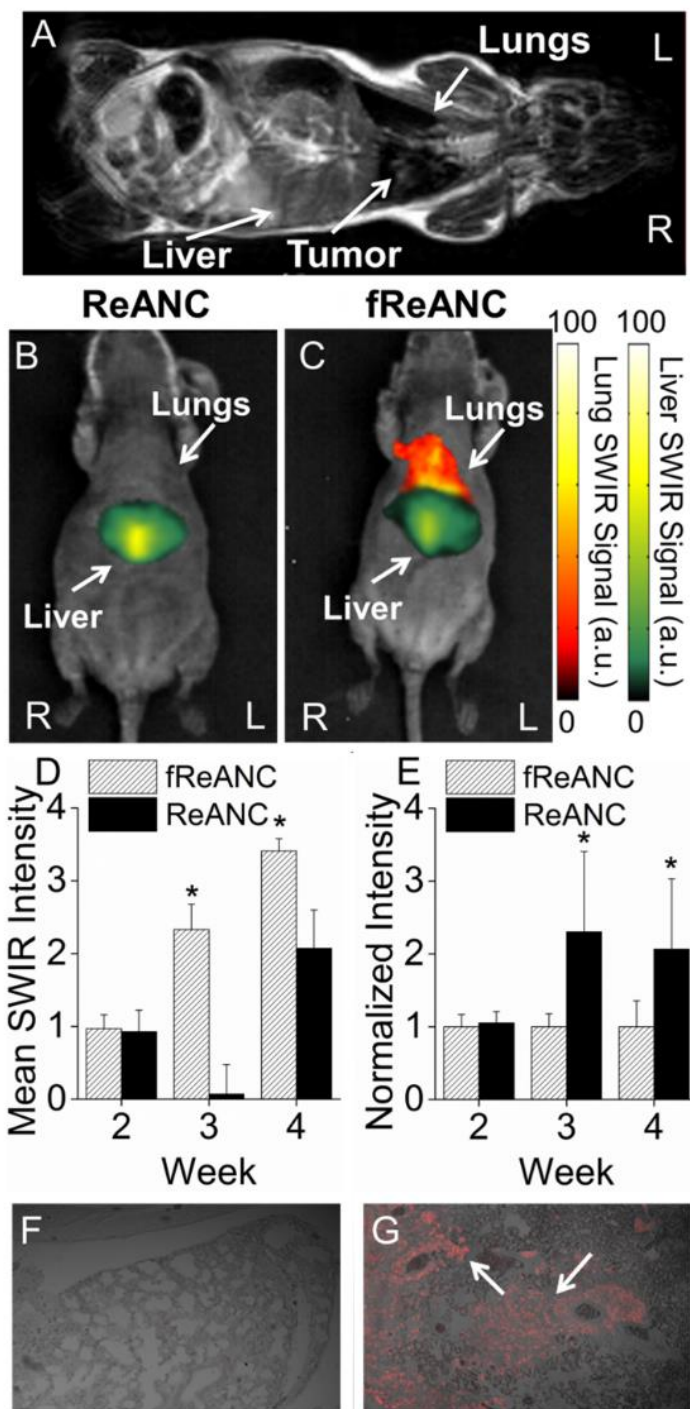


Figure 2.6- Targeted fReANCs allow for detection of microscale lung lesions

Nude mice were inoculated i.v. with CXCR4 expressing MBA-MB-231 cells. Cells colonized in the lungs and were monitored using MRI (A). Xenograft mice were administered either ReANCs (B) or fReANCs (C) at early stages (< 6 weeks) after inoculation. SWIR signal from the lung region was quantified at 24 h (D) post-injection. The fReANC associated SWIR signal was greater than the ReANC signal for early time-points, correlating to the presence of microlesions quantified by volumetric reconstruction of the MRIs. The SWIR signal from the liver was quantified for 0 h post injection (E) and showed a 2 fold increase in ReANC accumulation in the organs of clearance. Representative images (n=6) shown in all instances from week 3 of the study. The presence of tumors in the lungs was confirmed with vimentin staining of healthy (F) and tumor bearing (G) lungs, with the red fluorescence marked by arrows indicating tumor cells. (D) Error bars indicate SEM for n = 6. * indicates $p < .01$ (Wilcoxon Rank-Sum test) (E) * = $p < .05$ (Wilcoxon Rank-Sum test)

Tumor burden and depth of lesions relative to the surface of the animal were determined by bi-weekly MRI from time of inoculation of tumor cells (**Figure 2.6A; Representative MRI**). An especially significant outcome was that the tumors detected using fReANCs were found to be 27.8 mm^3 in volume on average with the lowest tumor volume detectable being 18.9 mm^3 (**Figure 2.7B and C**). In contrast, tumors detected with ReANCs were an average of 62.6 mm^3 (2.25 times larger than those resolved with the functionalized particles) with a tumor minimum volume of 55.6 mm^3 (**Figure 2.7A and C**). Tumors were located 7-10 mm from the surface of the animal. SWIR fluorescence and MRI images were overlaid (data not shown) to determine particle accumulation at lesion sites, confirming that the SWIR signal was associated with the lesions. The volumetric analysis reveals that fReANCs, in addition to detecting tumor lesions in sub-tissue earlier than ReANCs, are also able to resolve micro-lesions approximately 2.25 times

smaller than those detected by ReANCs (**Figure 2.7**). *Ex vivo* analysis of excised organs revealed SWIR signal from multiple lesions in the lungs and chest wall (**Supplementary Figure 2.4**), thus establishing the tumor-specific targeting ability of fReANCs in the lung model.

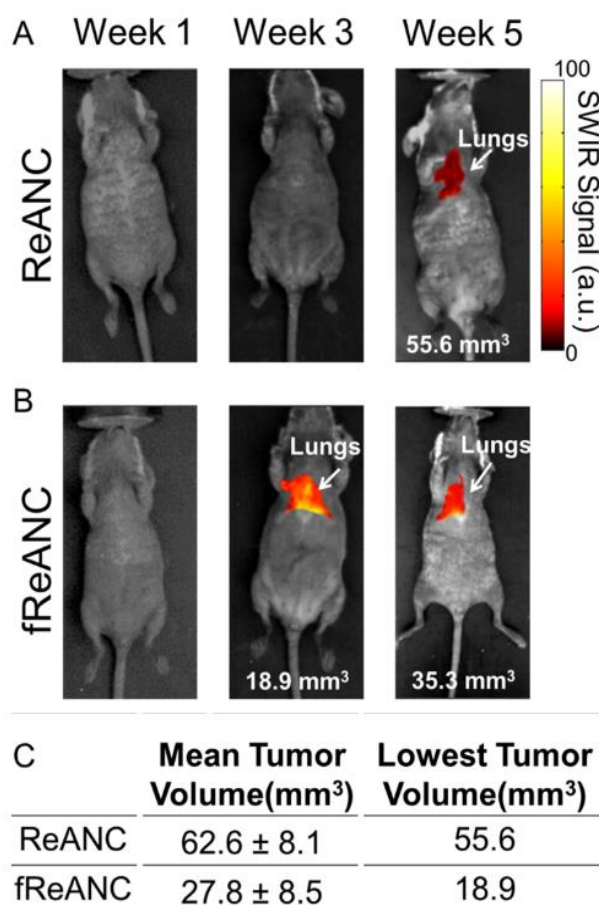


Figure 2.7- Longitudinal tracking of internal lesions with SWIR imaging

SWIR fluorescence images were taken each week for animals treated with both ReANC (A) and fReANC (B). Tumor burden was determined each week through MRI and compared to SWIR signal. Mean and minimum volume (C) of tumors detectable via SWIR imaging was calculated to determine the smallest tumors capable of resolution using the InGaAs camera. Treatment with fReANCs enabled detection of tumors on average 2.25 times smaller than those detected using ReANCs. (n=6)

Ex vivo tumors were analyzed for presence of infiltrating tumor cells by immunohistochemical staining for vimentin, a tumor-cell specific marker (**Figure 2.6F and 2.6G**). Taken together, these results confirm the ability of fReANCs to detect small ($< 30 \text{ mm}^3$) tumors up to 1 cm into biological tissue.

2.4. Discussion

Breast cancer, one of the most common causes of cancer death among women, is difficult to treat due to the frequency of micrometastatic populations that are phenotypically distinct from the parent tumor. It is therefore of critical importance to develop technologies capable of safe and sensitive detection and characterization of small sub-tissue tumors, based on their distinct molecular phenotype, with accurately defined margins. This study provides the first proof of concept model for optical-probe based molecular detection of sub-tissue micro-lesions. Here we demonstrate cancer-targeted SWIR emitting fREANCs target CXCR4-positive tumors in a bilateral tumor model of receptor-positive and negative tumors. Specifically, fREANCs are also shown to molecularly target CXCR4-positive tumors that are 4X smaller than receptor-negative tumors. The most significant observation from this study was the ability of cancer-targeted nanoprobes to detect sub-tissue lesions at a depth of approximately 1 cm and also to resolve micro-scale lesions. fREANCs were able to resolve tumors as small as 18.8 mm^3 compared to lesions that were 62.6 mm^3 detected by control REANCs.

SWIR emitting rare-earth albumin nanocomposites have previously been shown to be effective *in vivo* contrast agents that passively accumulate at the site of malignant lesions, possibly due to the enhanced permeability and retention (EPR) effect, allowing for imaging *in vivo*.¹²⁵ However, imaging of metastatic micro-lesions present additional challenges as the malignancy has not yet established its own vasculature to enable passive targeting. Prior work has shown that active targeting of nanoparticle based contrast agents to a specific disease marker can greatly improve their localization to targets of interest.^{152,153} Active targeting of contrast agents has been shown to

improve particle biodistribution, improve signal-to-noise ratio, provide molecular information about a region of interest, and increase the optical signal allowing for more sensitive imaging.¹⁵⁴⁻¹⁶⁰ Here, we have designed and characterized a novel targeted imaging probe consisting of rare-earth doped phosphors and human serum albumin onto which is adsorbed AMD3100 as the targeting ligand.

The approach to targeting of the ReANCs was designed based on the native drug binding properties of human serum albumin.^{145,161} HSA has been shown to simultaneously bind multiple distinct moieties at various ‘drug binding pockets’ across its surface.¹⁴⁵ Albumin nanocarriers retain the ability to strongly bind multiple therapeutic agents with little loss of efficacy.^{138,161} We utilized this property to adsorb AMD3100 as a targeting ligand onto the surface of the particles for tumor cell targeting with a high (up to 70%) efficiency of loading and affinity ($K_d=1.8 \times 10^{-7}$ M) owing to the several albumin drug binding sites within a nanoshell. The loading efficiency and binding affinity were found to be similar to reported values for albumin loading with other small molecule therapeutics such as paclitaxel and doxorubicin.¹⁴⁶ The resulting nanoprobe localization, combined with the sensitivity of an in-house SWIR imaging system, enables detection of small internal tumors with high specificity.

The fReANCs were synthesized and loaded with varying concentrations of the small molecule antagonist, AMD3100. fReANCs not only showed improved association with receptor positive MDA-MB-231 and MCF7 cells *in vitro* but also exhibited a lack of association with receptor negative MDA-4175 cells, with no appreciable effect on cell viability. This effect was largely independent of bound AMD3100 concentration on fReANCs (**Supplementary Figure 2.2**), suggesting that the particles with modest net loading and a maximum loading efficiency (approximately 70% by HPLC) could provide efficient targeting selectivity. Confocal fluorescence microscopy of fReANCs’ association with malignant cells confirmed visually the increased association of fReANCs when compared to unfunctionalized ReANCs.

Proof of concept studies in a mouse xenograft breast cancer model showed tumor-specific binding of fReANCs to receptor-positive tumors and successful targeting of tumors that were 4x smaller than the corresponding receptor negative tumors. This clearly highlights the ability of fReANCs to accurately detect and molecularly phenotype early tumor lesions. Future longitudinal studies will address the ability of molecularly targeted ReANCs in tumor-dynamic tracking. It is important to note that fReANCs were able to accumulate in tumors enabling detection in contrast to unfunctionalized ReANCs that post-injection cleared immediately to the liver.

Thus far, one of the hurdles faced by optical imaging agents has been their inability to be resolved deeper for detection of lesions in internal organs.¹⁶²⁻¹⁶⁴ Notably, targeted fReANCs were able to resolve lesions as small as 18.9 mm³ in the lungs of tumor bearing animals, with a depth of penetration of 10.5 mm through the tissue. Furthermore, the preferential accumulation in lung lesions was seen up to 24 h post-injection with little loss in SWIR signal. Future studies using large animal models will need to address improvement in depth of penetration using these probes to clinically acceptable depths. A limitation of near infrared excitation is localized photothermal effects.¹⁶⁵ Due to strong absorption of 980nm photons by water molecules, prolonged exposure of tissue to NIR wavelengths can induce non-localized temperature fluctuations.^{166,167} This effect can be mitigated by limiting the exposure of near infrared light to the skin. Thermal heating effects are typically generated after minutes of exposure at a high laser power (from 3-6 W cm⁻²).^{166,168} In contrast, the system presented here requires an intensity of only 1.7 W cm⁻² with seconds of exposure. By limiting laser power and duration it is possible to circumvent detrimental effects on biological tissues post exposure.

Of significance is the fact that we were able to perform real-time imaging with no observed toxicity for a period of 11 weeks, as shown by consistent body weight and the lack of pathological evidence of toxicity in major organs of clearance such as the liver and spleen. Both nanoparticle formulations cleared completely from the animal's body within 7 days. There was no apparent

difference in organ accumulation between the functionalized and unfunctionalized particles (**Supplementary figure 2.4**). Since athymic nude mice used in this study lack a robust immune system, studies to validate lack of immunogenicity and toxicity to establish safety profile of the probes will be done in immunocompetent mice.

Emergent patient therapy towards metastatic disease is currently centered on a molecularly targeted therapeutic strategy.¹⁶⁹ Several recent preclinical studies have provided proof of concept that early targeting of metastasis-specific signaling pathways can result in enhanced therapeutic responses.^{149,150,154,170,171} Implicit in the precision medicine approach is the need for cost-effective, safe and easy to use molecular diagnostic agents. Targeted nanoprobes from this study exhibit translational potential to monitor tumor progression, molecularly phenotype tumors and provide physicians with a diagnostic tool to make improved choices for tailored therapy and monitor in real-time response to therapy.

2.5. Conclusion

The albumin nanoshells utilized in this work show a high affinity and capacity for ligands and upon functionalization are capable of cellular discrimination based on receptor phenotype *in vitro*. Functionalized nanoprobes are able to preferentially localize to receptor positive tumors in mice, allowing for detection of positive tumors 4x smaller than receptor negative tumors. The most significant observation of clinical importance from this study was the ability of functionalized nanoprobes a) to detect sub-tissue microlesions approximately 1 cm from the imaging surface and b) to resolve microlesions as small as 18.9 mm³ when compared to 2.25 times larger lesions detected by ReANCs. The safety profile of both fReANCs and ReANCs, as indicated by no overt toxicity during the course of the study, is an added benefit for plausible clinical applicability of these agents.

2.6. Experimental Methods

2.6.1 Reagents: AMD3100 was purchased from EMD Millipore (Billerica, MA, USA) and used without further modification.

2.6.2 Cell Culture: MDA-MB-231, MCF7 (ATCC, Manassas, VA) and MDA-MB-231 derived 4175-TR cells (kind gift from Dr. Yibin Kang, Princeton University, USA) were cultured in DMEM (ATTC, Manassas, VA) supplemented with 10% FBS and 1% penicillin-streptomycin (Invitrogen, Carlsbad, CA, USA) at 37°C in an atmosphere of 5% CO₂.

2.6.3 ReANC Fabrication: ReANCs were synthesized as previously described.^{124,125} Briefly, 2% (w/v) solution of human serum albumin (Sigma-Aldrich, St. Louis, Mo) was dissolved in NaCl (2 mM) and the pH was adjusted to 8.50 ± 0.05 with NaOH (.1 M). Under continuous stirring at 700 rpm at room temperature, ethanol (2 mL) sonicated with rare-earth nanoprobe (0.2 mg mL⁻¹) was added at 1.5 mL min⁻¹ to the HSA solution (500 µL) with a syringe pump (Harvard Apparatus PHD 2000, Holliston, MA). Subsequently glutaraldehyde (2.34 µL) (Sigma-Aldrich, St Louis, Mo) was added to the suspension as a cross-linker following ethanol addition and particles were allowed to crosslink overnight. Particles were then purified by 3 cycles of centrifugation at 48,400 g. Particles were characterized by BCA assay (Pierce Biotechnology, Rockford, Il) to determine % yield. DLS was performed to determine particle size and polydispersity.

2.6.4 Preparation of functionalized nanoparticles (fReANCs): AMD3100 (EMD Millipore, Darmstadt, Germany) was dissolved in sterile water (1 mg ml⁻¹) and was added into a suspension of ReANCs in PBS+1 mM EDTA to yield final concentrations ranging from 0.0125-12.5 µM. AMD3100 adsorption was achieved by constant agitation of samples at room temperature for 3h followed by purification through centrifugation. AMD3100 functionalized ReANCs (fReANCs) were characterized as described above.

2.6.5 Quantification of loading: The concentration of AMD3100 loaded on ReANCs was determined via high-performance liquid chromatography (HPLC, Beckman Coulter Model 166, Brea, CA) used with a Luna C18 column (3 μm , 100 x 4.6 mm i.d., Phenomenex, Torrance, CA). Briefly, the functionalized fReANCs were flash frozen and lyophilized for 48 hours. The powders were re-suspended in water and assayed on HPLC to determine AMD3100 concentrations. For chromatographic elution the flow rate was 1 mL minute⁻¹. The mobile phase consisted of 0.1% TFA in de-ionized water and acetonitrile. AMD3100 was detected at 212 nm. Binding affinity between albumin nanoparticles and AMD3100 was determined via scatchard analysis: The ratio of bound/free ligand was determined for various concentrations of ligand from the HPLC data and plotted against the amount of ligand loaded onto the particles. Slope of the resulting best fit line was used to determine the particle dissociation constant.

2.6.6 *In vitro* cellular uptake of fReANCs: MDA-MB-231, MCF-7, and 4175-TR cells expressing different relative amounts of CXCR4 were seeded onto 96-well microtiter plates at a density of 5×10^5 cells/well and incubated for 24 hours at 37 °C. To quantify the amount of nanoparticle uptake, cells were treated with 10% w/v of either ReANCs or differently functionalized fReANCs for up to 48 hours. Cells were subsequently trypsinized, washed and fixed in 1% PFA prior to being analyzed with fluorescent flow cytometry (FACScalibur, BD Biosciences, San Jose, CA) using the autofluorescence of the albumin shell to determine uptake as described previously. Data was collected for 10,000 cells.

2.6.7 Cell uptake and confocal imaging: To further visualize and confirm active targeting of receptor + cells, MDA-MB-231 and MCF7 cells (with elevated expression of CXCR4) and 4175-TR cells (with low expression of the receptor) were seeded on borosilicate Lab-Tek chambers (Nuc, Rochester, NY) and incubated overnight at 37 °C. Cells were then treated with either unfunctionalized ReANCs or AMD3100 loaded fReANCs for 24 hours. Cells were then washed, fixed, and stained with DAPI. NIR imaging was performed using a titanium:sapphire laser on a

Leica TCS SP2 fluorescence microscope (Leica Microsystems, Exton, PA) to confirm cellular uptake.

2.6.8 Cell viability assay: The metabolic activity of cells treated with ARAs was assessed using the CellTiter96 Aqueous One Solution Reagent (3-(4,5-dimethylthiazol-2-yl)-5-(3-carboxymethoxyphenyl)-2-(4-sulfophenyl)-2H-tetrazolium, MTS) (Promega, Madison, WI). MDA-MB-231 and 4175-TR cells were cultured on 96 well microtiter plates at a density of 5000 cells/well and treated with 10% w/v ReANCs or fReANCs suspended in PBS for 24 hours. After 24 hours culture media was changed and MTS reagent was added to each well, and the plate was allowed to incubate for an additional 4 hours at 37°C. Absorbance was measured at 450 nm using a microplate reader (Bio-Rad Model 680, Hercules, CA). Cell viability was calculated relative to the absorbance of the untreated cell population.

2.6.9 *In vivo* imaging: Imaging studies were conducted using female homozygous nude mice (Taconic, Hudson, NY). For subcutaneous tumor imaging studies, MDA-MB-231 and 4175-TR human breast cancer cells were injected into the dorsal area at 10^7 cells per site. Animals were used for imaging studies once tumors became palpable. For imaging of internal organs at a sub-tissue level, MDA-MB-231 cells were injected via the tail vein at 3×10^5 cells per animal. All animal studies were approved by the Institutional Review Board for the Animal Care and Facilities Committee of Rutgers University and performed in accordance with institutional guidelines on animal handling.

2.6.10 SWIR-imaging: Animals were imaged using a previously described in-house small animal SWIR imaging prototype for real time non-invasive optical imaging. Mice were fully anesthetized using 2% isoflurane (Butler-Schein, Dublin, OH) and were continuously scanned with a 1.7 W collimated 980 nm laser in various positions to excite nanoparticles. SWIR fluorescence was detected with an IR sensitive InGaAs camera (Sensors Unlimited, Princeton, NJ) equipped

with long-pass 1000 nm and band-pass 1550 nm filters (Semrock, Rochester, NY) and a 25 mm SWIR lens (StingRay Optics, Keene, NH). This system is capable of real-time live animal imaging with an exposure time of ~ 50 ms frame⁻¹.¹²⁵ Images were acquired as .bin video files and were processed using custom Matlab scripts (**Supplementary Figure 2.6**).

2.6.11 MRI Imaging: MR images are acquired using 1 tesla M2-High Performance MRI System (Aspect Magnet Technologies Ltd, Netanya, Israel). All imaging procedures were performed under inhalation anesthesia with isoflurane at a concentration of 4% for induction of anesthesia and 1–2% for maintenance. MRI images were analyzed using VivoQuant software (Aspect Magnet Technologies Ltd, Netanya, Israel).

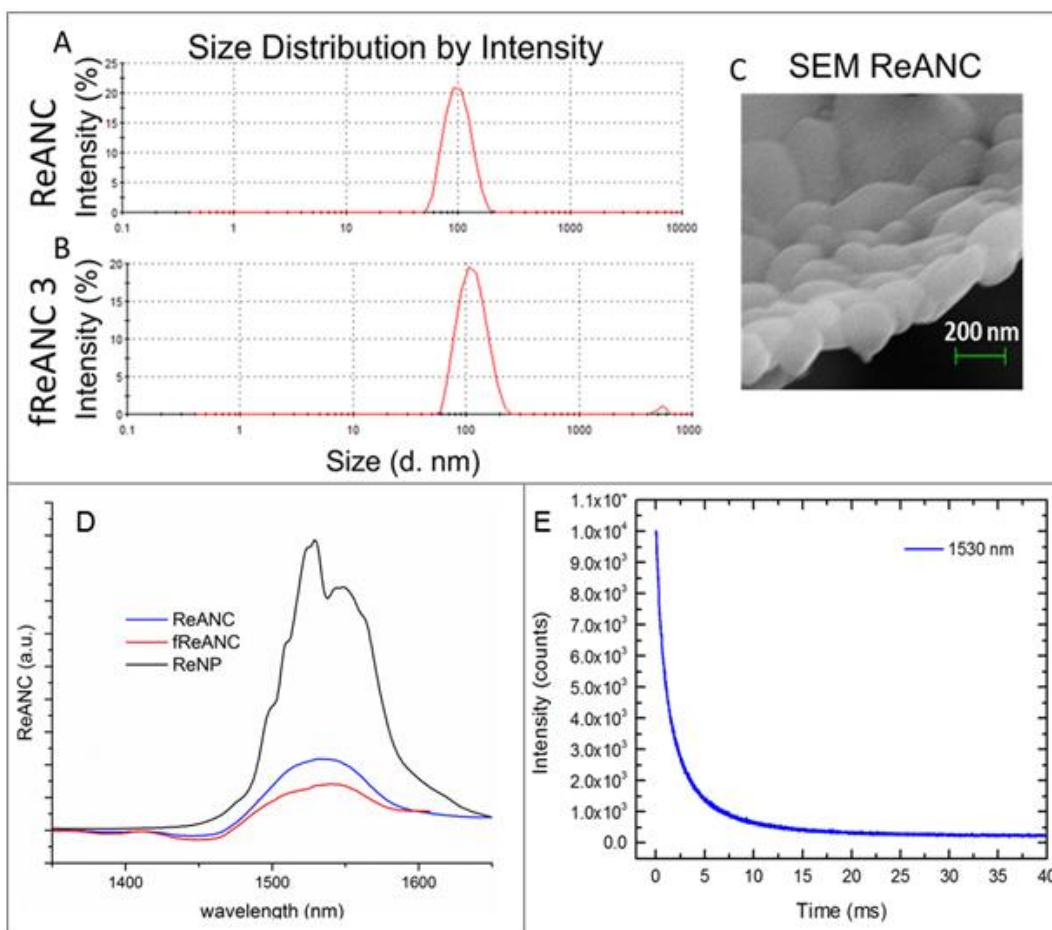
2.6.12 Detection of subcutaneous cancer lesions: MDA-MB-231 (CXCR4+) and 4175-TR (CXCR4 -) cells were cultured in DMEM supplemented with 10% FBS (Invitrogen, Carlsbad, CA) and 1% penicillin-streptomycin. Female athymic nude mice were purchased from Taconic laboratories at 3-4 weeks of age and inoculated with bilateral dorsal injections of MDA-MB-231 and 4175-TR cells at 10^7 cells per site and allowed to grow until palpable. Animals were treated with weekly i.p. injections of ReANCs or fReANCs at a dose of 10 mg kg⁻¹ and imaged with SWIR imaging at 24 h post injection to determine particle accumulation in the tumor space. Animals were sacrificed once tumor volume reached 500 mm³ and organs were excised and imaged *ex vivo* to determine particle distribution.

2.6.13 Ex vivo analysis of subcutaneous tumors: At experimental endpoints animals were euthanized and subcutaneous tumors were excised and flash frozen. Tumors were cut to 25 μ M sections with a cryotome (Thermo Fisher, Waltham, MA) and counterstained with Hoechst to detect cell nuclei. Sections were imaged using confocal microscopy to determine particle accumulation in the tumor mass.

2.6.14 Detection of lung metastatic lesions: Female homozygous athymic nude mice were obtained from Taconic Laboratories (Hudson, NY) at 3-4 weeks of age and were injected through the tail vein with MDA-MB-231 cells in an established model of lung metastasis. Tumor burden and location was evaluated using twice-monthly MRI (Aspect Imaging, Shoam, Israel) as described above. Animals were treated with weekly i.v. injections of either ReANCs or fReANCs at a dose of 10mg kg⁻¹ body weight and imaged at 24h post treatment to determine the ability of functionalized nanoprobes to resolve changes in the tumor burden over time. SWIR signal was correlated to tumor size and location as determined by MRI. Animals were sacrificed upon weight loss and organs were excised and imaged with SWIR imaging *ex vivo* to determine particle biodistribution and localization to lesion sites.

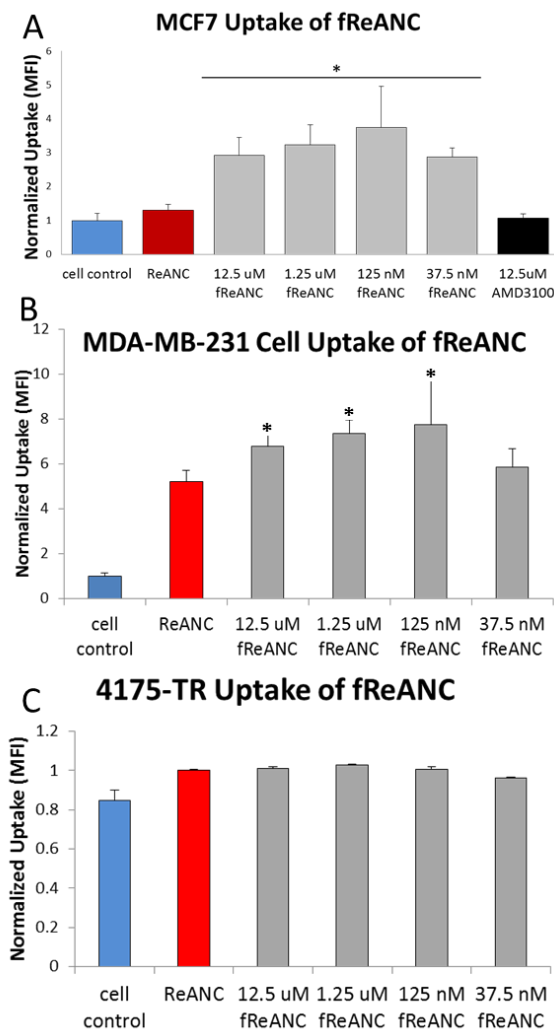
2.6.15 *Ex vivo* analysis of metastatic tumors: At experimental endpoints, animals were euthanized and tumors were excised, and fixed in formalin. Paraffin-embedded sections were imaged using confocal microscopy to determine particle accumulation in the tumor microenvironment. Slides were stained with Haematoxylin and Eosin (Sigma-Aldrich, St. Louis, MO) to determine changes in microlesion architecture and photographed using (Nikon, Chiyoda, Japan). For staining with Vimentin, paraffin-embedded sections were warmed at 40⁰C for 1h and deparaffination procedure performed. Antigen retrieval using citrate buffer at pH 6.0 was performed by microwave heating method. Following staining with anti-human Alexa647 conjugated Vimentin antibody (Santacruz Biotechnology, St.Louis,MO, USA) sections were counterstained with Hoechst 3342 to stain nuclei. Vimentin staining was visualized by fluorescence microscopy. Isotype matched control antibody staining was performed for non-specific binding.

2.7 Supplemental Figures



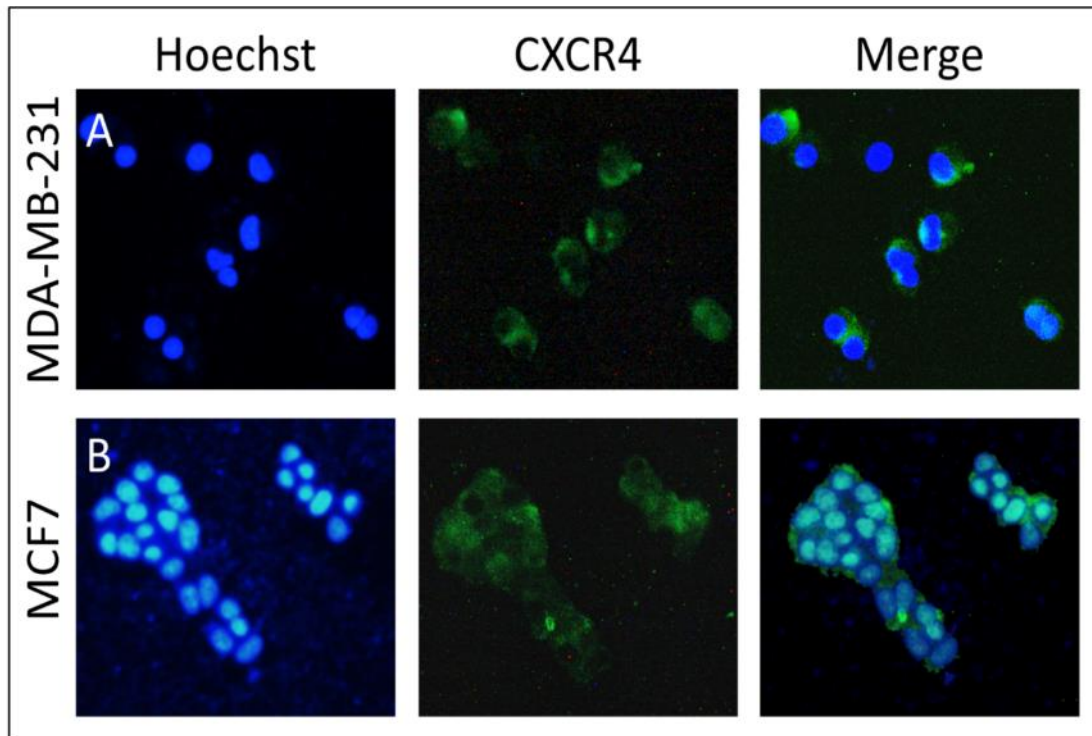
Supplementary Figure 2.1- Size distribution histograms of ReANC and fReANC showing nanoscale, monodisperse populations:

ReANC (A) and fReANC (B) formulations were physically characterized using a zetasizer. Sizing histograms (shown here for unfunctionalized ReANCs and fReANCs functionalized with 125 nm AMD3100) revealed populations centered around 100 nm. SEM of ReANCs (C) revealed spherical particles with a smooth surface texture. Infrared emission spectra (D) showed that functionalization slightly decreased SWIR emission strength. Temporal emission intensity (E) at 1530 nm for NaYF₄: Er, Yb rare earth nanoparticles was measured under 980 nm laser excitation. The calculated decay time was found to be approximately 3.55 ms.



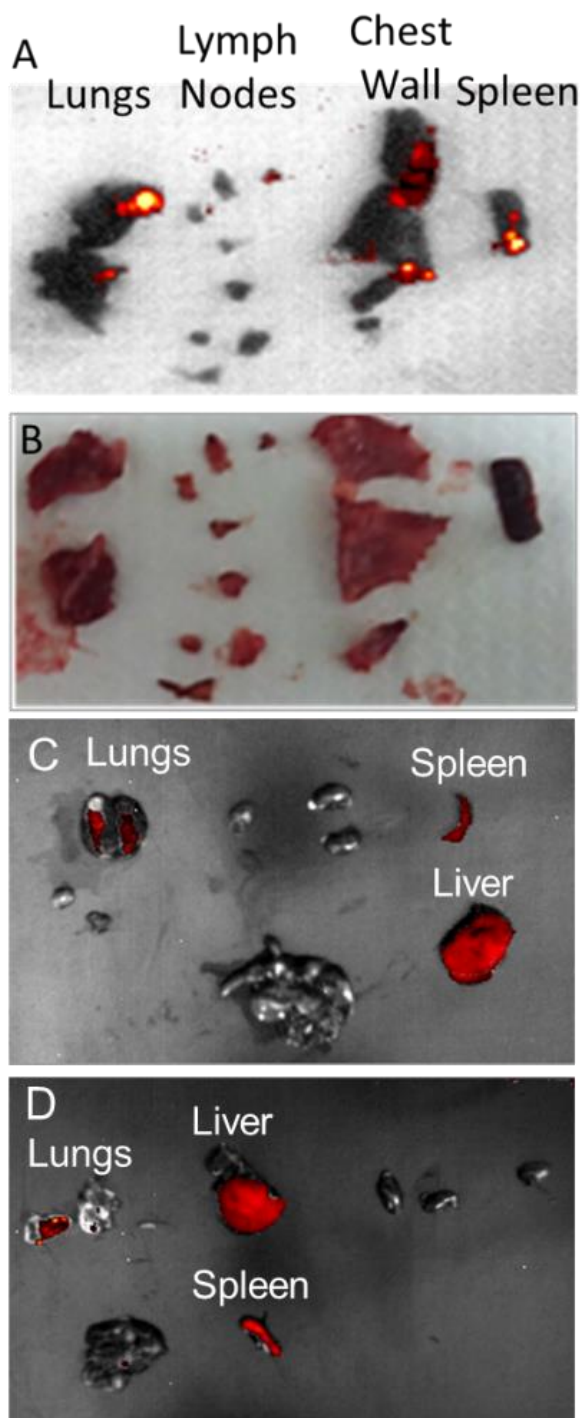
Supplementary Figure 2.2- Effect of various concentrations of AMD3100 on cellular uptake of fReANC, showing that uptake is largely independent of loading concentration:

Effect of various concentrations of AMD3100 on cellular uptake of fReANC, showing that uptake is largely independent of loading concentration. Optimal loading was determined to be 125 nM AMD3100 based on results. Constructs were tested on cells lines with varying receptor expression. Uptake was determined via flow cytometry for (A) receptor positive MCF7 cells, (B) receptor positive MDA-MB-231 cells, and (C) receptor negative 4175-TR cells. Cellular uptake for all cell lines tested was largely independent of degree of functionalization. Error bars denote standard deviation for n=3. * $p < .05$ (t test, comparing between ReANC and fReANCs groups)

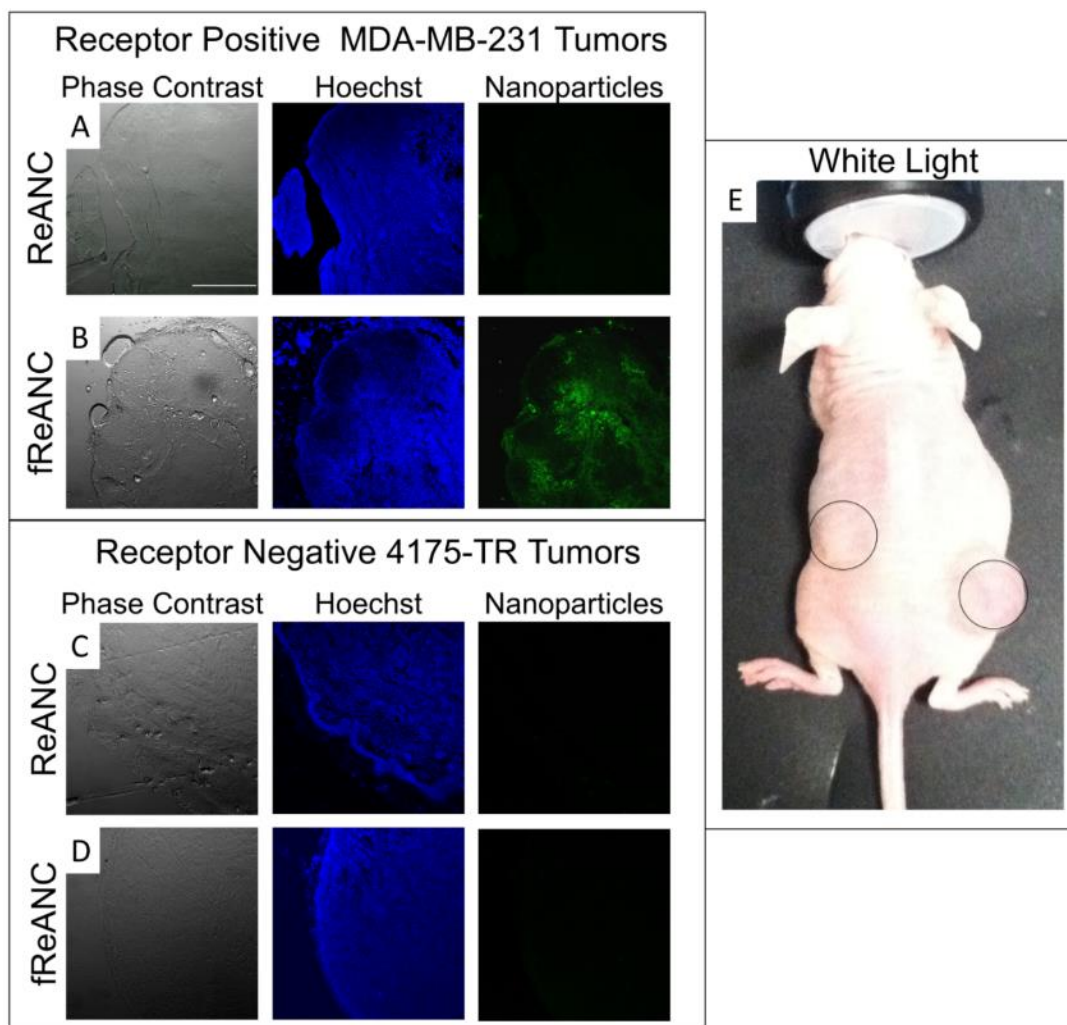


Supplementary Figure 2.3- Quantification of receptor expression of relevant cell lines:

Showing co-localization of Hoechst (identified by blue nuclei) and anti-CXCR4 (green fluorescence). MDA-MB-231 (A) and MCF7 (B) cell lines were plated on glass slides prior to being fixed and treated with a CXCR4 antibody to confirm the presence of the receptor on the cell membrane. Cells were counter stained with Hoechst to detect nuclei. Results indicate that both cell lines express the receptor of interest.

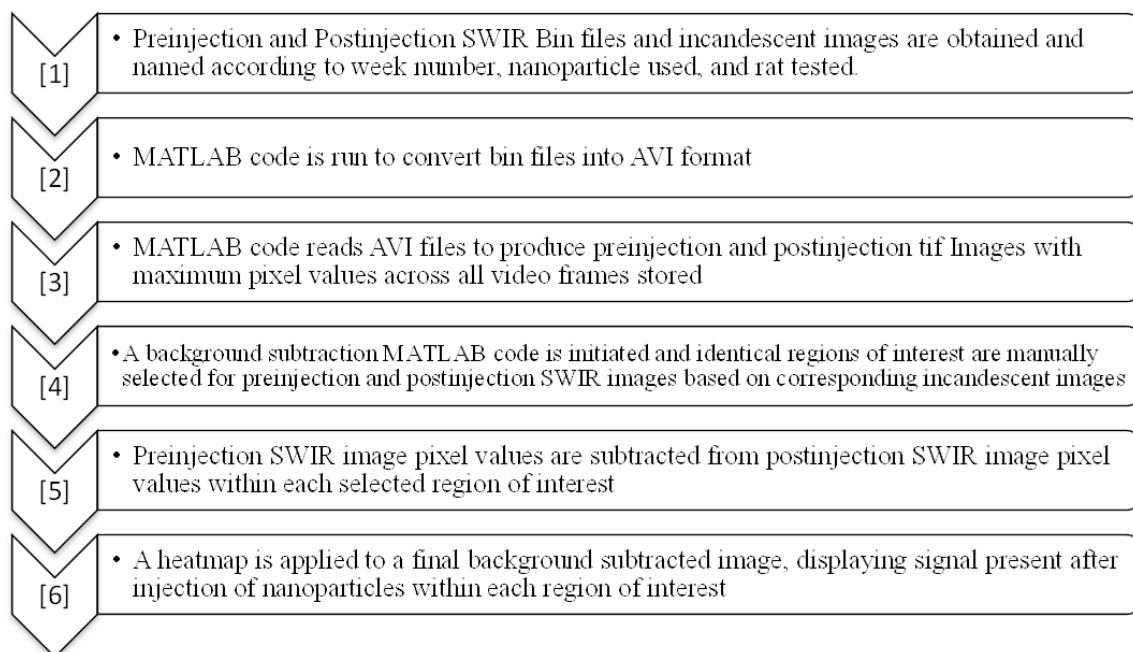


Supplementary Figure 2.4- *Ex vivo* analysis of organs showing punctate pattern of fluorescence associated with visible metastatic tumors: (A) SWIR signal from excised organs was punctate and confined to the lungs, areas with tumors on the animal chest wall, and organs of clearance. The areas of SWIR fluorescence in the lungs correspond to tumors visible in the white light image (B). Animals treated with ReANCs (C) and fReANCs (D) were sacrificed at experimental endpoints and organs were excised and imaged to determine particle accumulation. Analysis showed SWIR fluorescence in the liver and spleen as well as the lungs, at the site of the tumors. There was no apparent difference in organ accumulation between the functionalized and unfunctionalized particle formulations. Both formulations cleared from the body within 7 days.



Supplementary Figure 2.5- *Ex vivo* analysis of excised subcutaneous tumors:

Receptor positive MDA-MB-231 (A,B) tumors and receptor negative 4175-TR (C,D) tumors showing selective nanoparticle accumulation. Significant particle fluorescence was only observed in receptor positive tumors treated with fReANCs. Particle distribution was determined for receptor positive tumors treated with ReANCs (A) and fReANCs (B); receptor negative tumors treated with ReANCs (C) and fReANCs (D) by analysis of phase contrast, Hoechst, and nanoparticle fluorescence imaging. The subcutaneous tumors were allowed to develop in nude mice until they were palpable (E) and were distinguishable on the animal's flanks.



Supplementary Figure 2.6- flow chart detailing the matlab scripts used to process videos:

The SWIR video files were obtained from the imaging prototype in .bin format. For each animal, pre-inject and post-inject images were taken and named according to the conditions of each animal. The matlab scripts converted each .bin file into an .avi file and background values determined from pre-inject images were subtracted from individually set regions of interest. A uniform heatmap was applied to the final image to indicate the relative intensity of the SWIR signal in the region of interest, and the image was overlaid onto single frame images of the mice captured with ambient light.

CHAPTER 3

SURVEILLANCE NANOTECHNOLOGY FOR MULTI-ORGAN CANCER METASTASES

Note: This chapter has been reproduced with permission from the following publication:

Kantamneni H, Zevon M, Donzanti MJ, Zhao X, Sheng Y, Barkund SR, McCabe LH, Banach-Petrosky W, Higgins LM, Ganesan S, Riman RE, Roth CM, Tan M-C, Pierce MC, Ganapathy V, Moghe PV. Surveillance nanotechnology for multi-organ cancer metastases.

Nature Biomedical Engineering. 2017;1(12):993-1003. doi: 10.1038/s41551-017-0167-9.

3.1. Abstract

The identification and molecular profiling of early metastases remains a major challenge in cancer diagnostics and therapy. Most *in vivo* imaging methods fail to detect small cancerous lesions, a problem that is compounded by the distinct physical and biological barriers associated with different metastatic niches. Here, we show that intravenously injected rare-earth-doped albumin-encapsulated nanoparticles emitting short-wave infrared light (SWIR) can detect targeted metastatic lesions *in vivo*, allowing for the longitudinal tracking of multi-organ metastases. In a murine model of human breast cancer, the nanoprobe enabled whole-body SWIR detection of adrenal-gland microlesions and bone lesions that were undetectable via contrast-enhanced magnetic resonance imaging as early as three and five weeks post-inoculation, respectively. Whole-body SWIR imaging of nanoprobe functionalized to differentially target distinct metastatic sites and administered to a biomimetic murine model of human breast cancer resolved multi-organ metastases that showed varied molecular profiles in the lungs, adrenal glands and bones. Real-time surveillance of lesions in multiple organs should facilitate pre- and post-therapy monitoring in preclinical settings.

3.2. Introduction

Metastasis is the primary cause of breast cancer deaths^{172,173}, where the median survival rate for patients with multiorgan metastases is less than two years¹⁷². At present, about 10% of clinical cases present distal metastatic disease at diagnosis, and 20–40% develop distal metastasis within five years^{26,174}. The bones remain the most common site of distant metastasis in breast cancer, accounting for about 70% of diagnosed cases^{28,175} followed by the liver, lungs, adrenal glands and brain. To improve patient prognosis and survival rate, robust surveillance techniques and lesion site-specific therapies are needed. Here, we report an integrated cancer-surveillance system based on the design of nanoscale photonic probes for differential accumulation at distinct metastatic sites, coupled with deep-tissue optical detection of emergent lesions (**Figure. 1**). We demonstrate the

efficacy of this approach by longitudinal surveillance of multi-organ metastatic signatures in biomimetic metastatic murine models^{176,177}.

The detection of early, multi-organ cancer metastasis is a significant challenge because distinct sites rely on unique mechanisms of microcirculation. The functional design of nanoscale probes to detect metastases needs to account for differences in the infiltration barriers and microenvironment of individual target sites. For instance, passive nanoparticle targeting to a distant site such as the bone marrow exploits the discontinuous fenestrated sinusoid capillaries and an almost absent basement membrane to increase nanoparticle infiltration¹⁷⁸. In contrast, other distal sites such as the adrenal glands are not permissive to passive nanoparticle infiltration due to their continuously fenestrated sinusoid capillaries and a tight basement membrane. In this case, active functionalization of nanoparticles is necessary to achieve targeted delivery to the metastatic niche¹⁷⁹. In this study, we tailored the physiochemical properties of nanoparticle formulations based on published^{180,181} tumour and distal organ pathophysiology for site-specific accumulation and simultaneous detection of multi-organ metastasis, specifically to the bone, lungs and the adrenal glands^{180,181}.

New classes of optical imaging agents that exhibit improved tissue transmittance and deep tissue penetration^{182,183} are candidates for imaging micro-metastases. We designed imaging probes based on rare-earth albumin nanocomposites (ReANCs), which are ceramic rare-earth (Re)-doped particles encapsulated in human serum albumin.

These probes emit short-wave infrared (SWIR) light⁷¹, which has several advantageous properties for biological imaging^{184,185}. The lack of excitation– emission band overlap and elimination of tissue autofluorescence produces significantly improved signal-to-noise ratios⁷¹, while the narrow emission bands of the rare earths allow for multiplexed labelling. In this study, we exploit the optical emissions of ReANC probes in the SWIR (or near-infrared II) window¹⁸⁶ (900–1,700 nm), which is characterized by deep penetration through tissue¹⁸⁷ and reduced loss of spatial resolution due to scattering.

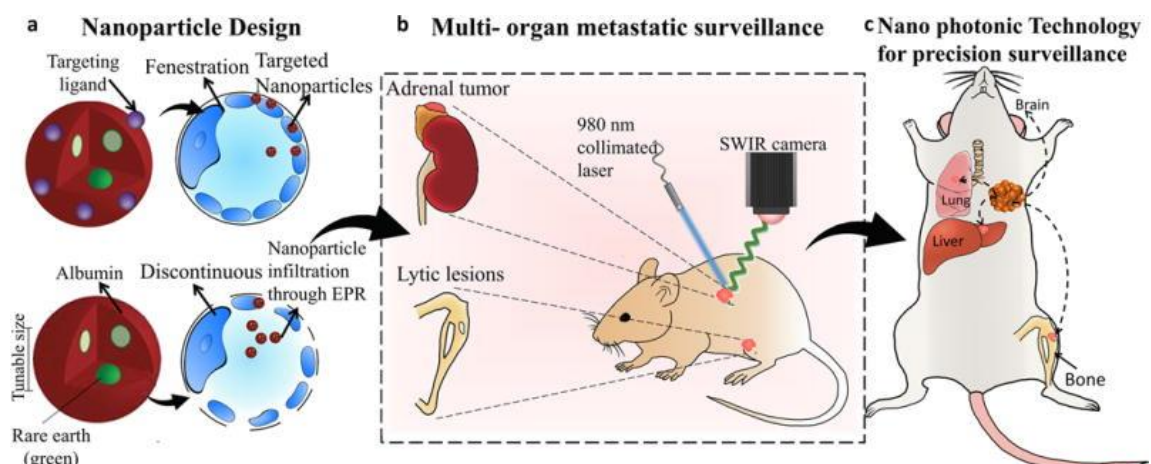


Figure 3.15- Design and workflow of photonic nanotechnology for cancer-metastasis

detection and profiling: Distinct nanoparticles were designed with rare-earth-doped cores based on differences in tissue microenvironment (a) to enable whole body screening based on deeper-tissue emanating short-wave infrared emissions. When administered *in vivo* to biomimetic breast cancer models, these nanoparticles are targeted to reach multi-organ metastatic sites across different pharmacologic barriers(b). Metastatic lesions (in the long bones or adrenal glands) can be detected earlier than conventional methods (bioluminescence, MRI, CT) and molecular changes in cancer cell signatures can be obtained, forming the basis for future metastatic-site specific, personalized cancer therapies(c).

We initially sought to resolve micro-metastatic bone lesions *in vivo* in a biomimetic model of basal breast cancer by intravenous administration of ReANC probes. The goal was to demonstrate that SWIR-based surveillance is more robust for emergent metastases than conventional imaging modalities such as magnetic resonance imaging (MRI) or computed tomography (CT). Next, we challenged our surveillance technology using a biomimetic model of metastatic breast cancer, which results in metastases at different anatomical sites and also shows dichotomous molecular profiles at these sites¹⁸⁶.

Figure 3.1 illustrates a non-invasive surveillance system that provides an integrated imaging system to track multi-organ metastases for xenogeneic and potential patient-derived models of cancer. This approach integrates distinct SWIR-emitting nanoparticles each designed to penetrate different metastatic organs and to enable longitudinal tracking of lesion development. The use of this surveillance system in the clinic will lead to major advances in altering and tailoring patient-specific niche-based therapeutic regimen.

3.3. Results

3.3.1 Design and characterization of C-X-C chemokine receptor type4 (CXCR4)-targeted photonic nanoparticles:

The dopant– host chemistries and heterostructure of rare-earth-doped nanoparticles govern their optical emission wavelengths and efficiencies^{184,188}, which have been optimized in our previous work^{71,185}. Rare-earth nanoparticles synthesized via a burst nucleation reaction^{188,189} were incorporated into ReANCs via solvent-induced controlled coacervation of albumin¹²⁴ (**Supplementary Figure 3.1a**). The sizes of the rare-earth nanoparticles (~18–25 nm diameter) and ReANCs (85–100 nm diameter) were tailored by controlling the reaction chemistry and kinetics to allow for the size-dependent enhanced permeation and retention (EPR) effect (at approximately below 100 nm) to permit passive targeting¹⁸⁰. ReANCs were also engineered to actively target tissues such as the adrenal glands where the microcirculation prevents passive uptake. Briefly, functionalized ReANCs (fReANCs) were generated by decorating the surface of ReANCs with AMD-3100, a small molecule antagonist of the chemokine receptor and cancer biomarker CXCR4^{190,191}. AMD-3100 was adsorbed onto the surface of ReANCs to use native drug binding pockets on human serum albumin^{192,193}. Dynamic light scattering (DLS) analysis revealed monodisperse populations and minimal change in the hydrodynamic diameter of fReANCs compared with ReANCs (**Supplementary Figure 3.1b**). Nanoparticle yield was quantified as approximately 58% using the bicinchoninic acid assay (BCA) protein assay. AMD-3100 loading

efficiency was determined to be 70% by high-performance liquid chromatography, consistent with our previous study¹⁸⁷. The fReANCs demonstrated active targeting as validated by competitive CXCR4 blockage and inhibition of cancer cellular migration assays (**Supplementary Figures 3.2 and 3.3**). Both native and functionalized ReANC formulations have exhibited no overt toxicity^{71,187}, which is consistent with our findings of no or little change in body weight (data not shown). Histopathology of major organs of clearance, such as liver, lung, kidney and spleen, extracted at various time points post-nanoparticle injection showed no abnormalities in tissue architecture (**Supplementary Figure 3.4**). In addition, normal histopathology from the organs of accumulation, such as the liver and lungs, following repeated weekly administration of nanoparticles (**Supplementary Figure 3.5**) indicated no signs of nanoparticle toxicity. Liver, lungs and spleen seem to be major organs of accumulation based on yttrium content per gram of tissue correlated with the content in the injected dose, as determined by inductively coupled plasma-mass spectrometry (ICP/MS) (**Supplementary Figure 3.6a**). The clearance pattern of ReANCs from animals, determined using ICP/MS, showed a decrease in nanoparticle content from all organs over the course of seven days. Accumulation in the spleen increased until day three, after which the nanoparticle content began to decline, indicating clearance (**Supplementary Figure 3.6b**). The CP/MS data showed correlation with the *ex vivo* SWIR signal from these respective organs (**Supplementary Figure 3.6c,d**).

3.3.2. SWIR imaging of photonic nanoparticles discerns bone lesions *in vivo* that are undetectable by MRI and CT.

Detection of micrometastatic lesions in the bone marrow is challenging due to a lack of sensitive imaging modalities¹⁹⁴. Current approaches can successfully detect abnormal bone activity, but are unable to identify cancer-related activity associated with bone metastases. Thus, there is a need for

targeted imaging agents that enable sensitive imaging of the earliest metastatic cell clusters at otherwise inaccessible metastatic niches.

Female athymic nude mice were injected with bone-tropic MDA-MB-231-derived sterol carrier protein 2 (SCP2) cells in the intratibial cavity (**Figure 3.2a**). Animals received weekly injections of unfunctionalized ReANC probes, beginning a week after tumour cell inoculation and were monitored using a preclinical SWIR imaging system (**Figure 3.2b,c**)⁷¹. Longitudinal imaging showed greater than twofold higher SWIR fluorescence in tumour-bearing animals compared with healthy controls, from five weeks post-inoculation until the study endpoint (**Figure 3.2d**). SWIR-imaging-based detection of tumours in the tibial cavity was validated by whole-body bioluminescence imaging (BLI) (**Figure 3.2e**). *Ex vivo* SWIR imaging of the skeletons at the endpoint confirmed accumulation of ReANC probes in the bone space (**Supplementary Figure 3.7**). Notably, tumour lesions were barely discernible using common preclinical imaging modalities such as CT and MRI (**Figure 3.2f,g**), even at the study endpoint. In addition, *ex vivo* hematoxylin and eosin (H&E) staining of tumour-bearing bone showed hypocellularization when compared with healthy controls, indicative of tumour-cell-mediated lytic activity in the bone (**Figure 3.2h**).

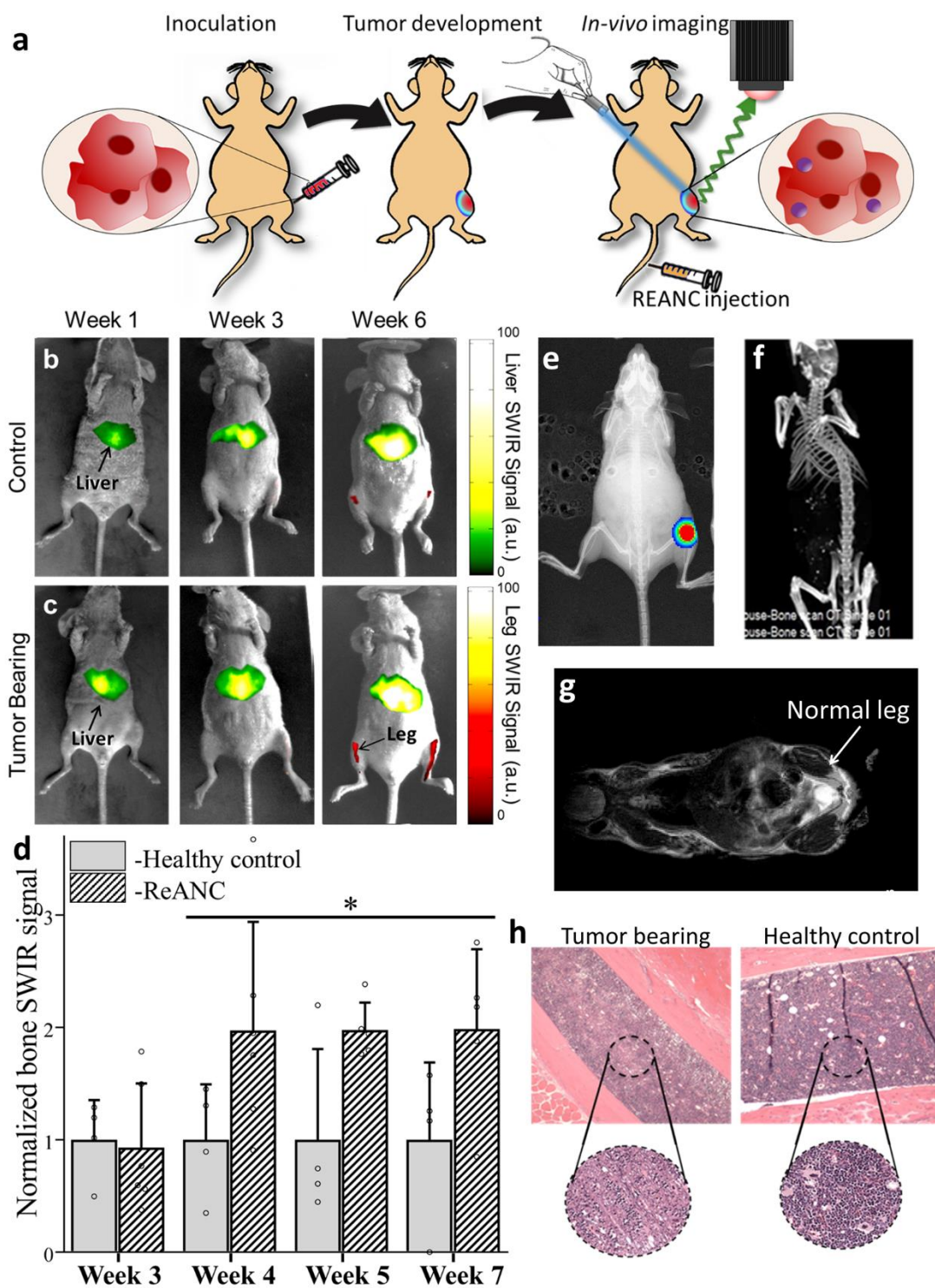


Figure 3.16- SWIR imaging of photonic nanoparticles discerns bone lesions in vivo that are undetectable by conventional MRI and CT: (a) Schematic diagram illustrating intra-tibial inoculation of MDA-MB-231 derived SCP2 cells followed by tail vein administration of ReANCs and *in vivo* SWIR imaging. Representative SWIR images from (b) healthy (non-tumor-bearing) animals and (c) tumor-bearing mice. (d) Quantification of SWIR signal in the tibiae of tumor-bearing and healthy controls shows a 2-fold increase in signal at 5-weeks post inoculation. Data is expressed as mean±S.D; n=6 for tumor-bearing group and n=3 for healthy control group. *P<0.1, determined by Welch's t-test. Data in (d) is represented as a fold increase compared to healthy control. (e) Validation of tumor presence by BLI. (f) End point CT and (g) MRI do not indicate bone deformities while (h) *ex vivo* histopathology shows possible hypo-cellularization, potentially indicating lytic activity due to the presence of tumors in tumor-bearing legs compared to healthy controls. SWIR intensities were normalized to those of the healthy control groups for the region of interest at each time point.

3.3.3. Distal bone lesions can be detected with SWIR imaging earlier than MRI in a biomimetic basal-like breast cancer metastasis model

Having successfully imaged small clusters of tumour cells in a localized intratibial model, we examined the ability of wholebody SWIR imaging to discern metastatic lesions in a breast cancer bone metastasis model. We established a MDA-MB-231 model previously shown by Minn et al. to follow different seeding kinetics and to colonize the lungs and bones following intravenous administration^{186,195}. This model exhibits low metastatic burden in the bones and hind legs in contrast with a relatively high burden in the lungs^{195,196}. We inoculated female athymic nude mice with MDA-MB-231- derived SCP28 cells via the tail vein, followed by weekly injection of ReANCs for SWIR imaging (**Figure 3.3a and Supplementary Video 3.1**). Compared with healthy controls (**Figure 3.3b**), tumour-bearing animals (**Figure 3.3c**) revealed a greater than twofold

increase in SWIR signal from the long bones, beginning at week five post-inoculation (**Figure 3.3d**). Most significantly, by week nine, we observed a greater than fivefold increase in SWIR signal from the bones of tumourbearing animals compared with controls (**Figure 3.3d**), while MRI still showed no abnormalities in the bone space (**Figure 3.3e**) and BLI showed absence of tumour burden in the bone (**Figure 3.3f**).

Nanoparticles encounter the lungs as their first barrier organ when administered intravenously, making the architecture of the lung vasculature an important determinant in their subsequent biodistribution to distant sites. A possible hypothesis for increased accumulation of ReANCs in the bone in this biomimetic model (**Figure 3.3**) compared with the previous intratibial model (**Figure 3.2**) could be that an altered vascular architecture due to tumour lesions in the lung is responsible for differences in nanoparticle biodistribution¹⁹⁷. MRI analysis also revealed moderate tumour burden in the lungs ($31.3 \pm 25.4 \text{ mm}^3$; mean \pm s.d.). Previous studies have shown passive uptake of ReANCs in the lungs only when the lesions are large and highly vascularized¹⁸⁷. During the studies reported here, no discernible SWIR signal from the lungs was detected (**Figure 3.3c,d**). This lack of lung signal reinforces the need to engineer nanoparticles for targeted uptake to organs such as lungs and adrenal glands where the infiltration barrier prevents passive uptake¹⁸¹.

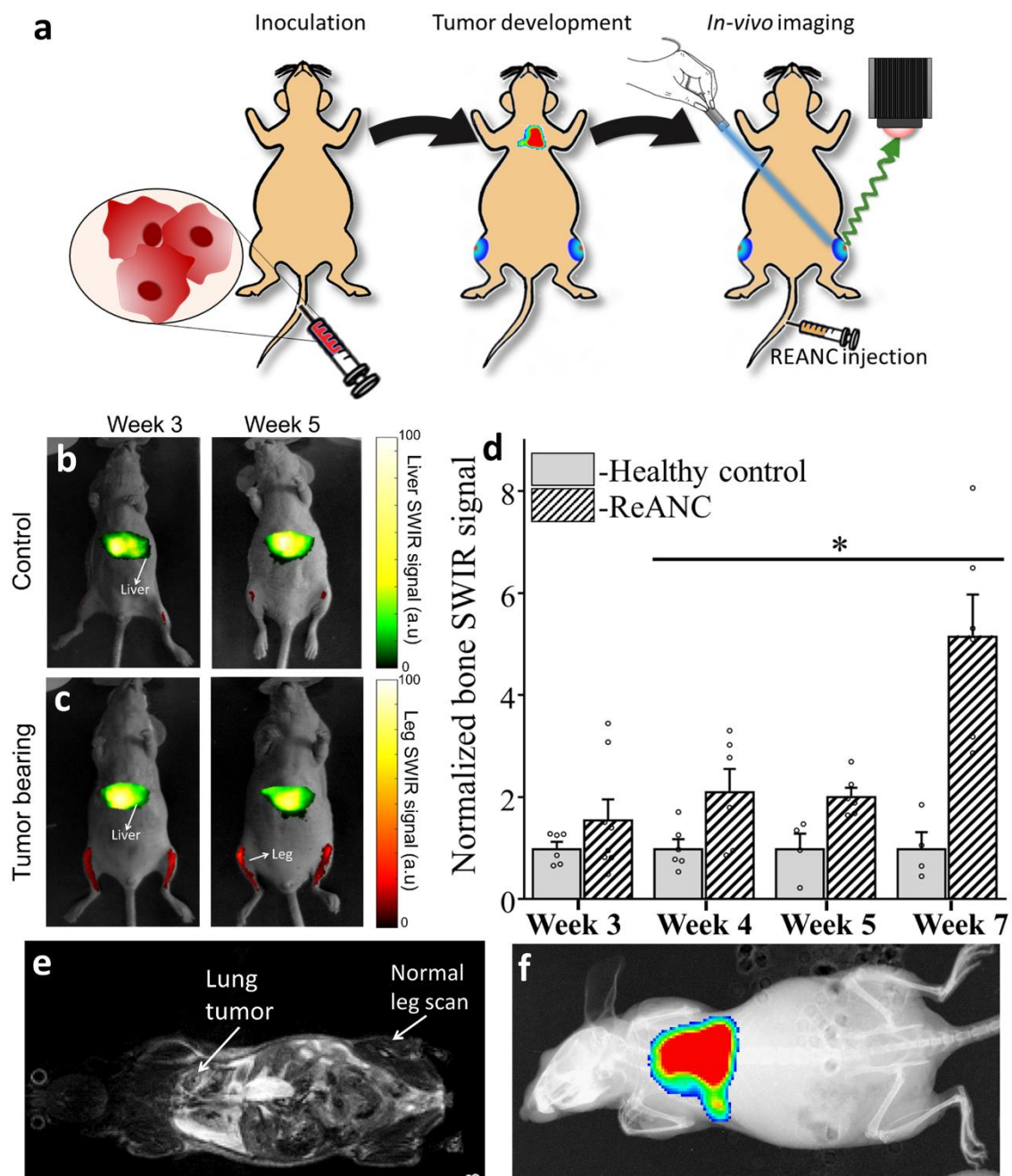


Figure 3.17- Distal bone lesions can be detected with SWIR imaging earlier than by MRI and CT in a biomimetic metastasis model: (a) Schematic diagram illustrating intravenous inoculation of MDA-MB-231 derived SCP28 cells followed by tail vein administration of ReANCs and *in vivo* SWIR imaging. Representative images from (b) non-tumor-bearing control animals and (c) tumor-bearing animals at weeks 3 and 5 post-inoculation. (d) Quantification of SWIR intensity shows at least a 2-fold increase in signal over healthy controls from week 5 onwards. Data is expressed as mean \pm S.D; n=4 for tumor-bearing group and n=3 for healthy control group. *two-tailed P<0.06, determined by Welch's t-test. Data in (d) is represented as a fold increase compared to healthy control. (e) MRI and (f) BLI show no visible bone abnormalities at the study end point. SWIR intensities were normalized to those of the healthy control groups for the region of interest at each time point.

3.3.4. Differential niche-based accumulation of ReANC and fReANC formulations leads to multi-organ detection of metastases in a luminal breast cancer model.

While bone physiology favours the uptake of nanoparticles such as ReANCs (**Figures 3.2 and 3.3**), other tissues require active targeting to facilitate nanoparticle labelling. In addition, cancer patients with metastases at multiple sites frequently have a lower quality of life and poorer prognosis than those with a single distant lesion¹⁹⁸. Therefore, it is imperative that metastasis imaging agents be designed to label phenotypically distinct lesions at physiologically distinct sites. To this end, we hypothesized that fRe-ANCs targeting the CXCR4 biomarker and non-targeted ReANCs could provide differential labelling of lesions at distinct organ sites in a biomimetic model of breast cancer metastasis.

The MCF-7-derived human metastatic breast cancer line was shown to express CXCR4 (**Supplementary Figure 3.8**). Athymic nude mice received intracardiac injections of MCF-7 cells to the left ventricle (**Figure 3.4a**). This model of luminal breast cancer is known to phenocopy

human disease, leading to both adrenal and bone metastases in mice supplemented with oestrogen⁷. Animals were given weekly injections of either fReANCs targeted to CXCR4 or non-targeted ReANCs, followed by SWIR imaging in both supine and dorsal positions. fReANCs preferentially accumulated in adrenal tumours (**Figure 3.4b,d**), exemplified by an almost 15-fold increase in SWIR intensity at this site in tumour-bearing animals compared with healthy controls, even as early as three weeks postinoculation (**Figure 3.4b–d**). Notably, there was no significant difference between SWIR signal intensity in tumour-bearing versus healthy control animals when unfunctionalized ReANC's were used (**Figure 3.4b,c,e**). In contrast, we observed a fourfold increase in SWIR signal from the bones of tumour-bearing animals compared with healthy controls (**Figure 3.5a,b**) when unfunctionalized ReANCs were administered for imaging. In this case, the SWIR signal from the bones of animals receiving fReANCs was not elevated compared with healthy controls (**Figure 3.5b**).

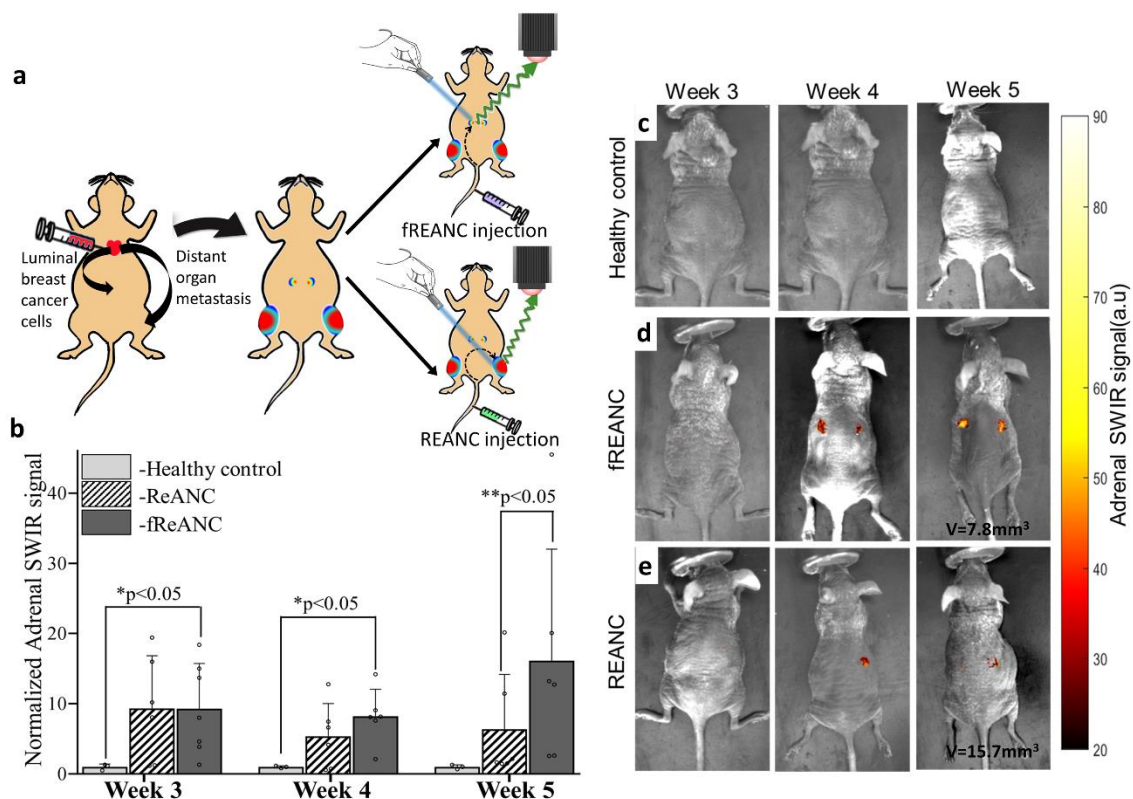


Figure 3.18- Differential niche-based accumulation of ReANC and fReANC formulations leads to multi-organ detection of metastases in a luminal breast cancer

model: (a) Athymic nude mice were injected with MCF7 derived cells via the left ventricle to form¹⁵ metastases in adrenals and bones; (b) Weekly intravenous administration of fReANCs show earlier detection of adrenal metastases compared to untargeted ReANCs. Quantitative analysis of SWIR intensity shows significantly higher accumulation of fReANCs compared to ReANCs at 5 weeks post inoculation whereas comparison between healthy controls and tumor-bearing animals injected with fReANC shows higher SWIR signal from adrenal lesions as early as 3 weeks post inoculation. Volumetric MRI analysis found the smallest tumor volume detected 5-weeks post inoculation with fReANCs to be 7.8 mm³, compared to a volume of 15.7 mm³ with REANCs. Representative dorsal (prone) images showing SWIR signal from adrenal lesions of healthy controls (c) and tumor-bearing animals injected with fReANC (d) and ReANC(e) shows earlier detection of adrenal metastases with active targeting. Data in (b) is expressed as mean±S.D; n=6 for tumor-bearing group and n=3 for healthy control group. *two-tailed P<0.05, determined by Welch's t-test. ** two-tailed P<0.05, determined by Welch's t-test. SWIR intensities were normalized to those of the healthy control groups for the region of interest at each time point.

The progression and location of metastases was monitored with bi-monthly MRI and validated by in situ and *ex vivo* SWIR imaging (**Supplementary Figures 3.9 and 3.10**). The smallest adrenal tumours detected by SWIR imaging were 7.8 mm³ in volume following fReANC administration and 15.7 mm³ with ReANCs, confirming the ability of fReANCs to target and resolve smaller metastatic clusters when compared with untargeted ReANCs. Fixed tissue sections were stained for oestrogen receptor and confirmed the presence of tumours in the adrenal glands (**Supplementary Figures 3.11 and 3.12**).

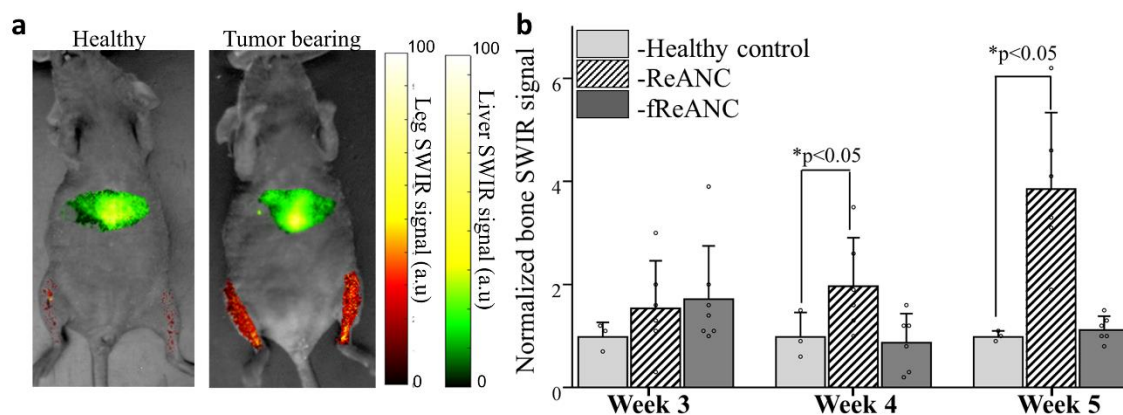


Figure 3.19- Passive accumulation of ReANCs, via the discontinuous fenestration architecture of bone tissue, in a metastatic luminal breast cancer model: Athymic nude mice were injected with MCF7 derived cells via the left ventricle to form metastases in bones followed by weekly injections of ReANC nanoprobe. (a) Representative ventral (supine) images showing SWIR signal from the bone space of tumor-bearing and healthy control animals show significant accumulation of ReANCs in the bone lesions 5 weeks post inoculation. (b) There is significant increase in SWIR emission intensity in bone starting 4 weeks post inoculation in tumor-bearing and healthy controls injected with ReANCs. There was no significant increase in accumulation of fReANC in bones of tumor-bearing and healthy control animals. Data in (b) is expressed as mean \pm S.D; n=6 for tumor-bearing group and n=3 for healthy control group represented as a fold increase compared to healthy control group.*two-tailed $P<0.05$ determined using a Welch's t-test. SWIR intensities were normalized to those of the healthy control groups for the region of interest at each time point

While we were able to demonstrate differential accumulation of the nanoprobe in distinct metastatic organ sites, another goal of this nanotechnology system is to enable surveillance of multi-organ metastases within the same animal. To this end, we injected a cocktail of untargeted and targeted nanoprobe in a triple negative metastatic breast cancer mouse model. The MDA-

MB-231 metastatic xenograft model led to lung and bone metastases when cells were inoculated intravenously into the animal followed by injection of a cocktail of ReANCs and fReANCs (**Figure 3.6a**). We were able to reproduce enhanced localization of targeted nanoprobe to lungs (**Figure 3.6b**) and untargeted probes to leg lesions (**Figure 3.6c**) as evidenced by a statistically significantly higher SWIR signal in tumour-bearing animals compared with healthy controls. In a pilot study, we observed qualitative evidence of preferential accumulation of ReANCs (**Figure 3.6d**) in the leg and fReANCs in the lungs (**Figure 3.6e**). Notably, we demonstrate accumulation in both lungs and legs when a cocktail of ReANCs and fReANCs were co-administered (**Figure 3.6f,g**). Future studies will work on dose optimization and mechanistic insights for active and passive targeting of the nanoprobe in the same animal.

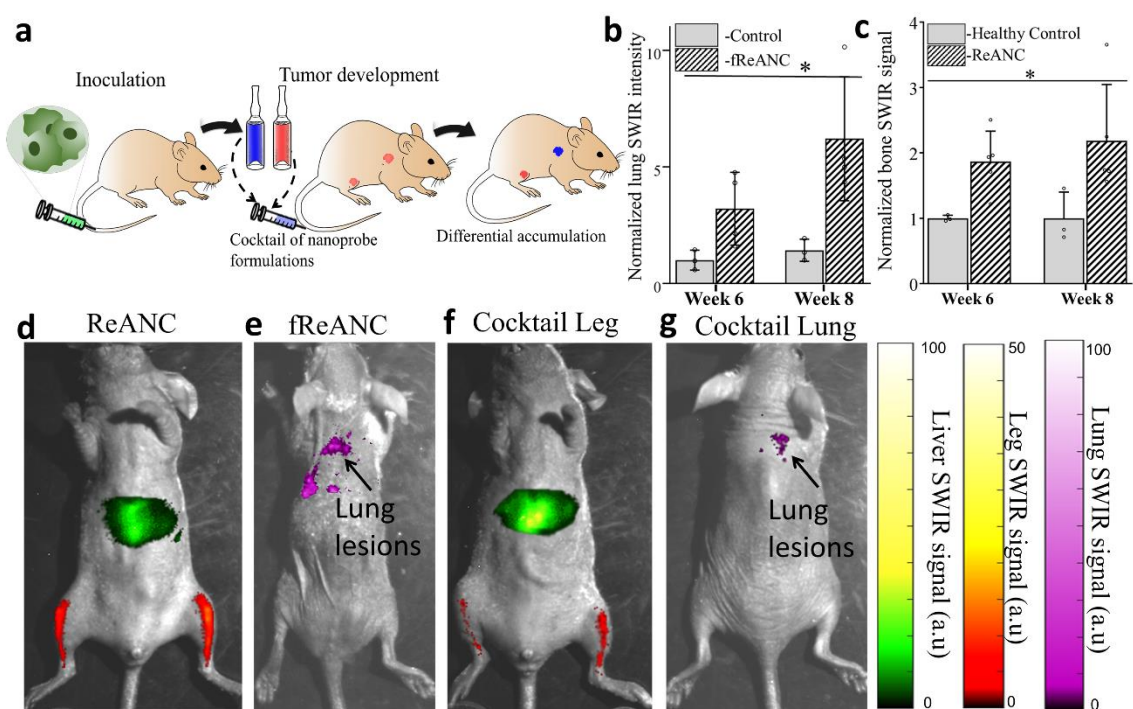


Figure 3.20- Differential accumulation of ReANCs in leg lesions and fReANCs in lung lesions in a multi-organ metastatic model: (a) Schematic illustrating intravenous inoculation of MDA-MB-231 cells followed by intravenous administration of a cocktail of nanoprobe formulations and SWIR imaging. Quantitative analysis of SWIR signal shows significantly higher lung intensity compared to healthy controls (b). Representative images show localization of ReANC localization to leg lesions (c); and fReANC localization to lung lesions (d). Representative animal injected with a cocktail of ReANC and fReANC probes showed leg signal (e) and lung signal (f). Data is expressed as mean \pm S.D; n=4 for tumor-bearing group and n=3 for healthy control group represented as fold increase compared to healthy control group. * $p < 0.07$, determined by Welch's t test. SWIR intensities were normalized to those of the healthy control groups for the region of interest at each time point.

3.3.5. Superior resolution with SWIR imaging compared with contrast-enhanced MRI for bone lesion detection in a biomimetic mouse metastatic model

SWIR imaging using ReANCs could detect bone lesions in orthotopic and metastatic models of breast cancer. We demonstrated that these bone lesions were undetectable by conventional MRI. However, to make a direct quantitative comparison to assess superior resolution with SWIR emitting nanoprobe, we performed contrast-enhanced MRI (CE-MRI) studies in an experimental metastatic triple negative breast cancer model with metastases to both lungs and bone. We proposed to use detection of lung lesions pre- and post-contrast as positive control for CE-MRI. We injected ReANCs bi-weekly to monitor SWIR signal in bones of animals. Bi-weekly MRI using contrast was performed in parallel for comparison.

In particular, we are able to detect bone lesions at week six postinoculation of tumour cells, as evidenced by a statistically significant, twofold increase in SWIR emission compared with non-tumour control animals. We also demonstrate that these lesions were not detectable by CE-MRI at

week six (**Figure 3.7a,b**) and that the apparent increase in MRI signal is not statistically significant until week eight (**Figure 3.7d**). Most notably, SWIR emission in tumour-bearing animals was visualized two weeks before and with far greater fold increase in signal than CE-MRI (**Figure 3.7c**). Quantitative changes with CE-MRI between non-tumour controls and tumour-bearing animals were not statistically significant at week six. In addition, as a control for contrast enhancement, we quantified MRI-contrast intensity in kidneys and found no significant change between tumour-bearing and non-tumour controls (**Supplementary Figure 3.13**). Contrast enhancement of lung lesions was used as positive control (**Figure 3.7e,f**).

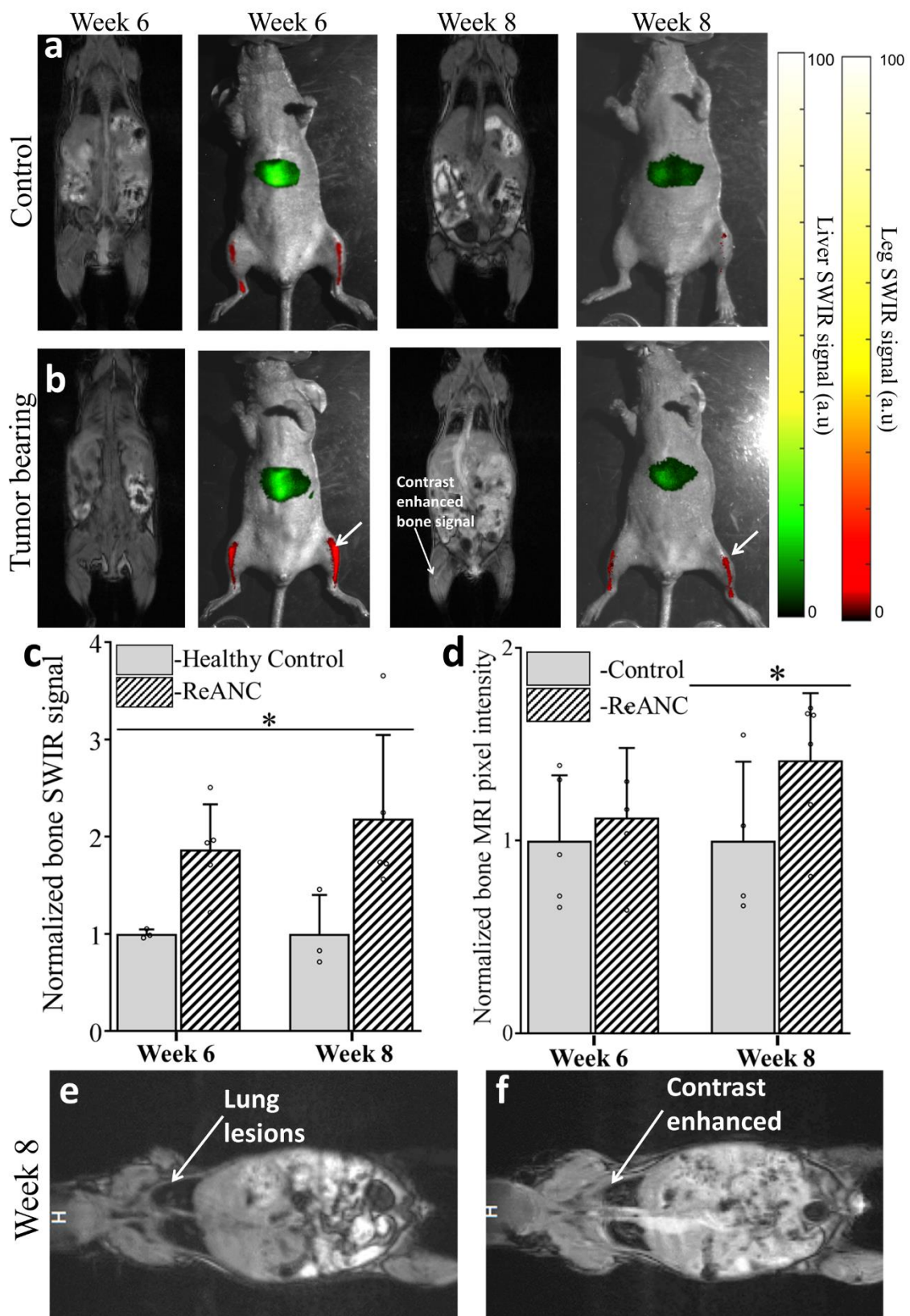


Figure 3.21- Distal bone lesions can be detected with SWIR imaging earlier than by contrast-enhanced MRI in a biomimetic metastasis model: Representative images from non-tumor control animals (a) and Tumor-bearing animals (b) shows enhanced SWIR signal 6 weeks' post inoculation with no significant changes in CE-MRI. At 8 weeks' post inoculation both SWIR and CE-MRI shows enhanced signal from the bone space. Quantitative comparison of SWIR emission intensity (c) in bone lesions shows significant increase starting week 6 post inoculation compared to non-tumor control animals. Quantitative analysis of increase in pixel intensity pre- and post-contrast injection in MR imaging does not show significant enhancement until week 8 (d). Representative image of lung metastases prior to (e) and post (f) contrast injection at week 8, used as positive control, to show enhanced uptake of MRI contrast by tumor lesions. Data is expressed as mean \pm S.D; n=5 for tumor-bearing group and n=3 for healthy control group. *two-tailed P<0.05, determined by Welch's t-test; n=5 **two tailed P<0.05 determined by Welch's t-test; n=6. Data in c and d is represented as a fold increase compared to healthy control. SWIR intensities were normalized to those of the healthy control groups for the region of interest at each time point.

3.3.6. Distinct metastatic lesions originating from a common cell line exhibit niche-dependent molecular signatures.

As the metastatic microenvironment of each pre-metastatic niche can cause site-specific variations in protein signatures, the ability for imaging agents to parse such site-specific molecular profiles will have far-reaching preclinical and clinical impact in developing diagnostic tools and therapeutic interventions in recurrent cancers. To further elucidate the role of the metastatic niche on the phenotypic signatures of metastatic lesions, cells were harvested from bones (MCF-7-5624a and

SCP28), adrenal glands (MCF-7 6124A) and lungs (SCP28) in the metastatic tumour models (**Supplementary Figure 3.14a**). Cell lysates extracted from these were analysed for differences in protein expression. In the luminal breast cancer model, analysis of microarray pixel density revealed upregulation of N-cadherin, ADAM17 (ADAM metallopeptidase domain 17) and JAM-A (junctional adhesion molecule-A) in adrenal-tropic cells (**Supplementary Figure 3.14b**), while bone-tropic cells were found to upregulate a separate set of markers, including Notch-1, amphiregulin and EGFR (epidermal growth factor receptor) (**Table 3.1**).

PROTEINS UPREGULATED IN ADRENAL-TROPIC MCF7-6124A CELLS			
Protein	Fold Change	Pathway activated	Clinical relevance
N-Cadherin	4.75	Sustains activation of ERK and activates MMP-9 production	Promotes invasive activity and increases tumor metastasis
ADAM17	6.5	Activates EGFR-MEK-ERK pathway and upregulates MMP-2 and MMP-9, stimulates the release of TGF α	Increases cellular invasion and proliferation
JAM-A	4.5	Activates Rap1 GTPase and upregulates β 1-integrin	Increases cell motility Indicates poor patient prognosis
PROTEINS UPREGULATED IN BONE-TROPIC MCF7-5624A CELLS			
Notch-1	2	Activated by downstream products of TGF β -SMAD pathway to promote osteoclast differentiation in bone	Promotes bone reabsorption and osteolytic lesions
Amphiregulin	2	Stimulates and increases EGFR signaling	Important for bone colonization
EGFR	2.27	Activation with MMP-1 leads to reduced production of osteoprotegrin, increasing RANKL activation of osteoclasts	Impacts recruitment of osteoblasts, limiting bone mineralization

Table 3.1: Distinct metastatic lesions originating from a common cell line exhibit niche-dependent molecular signatures

Cancerous cells isolated from adrenal and bones were cultured *ex vivo* and analyzed for changes in biomarker expression with a hematopoietic array. Cellular markers upregulated in adrenal-tropic lines were typically associated with increased tumor growth and invasion, while those upregulated in the bone-tropic line act to promote bone resorption

Bone-tropic 5624a cells expressed a twofold increase in Notch-1 relative to adrenal-tropic cells. Notch-1 upregulation has previously been correlated with bone metastases and the presence of lytic lesions¹⁹⁹, while N-cadherin is associated with tumour invasiveness, growth and metastasis²⁰⁰. Adrenal-tropic cells exhibited a 4.75-fold increase in N-cadherin expression compared with bone-tropic cells, suggestive of a more aggressive tumour phenotype.

In the triple negative breast cancer model (SCP28), we found niche-based differences in protein expression in the lung-tropic and bone-tropic lines using a human oncology array. We found in the lung-tropic line upregulation of metastasis-associated proteins such as amphiregulin, endoglin and carbonic anhydrase- IX (**Supplementary Figure 3.14c**). Interestingly, the bone-tropic cells showed upregulation of two of the proteins present in the lung niche-signature namely amphiregulin and endoglin. In addition, we found an increase in MMP-3 (matrix metalloproteinase-3) and EpCAM (epithelial cell adhesion molecule) in the bone niche (**Supplementary Figure 3.14d**). The significant differences observed in molecular signatures between cell populations at various metastatic sites correlate with our ability to target these two metastatic lesions using divergent design criteria for our SWIR-emitting nanoparticles.

These distinct molecular signatures also exemplify potential targets to develop niche-specific targeted nanoparticles for imaging and therapy.

3.4. Discussion

Cancer metastasis is a process whose dynamics remain poorly understood due to the limited ability of existing techniques to obtain meaningful information in real time. Optical imaging of metastasis in live animals under native physiological conditions has been innately difficult due to poor tissue penetration and high background levels due to tissue autofluorescence. Most preclinical imaging in multi-organ metastatic models has been invasive, using intravital imaging windows and genetically engineered cells that express luciferase or fluorescent reporters²⁰¹⁻²⁰⁴. The goal of this work was to develop an optical imaging system that could resolve multiorgan lesions at distant metastatic sites in real time without necessitating genetically altered reporter cells.

We demonstrated that appropriately sized rare-earth albumin nanocomposites are able to home to micro-metastatic lesions in the long bones (**Figures 3.2, 3.3 and 3.5**) and spine (represented in **Supplementary Video 3.1**) in multiple *in vivo* breast cancer models. Because of robust nanocomposite accumulation and deep-tissue imaging SWIR emissions, micro-metastatic lesions were observed as early as three weeks post-inoculation in an orthotopic model of breast cancer. We demonstrated that weekly injection of ReANCs showed consistent, rapid accumulation in the bones with complete clearance by 48 h post-injection (**Supplementary Figure 3.7**), rendering the nanoprobe safe for repeated use in longitudinal studies. Notably, the ReANC probes elicited no overt toxicity when compared with controls (**Supplementary Figures 3.4 and 3.5**) and control animals showed no signs of distress during the study period. The clearance of ReANCs through major organs of clearance was within acceptable limits up to seven days post-administration of probes (**Supplementary Figure 3.6**). Remarkably, MRI and CT did not reveal any changes in bone architecture. Histopathology also validated regions of possible changes in bone architecture when compared with tissue sections from control animals. Most notably, CE-MRI did not show significant quantitative changes at week six, when bone lesions detected by SWIR imaging were significant between tumour-bearing versus control animals (**Figure 3.7**).

In a biomimetic model where multi-organ metastases to the lung and bone are observed, we found differential accumulation of ReANCs to lesions in the bone as early as three weeks postinoculation. This was consistent with our previous findings, where ReANCs could not discern lung metastases until lesion volume reached around 56 mm³ ¹⁸⁷. Bone lesions were undetectable on MRI and BLI whereas lung lesions were detected by MRI and BLI. Differential uptake of nanoparticles based on size^{71,205} and surface functionalization²⁰⁵ has been demonstrated in previous *in vitro* and *in vivo* studies. An added benefit of the differential nanoparticle uptake, especially via active targeting, is that we can quickly reduce the percentage of particles remaining in systemic circulation therefore achieving further reduction in unwanted background signal. Of particular interest in metastasis imaging would be a nanoparticle formulation that can be modified and administered systemically to detect distal multi-organ metastases in real time. Simultaneous detection of metastases at multiple distinct sites is important for effective treatment as undetected lesions lead to recurrent disease. These persistent tumours are often resistant to therapy and require lesion-specific intervention²⁰⁶. The ability to detect phenotypically distinct tumours at distant sites is critical in predicting the likelihood of recurrence and in selection of effective therapies^{195,196}.

Intrinsic to the nanoprobe detection of multi-organ metastases is the design of multivariate targeting mechanisms. For the ReANC nanoprobes to penetrate through barriers in organs such as lungs, the design strategy would call for the display of a surface charge (to undergo transcytosis) or a targeting ligand (especially for chargeneutral particles such as human serum albumin-coated probes) to exhibit receptor mediated-endocytosis²⁰⁷. Other reports highlight the role of size, charge, shape and targeting ligand selection in altering nanoparticle infiltration through various barriers leading to the tumour in an animal model^{208,209}. In our study, a combination of passive and active targeting may be key to the detection of tumours in the bones and adrenal glands, respectively. Sinusoid capillary fenestrations play a major role in nanoparticle delivery and, in combination with leaky vasculature of tumours, this could play a role in the increased accumulation of unfunctionalized ReANCs in the bone. In addition, the changes in bone architecture associated with tumour progression may

also play a role in improved accumulation of ReANCs in the bone. In contrast, the adrenal glands showed poor accumulation of unfunctionalized ReANCs along with pronounced recruitment of the functionalized fReANCs, which indicates the role of active targeting. The active targeting of our functionalized fRe-ANCs is designed based on elevated CXCR4 binding (validation in **Supplementary Figures 3.2 and 3.3**). Tumour-targeted fReANCs were able to resolve adrenal lesions as small as 8 mm³ and detect these lesions earlier than ReANCs, suggesting that the continuous fenestration of capillaries around adrenal tissue is not amenable for EPR of ReANCs. This result, combined with our previous studies in a lung metastasis model, indicates that ReANCs require a certain tumour burden in certain niches for accumulation, whereas sites such as the bone permit uptake with a relatively low tumour burden. To explore the relevance of our probes to a different metastatic model, we tested accumulation of fReANCs on intravenous inoculation of MDA-MB-231 cells. Here, we demonstrated using a pilot study that the probes can effectively resolve a different profile of multi-organ metastases (actively targeted fReANCs bound to metastases in the lungs versus passively targeted ReANCs accumulated in the bone) (**Figure 3.6**). Future studies could exploit these differences to explore the use of our imaging tools to further track nanoparticle penetration through the vascular, perivascular and interstitial space in tumours. Understanding the molecular basis of interactions between a primary tumour, distant metastases and the metastatic niche is critical to fulfil the promise of improved and personalized therapies in cancer patients. Our study highlights an integrated approach for the sensitive and accurate detection and analysis of micro-metastatic lesions. Proteomic analysis of cells isolated from metastatic sites highlighted by distinct classes of the nanoprobe showed a clear dichotomy in molecular signatures. Specifically, increased Notch-1 in bone lesions vis-à-vis N-cadherin in adrenal-gland metastases provides molecular context to the metastatic process that can potentially be exploited for tailoring precision therapeutics to individual patients. Notably, early detection of lesions facilitated extraction and analysis of changes in niche-based signatures from tumour onset to endpoint. Collectively, these outcomes suggest that our system can longitudinally perform non-invasive

molecular assessment of metastases and also monitor treatment outcomes targeted to highly heterogeneous metastatic lesions^{196,210}.

In summary, we have developed an integrated multi-organ-metastasis imaging system for the detection and analysis of early metastatic lesions in distal organs. We demonstrated the applicability of this imaging system in several distinct *in vivo* breast cancer models. Future preclinical applications of this approach will expand on the customization of ReANC probes with markers specific for metastatic lesions, based on the niche surrounding these clusters. Researchers could design a cocktail of such site-interactive ReANC formulations to detect, track and understand interactions between cells in these different compartments, providing clues that will eventually lead to the development of better therapeutic agents for the clinic. As a whole-body surveillance system, we envision this to be a scanning imaging tool for pre- and post-therapy monitoring in preclinical settings, via real-time noninvasive molecular detection of lesions in multiple organs.

3.5. Methods

3.5.1. Fabrication of rare-earth nanoparticles.

Rare-earth nanoparticles were synthesized as previously described via burst nucleation reaction^{71,188,189}, and incorporated into ReANCs via solvent-induced controlled coacervation of albumin^{71,124}. Hydrodynamic diameters of ReANCs were determined via DLS (Malvern Instruments) (**Supplementary Figure 1a**), which also revealed monodisperse particle populations. Two classes of ReANCs were designed for targeting distinct classes of metastatic sites. Albumin-based ReANCs were administered as unfunctionalized composites for detection of bone cancer metastases. In contrast, fReANCs were designed for targeting of adrenal-gland metastases. fReANCs were generated through passive absorption of the CXCR4-antagonist AMD-3100 (EMD Millipore) onto the surface of fully formed ReANCs. A range of AMD-3100 concentrations from 12.5 μ M to 12.5 nM were generated for *in vitro* testing to determine the optimal loading conditions¹⁸⁷. An AMD-3100 loading concentration of 1.25 μ M was found to be optimal based on our *in vitro*

testing, and was used for all *in vivo* experiments. Nanoprobe diameter and polydispersity were determined through DLS; nanoprobe yield was determined by BCA protein assay.

3.5.2. *In vivo* imaging.

Imaging studies were conducted using athymic nude female homozygous nude mice^{71,187} (Taconic). Whole-body BLI was performed using an MsFxPRO system (Carestream Molecular Imaging). Anaesthetised animals were injected with D-luciferin (Perkin-Elmer) and imaged 10 min post-administration to obtain a significant signal. All animal studies were approved by the Institutional Review Board for the Animal Care and Facilities Committee of Rutgers University and performed in accordance with institutional guidelines on animal handling.

3.5.3. Whole-animal SWIR imaging.

A small animal SWIR imaging system was assembled in-house^{71,187}. Mice were fully anaesthetised using 2% isoflurane (Butler- Schein) and were continuously scanned with a collimated 980 nm laser (1.7 W). SWIR emission was detected with an InGaAs camera (Sensors Unlimited) equipped with two 1,020 nm long-pass filters and a band-pass 1538/82 nm filter (Semrock) and a 25 mm focal length SWIR lens (StingRay Optics). The system is capable of real-time animal imaging with an exposure time of 33 ms per frame. Images were acquired as video files and processed for quantitative analysis using custom Matlab scripts, as described in 'SWIR image analysis'. Animals injected with 200 µl of ReANCs intravenously were imaged at 20 fps and a representative video postprocessed to show localization of particles is shown in Supplementary Video 1.

3.5.4. MRI and CT imaging.

MRI images were acquired using 1 Tesla M2 highperformance MRI system (Aspect Magnet Technologies). CT images were acquired using ALBIRA PET/CT system (Carestream Molecular Imaging). All imaging procedures were performed under inhalation anaesthesia with isoflurane at a concentration of 4% for induction of anaesthesia and 1–2% for maintenance. Volumetric three-dimensional reconstruction to determine tumour volumes was performed using Vivoquant software

(Aspect Magnet Technologies). For CE-MRI, pre-contrast fast spin echo and gradient echo images were acquired followed by injection of Magnevist (gadopentetic acid; Henry Schein) and acquisition of postcontrast gradient echo and fast spin echo images. Analysis of *T1* and *T2* weighted images were performed as described under MRI image analysis.

3.5.5. Cell lines.

The cell lines used in this study were obtained from the following sources: SCP2 and SCP28, animal-derived, provided by Y. Kang; MCF7-5624a, animal-derived, provided by V.G.; MDA-MB-231 and MCF7 (ATCC). The authenticity of the animal-derived lines to the parental lines was tested using cellline authentication services utilizing short tandem repeat (STR) profiling (ATCC, VA). Animal-derived cell lines have not been tested for mycoplasma contamination on procurement but were tested for mycoplasma by using PCR detection methods.

3.5.6. Orthotopic model of bone metastasis.

Bone-tropic MDA-MB-231-derived SCP2 cells expressing luciferase¹⁸ (a gift from Dr Kang, Princeton University) were maintained in Dulbecco's modified eagle medium (DMEM) supplemented with 10% fetal bovine serum and 1% penicillin/streptomycin. 1×10^5 MDAMB-231-derived SCP2 basal-like breast cancer cells were injected into the tibiae of 3–4-week-old female homozygous athymic nude mice under inhalation anaesthesia with 2–3% isoflurane⁷. Whole-body SWIR imaging was performed on all animals both pre- and post-ReANC injection (200 μ l; 10 mg kg⁻¹; intravenous administration via tail vein). Tumour progression was monitored longitudinally by using SWIR imaging weekly over a ten-week time course. SWIR intensity from the tibia of tumour-bearing and healthy control animals was quantified to determine the accumulation of ReANCs. The presence of tumour in the bone space was confirmed using BLI at week nine. MRI was used to monitor any bone deformities due to the presence of lytic lesions.

3.5.7. Biomimetic model of bone metastasis.

Parental MDA-MB-231- and MDAMB- 231-derived SCP28 cells¹⁸ (a gift from Y. Kang, Princeton University) were maintained in DMEM supplemented with 10% fetal bovine serum and 1% penicillin/streptomycin. Three-to-four-week-old homozygous female athymic nude mice were intravenously inoculated via the tail vein with the MDA-MB-231-derived SCP28 breast cancer cell line (2×10^5 cells; a gift from Y. Kang, Princeton University; note that SCP28 are a subclonal population different from SCP2), leading to the development of lung and bone lesions¹⁸. Animals received weekly injections of ReANCs (200 μ l, 10 mg kg⁻¹, via intravenous administration) to detect and monitor tumour progression over a ten-week time course. In another study, MDA-MB-231 cells (3×10^5 cells) were injected intravenously into 4–5-week-old female athymic nude mice. Animals received weekly injections of ReANCs, fReANCs or a cocktail of ReANCs and fReANCs (200 μ l, 10 mg kg⁻¹, via intravenous administration) to detect and monitor tumour progression over a ten-week time course. Whole-body SWIR imaging was performed pre- and post- ReANC administration. Tumour burden was validated by bi-monthly MRI. CEMRI was also performed to determine tumour burden in legs.

3.5.8. Biomimetic model of multi-organ distal metastases.

Bone-derived MCF-7-5624A cells were maintained in DMEM supplemented with 10% fetal bovine serum and 1% penicillin/streptomycin⁷. The authenticity of the animal-derived line to the parental line was tested using the cell line authentication services using short tandem repeat profiling (ATCC). MCF-7-5624A tumour cells were injected into the left cardiac ventricle (5×10^5 cells) in 3–4-week-old homozygous female athymic nude mice (Taconic) supplemented with low-dose oestrogen pellets (0.18 mg; Innovative Research of America) that deliver 2 μ g d⁻¹ of 17 β estradiol. Tumour progression and size was monitored through BLI and MRI. Mice received weekly injections of ReANCs or fReANCs functionalized with 12.5 μ M AMD-3100 at 10 mg kg⁻¹ body weight and were imaged immediately post-injection and up to 24 h post-administration.

SWIR signal from the leg bones and the dorsal area corresponding to the location of the adrenal glands was quantified. Animals were killed on weight loss and organs were excised. Tumour volume was calculated using three-dimensional reconstructions generated from MRI imaging.

3.5.9. *Ex vivo* analysis of bone microlesions.

At experimental endpoints, animals were euthanized and bones were excised and fixed in formalin. Bones were later decalcified in 0.5 M EDTA for 24–48 h and stored at 4 °C in 70% ethanol before processing. Tissues were then embedded in paraffin and 5 µ m sections prepared. Tissue sections were de-paraffinized, rehydrated and stained with H&E before mounting and imaging under standard light microscopy (Nikon).

3.5.10. *Ex vivo* analysis of adrenal lesions.

Adrenal tumours were removed, fixed in 10% neutral-buffered formalin overnight and stored at 4 °C in 70% ethanol before processing. Tissues were then embedded in paraffin and 5 µ m sections prepared. Tissue sections were de-paraffinized, rehydrated and stained with H&E, as well as with rabbit monoclonal anti-human ER α IgG (catalogue no: ab16660, Clone SP1, Spring Bioscience) and rabbit monoclonal anti-human CXCR4 IgG antibody (catalogue no: ab181020, Clone EPUMBR3, Abcam). Control slides were stained using appropriate isotype control antibodies. Biotinylated secondary antibodies were used for detection.

3.5.11. SWIR image analysis.

SWIR emission from animals was collected pre-and postinjection of nanoparticles in the form of a video file in .bin format. A white light image of the animal for both time points was taken and labelled according to the condition. The bin file-converting Matlab file was used to process the video files to extract maximum pixel values from each frame of the video and saved as a tiff image file. Image processing was done through manual selection of regions of interest (ROI). ROIs corresponding to the desired organ were selected using anatomical landmarks present in background images. These ROIs were then applied to the associated infrared image, and the mean

SWIR signal intensity over space for the region of interest was calculated. These values were then used to perform statistical analyses to compare the SWIR signal from each ROI between tumour-bearing and healthy control groups.

3.5.12. MRI image analysis.

Post-contrast changes in signal intensity were quantified by exporting the images acquired using T2 MRI as dicom files and analysing them using vivoquant software. Unique image scale factor for each image is extracted and applied to the individual image before quantification for normalization. Post-normalization, the bone space of the animal is selected using the three dimensional ROI tool *in vivoquant*. The mean pixel intensity value in the selected three-dimensional space is generated as an Excel file by the software. The increase in pixel intensity due to contrast injection is evaluated by analysing both pre- and post-contrast MRI scans. The increase of pixel intensity was compared between the tumour-bearing and healthy control animal groups.

3.5.13. Human soluble receptor array and human oncology array for molecular phenotyping.

Organs bearing metastatic tumours were processed and the resulting cells collected and cultured. To isolate tumour cells from bone lesions, a 1 ml syringe with a 26 G needle was filled with phosphate buffered saline and inserted into one end of the tibia and cells expelled from the other end by applying positive pressure to the syringe. For adrenal and lung tumours, cells were crushed and homogenised using frosted glass slides and cells filtered to remove debris using a cell strainer (Falcon). After one to two weeks of culture, a pure population of human cancer cells was obtained. Cell line protein expression was evaluated using with the Human Soluble Receptor Array Kit Non-Hematopoietic Panel or Human Oncology Array (R&D systems) according to the manufacturer's instructions. Array results were quantified in terms of pixel density using ImageJ (National Institutes of Health) and the degree of fold change was determined by comparison with that of the parental line.

3.5.14. Quantitative biodistribution, clearance and toxicology studies.

Athymic nude mice were injected with 10 mg kg⁻¹ of ReANCs. Primary organs of clearance (liver, lung, kidney and spleen) were harvested at 0 h, 1 d, 3 d and 7 d post-injection and imaged *ex vivo* using the SWIR imaging system. *Ex vivo* SWIR intensity was correlated to nanoparticle (yttrium) content in organs as determined by ICPMS. Briefly, yttrium content of digested organs taken from mice was quantified using a Thermo X series II ICP-MS (Thermo Scientific) to determine particle concentration after injection. All samples were digested in 16 M nitric acid (Fisher Scientific) and evaporated to dryness, then reconstituted in 10% nitric acid to account for differences in sample volume. Count rates for yttrium were correlated to parts per billion using a standard curve generated with an yttrium standard (Sigma-Aldrich). Percentage of injected dose was calculated by correlating yttrium content in the injected nanoparticle dose to yttrium content per gram of tissue.

3.5.15. Competitive inhibition of CXCR4 as a measure of passive targeting.

MDAMB-231 cells were cultured in DMEM (Gibco, Thermo Fisher Scientific) supplemented with 10% FBS and 1% penicillin-streptomycin. Cells were plated in a 96 well plate (Falcon, Corning Brand) at a cell density of 100,000 cells per well. The ligand stromal cell-derived factor-1 α (PeproTech) was added to cells at concentrations of 10 nM and 100 nM, and incubated at 37 °C for 2 h. Following this, cells were treated with ReANC and fReANCs and incubated at 37 °C for 15–18 h. Cells were fixed in 1% paraformaldehyde subsequent to trypsinization and washes. The samples were then analysed via fluorescence-assisted cell sorting (FACSCaliber, BD Biosciences) and uptake quantified as a function of green fluorescence from the albumin shell. Data were analysed using Kaluza Analysis software (Beckman Coulter).

3.5.16. *In vitro* optimization of nanoprobes.

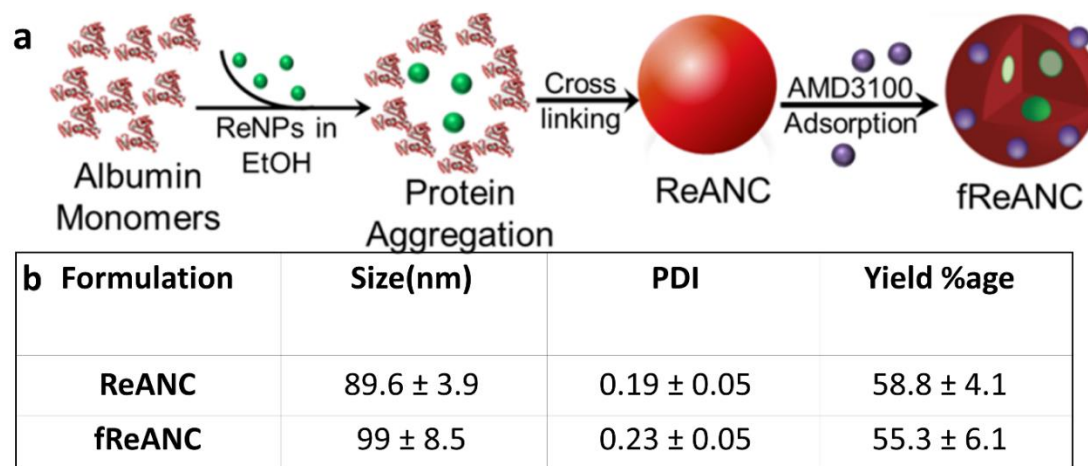
Scratch and cell migration assays were used to determine the effect of AMD-3100 functionalization on cell mobility. In the scratch assay, MCF-7 cells were plated in six-well plates and allowed to grow until confluent. These cell monolayers were scored with a pipette tip and samples were treated

with varying concentrations of ReANCs, fReANCs and free AMD-3100 in solution. The scratches were imaged over the course of 24 h to measure wound closure and cellular movement into the scratch. Cell migration was evaluated by measuring cell movement through 8 μ M transwell inserts. MDA-MB-231 cells were plated on top of 8 μ M transwell inserts and treated with ReANCs, fReANCs and free AMD-3100 in solution. Cells were then allowed to migrate through the mesh. Cell migration was evaluated through microscopy and crystal violet staining.

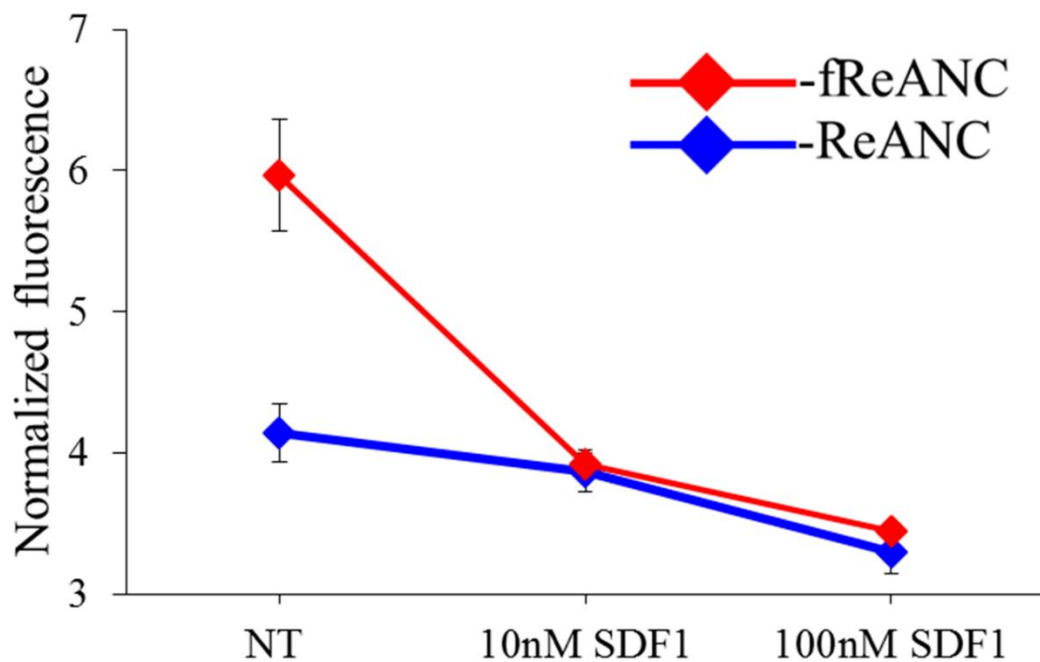
3.6.17. Statistical analysis.

For all *in vivo* studies, animal number was determined using G-power analysis (analysis of variance, one-way, omnibus) providing at least 70–80% power and an effect size of 0.8–0.85, with α set at 0.05. Full experimental details are provided in the Methods section(s) above, to ensure independent reproducibility by other investigators. For all *in vivo* studies, mice were randomly assigned to each experimental or control group and investigators were not blinded to the groups through the process of acquiring and analysis of data. Grubb's test for outliers was used to determine the inclusion or exclusion of data within groups for all datasets. The similarity of the variance between the groups was tested using the *F*-test of equality of variances using a confidence interval of 95%. Statistical tests were selected based on the normality of the distribution, sample size and the similarity in variance between groups. Statistical significance of the normal populations and was determined using a two-tailed Student's *t*-test or Welch's *t*-test. All statistical analysis was done using graphpad prism version 7.0 (GraphPad Software; www.graphpad.com).

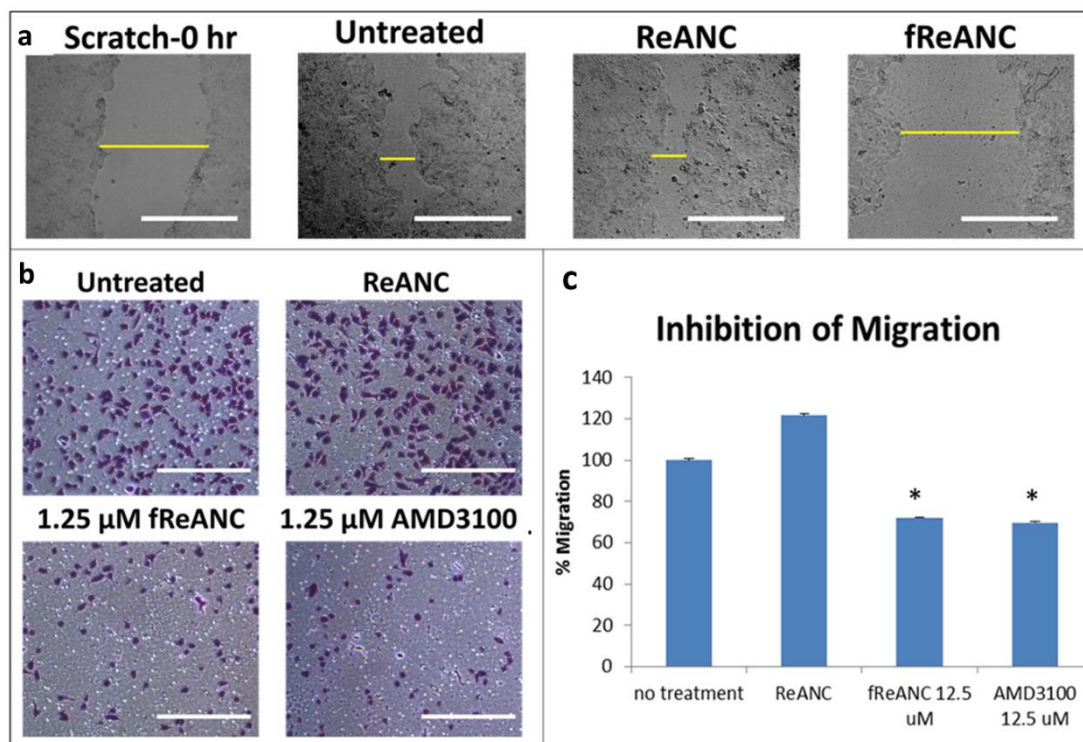
3.6. Supplementary Figures



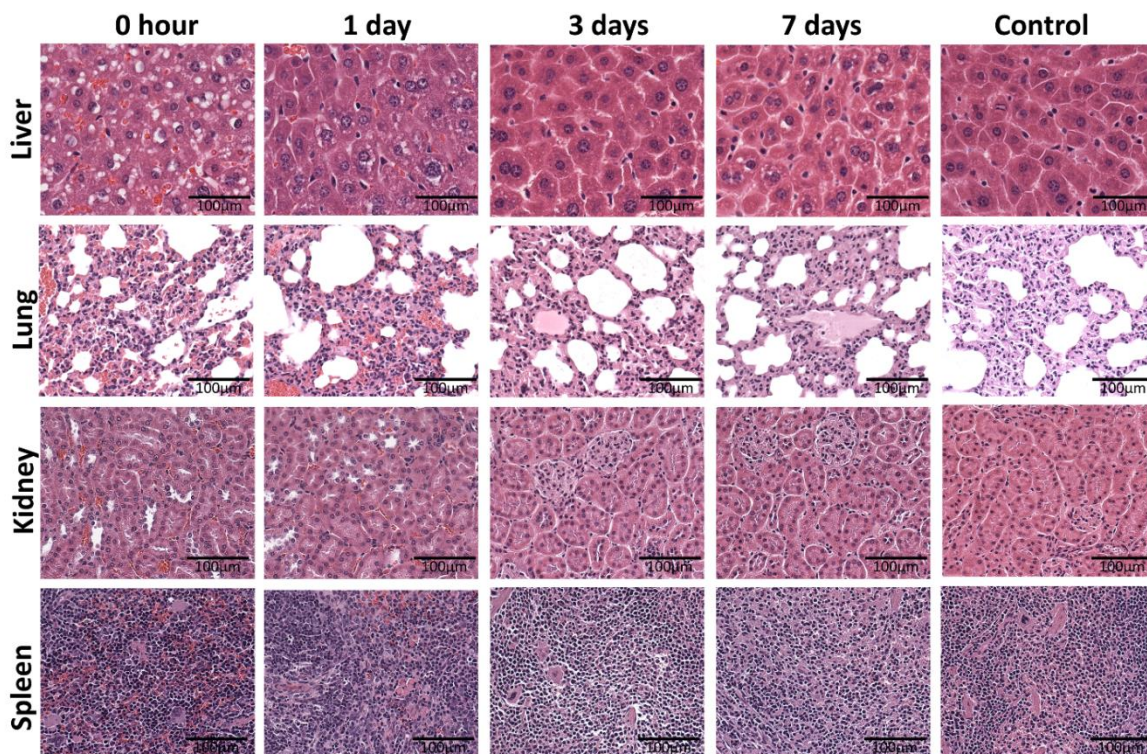
Supplementary Figure 3.7- Encapsulation of rare earth cores in albumin using a solvent induced controlled coacervation process forming rare earth albumin nanocomposites (ReANCs): (a). Functionalization of the encapsulated particles to achieve active targeting to adrenal metastases, was accomplished by adsorption of AMD-3100 on to the surface of ReANCs (a). Unfunctionalized (ReANCs) and functionalized (fReANCs) nanoparticles were characterized using a zetasizer (b). The hydrodynamic diameter of the particles measured using DLS was 89.6 nm and 99 nm for ReANCs and fReANCs respectively (b). The yield of nanoparticle encapsulation measured using BCA assay was ~ 58.7% .



Supplementary Figure 3.8- Validation of the active targeting mechanism of fReANCs vis-à-vis ReANCs: Competitive inhibition using SDF1 to block CXCR4 receptors shows decreased uptake of functionalized nanoparticles compared to unfunctionalized particles in triple negative breast cancer cells. Data is represented in n=1 in triplicates as mean \pm S.E.M.

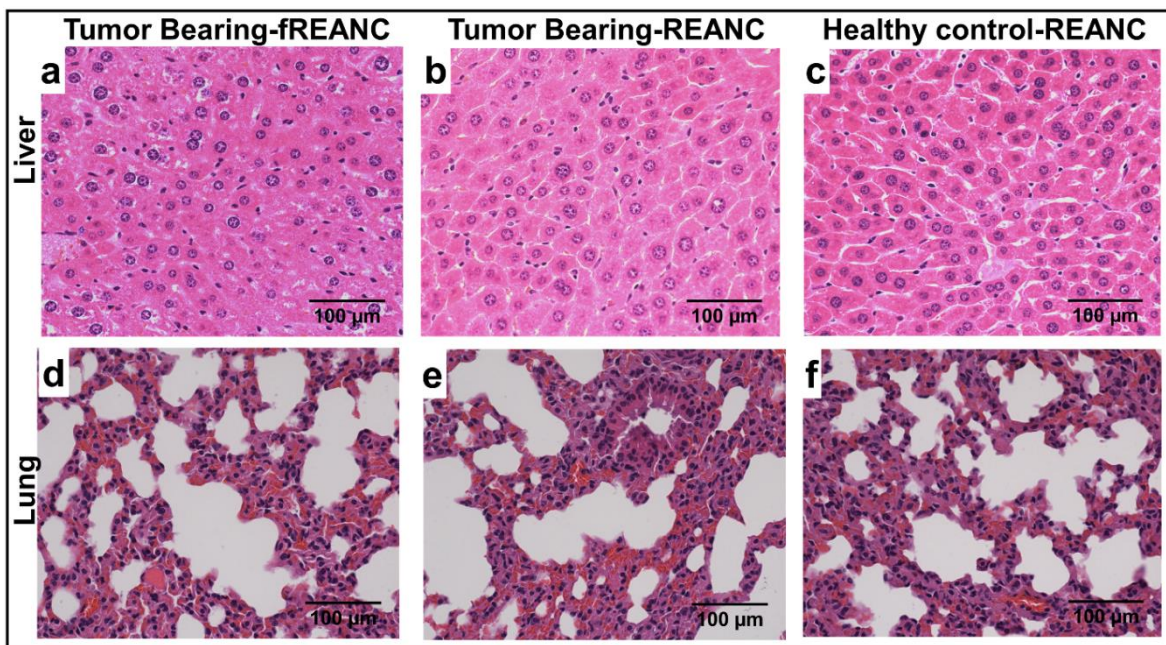


Supplementary Figure 3.9-Functional validation of molecular targeting features of fReANCs: *In vitro*, fReANC treatment was able to inhibit wound closure (A) and migration (B) of CXCR4 expressing cells, showing that CXCR4 inhibition is able to inhibit cellular metastasis. This effect was significant compared to treatment with ReANCs (C). * $p < .05$, $n=3$, one-way ANOVA, Tukey post-hoc. (A-B) scale bars 0.5 mm



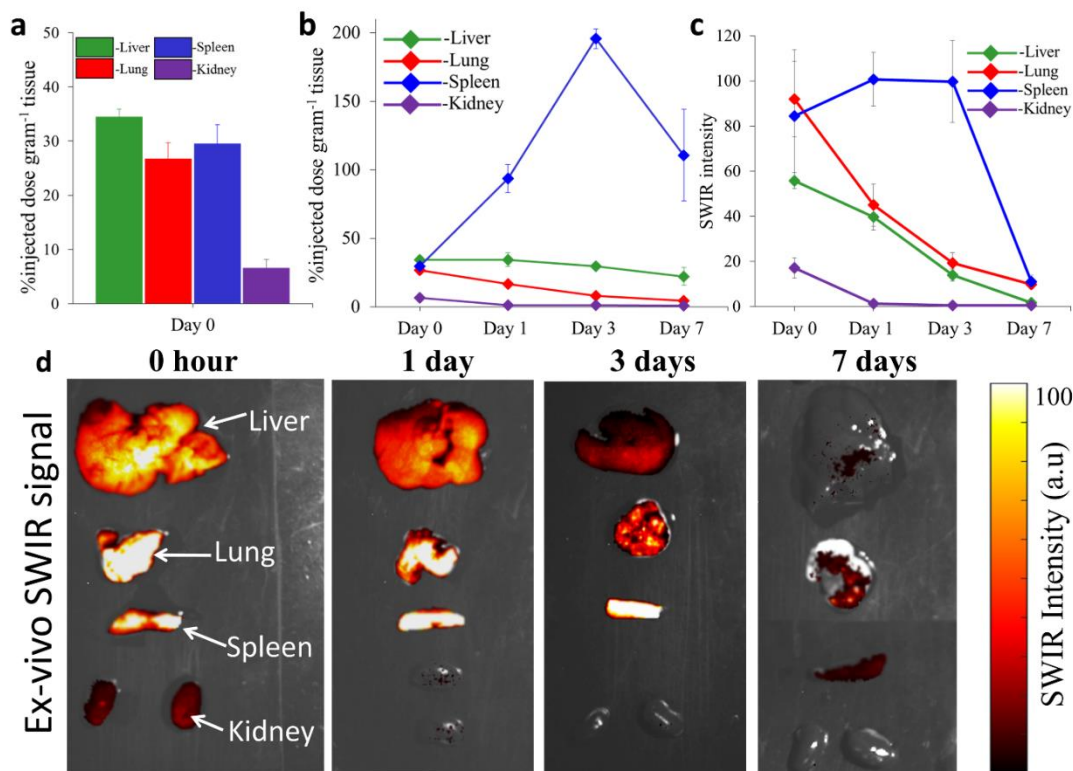
Supplementary Figure 3.10- Histopathological analysis of organs of clearance over time:

Ex vivo histopathological analysis of organs excised at various time points shows no change in tissue architecture, indicating the safety of nanoprobe over time. Animals (n=5 per time-point) were sacrificed at 0 h, 24 h, 3 days and 7 days post-injection and organs of major clearance (Liver, Lung, Kidney and Spleen) were collected for H&E analysis. Representative Images from excised organs are presented to show no change in tissue architecture over time.

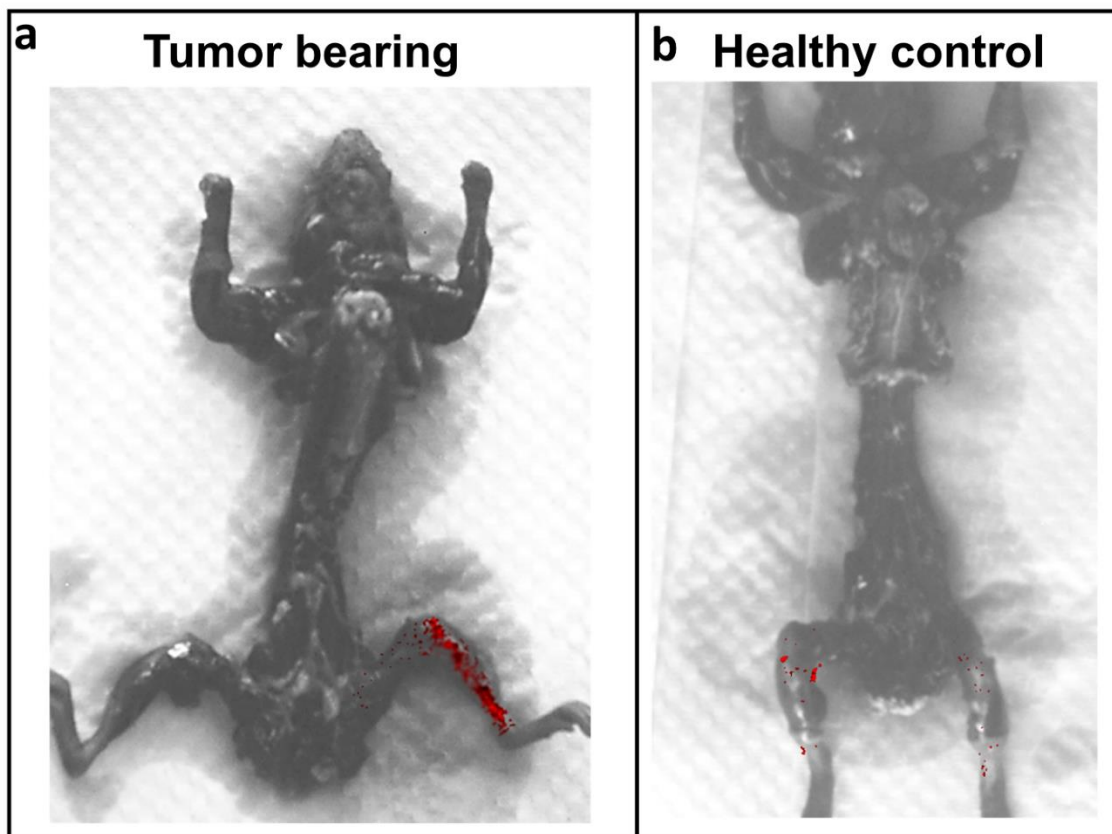


Supplementary Figure 3.11- Histopathological evaluation of organs of clearance for

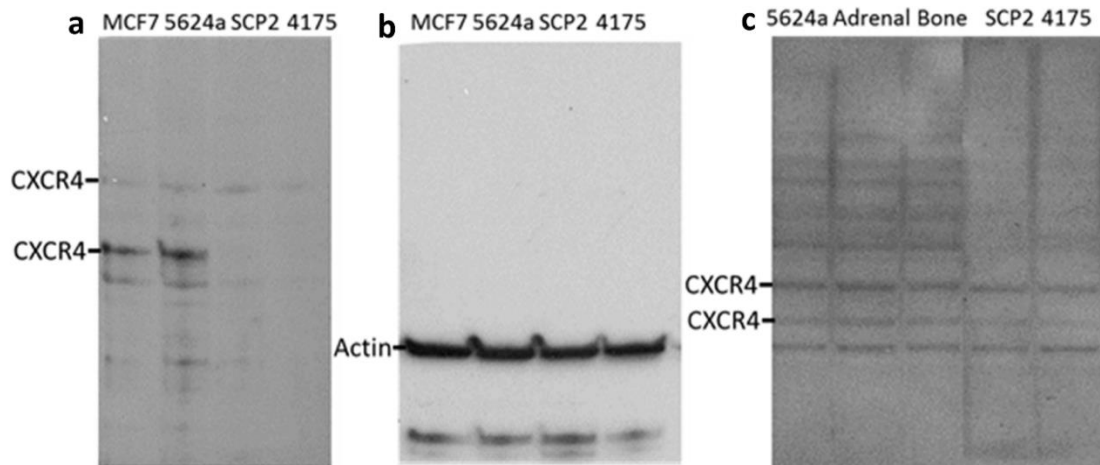
toxicity with repeated nanoparticle administration: Animals received intracardiac injections of MCF7-5624A. Tumor bearing and healthy animals received ReANC and fReANC weekly injections. Livers of tumor bearing animals receiving weekly injections of fReANC (a) and ReANC (b) were sectioned at the end point and were stained with H&E. There were no significant changes between animals treated with fReANC and ReANC and there was no loss of tissue integrity. Liver sections from healthy animals treated with ReANCs (c) also did not show any signs of damage. Additionally, lungs of tumor bearing animals injected with ReANCs (d) and fREANC (e) showed no signs of changes in lung architecture, similar to those in healthy animals injected with ReANC (f).



Supplementary Figure 3.12- Quantitative clearance studies highlight effective clearance of nanoprobe: (a) ICP/MS analysis of organs of major clearance at 0, 24h, 72h and 7 days show effective clearance of particles from all organs and a decreasing trend of probe RE content in the spleen. This correlates with the SWIR signal acquired over time from the excised organs (b). The biodistribution of the nanoprobe, calculated using ICP-MS, immediately after injection indicates major accumulation in liver, lungs and spleen as shown in (c). (d) *Ex vivo* SWIR signal validates the clearance of the probes from the major organs of clearance over time. Data are representative means of n=5 animals per time-point represented as mean \pm S.E.M.

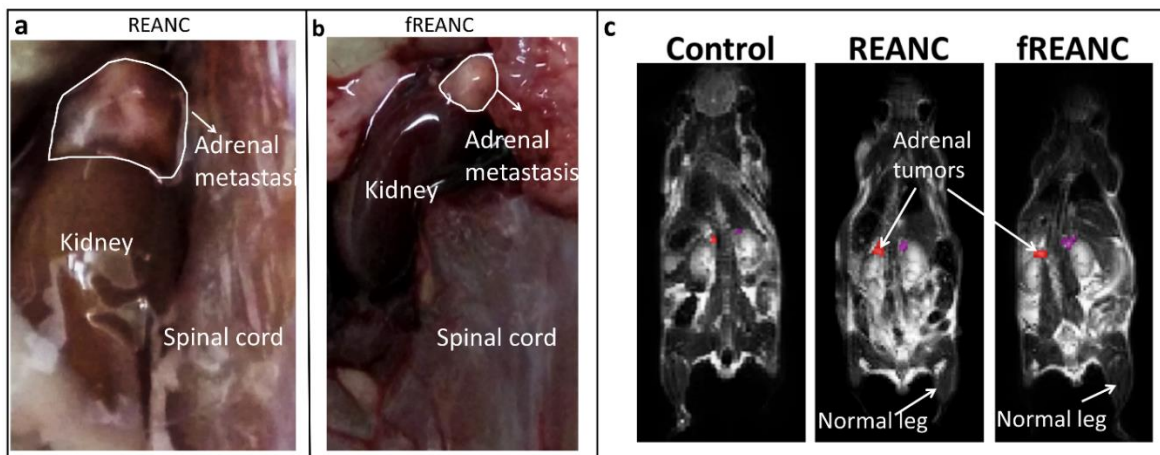


Supplementary Figure 3.13- *Ex vivo* validation of ReANCs in bones: Athymic nude mice were injected with MDA-MB-231 derived cells in the left tibiae followed by weekly intravenous injections of ReANCs. *Ex vivo* SWIR imaging of skeletons injected with ReANCs showed accumulation of ReANCs in bones of tumor bearing animals (a) compared to healthy controls (b).

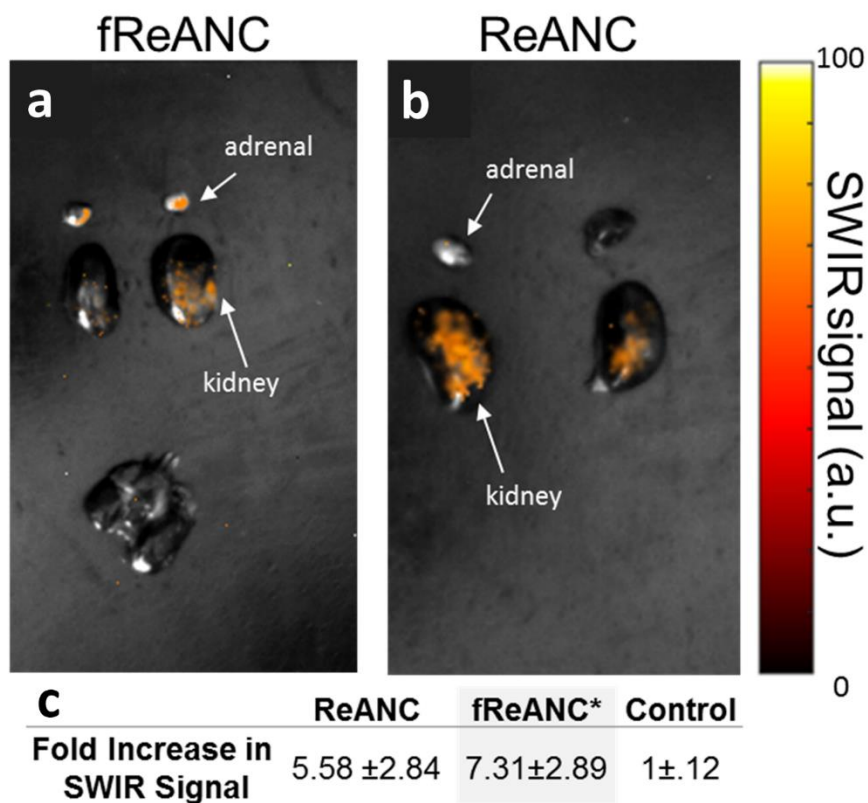


Supplementary Figure 3.14- Expression levels of CXCR4 in breast cancer cell lines:

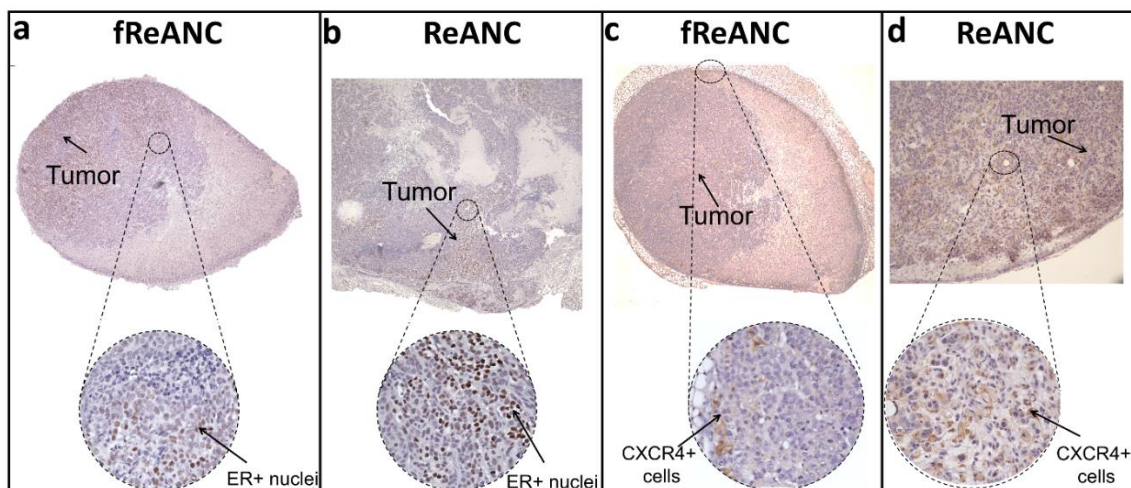
Western analysis shows a higher expression of CXCR4 receptor in MCF7 and MCF7-5624A breast cancer cells as compared to SCP2 or 4175 cell lines (a). Cells extracted from adrenal metastases and bone metastases also showed expression of CXCR4. The adrenal and bone tumor cells retain the same level of expression of CXCR4 as the parental MCF7-5624A cell line (b).



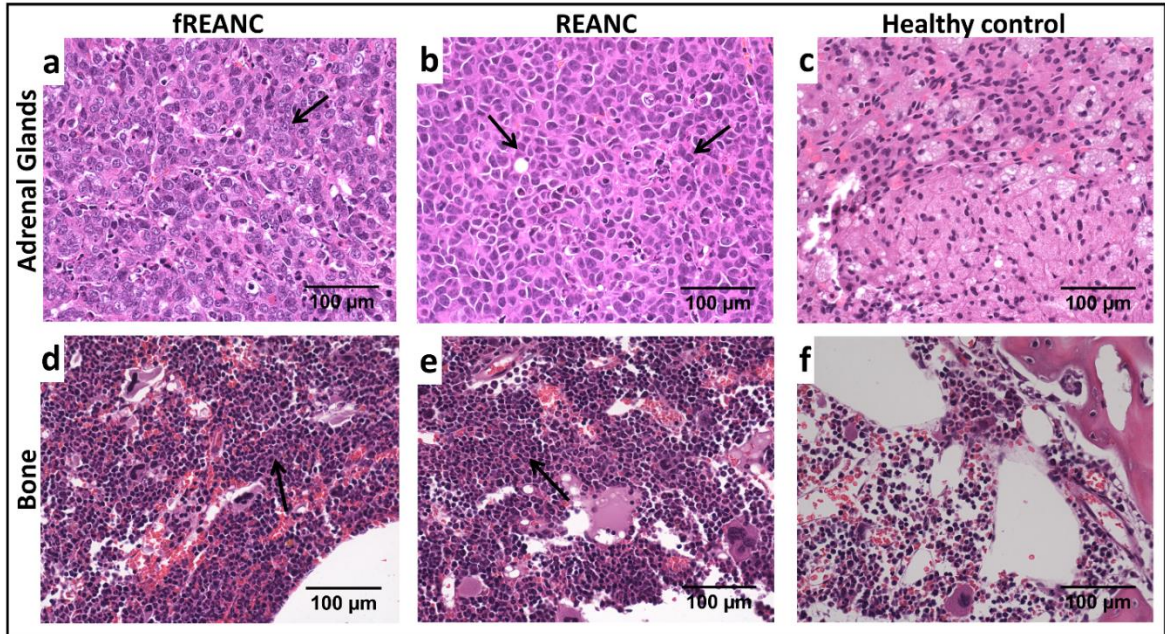
Supplementary Figure 3.15- MRI and In situ white light images indicate the presence of adrenal tumors: Animals inoculated with MCF7-5624A breast cancer cells via intracardiac injection were administered weekly doses of either REANC or fREANCs. Dissection of animals at the end point revealed the presence of enlarged adrenal glands in animals administered with (a) ReANC and (b) fReANCs compared to healthy controls (data not shown). (c) Representative MRI images of animals showing adrenal metastases and a lack of changes in bone architecture indicating the sensitivity of SWIR imaging in detecting bone metastasis.



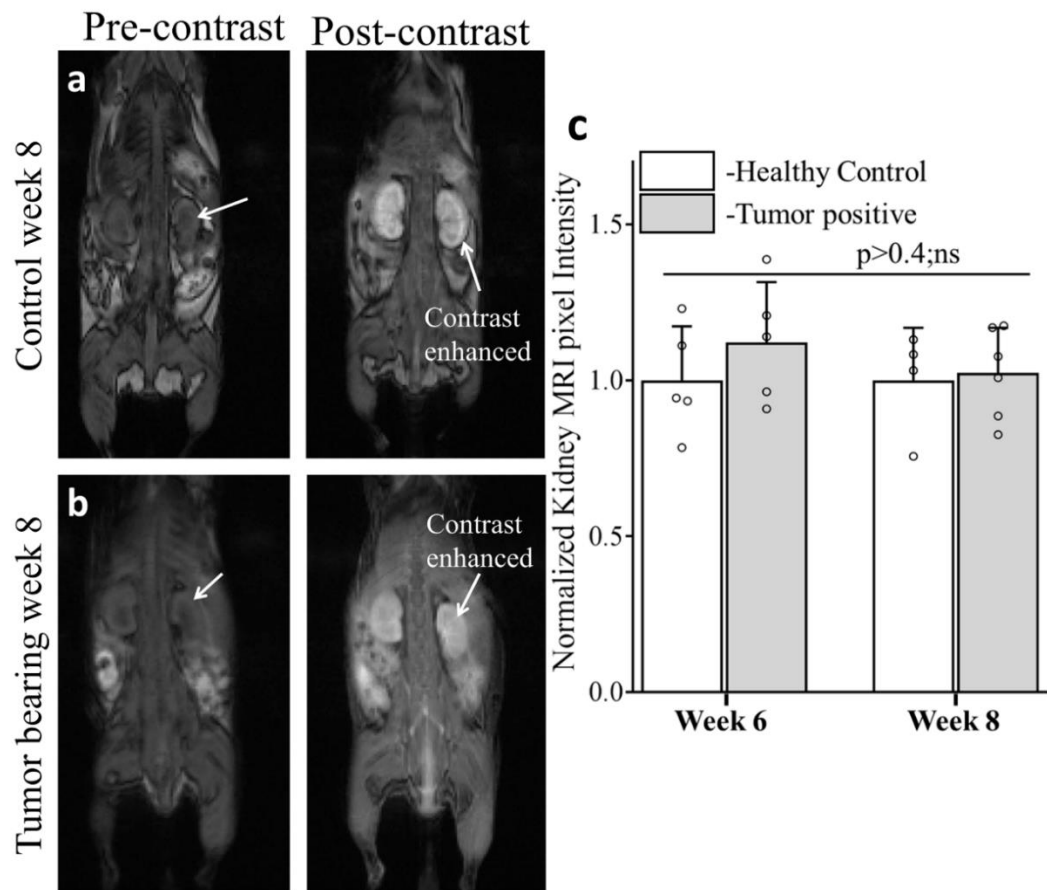
Supplementary Figure 3.16- Ex-vivo images showing presence of SWIR signal in adrenal glands of tumor bearing mice: Animals inoculated with MCF7-5624A breast cancer cells via intracardiac injection were administered weekly doses of either REANC or fREANCs. Post sacrifice at week 5 , SWIR imaging was performed on excised organs to determine the location of probe accumulation. Enhanced levels of SWIR fluorescence was observed from the adrenal glands of mice administered with functionalized fReANCs (a) whereas less SWIR signal could be resolved from the tumors of animals administered ReANCs (b). Administration of fReANCs led to a 7.3 fold increase in SWIR signal from adrenal lesions when compared to healthy controls (c) * $p < 0.05$, $n=6$, t-test, whereas the increase in SWIR signal with REANC administration was not significant as compared to healthy controls.



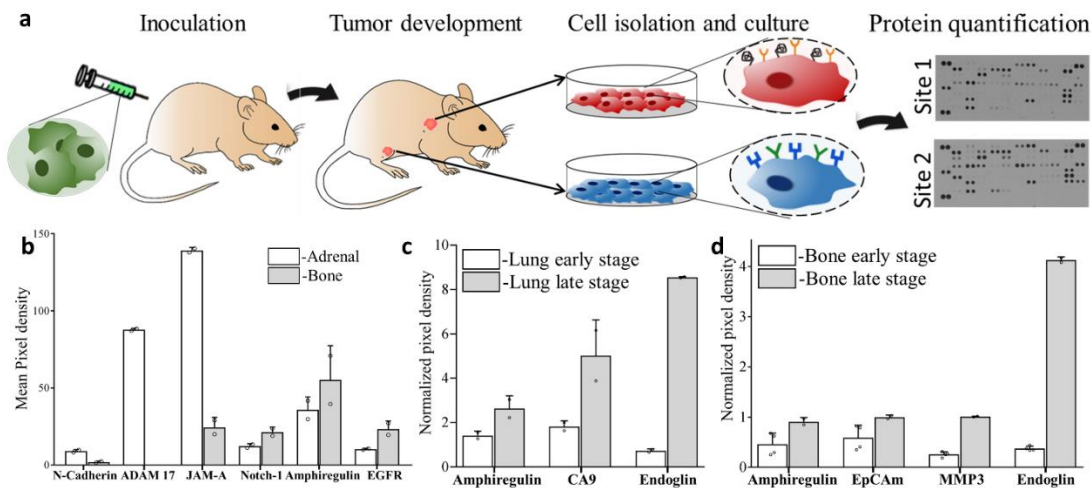
Supplementary Figure 3.17- Histopathological validation of ER-positive tumor cells in adrenal: *Ex vivo* immunohistochemical analysis of the adrenals verified the presence of tumor by positive estrogen receptor staining of tumor cells (a). Both tumor bearing groups injected with ReANCs and fReANCs (a & b) stained positive for the estrogen receptor. Adrenal metastases from animals injected with both ReANCs and fReANCs (c and d) also stained positive for CXCR4, as indicated by arrows.



Supplementary Figure 3.18- H and E staining of adrenal metastases: Adrenals from tumor-bearing animals (a and b) show the presence of irregular nuclei (shown by arrows) quite distinct when compared to healthy control (c). These structural changes are consistent with possible tumor infiltration. The H and E stains of bone structures of tumor bearing (d and e) in contrast with healthy control (f) shows possible hypo-cellularization indicative of presence of osteolytic lesions.



Supplementary Figure 3.19- Validation of contrast uptake by tumor bearing and healthy animals: Absence of change in contrast uptake by kidneys in tumor bearing (a) versus control animals (b) is shown in representative images at week 8 and (c) quantitative comparison shows no significant difference in average pixel intensity in kidneys between tumor bearing and control animals.



Supplementary Figure 3.20- Variations in molecular signatures based on metastatic

niche: (a) Cells were isolated and cultured from tumor tissues excised from multiple metastatic sites in the animal. Differential expression of proteins in various niches was determined using human soluble receptor array and human oncology array as described under materials and methods. Differences in protein expression were quantified based on antibody array pixel density. (b) Fold changes in protein expression calculated using difference in pixel density indicate the variations of protein expression between adrenal and bone tropic cell lines. We also determined protein expression changes at early (2weeks post-inoculation) and late (6weeks post-inoculation) stages of tumor progression. Fold changes in protein expression in lung tropic cell line(c) and bone tropic lines (d) with progression of tumor indicate increase in proteins involved in tumor invasiveness and metastatic ability.

Supplementary video 1: Real time SWIR imaging of athymic nude mice injected with 200ul of ReANCs intravenously imaged in supine position. Whole body imaging of the animal was performed using an InGaAs camera(Sensors Unlimited, Princeton, NJ) equipped with two 1020 long pass filters and one 1538/82 filter to resolve the emission specifically from ReANCs. The

video captured at 20 frames/second highlights the SWIR emission from ReANC probes in the tail vein (site of injection), the long bones in the hind limbs, the liver (the primary organ of clearance) and the spine.

CHAPTER 4

CANCER-SPECIFIC SHORT-WAVE INFRARED EMITTING MULTI-COLORED NANOPROBES FOR *IN-VIVO* IMAGING

Note: This chapter has been being prepared for publication elsewhere titled- “Cancer-specific short-wave infrared emitting multi-colored nanoprobes for *in vivo* imaging” - **Harini Kantamneni, Michael Donzanti, Daniel Martin, Shravani Barkund, Xinyu Zhao, Yang Sheng, Mei Chee Tan, Richard E. Riman, Mark C. Pierce, Charles M. Roth, Vidya Ganapathy, Prabhas V. Moghe**

4.1 Abstract

Background: The ability to detect disease-specific biomarkers in real-time using optical imaging plays a critical role in preclinical studies aimed at evaluating drug safety, efficacy, and treatment response. Biomarkers also provide valuable diagnostic targets for tumor detection, staging, and prognosis [1]. In this study, we engineered an imaging platform capable of targeting different tumor-specific biomarkers using a library of multi-colored nanoprobes. These probes contain rare-earth elements that emit light in the short-wave infrared (SWIR) wavelength region (900 – 1700 nm) and are rendered biocompatible by encapsulation in human serum albumin. The spectrally distinct emissions of the rare-earth cations that constitute the cores of these nanoprobes make them attractive candidates for optical molecular imaging of multiple disease biomarkers.

Results: We demonstrate the binding specificity of our multi-colored nanoprobes to distinct cellular subsets by *in vitro* competitive inhibition studies. Significantly increased accumulation of tumor-specific nanoprobes was subsequently measured relative to untargeted probes in mice bearing unilateral subcutaneous tumors. Preferential accumulation of tumor-specific nanoprobes was also observed in tumors overexpressing targeted biomarkers in mice bearing bilateral subcutaneous tumors, as evidenced by significantly higher signal intensities on SWIR imaging. These *in vivo* findings were validated by *ex vivo* SWIR imaging, fluorescence imaging, and confocal microscopy.

Conclusions: The results from this study show that tumors can be detected *in vivo* using targeted rare-earth based multi-color nanoprobes. Significantly, these nanoprobes enabled imaging of biomarkers in mice bearing bilateral subcutaneous tumors with distinct molecular phenotypes. In future work, the findings from this study will be extended towards development of a multiplexed optical imaging platform that can: (i) color-code tumors and their microenvironment based on

individual biomarkers in response to therapy, and (ii) lead to non-invasive molecular signature mapping of tumors.

4.2. Introduction

Targeted therapy relies on variability in molecular drivers to inform the oncologist on treatment decisions and predict the success of a chosen regimen [2-7]. Current methods of assessing a tumor's molecular signature involve biopsy sampling, which underestimates molecular phenotypic variability [8, 9] and is impractical for evaluation of temporal changes in tumor properties. These molecular drivers can also serve as imaging biomarkers for non-invasive study of tumor composition and dynamic behavior [1], with particular relevance in early preclinical studies of safety and therapeutic efficacy [10-19]. Imaging biomarkers allow for longitudinal mapping of tumors during treatment, providing critical information on drug resistance and therapy failure even before a survival benefit marker can be determined, potentially enabling earlier regulatory approval of new molecules [20-24]. Unfortunately, existing imaging modalities such as MRI, CT, PET/SPECT offer limited options for molecular phenotyping. Optical imaging can potentially fill this gap in preclinical evaluation of targeted therapies, but new probes capable of labeling multiple imaging biomarkers are required.

Here we demonstrate multi-color, biomarker-specific, optical nanoprobes for detection of different molecular subtypes in in vivo murine subcutaneous tumor models. The precision-targeted probes are based on ceramic rare-earth (RE) doped nanoparticles encapsulated in human serum albumin, forming Rare-earth Albumin NanoComposites (ReANCs) [25, 26]. ReANCs are excited using near-infrared (NIR) light and emit at short-wave infrared (SWIR) wavelengths (900-1700 nm), allowing for superior imaging depth, contrast, and resolution compared to visible fluorophores [25-27]. Both passive and active targeting of ReANCs have been shown to improve nanoprobe bio distribution, provide molecular information about a region of interest, and improve

signal-to-background ratio, allowing for highly sensitive imaging of microscopic lesions [28, 29]. We have previously shown the unique capability of ReANCs for surveillance of multi-organ metastases using a cocktail of niche-targeted probes in a single animal with excellent safety and clearance profiles [30].

In this study, we used three different rare-earth dopants to generate a library of nanoprobe with distinct emission spectra [31, 32], for multi-colored imaging of different tumor biomarkers. We used Holmium (Ho) emissions at 1185 nm, Erbium (Er) emissions at 1525 nm, and Thulium (Tm) emissions at 1475 nm to target cellular subsets with unique cell-surface receptor expression patterns (**Figure 4.1**). The nanoprobe were further engineered with conventional visible light emitting fluorophores (FITC, Rhodamine-B, and Alexa Fluor 647) for microscopic imaging since commercial SWIR microscopes are not yet available. We quantify uptake of each nanoprobe to its biomarker of interest using flow cytometry. We then demonstrate the in vivo targeting capability of each nanoprobe by imaging mice bearing subcutaneous tumors expressing three biomarkers of relevance in breast cancer; CAV-1, CXCR4, and folate receptor (FR). Finally, we show that these multi-colored targeted nanoprobe enable imaging of tumors with different molecular phenotypes in the same animal. We believe that the findings from this study provide a foundation toward the development of a multi-color imaging biomarker technology that can

provide physicians with a real-time tool for patient-centered treatment of cancer.

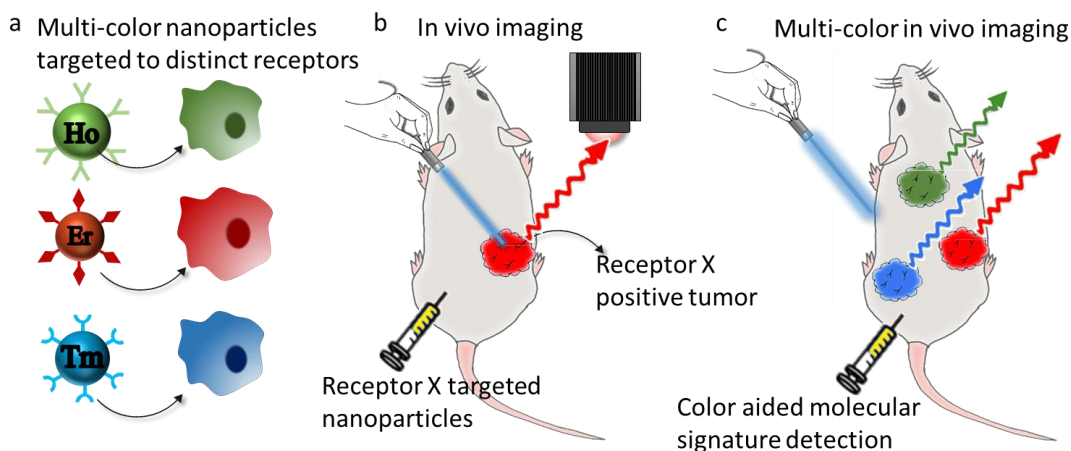


Figure 4.1: Multi-color nanoparticles for biomarker specific *in vivo* imaging: (a) Multi-color nanoparticles were engineered to target biomarker specific to various breast cancer cell lines. (b) Whole body SWIR imaging was used to assess *in vivo* localization of targeted nanoparticles was evaluated in a sub-cutaneous tumor model to establish targeting ability of multi-color probes. (c) A bilateral tumor model was used to show specificity of multi-color probes to respective biomarker positive tumors.

4.3. Results

4.3.1. Synthesis and characterization of multi-colored nanoprobe:

The optical emission properties of RE nanoprobe can be modulated by altering the dopant chemistry as demonstrated in our previous work²¹¹. RE nanoprobe were synthesized through a burst nucleation process with Ho, Er, and Tm as dopants with distinct spectral properties (supplementary figure 4.1). These multi-colored REs were rendered biocompatible by encapsulation in human serum albumin via a controlled coacervation method, forming HoANCs, ErANCs, and TmANCs^{71,124,212}. ReANCs with diameters ranging from 133-161 nm (supplementary figure 4.2) were synthesized by optimizing salt concentration and stir rate during

formation. The visible light emitting fluorophores rhodamine (Rh), fluorescein (FITC), and Alexa Fluor 647 (647) dyes were incorporated during the coacervation process to enable *in vitro* and *ex vivo* imaging on conventional microscope platforms, generating Rh-HoANCs, FITC-ErANCs, and 647-TmANCs, (supplementary figure 4.3)

4.3.2. Synthesis of biomarker-specific nanoprobes:

Our previous work has shown the ability of targeted nanoprobes to detect micro-lesions earlier than conventional imaging methods ²¹³. Biomarker-specific functionalized nanoprobes (fReANCs) were generated by physical ^{187,212} or chemical surface modification of ReANCs. The small molecule inhibitor daidzein was used to target caveolin-1 (CAV1) ^{214,215}, AMD-3100 was used to target C-X-Chemokine Receptor-4 (CXCR4) ^{216,217}, and folic acid (FA) was used to target the folate receptor ^{218,219} (Table 4.1). Briefly, Rh-HoANCs and FITC-ErANCs were functionalized with daidzein and AMD-3100 respectively through physical absorption onto the albumin surface to create Rh-fHoANCs and FITC-fErANCs. 647-fTmANCs were generated by chemical conjugation of FA using a 1-ethyl-3-(3-dimethylaminopropyl) carbodiimide (EDC) crosslinker.

zReceptor	CXCR4	CAV1	FR
MCF7 expression	+++	+	++
4175-TR expression	+	+++	n/a
SKOV3	n/a	+++	+++
Ligand	AMD-3100	Daidzein	Folic acid
Targeting nanoprobes	FITC-ErANC	Rh-HoANC	647-TmANC

4.3.3. *In vitro* target validation of functionalized multi-color probes:

As shown in figures 2 a, b, we found essentially exclusive expression of CAV1 on 4175-TR cells compared to MCF7 and much higher expression of CXCR4 on MCF7 cells as compared to 4175-TR cells. SKOV3 cells showed expression of folate receptor (figure 2c). The ability of nanoprobe to specifically target differentially regulated receptors present on 4175-TR and MCF7 cells was evaluated by flow cytometry. As expected, there was a statistically significant increase in uptake of nanoprobe (FITC-fErANCs) targeted to CXCR4 by MCF7 (CXCR4+ cell line) compared to 4175-TR (CXCR4- cell line) (figure 2d). Similarly, we observed a significant increase in uptake of CAV1 targeted nanoprobe (Rh-fHoANCs) on 4175-TR (Cav1+ cell line) compared to MCF7 cells (Cav1- cell line) (figure 2e). The optimal target ligand concentrations (3.93×10^{-4} M daidzein and 1.25×10^{-6} M AMD-3100) were estimated by determining cellular uptake of targeted vs untargeted nanoprobe over a range of ligand concentrations (supplementary figure 4). Additionally, relative localization of untargeted and targeted nanoprobe to MCF7 and 4175-TR cells was examined using confocal microscopy, showing increased uptake of nanoprobe by their targeted cell lines (supplementary figure 5). Folate receptor targeting is currently being explored in clinical trials for a variety of applications including surgical guidance [41-44] and targeted therapy [45, 46] particularly in ovarian cancer [47-49]. FA was conjugated via chemical crosslinking to 647-TmANCs as described above. We showed significantly increased uptake of targeted probes when

compared to untargeted probes in SKOV3 cells as determined by flow cytometry (figure 2f).

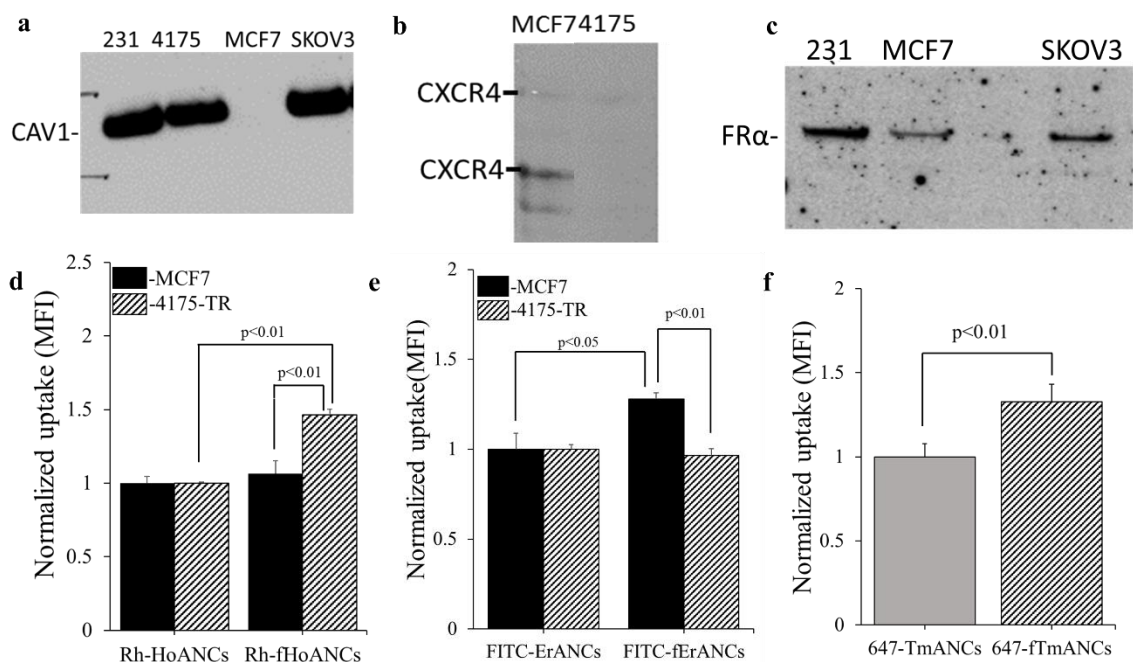


Figure 4.2- *In vitro* analysis of functionalized multi-color probes: Western blots show the relative expression of receptors of interest (a-c): (a) 4175-TR cell line shows increased CAV1 receptor expression in comparison to MCF7 cell line whereas MCF7 shows higher CXCR41 expression (b). Analysis of folate receptor show higher expression on SKOV3 ovarian cancer cells (c). Flow cytometry analysis of rhodamine fluorescence, normalized to cells treated with untargeted probes shows significantly increased uptake of Rh-fHoANCs in CAV1 positive 4175-TR cells (d). Similarly, FITC-fErANCs targeted to CXCR4 receptor exhibit increased rhodamine intensity with MCF7 cells indicating specificity of targeted probes to their respective cell line (e). 647-fTmANCs exhibit increase uptake with folate receptor positive SKOV3 cells compared to untargeted nanoprobe (f).

4.3.4. *In vivo* target validation of multi-color nanoprobe:

4.3.4.1. Targeting of CAV1 receptor positive 4175 subcutaneous tumors:

The targeting ability of Rh-fHoANCs was validated in a subcutaneous mouse tumor model. 4175-TR (overexpressing CAV1 receptor) tumors were targeted with daidzein-conjugated nanoprobe. Analysis of holmium SWIR signal intensities showed a statistically significant increase with targeted nanoprobe 24 hours' post injection. Targeted nanoprobe show a two-fold increase in SWIR signal at the tumor site as compared to marginal non-specific binding from untargeted probe (**figure 4.3a-d**). *Ex vivo*, SWIR imaging (**figure 4.4a**) and fluorescence imaging of rhodamine (**supplementary figure 4.6a**) with MsFxPro validated *in vivo* findings. Additionally, tumor sections imaged with confocal microscopy showed accumulation of Rh-fHoANCs at tumor site as shown by increased rhodamine intensity (**figure 4.4d**).

4.3.4.2. Targeting of CXCR4 receptor positive MCF7 subcutaneous tumors:

We determined the preferential accumulation of FITC-fErANCs in a subcutaneous mouse tumor model compared to untargeted nanoprobe. Briefly, subcutaneous MCF7 (overexpressing CXCR4 receptor) tumor bearing, female, athymic nude mice were injected intraperitoneally with targeted and untargeted nanoprobe followed by SWIR imaging. Quantitative analysis based on erbium SWIR signal intensity shows significantly higher nanoprobe accumulation 24 hr post injection at the tumor site of animals injected with targeted nanoprobe. Accumulation of untargeted nanoprobe was 5-fold less than targeted probe in tumor bearing animals (**figure 4.3e-f**). *In vivo* data were validated *ex vivo* by SWIR imaging (**figure 4.4b**) and FITC fluorescence intensity (**supplementary figure 4.6b**) imaged with MsFxPro. Additionally, confocal microscopy for FITC confirmed localization of nanoprobe in tumor sections (**figure 4.4e**).

4.3.4.3. Targeting of Folate receptor positive SKOV3 subcutaneous tumors:

Folate receptor positive SKOV3 ovarian cancer cells ²²⁰ were injected subcutaneously followed by intraperitoneal injections of targeted (647-fTmANC) and untargeted (647-TmANC) nanoprobes. Comparison of mean thulium SWIR signal intensity showed a significant increase in animals injected with targeted nanoprobes (**figure 4.3i-l**). *Ex vivo* imaging of Alexa-647, using a confocal microscope (**figure 4.4f**) and MsFxPro (**supplementary figure 4.6c**) confirmed the presence of nanoprobes along with SWIR imaging (**figure 4.4c**).

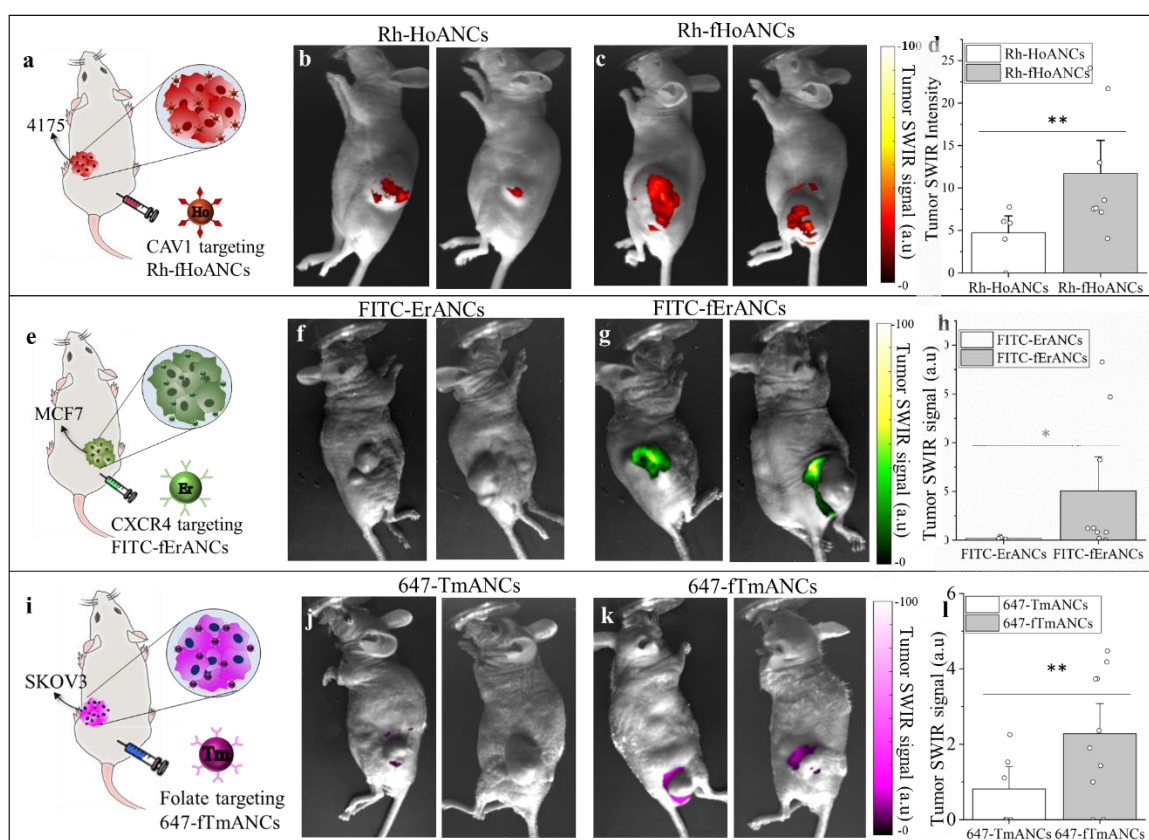


Figure 4.3: *In vivo* targeting validation of multi-color nanoprobes in subcutaneous tumors:

(a) Schematic illustrating 4175 subcutaneous tumor-bearing mice injected with targeted (Rh-fHoANCs) and untargeted (Rh-HoANCs) nanoparticles. (b) Quantitative comparison of SWIR signal intensity shows statistically significant higher emission from animals injected with Rh-fHoANCs. Representative images of Rh-HoANCs (c) and Rh-fHoANCs (d) accumulation in

4175 tumors 6 weeks post inoculation showing higher holmium SWIR signal in animals injected with targeted nanoparticles. (e) Schematic of MCF7 subcutaneous tumor-bearing mice injected with CXCR4 targeting (FITC-fErANCs) and non-targeting (FITC-ErANCs) nanoparticles. (f) Quantitative analysis of MCF7 tumors show statistically significant increase in mean SWIR intensity with targeted nanoparticles. Representative images show higher accumulation of FITC-fErANCs(h) as compared to untargeted FITC-ErANCs(g) nanoparticles. (i) SKOV3 subcutaneous tumor bearing animals injected with targeted (647-TmANCs) and untargeted (647-TmANCs) probes. (j) SWIR intensity analysis shows increased tumor uptake of targeted probes with representative animals for untargeted (k) and targeted nanoprobe (l) corresponding with quantitative analysis. (d),(h) and (j) is expressed as mean \pm s.e.m; Data in (d) has n=8 for Rh-fHoANCs and n=5 for Rh-HoANCs injected animals. Data in (h) has n=9 for FITC-fErANCs and n=5 for FITC-ErANCs injected animals, . Data in (j) has n=10 for 647-fTmANCs and n=6 for 647-TmANC injected animals.*two-tailed $P<0.05$, determined by Mann Whitney U-test; ** two-tailed $p<0.05$ determined by Welch's t-test.

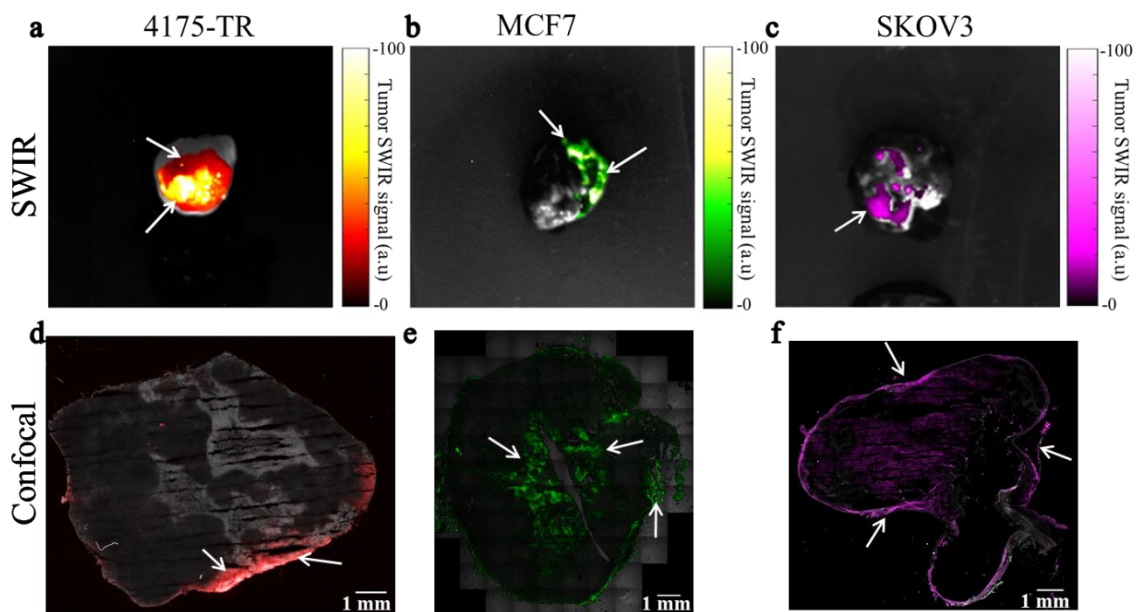


Figure 4.4: *Ex vivo* analysis of multi-color probes localization: *Ex vivo* imaging of nanoprobe in the SWIR and visible region was used to validate localization of multi-color nanoprobe corresponding targeted tumors. Tumors of animals injected with functionalized nanoprobe were excised 24 hr post injection and analyzed *ex vivo*. SWIR and confocal imaging of Rh-fHoANCs in 4175-TR tumors (a, d), FITC-fErANCs in MCF7 (b, e) and 647-fTmANCs in SKOV3 tumor (c, f) confirmed the presence of multi-color nanoprobe validating the *in vivo* results. Arrows indicate emission from nanoprobe from parts of tumors *ex vivo*.

4.3.5. Biomarker level based preferential accumulation of multi-color nanoprobe:

We demonstrated simultaneous detection of two different biomarkers in the same animal using multi-color imaging. First, we show biomarker specificity of targeted nanoprobe in a bilateral subcutaneous tumor model by injection of a single-color targeted nanoprobe. We injected MCF7 (CXCR4 positive) cells in the right dorsal flank and 4175-TR (CAV1 positive) cells in the left dorsal flank of female athymic nude mice, followed by nanoprobe injection and whole body SWIR imaging at 24 hours post injection. We found that animals injected with CXCR4-targeted FITC-fErANCs nanoprobe showed almost 20-fold increase in erbium signal from the MCF7 tumor site compared to 4175 tumors (**figure 4.5d-f**). Furthermore, bilateral tumor bearing animals injected with CAV1 targeted Rh-fHoANCs showed approximately 3-fold higher uptake in 4175-TR tumors compared to MCF7 tumors, indicating biomarker specific localization of nanoprobe (**figure 4.5a-c**).

Finally, in a preliminary study, bilateral tumor bearing animals were injected with multi-color nanoprobe targeted to 4175 and MCF7 tumors at 0 hr and 24 hr time points, respectively. We observed differential localization of nanoprobe based on their distinct SWIR emissions, with increased accumulation of CXCR4 targeted nanoprobe to the MCF7 tumor, versus CAV1 targeted

probes to the 4175-TR tumor in a single representative animal (**supplementary figure 4.7**).

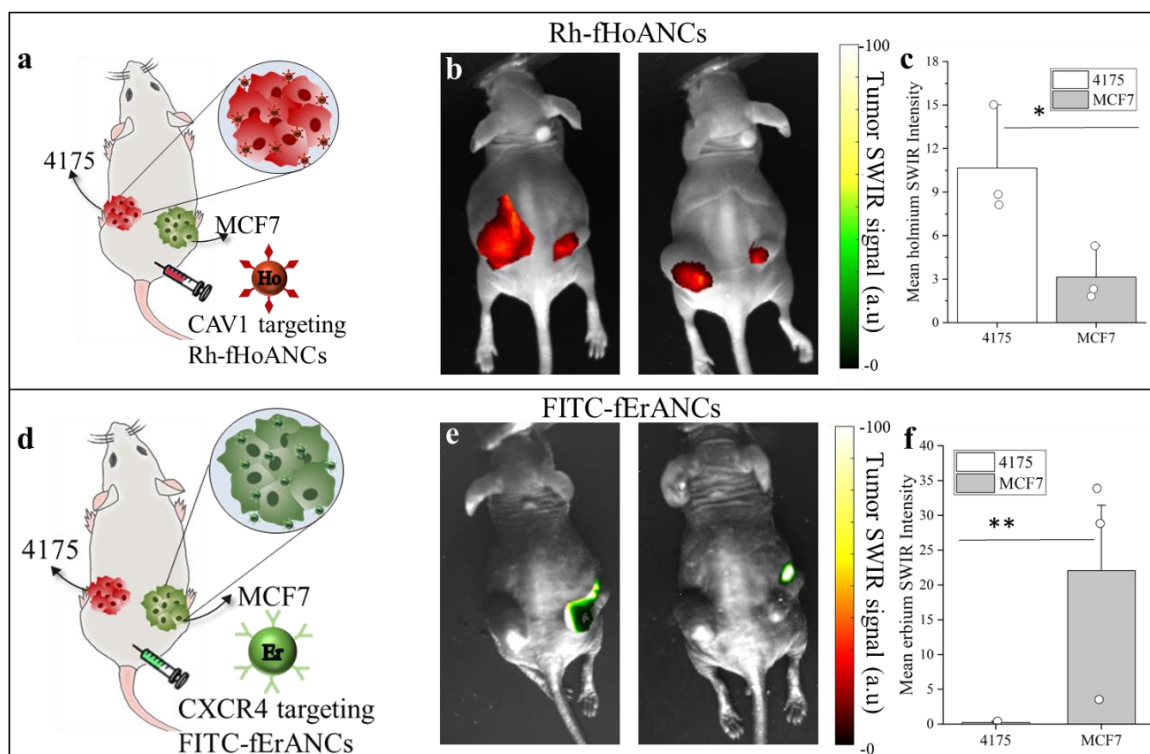


Figure 4.4: In vivo specificity of FITC-fErANCs and Rh-fHoANCs in a bilateral tumor model:

(a) Schematic illustrating bilateral subcutaneous tumor bearing mice injected with CAV1 targeted Rh-fHoANCs nanoparticles. Representative images of animals injected with Rh-HoANCs (b) show higher accumulation in 4175 (left dorsal flank) as compared to MCF7 (right dorsal flank) tumors. (c) Quantitative analysis shows significant increase in holmium SWIR emission from 4175 tumors indicating selective localization of targeted Ho-fReANCs. (d) Schematic of bilateral subcutaneous tumor bearing animals were injected with MCF7 targeted FITC-fErANCs nanoparticles. (e) Representative images of animals validates the targeting ability of FITC-fErANCs with higher signal from MCF7 (right dorsal flank) compared to 4175 (left dorsal flank) tumors. (f) Quantitative comparison of SWIR signal intensity shows higher erbium SWIR emission from MCF7 tumors compared to 4175 tumors. Data in (c) and (f) is expressed as mean \pm s.e.m and has

n=3 for tumor bearing animals. *two-tailed $p < 0.06$ determined by Welch's t- test; ** $p = 0.1$ determined by Mann-Whitney U-test.

4.4. Discussion

Chemo resistance in cancer²²¹, failure of targeted therapy²²² and inability to predict immunotherapy responses²²³ in cancer have been major clinical challenges that contribute to rising healthcare-costs and affect patient quality of life. In order to overcome this challenge, a precision technology platform that can interrogate multiple biomarkers leading to a molecular-signature based pathway analysis is required. This will lead to a richer understanding of tumor heterogeneity dictated by tumor-microenvironment interactions and immune-tumor interactions. The goal for this study was to advance the SWIR based surveillance nanotechnology towards a proof of concept multi-color imaging platform by developing a library of biomarker-specific nanoprobes that can discern respective cellular subsets.

We engineered biomarker-specific nanoprobes with distinct emission spectra, which perform macroscopic imaging *in vivo* through capturing emitted SWIR signals when excited with NIR light (**figure 4.4 and 4.5**). An added design feature in these probes was incorporation of conventional fluorophores that emit in the visible and far-red regions, allowing for microscopic imaging *ex vivo* (**figure 4.4d-f and supplementary figure 4.4**). We show optimal ligand loading kinetics for three selected targeting ligands in biomarker-high cellular subsets (determined by expression levels of targeted protein by immunoblotting) by FACS-based target validation. The biomarker-specific rare-earth based nanoprobes used in this study have been shown to detect deeper lesions with superior resolution^{187,213,224}.

Hence, we explored the ability of three different biomarker-specific nanoprobes to discern distinct tumor populations in an *in vivo* subcutaneous tumor model. We show that the engineered nanoprobes not only target biomarker-specific tumors of MCF7 (overexpressing CXCR4) and

4175 (overexpressing CAV-1) but also lead to higher accumulation of probes in tumors compared to their untargeted counterparts. Most importantly, we were able to show, in a bilateral tumor model, a high degree of selectivity in targeting of AMD-3100 functionalized probes to MCF7 tumors and daidzein-targeted nanoprobe to 4175 tumors. In a preliminary bilateral tumor model, sequentially injected with biomarker-specific nanoprobe, we observed preferential accumulation of target specific probes to their respective tumors (CXCR4 targeted probes to MCF7, a CXCR4⁺ cell line and Cav1 targeted probes to 4175, a Cav1⁺ cell line). The use of albumin as a nano-encapsulating agent facilitates the development of a biomarker-imaging platform, as a variety of targeting ligands can be incorporated either by physical adsorption or by chemical conjugation.

The novel design that combines the SWIR emissions for macroscopic imaging with the traditional fluorophore emissions for microscopic imaging allows for *ex vivo* validation and opens the possibility for future molecular pathway analysis of different cellular subsets at a microscopic level. Additionally, we have shown *ex-vivo* microscopic validation of nanoprobe accumulation by confocal microscopy of tumor sections, which provides a foundation for conventional histopathological evaluations in clinical practice when the technology is translated for human use.

Several studies have explored multi-color real time imaging for tumor heterogeneity mapping and organelle barcoding^{225,226}. These studies highlight the promise for the use of imaging biomarkers such as those used in this study for diagnosis, to be incorporated in drug development process to unravel changes in molecular pathways in response to drugs²²⁷. The power of imaging biomarkers integrated with a contrast agent that has deeper penetration potential than the fluorophores shown thus far in established studies²²⁸⁻²³² will be beneficial for numerous applications in cancer research.

Tumor heterogeneity can be attributed to: a) spatial heterogeneity; b) temporal heterogeneity as a result of either natural progression of disease or treatment; c) population-based heterogeneity

and/or d) heterogeneity based on micro-environmental changes²³³⁻²³⁶. The ability of our multi-colored engineered probes to interrogate different tumor subsets *in vivo* will provide for a non-invasive optical signature mapping system for tumors. Future studies will focus on further development of these biomarker-specific nanoprobe towards an imaging biomarker library that will allow for signature-specific molecular mapping of tumors. The vision for the future generations of this imaging platform will be to address the clinical challenges of tumor heterogeneity in bridging the gap between detection, diagnosis, treatment and therapeutic decisions.

4.5. Methods

4.5.1. Cell lines

MCF7 (ATCC) and 4175-TR cells (a kind gift from Dr. Yibin Kang)^{150,151} were cultured in DMEM media supplemented with 10% FBS and 1% penicillin-streptomycin. SKOV3 cells (a kind gift from by Dr. Steve Libutti) were cultured in McCoy's media with similar FBS (Atlanta biologicals) and P/S (Gibco Inc.) supplements.

4.5.2. Rare-earth nanoprobe synthesis and modification:

RE core nanoprobe were synthesized via a burst nucleation process⁷¹. Three differently doped ReANCs generated distinct spectral emissions for labeling different cancer cell sub-populations.

FITC-Erbium-ReANCs: Erbium doped rare earth (Er-RE) core nanoprobe were encapsulated in albumin using a controlled coacervation method as described in previous publications^{71,187,213}. Nanoprobe were further loaded with FITC during the coacervation process. Briefly, Er-REs in ethanol (0.2 mg mL⁻¹) were sonicated with 2.53% (v/v) of FITC stock solution (1 mg mL⁻¹). 2 mL of the FITC-infused Er-RE solution was added at a rate of 1.5 mL min⁻¹ to 500 μ l of 20% (w/v) human serum albumin solution in 10 mM NaCl, with pH adjusted to 8.5, under constant stirring at

700 rpm. 2.34 μL of glutaraldehyde was added to the resulting mixture and the solution was allowed to crosslink overnight under constant stirring. The FITC-ErANCs were then purified by centrifugation at 20,000 rpm for three cycles of 10 min each.

Rhodamine-Holmium-ReANCs: Holmium doped rare-earth (Ho-RE) core nanoprobe were encapsulated similar to the method described above. However, the Ho-REs in ethanol (0.5 mg mL⁻¹) were sonicated with 2.53% (v/v) of Rhodamine stock solution (1 mg mL⁻¹). Post-encapsulation, the resulting Rh-HoANCs were purified via centrifugation as described above.

Alexa Fluor-647-Thulium-ReANCs: Thulium doped rare-earth (Tm-RE) core probes were encapsulated as above with the Tm-REs in ethanol at a concentration of 1 mg mL⁻¹ sonicated with 0.31% (v/v) of Alexa Fluor 647 stock solution (1 mg mL⁻¹). The final 647-TmANCs were purified by centrifugation as described above.

Dynamic Light Scattering (DLS) (Malvern Instruments) was used to measure the hydrodynamic diameter and Poly-Dispersity Index (PDI) of all formulations of ReANCs (**supplementary figure 4.1**).

4.5.3. Synthesis of functionalized nanoprobe (fReANCs):

AMD-3100 modification of FITC-ErANCs: FITC-ErANCs were modified with AMD-3100 via physical adsorption onto albumin drug binding pockets¹⁸⁷. AMD3100 was conjugated at varying concentrations ranging from 12.5 nM to 125 μM to estimate optimal concentration by cellular uptake assays, as described below. A concentration of 1.25 μM was found to be optimal and was used to fabricate functionalized nanoprobe (FITC-fErANCs) for subsequent *in vivo* applications.

Daidzein modification of Rh-HoANCs: Rh-HoANCs were conjugated to daidzein via adsorption at daidzein concentrations ranging from 3.93 μM to 393 μM . Higher concentrations of daidzein resulted in the formation of aggregates. Relative cellular uptake by FACS analysis determined the

optimal concentration to be 393 μM , which was used to fabricate Rh-fHoANCs for all subsequent *in vivo* experiments.

Folic Acid modification of 647-TmANCs: 647-fTmANCs were synthesized by chemical conjugation of FA using an EDC crosslinker with a zero space linker. The conjugation was achieved by crosslinking the amine groups present on nanoprobe with carboxylic acid groups on the FA ligand. 3.5 mLs of FA stock solution (concentration of 10 mg mL⁻¹ in 0.1 N NaOH) was activated by the addition of 7 mg of EDC (at a final concentration of 2 mM) and incubation in the dark at room temperature for 15 minutes. The activated folic acid was added dropwise to 3.5 mLs of 647-TmANCs and stirred on a shaker at 1500 rpm for 30 minutes. The ratio of EDC to FA was optimized based on the loading efficiency of FA on nanoprobe in addition to cellular uptake assays. The loading efficiency of FA was determined using the TNBS assay calculated by the number of free amine groups on nanoprobe surface. Using 0.1 M sodium tetraborate buffer the percentage of FA loading was determined by comparing the number of free amine groups on unfunctionalized versus functionalized probes. The optimal loading was established to be 36%.

All functionalized nanoprobe were characterized similar to ReANCs by using DLS to analyze their size distribution and BCA to calculate the percentage yield.

4.5.4. *In vitro* uptake of functionalized ReANCs:

Relative receptor expression of CXCR4, CAV1 and Folate Receptor was examined in MCF7, 4175-TR and SKOV3 cells using western blots. Target validation was assessed by cellular uptake and measured by flow cytometry. Briefly, cells were seeded at 5×10^5 cells per well in a 96-well plate, and treated with 10% (v/v) nanoprobe (unfunctionalized or functionalized) for 24 hours at 37°C, 5% CO₂. Subsequently, the cells were trypsinized and fixed in 1% paraformaldehyde (PFA) and flow cytometry analysis performed using FACsCalibur™. For confocal imaging, cells were plated at a density of 20,000 cells per well in 8 well borosilicate LabTek plates and treated with

nanoprobes overnight at 37°C, 5% CO₂. Following treatment, cells were washed and fixed in 4% PFA and imaged using fluorescence microscopy (Nikon).

4.5.5. *In vivo* imaging

Imaging studies were conducted using female homozygous nude mice (Taconic, Hudson, NY). For subcutaneous tumor imaging studies, MCF-7 and 4175-TR human breast cancer cells, and SKOV-3 ovarian cancer cells were injected into the dorsal area at 10⁷ cells per site. Animals underwent whole body SWIR imaging once tumors became palpable. All animal studies were approved by the Institutional Review Board for the Animal Care and Facilities Committee of Rutgers University and were performed in accordance with institutional guidelines on animal handling.

4.5.6. Whole body SWIR imaging:

An in-house built SWIR imaging system, as described in previous studies^{71,187,213}, was used for *in vivo* imaging. Mice were fully anesthetized using 2-3% isoflurane (Butler-Schein, Dublin, OH) and were continuously scanned with a 1.7 W collimated 980 nm laser (output beam collimated to 9.6 mm) to excite nanoprobes. Rare earth emissions were detected with a SWIR-sensitive InGaAs camera (512 X 640 pixels)²³⁷ (Sensors Unlimited, Princeton, NJ), equipped with different filter sets capable of discerning distinct emissions. The filter sets used were: ErANCs: two long-pass 1350 nm filters (Thorlabs) and a 1497-1579 nm band-pass filter (Semrock); HoANCs: two long-pass 1064 nm and one short-pass 1250 nm filter (Edmund Optics); TmANCs: two long-pass 1350 nm filters. This system is capable of real-time live animal imaging with a frame exposure time of 33 ms⁷¹. Images were acquired as .bin video files and processed using custom Matlab scripts²¹³.

4.5.7. *In vivo* MCF7 subcutaneous model:

5 x 10⁶ MCF7 (CXCR4 receptor positive) breast cancer cells were inoculated in the right dorsal flank of 3-4 week old athymic female homozygous nude mice that were supplemented with 1.5 mg

17 β - estradiol pellets (Innovative Research of America) releasing estradiol at a rate of 16.66 $\mu\text{g day}^{-1}$. Tumors were allowed to grow until palpable with tumor volume measured by calipers. Animals subsequently received intraperitoneal injections (100 μl , 10mg kg^{-1} dose per animal) of either untargeted (FITC-ErANCs) or targeted Erbium nanoprobe (FITC-fErANCs), followed by whole body SWIR imaging to determine the localization of functionalized vs un-functionalized nanoprobe. Animals were sacrificed after imaging and tumors were collected for *ex vivo* analysis.

4.5.8. *In vivo* 4175 subcutaneous model:

1 x 10⁷ 4175 (Cav1 receptor positive) breast cancer cells were injected subcutaneously in the left dorsal flank of three-four week old female athymic homozygous nude mice. Tumor growth was monitored weekly and once tumor volume reached, around 500 mm³ animals received 100 μL at a dose of 10 mg kg^{-1} of either untargeted (Rh-HoANCs) or targeted Holmium nanoprobe (Rh-fHoANCs) via intraperitoneal injection. Whole-body SWIR imaging was performed 6-weeks post-inoculation to determine the differential localization of targeted vs untargeted nanoprobe formulations. Animals were sacrificed after imaging and tumors collected for *ex vivo* analysis.

4.5.9. *In vivo* SKOV3 subcutaneous model:

16- 17 week old female athymic nude mice were injected subcutaneously with 5 x 10⁶ SKOV3 cells (Folate Receptor positive) in the left dorsal flank. Tumor volumes were monitored weekly and once palpable, animals received 100 μl at a dose of 10 mg kg^{-1} of either untargeted (647-TmANCs) or targeted Thulium nanoprobe (647-fTmANCs) via intraperitoneal injection. Whole body SWIR imaging was then performed to evaluate the relative localization of nanoprobe. Animals were sacrificed following imaging and tumors were collected for *ex vivo* analysis.

4.5.10. *In vivo* bilateral subcutaneous model:

3-4-week-old female athymic nude mice were supplemented with 17β -estradiol pellets releasing estradiol at a rate of $16.66 \mu\text{g day}^{-1}$. 1×10^7 4175-TR cells were inoculated in the left dorsal flank and 5×10^6 MCF7 cells were inoculated in the right dorsal flank. Tumors were monitored weekly and once at the desired volume, animals were injected with nanoprobe as described above. To assess nanoprobe targeting to 4175 tumors (**figure 4.5a**), animals were either injected with Rh-HoANCs (untargeted) or Rh-fHoANCs (targeted to 4175 tumor) at a dosage of $100 \mu\text{l}; 10 \text{ mg kg}^{-1}$. To assess nanoprobe targeting to MCF7 tumors (**figure 4.5b**), animals either received intraperitoneal injections of FITC-ErANCs (untargeted) or FITC-fErANCs (targeted to MCF7 tumor), at a dosage of $100 \mu\text{l}; 10 \text{ mg kg}^{-1}$. To assess nanoprobe targeting to both MCF7 and 4175 tumors in the same animal (**supplementary figure 4.7**), sequential injections of Rh-fHoANCs followed by FITC-fErANCs 24 hours later were administered.

4.5.11. SWIR image analysis:

SWIR emission from animals was collected pre- and post-injection of nanoprobe in the form of a video file in .bin format. Custom image processing code (Matlab, Math works, Natick MA) was used to extract maximum pixel values from each frame of the video and save the resulting maximum intensity projection as a .tiff image file. Image processing required manual selection of regions-of-interest (ROIs) around tumor lesions, based on images of animals acquired under white light. These ROIs were then applied to the associated SWIR image and the mean signal intensity for the region was calculated. These values were then used to perform statistical analysis to compare the mean SWIR intensities from each ROI between experimental groups receiving untargeted and targeted nanoprobe.

4.5.12. *Ex vivo* tumor imaging:

All tumor-bearing animals were sacrificed at experimental end points 24 hours post nanoprobe injection and the tumors were excised. *Ex vivo* SWIR imaging was performed along with whole body fluorescence imaging using MsFxPro (Carestream Molecular Imaging). Tumor samples were flash frozen for further analysis.

4.5.13. *Ex vivo* confocal imaging:

Flash frozen tumor samples were cryosectioned at 50 μm onto slides and then imaged on a Zeiss LSM 780 confocal microscope, equipped with the spectral detector (Quasar) for taking lambda stacks. FITC, Rhodamine-B and Alexa Fluor-647 dissolved in ethanol were used to build reference spectra with the Quasar detector, with an untreated tumor used a control for auto-fluorescence. An 18-channel lambda-stack was acquired for each reference sample, detecting an emission range of 498-695 nm, and using 488 nm, 561 nm and 647 nm lasers for excitation. Once reference spectra were obtained, online fingerprinting was used for spectral un-mixing of all four signals (FITC, Rhodamine-B, Alexa Fluor-647 and tissue auto-fluorescence). Samples were imaged using a 10x objective, and tile-scanning was implemented to scan each tissue section.

4.5.14. Statistical analysis:

For all *in vivo* studies, mice were randomly assigned to each experimental group; investigators were not blinded to the groups during acquisition and analysis of data. Grubb's test for outliers was used to determine the inclusion or exclusion of data within groups for all data sets. Statistical tests were selected based on the normality of the distribution of the mean SWIR intensity values, sample size and the similarity in variance between groups. Statistical significance of the normal populations was determined using the Mann Whitney U test and Welch's t-test.

4.6. Future studies:

One of the main limitations of multi-color imaging of erbium, holmium and thulium nanoprobe in a single animal model is the vast difference in the optical efficiency and emission intensities in the SWIR region. The ratio of the optical efficiencies of erbium doped: holmium doped: thulium doped nanoprobe of the differently doped systems is 137.6: 2.4: 1⁷¹. The measurements of nanoprobe emission intensities in supplementary figure 4.1 was collected with different laser excitation powers to account for the variation in optical efficiency. The proposed work described below will highlight the multi-color aspect of chapter 4.

4.6.1. Bilateral tumor model with varied time point of erbium and holmium injections

A parallel pilot study was performed, in a different group of bilateral tumor bearing animals, that were injected first with FITC-fErANCs (targeted to MCF7 tumors) followed 24 hours later by Rh-fHoANCs (targeted to 4175 tumors). For this study, the optimal time point for erbium nanoprobe to accumulate in the tumor is 12 hours post injection whereas for holmium nanoprobe is 24 hours post injection. We observed that the erbium signal was clearing out of the MCF7 tumors by the time point that holmium was able to efficiently localize to the 4175 tumors. In the future, additional imaging time points could shed insight into an optimal window for imaging of erbium and holmium simultaneously in their respective tumors. Ideally, the optimal imaging window can be determined by varying both the injection and imaging time intervals for erbium and holmium nanoprobe. For instance, one such condition could be erbium injections followed by 12 hours, 24 hours imaging and holmium injections performed beginning 12 hours post-erbium injection.

4.6.2. In vivo imaging of multi-color nanoparticle in a single mass

An alternative approach to strengthen the focus of multi-color imaging in this work would be the development of a heterogeneous tumor mouse model.

Initial proof of principle studies can focus on an in vitro heterogeneous 3D spheroid model.

Specifically, multi-cellular spheroids composed of Rh-fHoANCs pre-labelled 4175 cells and FITC-fErANCs pre-labelled MCF7 cells will be generated as shown in **figure 4.5**. These spheroids will be engineered to exhibit different spatial distribution of 4175 and MCF7 cells.

Confocal imaging will validate the distribution of the nanoprobe in cells within the spheroid.

The number of cells detectable by SWIR imaging will be optimized by imaging cell clusters and provide a base number to develop the spheroids. The cell cluster SWIR imaging can also provide information of least number of cells treated with FITC-fErANCs to avoid bleed through into the holmium wavelength range (1064 nm-1250 nm). Furthermore, the spheroids could be implanted into a subcutaneous pocket in-vivo with/without matrigel for in vivo SWIR imaging. This study will highlight multi-color imaging of a single mass and support the bilateral tumor model in vivo data.

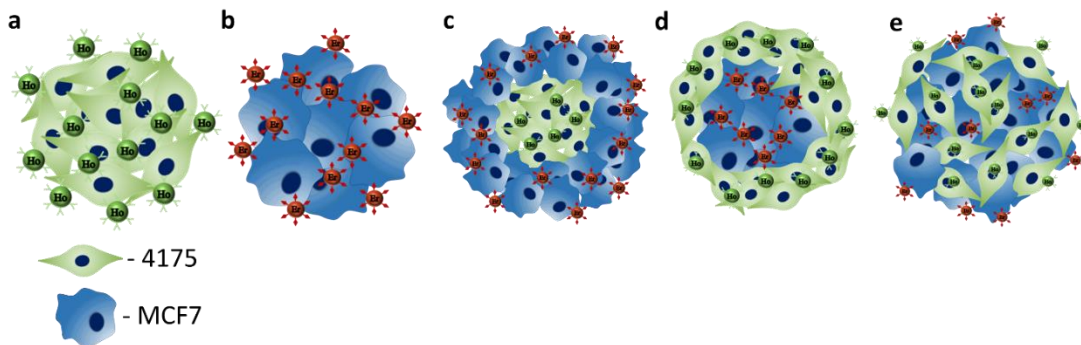


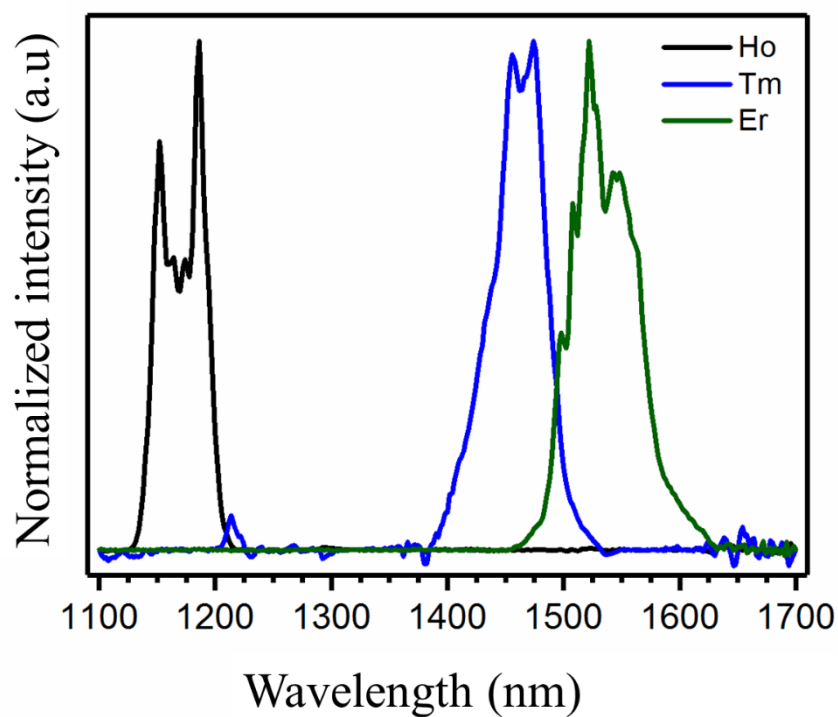
Figure 4.5: Schematic of heterogeneous 3D tumor spheroids: Spheroids created with different distribution of 4175 and MCF7 cells pre-labelled with Rh-fHoANCs and FITC-fErANCs respectively can be imaged via 3D confocal imaging in vitro and in vivo multicolor imaging post spheroid implantation. 4175 and MCF7 cells pre-labelled with Rh-fHoANCs and FITC-fErANCs respectively, would be plated to different densities to form spheroids (a and b) Spheroids with concentric populations of 4175 and MCF7 labeled with corresponding targeted NP formulations(c and d) will be developed by sequential plating of cell types. A mixture of both cell types will be used to generate a heterogeneous spheroid (e).

However, it is important to bear in mind that this would not be as biologically relevant as a truly heterogeneous tumor. Since animal models with heterogeneous tumors do not exist, future work would have to begin with the development of heterogeneous tumor mouse model. Such a model can be development by the following experimental approach:

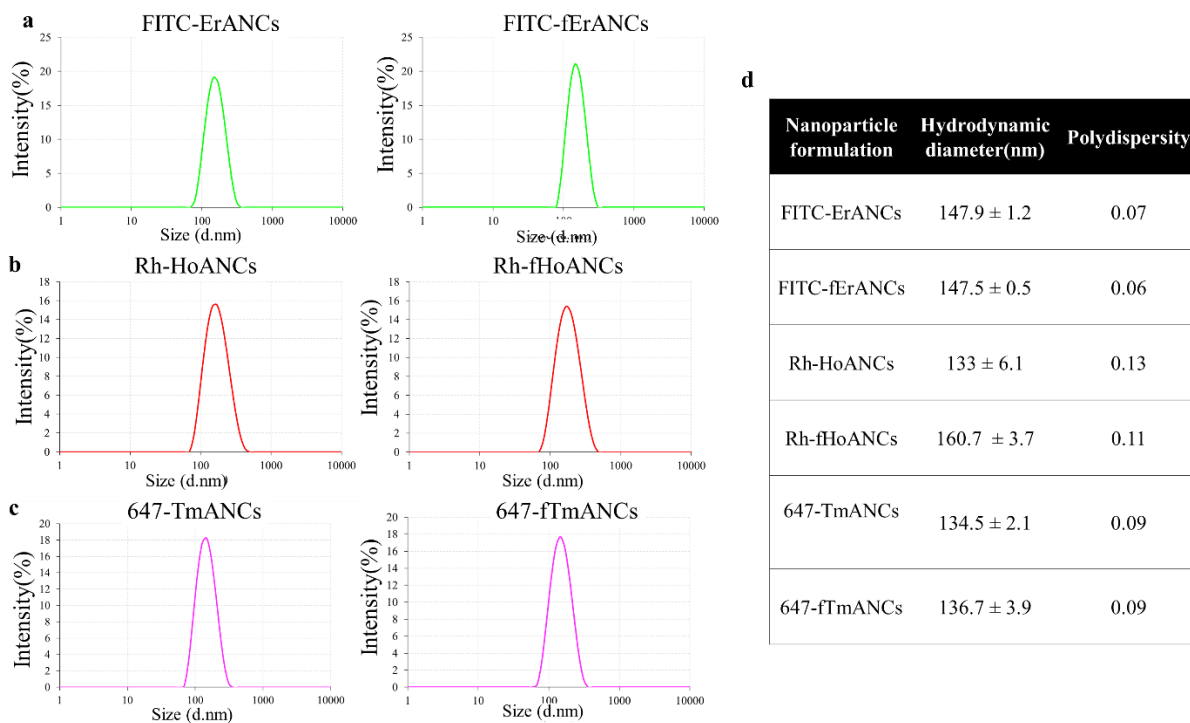
The development of a heterogeneous tumor model depends on several factors. First, the study requires understanding of the evolution of heterogeneous tumor mass based on the relative growth kinetics of 4175 vs MCF7 cells. The growth patterns of individual 4175 and MCF7 tumors with different initial cell numbers have been explored in a previous *in vivo* study. Based on these findings, the maximum number of 4175 cells for inoculation can be changed from 5×10^6 to 2×10^6 cells and the MCF7 inoculation density set at 10×10^6 cells. For example, we could

inject ratios of 1:4, 1:2 and 1:1 with 4175:MCF7 cells and optimize the ratio to get a final tumor with adequate percentage of both cell lines for SWIR imaging. The analysis of the tumor once it reaches a volume of 500-600mm³, at which point the tumors are well vascularized, can be done ex-vivo where the tumor will be extracted and crushed to perform flow cytometry using distinct biomarkers. This heterogeneous tumor model will give us a platform to test the multi-color nanoparticle targeting ability in a mixed tumor in vivo.

4.7. Supplementary Figures

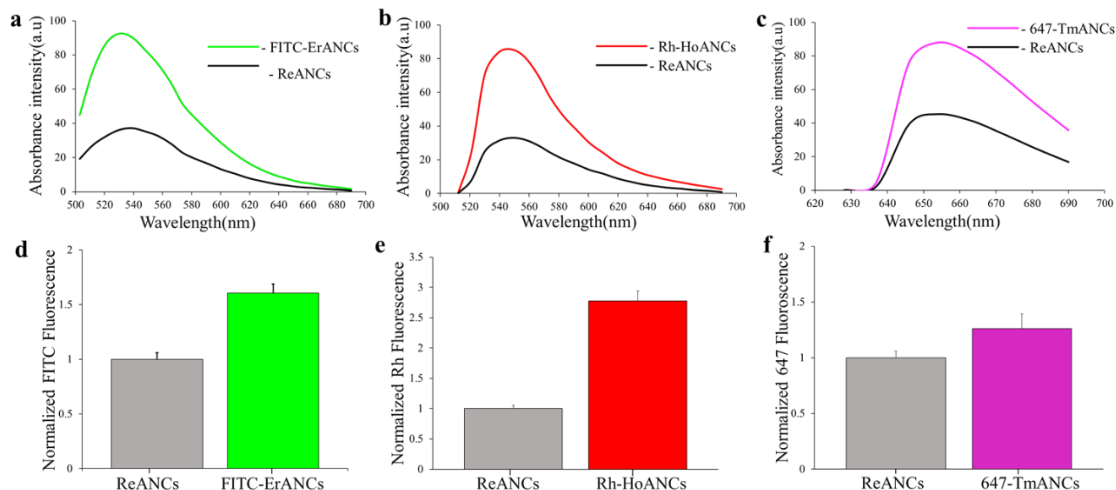


Supplementary figure 4.1: SWIR emission spectra: Holmium, erbium and thulium doped rare earth nanoparticles when excited with 980 nm excitation emit at 1185nm, 1525nm and 1475 nm respectively exhibiting distinct narrow emission patterns in the SWIR region.

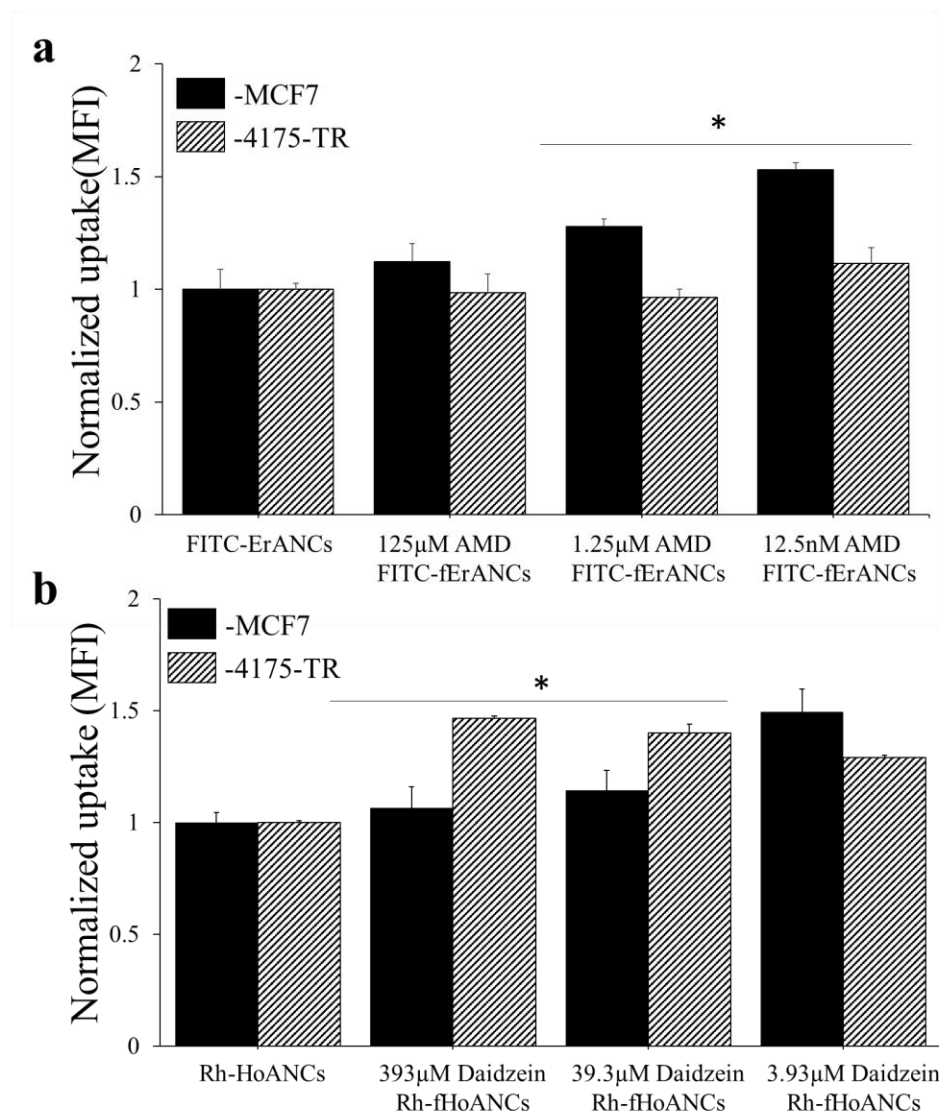


Supplementary figure 4.2: Size characterization of untargeted and targeted multi-colored

nanoparticles: Dynamic Light scattering(DLS) was used to characterize the size of different nanoparticle formulations. Hydrodynamic diameter of FITC loaded untargeted (FITC-ErANCs) and targeted (FITC-fErANCs) nanoprobe was 147.9 nm and 147.5 nm respectively(a) Rhodamine loaded untargeted (Rh-HoANCs) and targeted (Rh-fHoANCs) nanoprobe was measured to be 133nm and 160.7nm respectively (b). Additionally, Alexa-647 dye loaded untargeted(647-TmANCs) and targeted (647-fTmANCs) was 134.5 nm and 136.7 nm (c)

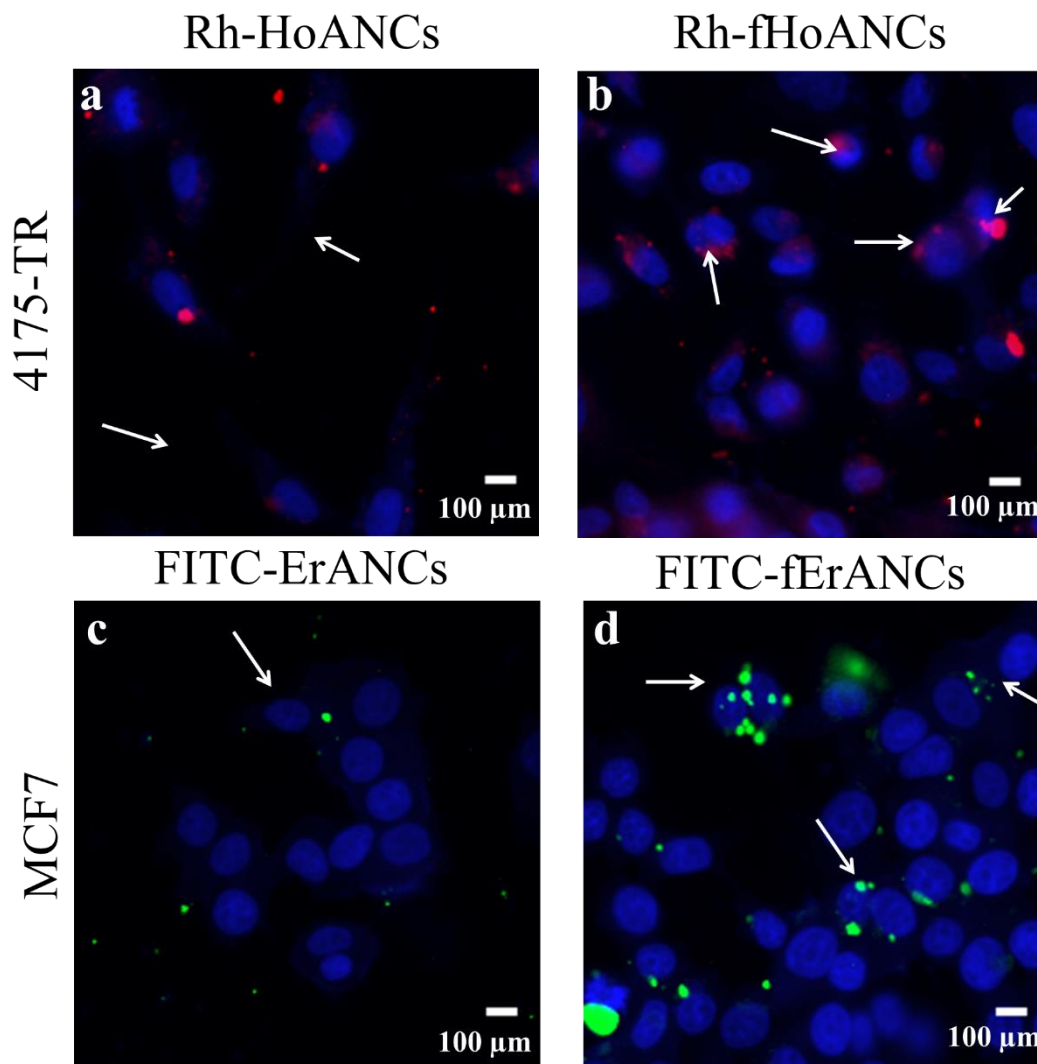


Supplementary figure 4.3: Spectra of visible fluorophore loaded ReANCs: Spectral analysis of fluorophore loaded nanoparticles showed increased absorbance intensity in respective wavelength regions validating fluorophore loading. FITC-ErANCs (a), Rh-HoANCs (b) and 647-TmANCs show higher intensity as company to unmodified ReANCs in FITC, rhodamine and alexa-647 channels respectively. Quantification of emission using a plate reader also showed an increase in intensity compared ReANCs (d-f).

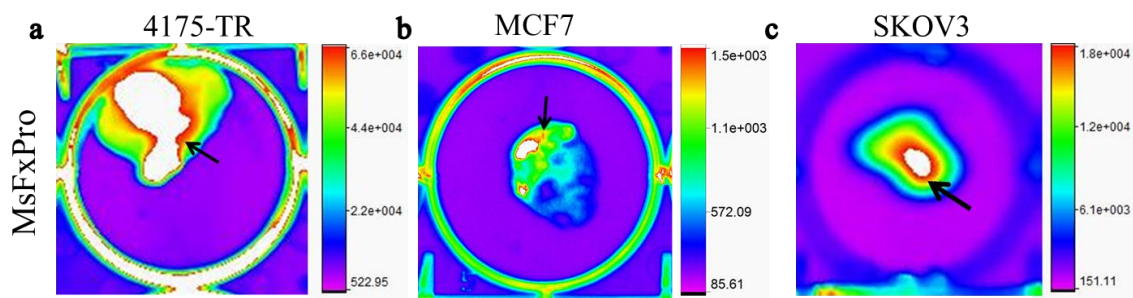


Supplementary Figure 4.4: Flow cytometry to determine optimal concentration of targeting

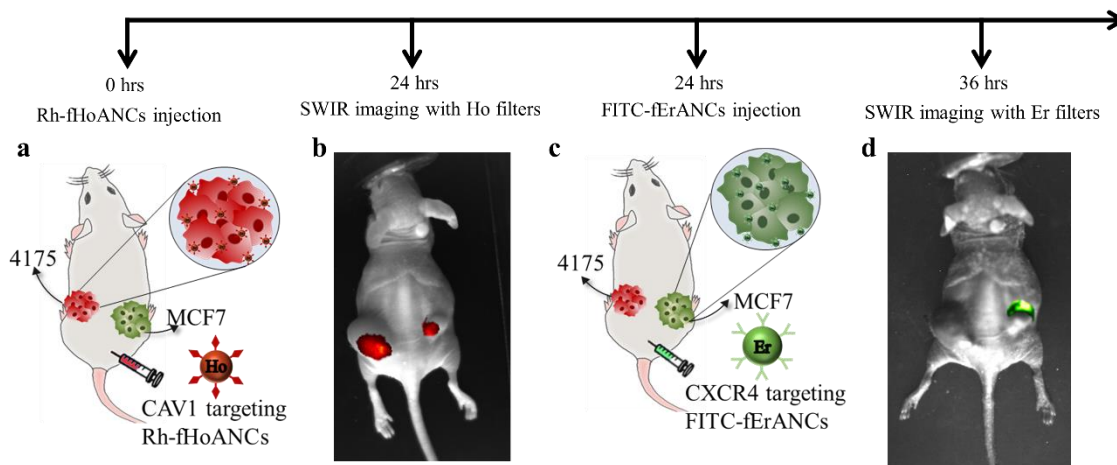
ligand: (a) MCF7 and 4175 cells were treated with ErANCs loaded with various concentrations of AMD3100. Mean fluorescence intensity normalized to cells treated with untargeted particles showed increased uptake of targeted particles in CXCR4 positive MCF7 cells compared to 4175 cells. (b) Similarly, MCF7 and 4175 cells treated with HoANCs loaded with varying concentration of daidzein. Targeted nanoparticles showed increased uptake in cav1+ 4175 cells compared to MCF7 cell line. * $p < 0.05$ as determined by a student t-test.



Supplementary figure 4.5: Validation of targeted probes to corresponding receptor positive cell lines: 4175-TR cells were plated on LabTek slides and treated with untargeted (Rh-HoANCs) and targeted (Rh-fHoANCs). Confocal imaging in the rhodamine channel showed increased uptake by 4175 (Cav1+) cells with Rh-fHoANCs (b) compared to Rh-HoANCs (a). Similarly, MCF7 cells were treated with untargeted (FITC-ErANCs) and targeted (FITC-fErANCs). Microscopic imaging in the FITC channel showed increased cellular localization by CXCR4 positive MCF7 of FITC-fErANCs (d) compared to FITC-ErANCs (c).



Supplementary figure 4.6: *Ex vivo* MsFxPro imaging of tumor samples: Tumors of animals injected with targeted probes were sacrificed 24 h post injections and the tumors were imaged for using Ms Fx Pro to show presence of Rh-fHoANCs in 4175 (a), FITC-fErANCs in MCF7 (b) and 647-fTmANCs in SKOV3 tumors(c).



Supplementary figure 4.7: Bilateral tumor bearing animal show increased localization of targeted nanoprobes to corresponding receptor positive tumor: In a pilot study, a bilateral tumor bearing animal was injected with 4175 targeting Rh-fHoANCs (a) followed by whole body SWIR imaging showing increase nanoprobe localization in 4175 compared to MCF7 tumor (b). The animal was then injected with MCF7 targeting FITC-fErANCs (c). SWIR imaging at 36 h showed increased FITC-fErANCs localization in MCF7 compared to 4175 tumors (d).

CHAPTER 5

SURFACE-MODIFIED SHORTWAVE-INFRARED-EMITTING

NANOPHOTONIC REPORTERS FOR GENE-THERAPY

APPLICATIONS

Note: This chapter has been reproduced with permission from the following publication:

Zhao Z, Kantamneni H, He S, Pelka S, Venkataraman AS, Kwon M, Libutti SK, Pierce M, Moghe PV, Ganapathy V, Tan MC. Surface-Modified Shortwave-Infrared-Emitting Nanophotonic Reporters for Gene-Therapy Applications. ACS Biomater Sci Eng. 2018;4(7):2305-63. doi: 10.1021/acsbomaterials.8b00378. PubMed PMID: 30417087; PMCID: PMC6226244.

This author's primary contribution to this work is towards evaluating the RE@PEI nanoparticles *in vitro* cellular uptake and toxicity, *in vivo* bio-distribution studies and RE@PEI mediated gene delivery.

5.1 Abstract

Gene therapy is emerging as the next generation of therapeutic modality with United States Food and Drug Administration approved gene-engineered therapy for cancer and a rare eye-related disorder, but the challenge of real-time monitoring of on-target therapy response remains. In this study, we have designed a theranostic nanoparticle composed of shortwave-infrared-emitting rare-earth-doped nanoparticles (RENPs) capable of delivering genetic cargo and of real-time response monitoring. We showed that the cationic coating of RENPs with branched polyethylenimine (PEI) does not have a significant impact on cellular toxicity, which can be further reduced by selectively modifying the surface characteristics of the PEI coating using counter-ions and expanding their potential applications in photothermal therapy. We showed the tolerability and clearance of a bolus dose of RENPs@PEI in mice up to 7 days after particle injection in addition to the RENPs@PEI ability to distinctively discern lung tumor lesions in a breast cancer mouse model with an excellent signal-to-noise ratio. We also showed the availability of amine functional groups in the collapsed PEI chain conformation on RENPs, which facilitates the loading of genetic cargo that hybridizes with target gene in an *in vitro* cancer model. The real-time monitoring and delivery of gene therapy at on-target sites will enable the success of an increased number of gene- and cell-therapy products in clinical trials.

5.2. Introduction

Nanomedicine has evolved over the years due to major advances made in material science, which has ensured that the properties of nanoparticles are more tunable for the efficient delivery of cargo, with improved accumulation in the tissues of interest²³⁸⁻²⁴². This has led to the successful translation of a large number of nanobased formulations to clinical trials²⁴³⁻²⁴⁵. Nanotheranostics, a nascent branch of nanomedicine, has led to the development of several formulations,²⁴⁶⁻²⁴⁸ with some currently being tested as magnetic

resonance imaging (MRI) contrasts²⁴⁹ or single-photon emission computed tomography and positron emission tomography (SPECT and PET) contrasts²⁴⁷ in preclinical studies. Optical imaging provides a potential nanotheranostic alternative for the molecular tracking of disease lesions and would be a safer option than the targeted radionuclides used in SPECT and PET imaging. Optical-imaging agents as nanotheranostics already show promise with near-infrared (NIR) dyes such as the quantum dots being tested widely in preclinical models.^{246,250,251} However, one of the challenges with NIR dyes as theranostics is the tissue interference and depth of penetration into tissues^{71,112,252}. In the study we designed, our imaging probes were based on ceramic rare-earth (RE)-doped nanoparticles with tunable size and surface charge. These probes emit shortwave infrared (SWIR) light upon excitation by NIR light (980 nm), which has several advantageous properties, including deeper penetration through biological tissue, for biological imaging.²⁵²⁻²⁵⁴ Additionally, the absence of excitation–emission band overlap and elimination of tissue autofluorescence produces significantly improved signal-to-noise ratios. We have previously shown that RENPs can be rendered biologically safe by encapsulation in albumin nanocomposites⁷¹ and can be targeted for the detection of micrometastatic lesions in multiple organs^{187,213}. However, the lack of cationic charge on the surface of the albumin nanocomposites renders them unsuitable for the loading of genetic cargo. In the present study, by the surface modification of RENPs using PEI, we have developed a biologically well-tolerated formulation capable of detecting micrometastatic lesions with excellent signal-to-noise ratios and of carrying genetic cargo on its surface. Studies with PEI surface-modified RENPs thus far have focused on up-converting particles (emitting at 560 nm)

with suboptimal signal-to-noise ratios that render them unsuitable for deep-tissue imaging and response monitoring²⁵⁵.

The present study exploits the optical emissions of RENPs in the SWIR (or NIR) window (900–1700 nm), which is characterized by deep penetration through tissue and a reduced loss of spatial resolution due to scattering^{71,187,213,252}. We show that the surface charge of RENPs are tunable by modification with PEI coating (RENPs@PEI). PEI, a polycation typically used as a gene-delivery nanosystem²⁵⁶⁻²⁵⁸, was used to improve solubility of RENPs. Although a number of studies have highlighted the cytotoxicity associated with PEI^{259,260}, we found that in cell-based cytotoxicity studies, RENPs@PEI led to a decrease cellular viability by approximately 10–20% in 48 hrs at concentrations (625 $\mu\text{g/mL}$) much higher than reported in previous studies^{261,262}. Previous studies have established that primary and secondary amines increase toxicity, while tertiary amines reduce cellular toxicity²⁶³. Moreover, modifications of these amine groups by acetylation with little or no change in ζ potential has shown to improve the tolerability of PEI nanoparticles²⁶³. We designed RENPs@PEI coated with Yb-acetate, leading to a significant decrease in ζ potential and a significant reduction in cytotoxicity compared to RENPs@PEI. The use of a small molecule such as Yb-acetate to study the PEI chain interactions and conformation (i.e., extended versus collapsed) on the RENP surfaces also revealed that a high density of primary amines was available for subsequent conjugation to genetic cargo. Using Yb-acetate, the optical absorption at selected wavelengths is made possible, leading to expanded functionalities of the RENPs for photothermal therapy or photoacoustic imaging^{264,265}. The cationic surface charge of PEI has been attributed to its enhanced cellular uptake, and a change in surface charge by counter-ions would likely lead to

decreased cellular uptake or differential intracellular localization. We show in this study that the addition of Yb-acetate to the surface of RENPs@PEI did not significantly change cellular uptake or change the intracellular distribution of particles.

Yescarta, cell-based gene therapy for cancer, and Luxturna, gene therapy for a rare eye disease leading to blindness in infancy, are the only gene-therapy agents approved by the United States Food and Drug Administration to date. The struggle to bring gene-based therapeutics to the clinic is multifaceted, ranging from the safety of vectors *in vitro* and in animal models, optimal gene transfer, and long-term persistence or integration in the host in terms of viral vectors to the ability to maintain transgene expression *in vivo* for a desired period of time. However, once these safety and regulatory issues are resolved, clinically, one of the challenges that face the development of gene therapeutics is the monitoring of therapeutic genes and cells in real time as a function of on-target therapy response. Nanotheranostics that can deliver genetic cargo will bridge the gap between gene delivery and monitoring. Curtis et al. have previously shown that the protonation state of linear PEI determines the effective DNA-PEI interactions²⁶⁶. We show that the changes in protonation state as a result of the aggregation state of RENPs@PEI determines the efficiency of DNA complexation. RENPs@PEI at physiological pH leads to aggregation, resulting in a collapsed-chain conformation, increasing NH₂-group availability. This increased protonation enabled the effective loading of genetic cargo, rendering the RENPs@PEI as theranostic agents. We subsequently demonstrate that RENPs@PEI are capable of delivering genetic cargo *in vitro* and can detect tumor lesions in a lung metastases model of breast cancer with an increased signal-to-noise ratio. One of the requirements necessary for a safe nanotheranostic to progress to clinical use will be low

toxicity profiles in preclinical animal studies, and we show that RENPs@PEI is well-tolerated in mice with no signs of distress or weight loss when monitored for up to 2 months after RENP administration. The unique design of RENPs@PEI will enable the development of a nanotheranostic platform that will be successful in clinical trials for gene therapeutics.

5.3. Results

5.3.1. Size, Morphology, and Crystal Structure of Surface-Modified RENPs

Monodisperse core-shell nanoparticles of β - $\text{NaY}_{0.78}\text{F}_4:\text{Yb}_{0.20},\text{Er}_{0.02}$ (core) and @ NaYF_4 (shell) were synthesized using the previously reported thermal decomposition method in a mixed solvent of oleic acid (OA) and oleylamine (OM)^{213,264}. The OA- and OM-coated RENPs (denoted as RENPs@OA/OM) were typically hydrophobic due to the long hydrophobic carbon chains of OA and OM, leading to poor colloidal stability in aqueous systems. Therefore, a surface-modification method for the coating of these as-synthesized nanoparticles with a cationic branched PEI coating (RENPs@PEI) was developed for the improved stable dispersion of RENPs in aqueous media. Based on earlier reports, using a cationic coating would also increase cellular uptake^{256,257,259,260,263}. However, at much-higher particle concentrations, the increased cell uptake may also lead to increased cell lysis and cell death²⁶⁷. Consequently, to mediate the cell uptake with reduced cytotoxicity, we have proposed a strategy to mediate the surface charges on the particles with the adsorption of ytterbium acetate on the PEI-coated RENPs (denoted as RENPs@PEI-Yb). The adsorption of ytterbium acetate within the organic layer would also lead to an increase in the infrared absorption of the 975 nm source that is typically used to excite the RENPs to generate either visible or infrared emissions. The increase in infrared absorption could potentially lead to an enhancement in either the photoacoustic or photothermal properties of these probes, which would be beneficial in expanding its applications as a dual-modality probe or theranostic agent.

Analysis of the scanning electron microscope (SEM) images for the as-synthesized and surface modified particles shows that the as-synthesized RENPs@OA/OM were mostly spherical with a uniform monodisperse distribution and an average size of $\sim 24 \pm 3$ nm (**Figure 5.1a**). These ranges of particle sizes and morphologies were consistent with earlier reports, in which core particles of ~ 20 nm and shell thicknesses of 2–3 nm were synthesized^{264,265}. No obvious morphological changes were observed after PEI coating and ytterbium acetate adsorption (**Figure 5.1b and 5.1c**). In addition, we have observed an overall increase in average sizes to ~ 28 nm for both RENPs@PEI and RENPs@PEI-Yb. The difference in particle sizes suggested the successful coating of PEI and ytterbium acetate to form an organic layer around the inorganic RENPs. The estimated PEI coating thickness is ~ 1 – 2 nm, determined based on the difference in the average particle sizes. It was established from the XRD measurement that phase-pure RENPs@OA/OM, RENPs@PEI, and RENPs@PEI-Yb with a hexagonal crystal structure were synthesized (**Figure 5.1d**). NaYF₄ typically exists as two phases, cubic (α) and hexagonal (β), in which the hexagonal phase results in fluorescence emissions ~ 4 – 10 times higher than its cubic-phase counterpart^{112,253}. Therefore, the successful synthesis of the hexagonal-phase RENPs is critical toward obtaining brightly emitting probes that ensures the full potential of the SWIR imaging sensitivity and resolution. In addition, the average grain size of 20 to 25 nm for RENPs@OA/OM, RENPs@PEI, and RENPs@PEI-Yb were estimated from the full width at half-maximum of the X-ray diffraction (XRD) peak profiles in **Figure 5.1d**. Based on the similarities in the average particle

sizes and average grain sizes, we can conclude that single crystals of RENPs were synthesized in this work.

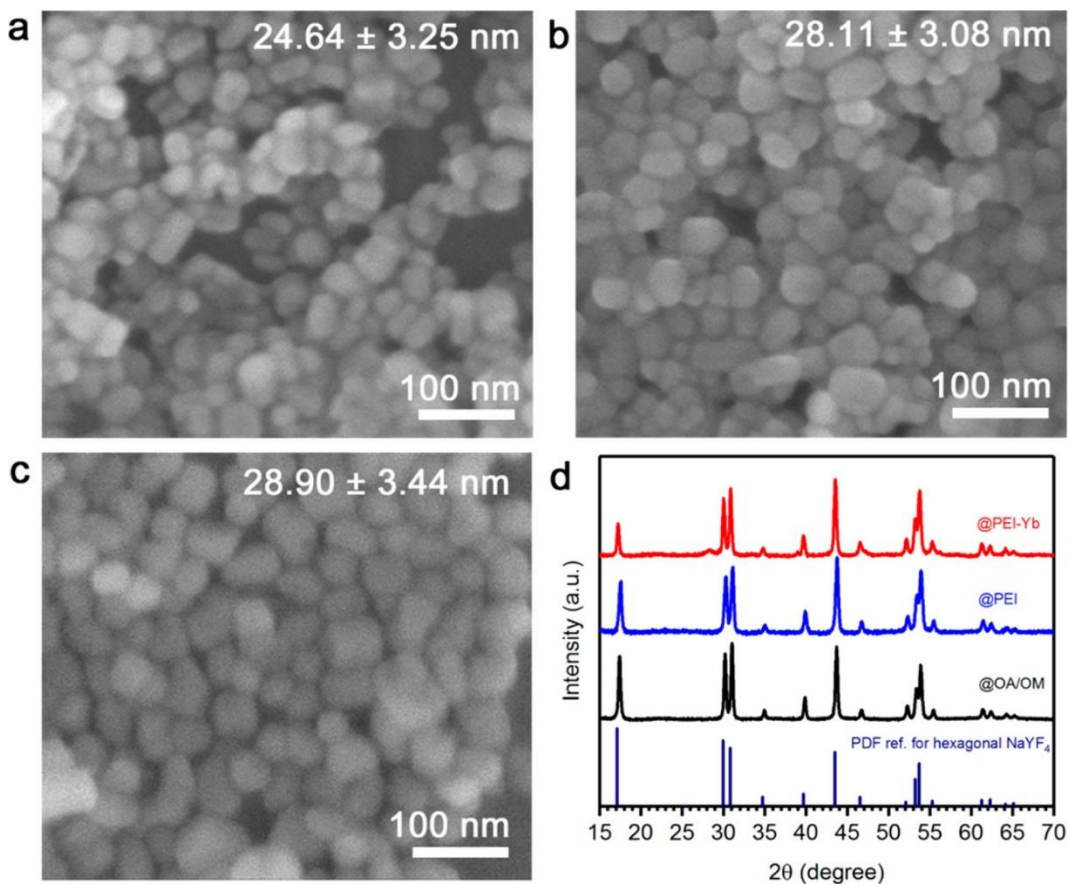


Figure 5.22- Size and crystal structure characteristics of as-synthesized and surface modified core-shell RENPs: The size and morphology analyzed from the SEM micrographs of (a) RENPs@OA/OM, (b) RENPs@PEI, and (c) RENPs@PEI-Yb show that spherical and monodispersed particles were obtained. The XRD profile shows that phase-pure NaYF₄ isotropic powders with a hexagonal crystal structure and a grain size of ~20–25 nm were obtained for all samples, in comparison to the standard reference pattern

5.3.2. Surface Characteristics and Charges of Surface-Modified RENPs

5.3.2.1 Analysis of Molecular Interactions within Organic Layers

To identify the chemical functional groups of as-synthesized and surface modified RENPs, the Fourier transform infrared spectroscopy (FTIR) spectra of the powders were measured (**Figure 5.2**), and the vibrational modes of the chemical groups were subsequently assigned (**Table S5.1**). The FTIR spectra of the pure solvents (e.g., OA and OM) or macromolecules (e.g., PEI) were also collected for comparison purposes. All samples showed the characteristic absorption bands at ~ 2926 and ~ 2856 cm^{-1} , which are attributed to the C–H asymmetric and symmetric stretching vibrations of the methylene units found on the hydrocarbon chains of most organic molecules such as OA, OM, and PEI. Similarly, at below 1400 cm^{-1} , the characteristic C–C vibrational frequencies of a hydrocarbon backbone that is characteristic of organic molecules, such as OA, OM, and PEI, were also observed in all samples. The characteristic OA or OM bands associated with its chemical functional groups (**Table S5.1**) on RENPs@OA/OM suggested that a layer of OA and OM remains on the RENPs surface despite numerous washings. The coordination affinity of amine groups ($-\text{NH}_2$) with the rare-earth metal ions on the surfaces of RENPs is relatively lower than the carboxyl groups ($-\text{COO}$). Hence, it is most likely that an intercalation of bilayers (OA bilayer with OM molecules) as a consequence of hydrophobic interactions led to the exposure of the NH_2 groups (i.e., peak at 3343 cm^{-1}) on the RENP surface (**Scheme 5.1**). The COO^- or CONH amide group and the $^+\text{NH}_3$ and N–H bending vibrational modes of amine functional groups were also found on the RENPs@PEI and RENPs@PEI-Yb (peaks found at 1400 to 1700 cm^{-1} ; **Supplementary table 5.1**) due to the high densities of primary amine groups on PEI that were coated on the RENPs@OA/OM. The relatively higher amine group surface densities on RENPs@PEI and RENPs@PEI-Yb due to PEI adsorption were also evidenced by the increase in the relative strength between the N–H peak (1562 cm^{-1}) and the C–H peak (2922 cm^{-1}). The large number of free NH_2 groups implies that it is possible to conjugate additional

biomolecules (e.g., drugs and targeting peptides) on the surfaces of these particles. The possible presence of amide, COO^- , and $^+\text{NH}_3$ functional groups suggests that the PEI layer was coated on the OA and OM layer via either electrostatic interactions between COO^- and $^+\text{NH}_3$ or the formation of a covalent CONH amide linkages between OA and PEI (**Scheme 5.1**). Likewise, the continued presence of COO^- and $^+\text{NH}_3$ and the covalent CONH amide linkages in RENPs@PEI-Yb indicates the possible formation of electrostatic interactions or covalent linkages between PEI and ytterbium acetate (**Scheme 5.1**).

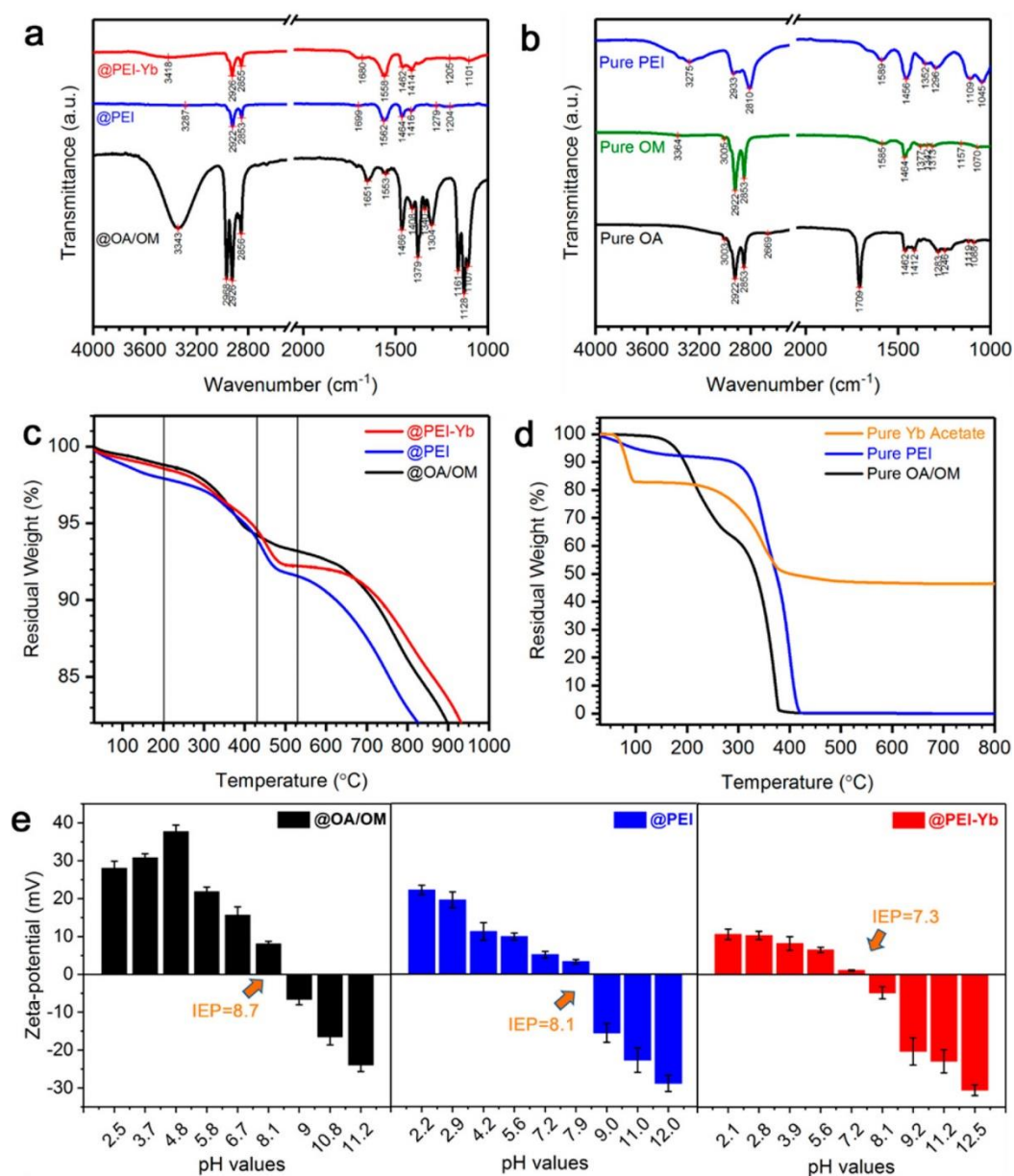
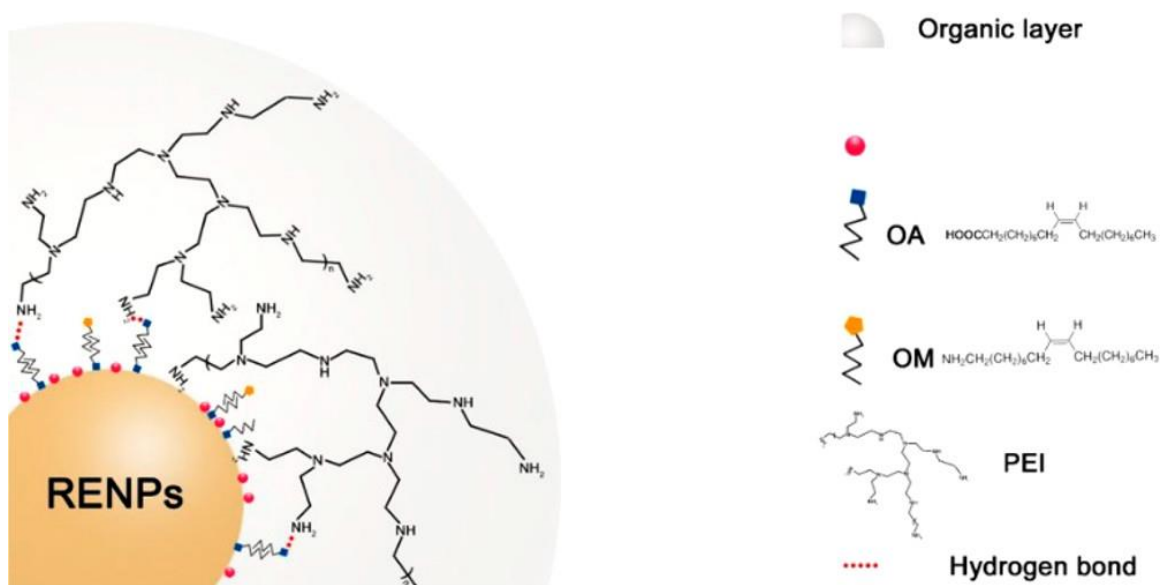


Figure 5.23- Surface characteristics of as-synthesized and surface-modified core-shell RENPs

:Characteristics chemical functional groups of the (a) various RENPs and (b) pure solvents and surfactants were identified using FTIR to determine the molecules found on the particle surfaces. The amount of each molecule found within the organic layer was estimated from TGA measurements of (c) as-synthesized and surface modified core-shell RENPs, where (d) reference TGA measurements of the pure solvents and surfactants were made to determine the decomposition temperature ranges of each molecular specie. (e) Surface charge of the various RENPs at different pH values were evaluated from ζ -potential measurements, where the shift in the isoelectric point (IEP) was also estimated to determine the point of surface-charge transition for each type of RENP.



Scheme 5.1: Schematic Representation of the Molecular Conformation and Interactions within

the Organic PEI Coating: Detailed schematic representation of the interactions between the different molecules, such as oleic acid (OA), oleylamine (OM), and branched polyethylenimine (PEI, MW \approx 25 000 g/mol) within the organic layer coated around the inorganic core-shell RENPs are shown here.

The peak shifts at 3 distinctive regions of (1) $\sim 3200\text{--}3400\text{ cm}^{-1}$, (2) $\sim 1650\text{--}1700\text{ cm}^{-1}$, and (3) $\sim 1400\text{--}1420\text{ cm}^{-1}$ allow us to further elucidate details of the likely molecular interactions within the organic layer for the RENPs@OA/OM, RENPs@PEI, and RENPs@PEI-Yb particles. The types of molecular interactions were evaluated to assess the likelihood of the leaching of the surface adsorbed molecules, such as PEI or ytterbium acetate, during *in vitro* or *in vivo* testing. The shifts in the broad peak at $\sim 3200\text{--}3400\text{ cm}^{-1}$ associated with the primary NH_2 bonds would be indicative of the extent of hydrogen bonding between the various molecular species (e.g., OA, OM, and PEI) within the organic layer. Upon the coating of a PEI layer on RENPs@OA/OM, the peak shifted to lower wavenumbers from 3343 to 3287 cm^{-1} . The shift to lower wavenumbers suggests an increase in hydrogen bonds (e.g., between OA or OM and PEI) (**Scheme 5.1**). The addition of ytterbium acetate led to a shift to higher wavenumbers from 3287 to 3418 cm^{-1} , which suggests a disruption of the PEI-OM or PEI-OA hydrogen bonds. The disruption of these hydrogen bonds was most likely caused by the formation of electrostatic interactions (COO^- with $+\text{NH}_3$) or covalent CONH amide linkages between PEI and ytterbium acetate in RENPs@PEI-Yb.

Surface coating	Temperature range($^{\circ}\text{C}$)	Weight loss (%)	Estimated thickness(nm)	Total layer thickness (nm)	Estimated particle size(nm)
@OA/OM	200 to 430	4.16	0.7 to 0.9	0.7 to 0.9	21.4 to 26.7
@PEI	200 to 520	6.27	0.30 to 0.31	1.0 to 1.2	22.0 to 27.5
@PEI-B	200 to 550	6.38	0.04	1.0 to 1.2	22.1 to 27.6

Table 5.1: Estimated Thickness of Each Surfactant (Or Polymer) from the TGA Weight-Loss Measurements, Assuming That a Uniform Layer Is Coated around the Inorganic RENPa

^aThe size of the inorganic RENP without any coating is approximated to be equal to the XRD crystallite size of ~20 to 26 nm, determined from the XRD profiles.

The peaks found in the region of ~1650–1700 cm^{-1} were assigned to either the presence of amide bonds or the formation of the carboxylate anion (COO^-). The shift to higher wavenumbers from 1650 to 1699 cm^{-1} upon PEI coating suggests the increased protonation of COO^- of OA leading to the increased formation of COOH functional groups, which would at the same time facilitate the formation of PEI–OA hydrogen bonds or amide bonds with PEI. In contrast, the addition of ytterbium acetate resulted in a shift to lower wavenumbers from 1699 to 1680 cm^{-1} , which suggests that the hydrogen bonds were disrupted, most likely due to the formation of COO^- -based electrostatic interactions from the acetates or OA. The disruption of the hydrogen bonds is consistent with the earlier analysis based on the 3200–3400 cm^{-1} peak shifts. The peak at ~1400–1420 cm^{-1} is usually found with that at 1650–1700 cm^{-1} , such that both are commonly associated with the anionic COO^- vibrational bond and its interactions²⁶⁸. In particular, the shift of the peak at ~1400–1420 cm^{-1} would offer further details on the extent of electrostatic interactions between COO^- with $^+\text{NH}_3$. With the addition of PEI, the shift to higher wavenumbers from 1408 to 1416 cm^{-1} suggests a disruption of the electrostatic interactions between the COO^- of OA and the $^+\text{NH}_3$ of OM, which was most likely due to the earlier mentioned PEI–OA hydrogen bond formation. In contrast, the addition of ytterbium acetate led to a shift to lower wavenumber from 1416 to 1414 cm^{-1} , which suggests a slight increase in the formation of COO^- -based electrostatic interactions (e.g., the COO^- of acetate with the $^+\text{NH}_3$ of PEI or the COO^- of OA with Yb^{3+}). The increase of COO^- interactions is consistent with the earlier peak shift analysis for the 1650–1700 cm^{-1} region. Briefly, the FTIR results and analysis suggests that PEI is coated on an OA and OM

layer on the RENPs (**Scheme 5.1**). The formation of the PEI coating is facilitated by the formation of hydrogen bonds or covalent amide linkages between PEI and OA or OM. The addition of ytterbium acetate led to the disruption of these hydrogen bonds of PEI, where an increased in COO^- -based electrostatic interactions (e.g., COO^- with $^+\text{NH}_3$ or COO^- with Yb^{3+}) was observed.

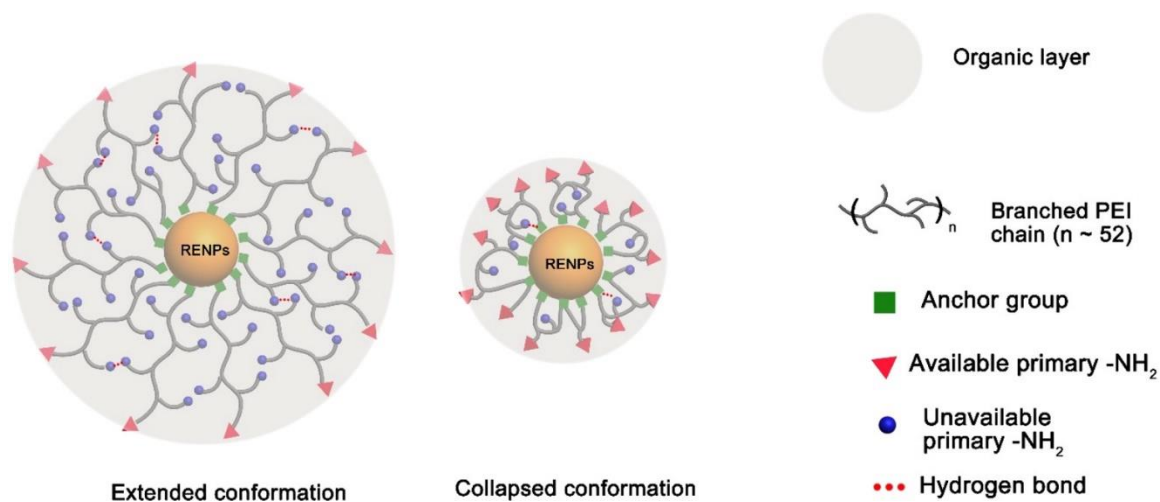
5.3.2.2. Estimation of the Thickness of the Organic Layer to Deduce Chain Conformation

To estimate the relative amount and coating thickness of the organic layer on the RENPs, the residual weight upon heating the RENP samples and the pure organic molecules (e.g., OA or OM and PEI) in an inert N_2 environment were measured using a thermogravimetric analyzer (TGA) (**Figure 5.2c and 5.2d**). The corresponding first derivatives of the TGA results were used to identify the major weight loss transition points (**Supplementary Figure 5.1 and Table 5.1**). The initial weight loss associated with temperatures ranging from 25 to 200 °C of all RENP samples was most likely due to the vaporization of residual solvents, such as water and ethanol. The final weight loss from ~525–1000 °C of RENPs was associated with the decomposition of the fluoride-based NaYF_4 hosts (**Figure 5.2c**) because all organics (e.g., OA, OM, PEI, and Yb acetate) were found to completely decompose by ~450 °C (**Figure 5.2d**). The second observed major weight-loss region was ascribed to the corresponding decomposition of the adsorbed molecule, such as OA, OM, and PEI. From ~525–1000 °C, depending on the surface composition of the RENPs, different transitions were observed (**Supplementary Figure 5.1**). One transition at ~372 °C was observed for RENPs@OA, while two transitions at ~330–360 °C and ~445–454 °C were observed for both RENPs@PEI and RENPs@PEI-Yb.

Through comparison with the thermal decomposition characteristics of a mixed OA and OM solvent system (**Figure 5.2d and Supplementary Figure 5.1**), the transition at ~330–372 °C for all RENP samples were attributed to the presence of OA and OM in all samples. Based on the weight loss corresponding to this transition (200–430 °C), the calculated estimated thickness of the OA/OM layer was ~0.7 to 0.9 nm (**Table 5.1**), which suggested a bilayer composed of OA and OM

was formed. The formation of a bilayer was consistent with FTIR results and analysis of the interactions between OA and OM. With the addition of the calculated OA and OM layer thickness to the XRD calculated grain size (**Figure 5.1d**), a particle size of 21.4 to 26.7 nm was estimated. The calculated estimated particle size was consistent with the SEM data and was observed to be 24.6 ± 3.3 nm (**Figure 5.1**). Likewise, the $\sim 445\text{--}454$ °C transition for the RENPs@PEI and RENPs@PEI-Yb samples were attributed to the presence of PEI on the surfaces. These results confirm that PEI was adsorbed onto a OA and OM layer on the RENPs, which is consistent with the analysis from the FTIR results. The calculated estimated PEI layer thickness is ~ 0.30 to 0.31 nm (**Table 5.1**), which indicated that the single coated layer of PEI macromolecular chain adopted a collapsed-chain conformation, wrapping around the particle, instead of an extended conformation, in which only one end of PEI is anchored on the RENP surface (**Scheme 5.2**). The collapsed chain conformation of PEI and low PEI packing density had also most likely limited the change in its infrared dipole moments, leading to the observed reduced peak intensity of the RENPs@PEI compared to RENPs@OA/OM (see **Figure 5.2**). The resultant increase in particle size (22.0 to 27.5 nm) as a result of the PEI coating was consistent with our earlier observed increase in SEM PEI-coated particle sizes of 28.1 ± 3.1 nm. The collapsed chain conformation could lead to an enhance availability of the amine functional groups that is critical for further biomolecular functionalization and increased loading of genetic cargo. It should be noted that the transition temperature range at $\sim 445\text{--}454$ °C of RENPs@PEI and RENPs@PEI-Yb, was much higher than that of free PEI, which was measured at 401 °C (**Supplementary Figure 1**). The higher decomposition temperature of PEI coated on RENPs suggests that the interactions between PEI and the constituents within the organic layer (e.g., OA, OM, and ytterbium acetate) and RENP surface were much stronger than that between free PEI macromolecular chains. It was also observed that the residual weight of RENPs@PEI-Yb is higher than that of RENPs@PEI (i.e., the observed reduced weight loss in **Figure 5.2c**). The higher residual weight at ~ 550 °C of RENPs@PEI-Yb was attributed to the formation of ytterbium oxide at a much higher temperature, which partially

compensated for the reduced weight loss. The formation of ytterbium oxide leading to a reduced weight loss and higher residual weight was also observed for the thermal decomposition of pure ytterbium acetate (**Figure 5.2d**). Therefore, the reduced weight loss of RENPs@PEI-Yb reaffirms the successful impregnation of ytterbium acetate within PEI.



Scheme 5.2: Schematic Illustration of the Resultant Key Differences between Extended and Collapsed-Chain Conformations of PEI Coating around the Inorganic RENPs^a

^aFor an extended PEI chain conformation, in which ~ 1 anchor group per chain would typically be attached to the inorganic RENP, the thickness of the organic shell would theoretically be much thicker and the number of available primary amine functional groups would be limited due to the extensive hydrogen bonds between each PEI chain within the organic layer (as shown with a couple of highlighted examples in the schematic). In contrast, the thickness of a collapsed-chain conformation of PEI coated around the inorganic RENP, having more than 1 anchor group attached to the RENP per chain, would generally be substantially thinner. Consequently, the number of available primary amine functional groups would be much higher in the case of a PEI coating with a collapsed-chain conformation upon consideration of the restricted bond angles of the PEI hydrocarbon backbone.

Surface-Charge Characteristics of Surface-Modified RENPs

The surface charge characteristics of the as-synthesized and surface modified RENPs were characterized from ζ -potential measurements and subsequent estimation of the isoelectric point (IEP) of each sample, which dictates the relative acidity or basicity of the particle surfaces (**Figure 5.2e**). Due to the hydrophobic–hydrophobic interaction between OM and OA in water leading to the exposure of free primary amine groups, a large positive charge with an IEP at ~ 8.7 was observed in RENPs@OA/OM. The presence of free amine groups leading to particle surfaces exhibiting a basic character is consistent with earlier FTIR results (**Figure 5.2a**). The ζ -potential values were slightly lowered from ~ 35 to 20 mV, and the isoelectric point was shifted from ~ 8.7 to ~ 8.1 upon modification of the particle surface with a PEI coating. The reduced surface charge and shift of the isoelectric point indicated that the PEI modification led to an electrical surface charge neutralization coupled with a reduced basic character of the surfaces. The observed change was consistent with earlier FTIR results, in which the increased protonation of anionic COO^- of OA led to an increase in hydrogen bonding between OA and PEI. Thus, the number of free amine groups on the surfaces were likely reduced, leading to a slight reduction of surface charge and basicity. The addition of ytterbium acetate to RENPs@PEI reduced the ζ -potential values further to ~ 10 mV and lowered the IEP to ~ 7.3 . The observed reduction of surface charge and IEP lowering was consistent with earlier FTIR results, in which an increase in COO^- -based electrostatic interactions was established (e.g., the COO^- of acetate with the $^+\text{NH}_3$ of PEI or the COO^- of OA with Yb^{3+}). The increase in COO^- -based electrostatic interactions led to the reduction of the surface charge and the lowering of the IEP toward a pH-neutral surface. Because the subsequent particle conjugation with genetic payload follows an identical conjugation chemistry, the use of a small molecule such as Yb acetate to systematically evaluate changes in the PEI surface potential would allow us to evaluate the impact of reduced surface charges on cellular uptake and toxicity.

5.3.3. Optical Properties of the RENPs

To evaluate the optical properties of RENPs, the absorption and fluorescent behavior was measured (**Figure 5.3**). The absorption spectra of RENPs@OA/OM, RENPs@PEI, and RENPs@PEI-Yb exhibited the typical absorption peaks for Yb and Er codoped material at 519, 650, and 975 nm (**Figure 5.3a**). The absorption peaks at 520 and 650 nm were characteristics of only Er, while the infrared absorption at 975 nm can be attributed to both Yb and Er. Because the amount of Er doped in all RENPs were the same, the integrated visible absorbance at 519 and 650 nm were also similar for all samples. However, a substantial difference of the IR absorbance at 975 nm was observed for RENPs@PEI-Yb compared with RENPs@OA/OM or RENPs@PEI. The higher IR absorption was attributed to much higher Yb amount arising from the impregnation of ytterbium acetate within the PEI layer in RENPs@PEI-Yb. This is consistent with earlier FTIR and TGA analysis of a successful Yb impregnation within PEI (**Figure 5.2**). In contrast, the IR absorbances of RENPs@OA/OM and RENPs@PEI were similar because the amount of Yb and Er in both materials were the same. The higher infrared absorption could potentially be harnessed to enhance the photoacoustic response or photothermal behavior of these particles for applications as dual-modal imaging probes or photothermic agents^{264,265}.

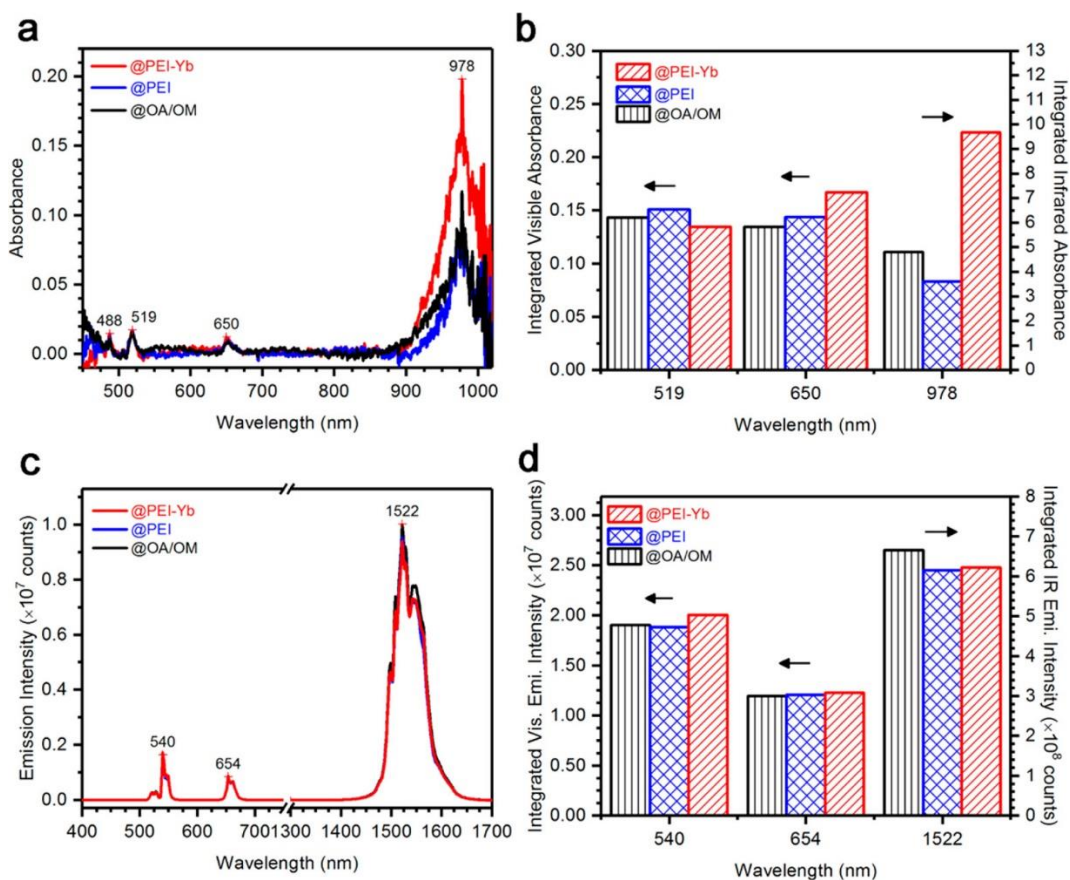


Figure 5.24- Optical characteristics of as-synthesized and surface-modified core-shell RENPs, evaluated to determine the effects of surface modification: (a) The absorption profile of various RENPs were measured; a typical Yb absorption peak at 975 nm and Er absorption peaks at 488, 519, 650, and 975 nm were identified. (b) The integrated absorbance for each type of RENPs was measured to estimate the relative amount of each element in the RENPs. (c) The fluorescence emission characteristics of the various RENPs upon excitation at 975 nm were measured; Er transitions of $^4S_{3/2} \rightarrow ^4I_{15/2}$ (~540 nm), $^4F_{9/2} \rightarrow ^4I_{15/2}$ (~654 nm), and $^4I_{13/2} \rightarrow ^4I_{15/2}$ (~1522 nm) were identified. (d) The integrated emission intensities of various RENPs were measured to evaluate the emission attenuation effects of each surface coating.

Next, we analyzed the steady-state visible and IR fluorescent emissions of all samples upon 975 nm excitation. Due to the resonant energy transfer between the Yb sensitizer and Er activator ions, all samples showed the characteristic visible and IR emissions at similar intensities (**Figure 5.3c**

and 5.3d), suggesting that the organic layer coating thickness was sufficiently thin so that the emitted signals were not attenuated due to the presence of the coating. The bright luminescence emissions would be critical toward enabling high-resolution and sensitive fluorescent imaging using these PEI-coated RENP probes. Similarly, based on the time-resolved measurements (**Supplementary Figure 5.2**), the fitted decay time of the 1522 nm infrared emission ranging from 5.88 to 5.93 ms for all 3 samples (RENPs@OA/OM, RENPs@PEI, and RENPs@PEI-Yb) were similar (**Table 5.2**). The identical fitted decay time for all three samples suggests that Yb–Er photon energy-transfer pathways were similar among them, whereas the undoped NaYF₄ shell (~2–3 nm) served as an effective barrier, limiting the undesired emission quenching due to the interactions between the functional groups (e.g., –CH₂) within the organic layer and rare-earth dopants, Yb and Er. These relatively long decay times indicate the low non-radiative losses and bright luminescence emission, enabling all samples with the ability to achieve high-resolution and sensitive fluorescent imaging with the potential for much-earlier detection using these probes.

Surface coating	A_1	$t_1(s)$	A_2	$t_2(s)$	Average t (ms)
@OA/OM	0.3328 ± 0.00299	1762.87 ± 18.3	0.6564 ± 0.00321	6484.39 ± 19.04	5.91
@PEI	0.3396 ± 0.00317	1836.56 ± 18.96	0.6365 ± 0.00397	6540.16 ± 20.45	5.93
@PEI-B	0.3303 ± 0.00273	693.01 ± 16.84	0.6609 ± 0.00294	6428.72 ± 17.58	5.88

Table 5.2: Estimated Average Lifetime of Each As-Synthesized or Surface-Modified RENP from Time-Resolved Spectroscopy Measurements Made Using a Pulse-Modulated 975 nm Source, Assuming Double-Exponential Decay Behavior^a

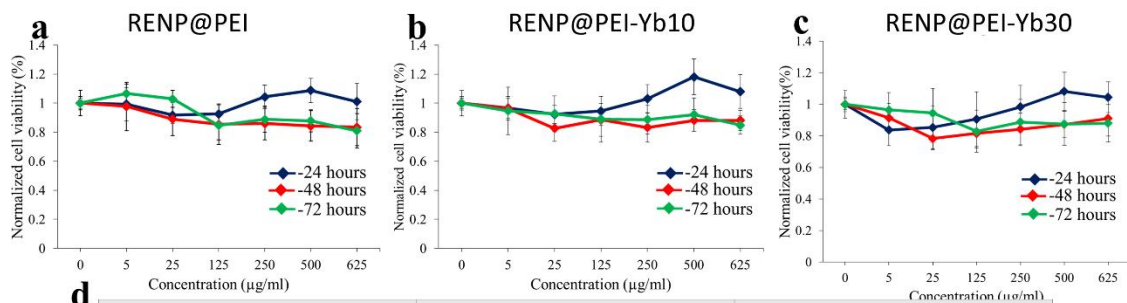
^a A_1 and A_2 were the fitting parameters used in the double-exponential decay time model.

5.3.4. Cellular Uptake and Toxicity of the RENPs

PEI-modified formulations have traditionally been associated with cellular toxicity, owing to their positive charge^{259,260}. Here, we determined the toxicity of RENPs (RENPs@PEI and RENPs@PEI-Yb₁₀ and Yb₃₀) in breast cancer cells by MTT assay as described in methods section. RENPs@PEI-Yb₁₀ and Yb₃₀ are Yb-impregnated PEI-coated RENPs prepared by dispersing them in 10 and 30 μ mol of aqueous ytterbium(III) acetate, respectively. Cytotoxicity studies using MDA-MB-231 breast cancer cells did not show significant toxicity from either of the 3 formulations at 24 h (**Figure 5.4a–c**). At 48 h, the cells display a viability of $83.4 \pm 12.8\%$, $88.1 \pm 6.9\%$, and $91.1 \pm 11.33\%$ for RENPs@PEI and RENPs@PEI-Yb₁₀ and Yb₃₀, respectively (see **Figure 5.4d**). These results were paradoxical because the current literature on PEI-modified nanoparticle systems have consistently suggested low tolerance and high cytotoxicity^{256,259,260}. The high cytotoxicity was previously attributed to high cellular uptake, leading to cell lysis due to imbalance of osmotic pressure²⁶⁷. Based on the measured hydrodynamic diameters (**Supplementary Figure 5.3**), RENPs@PEI generally existed as aggregates of ~ 80 nm (i.e., ~ 2 to 3 nanoparticles), while RENPs@PEI-Yb formed aggregates of ~ 125 nm (i.e., ~ 3 to 4 nanoparticles). These aggregates were most likely formed as a consequence of hydrogen bonding between the high densities of NH₂ available on the particle surfaces. The formation of smaller aggregates of RENPs@PEI compared to RENPs@PEI-Yb was most likely due to their higher NH₂ surface densities on RENPs@PEI that would lead to stronger interactions between particles via hydrogen bonding. The formation of these aggregates would reduce the effective surface area per unit volume of the

modified nanoparticles, leading to the reduced impact on the surface-charge effects of modified RENPs. The smaller aggregate size of RENPs@PEI compared to RENPs@PEI-Yb suggests that it had the highest surface positive charge per aggregate. The higher positive charge probably led to the slightly higher observed toxicity of RENPs@PEI. The aggregation leading to a reduced surface charge could have resulted in lowered cytotoxicity with the nanocarriers.

RENPs are taken up by MDA-MB-231 breast cancer cells and are distributed in the peri-nuclear space, as visualized using an in-house line scanning SWIR confocal microscope²⁶⁹. There seemed to be subtle changes to particle uptake as a function of surface charge (**Figure 5.4e and 5.4f**). The intracellular distribution of particles in all three formulations of RENPs (RENPs@PEI and RENPs@PEI-Yb₁₀ and Yb₃₀) seems to become increasingly punctate with reduced charge, and this also seems to follow an inverse correlation with aggregation of these particles, as measured by dynamic light scattering (DLS, **Supplementary Figure 5.3**). The strongly bonded RENPs@PEI aggregates showed larger areas with high fluorescence intensity, while the more loosely bonded RENPs@PEI-Yb₃₀ (due to reduced NH₂ groups for hydrogen bonding) had likely separated within the cell and exhibited much-smaller areas with high fluorescence intensity. The intracellular distribution analysis is a qualitative analysis of fluorescence intensities and changes in quantitative uptake of these particles will need further investigation. However, the relative fluorescence intensities from the RENPs in **Figure 5.4** were similar (e.g., no statistically significant difference in red-to-blue intensity ratios for areas with identical cell density), suggesting possible identical RENP internalization. Moreover, the effective intracellular uptake of RENPs@PEI (**Figure 5.4**) suggests that they could deliver genetic cargo into the cell.



d

Nanoparticle	Viability at 48 hr (625 $\mu\text{g/ml}$)	Viability at 72 hr (625 $\mu\text{g/ml}$)
RENP@PEI	83.4 \pm 12.8 %	80.9 \pm 11.9 %
RENP@PEI-Yb10	88.1 \pm 6.9%	84.8 \pm 6.3 %
RENP@PEI-Yb30	91.1 \pm 11.33 %	88.0 \pm 11.9 %

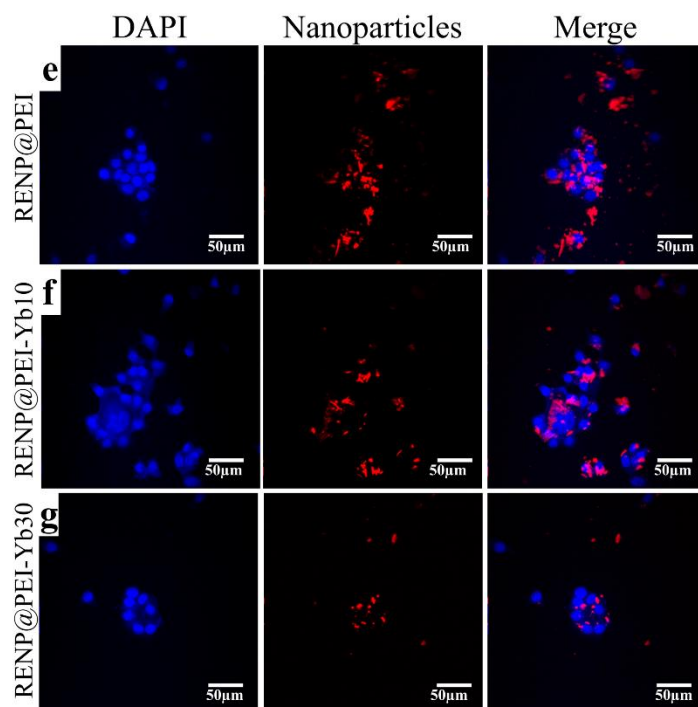


Figure 5.25- Effect of surface modification of core–shell RENPs on cell proliferation, viability, and intracellular distribution: MDA-MB-231 cells were treated with doses ranging from 0 to 625 $\mu\text{g/mL}$ of (a) RE-PEI, (b) RE-PEI@Yb₁₀, and (c) RE-PEI@Yb₃₀ nanoparticles. The effect of the nanoparticles on the cell proliferation was observed using a MTT assay over a time course of 72 h. (d) Quantitative analysis shows that, at a concentration of 625 $\mu\text{g/mL}$, RE-PEI nanoparticle treatments maintain a lower viability at 48 and 72 h, compared with RE-PEI@Yb₁₀ and RE-PEI@Yb₃₀; $n = 3$, values \pm SEM, $p < 0.2$. MCF7 breast cancer cells were treated with (e) RENPs@PEI, (f) RENPs@PEI-Yb₁₀, and (g) RENPs@PEI-Yb₃₀ for 18 h followed by microscopy using an in-house confocal microscope. Visible emissions from nanoparticles excited with 980 nm were recorded, and the results, when merged with nuclear staining (4',6-diamidino-2-phenylindole), show the intracellular localization of particles closer

5.3.5. *In vivo* SWIR Imaging for the Monitoring of RENPs@PEI Biodistribution and Bioavailability

To evaluate the imaging sensitivity using probes, SWIR signals from RENPs@PEIs after incubation with MDA-MB-231 (triple negative breast cancer cell line) were measured. Notably, the RENPs@PEIs (6.25×10^{-3} mg/mL) were able to resolve cellular clusters as low as 50 cells per cluster *in vitro* (**Supplementary Figure 5.4**).

To investigate the preferential accumulation of RENPs@PEIs *in vivo* and enhanced signal-to-noise ratio in discerning punctate lesions, the distribution of RENPs@PEIs in mice bearing metastatic lung lesions were monitored using SWIR imaging. Female athymic nude mice were injected with MDA-MB-231 cells via tail vein and developed metastatic lung lesions. Systemic administration of RENPs@PEI at 6–8 weeks post-inoculation showed enhanced SWIR signal from lesion space due to the preferential localization of particles, with a striking increase in the lesion-related contrast (signal-to-background ratio; **Figure 5.5a**, top row), especially in comparison with prior

works^{71,187}. Furthermore, in healthy athymic nude mice, whole-body *in vivo* SWIR imaging 6 days after intravenous injection showed little or no residual signal (**Figure 5.5b**, top row). The *in vivo* SWIR images at different time points showed a gradual decrease in SWIR emissions for various organs, with no significant signal after 6 days post-injection. Based on the observed decrease in SWIR intensity contributed only by the nanoparticles (**Figure 5.5b**), it was indicated that its clearance was via the reticuloendothelial system over time. This was validated by *ex vivo* SWIR imaging (**Supplementary figure 5.5**), and no overt toxicity as evidenced by little change in tissue architecture by the histopathology in the major organs of clearance (**Figure 5.5**, bottom row).

A theranostic agent needs to be (1) able to discern signal from target sites with increased signal-to-background ratio and (2) safe and well-tolerated. RENPs@PEI nanoplatform successfully discerned lung lesions with superior resolution and enabled the differentiation of signal from organs of clearance such as liver using an established preclinical lung metastases model of breast cancer. Additionally, they exhibited exceptional tolerance profile, as evidenced by clearance from major organs of clearance by day 7 and no toxicity based on histopathology. Notably, in a group of animals that received a bolus dose of RENPs@PEI, we did not see any overt signs of toxicity up to 2 months post-injection (data not shown).

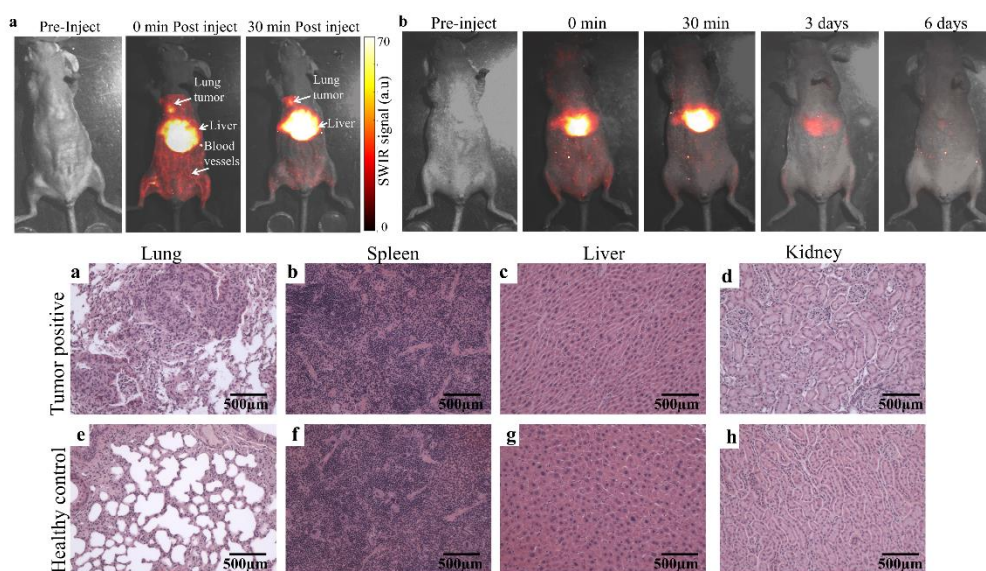


Figure 5.26- SWIR imaging showing enhanced signal-to-noise ratio with RENPs@PEI localization in lung lesions: (a) Female athymic nude mice injected with MDA-MB-231 cells intravenously develop metastatic lung lesions. RENPs@PEI nanoparticles are injected intravenously, and SWIR imaging follows immediately. A total of 0 min after injection, SWIR imaging shows nanoparticle circulation through blood vessels to lesion sites and organs of clearance. A total of 30 min after injection, SWIR imaging shows significant localization of particles at the lesion site, with a striking increase in lesion-related fluorescence, leading to sensitive SWIR imaging. SWIR imaging through time shows the effective clearance of nanoprobables. (b) Animals injected intravenously with RENPs@PEI nanoparticles are imaged with the SWIR imaging system at different time points. In vivo imaging at different time points indicates a decrease in SWIR emissions with no significant signal 6 days post-injection. Based on SWIR intensity, the nanoparticles indicate clearance via the reticuloendothelial system over time. (e-l) *Ex vivo* histopathological analysis of organs of clearance for toxicity. Animals injected intravenously with RENPs@PEI are sacrificed, and the organs of clearance are analyzed *ex vivo*. The histopathological evaluation of major organs of clearance such as (f, j) the spleen, (g, k) the liver, and (h, l) the kidney in both healthy and tumor-bearing animals shows no loss of tissue integrity. (e) Additionally, the lungs (the first capillary bed of clearance) of the healthy control injected with particles do not show any sign of damage. Hematoxylin and eosin stained lungs of tumor-bearing animals validate the presence of tumor, shown in panel a.

5.3.6. RENPs@PEI-Mediated Gene Targeting as Evidenced by the in Situ

Hybridization of Genetic Probes to Genes of Interest

The cationic charge of PEI makes it an ideal modification for genetic cargo to be taken into tumor sites for gene therapy. Additionally, the superior resolution of RENPs@PEI with an enhanced lesion-related contrast at tumor site (**Figure 5.5**) will allow for the noninvasive imaging of delivery

of genetic cargo to tumor sites while determining off-target effects. Here, we show in a cell line (ES2) that over-expresses the gene filamin A interacting protein 1 like (FILIP1L) when treated with doxycycline^{270,271} enhanced uptake of the genetic cargo when conjugated to RENPs@PEI than DNA alone (**Figure 5.6a**; DOX+). Briefly, in situ hybridization of FILIP1L expressing oligonucleotides showed enhanced fluorescence in cells treated with doxycycline to induce FILIP1L expression when delivered by conjugation to RENPs@PEI rather than alone, suggesting RENPs@PEI as a potential delivery vehicle for genetic cargo to target sites.

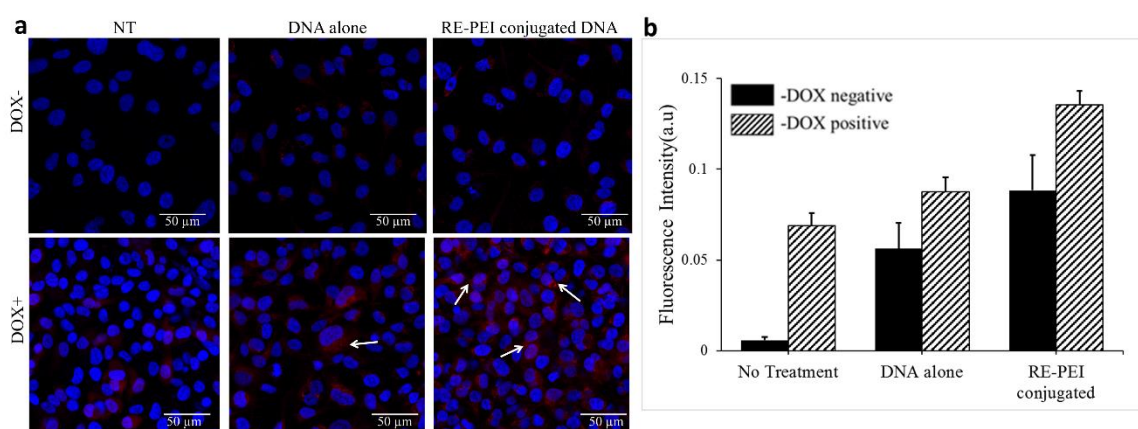


Figure 5.27- Delivery of genetic cargo enhanced by RE-PEI. ES2 cells were induced to over-express the FILIP1L gene by the addition of doxycycline (DOX): RENPs@PEI conjugated to 6-FAM-tagged FILIP1L oligonucleotides (RE-PEI conjugated) was used for in situ hybridization and successful hybridization, as determined by detection of 6-carboxyfluorescein (FAM) fluorescence intensity. We show the enhanced uptake of the oligonucleotide by RE-PEI conjugated compared to that of DNA alone, validating the increased delivery of genetic cargo by RENPs@PEI in cells induced to over-express FILIP1L (panel a; DOX+) and an increase of a factor of ~1.5 in fluorescence intensity, as shown in panel b.

Our preliminary studies showed that RENPs@PEI delivered the genetic cargo efficiently fluorescence increased by a factor of 1.5 compared to that of DNA alone (**Figure 5.6b**) in cells

that over-express FILIP1L(DOX+). The increased protonation state and aggregation of RENPs@PEI are likely to play a role in improved delivery of genetic cargo. We content that the RENPs@PEI-Yb acetate formulations will enhance this delivery further while also contributing to additional photothermally-mediated therapeutic effects, although the reduced primary amine groups on RENPs@PEI-Yb will limit the loading of genetic cargo. Further studies are warranted to address these modified RENP formulations as nanotheranostic agents in cancer.

5.4. Summary

Nanoparticle engineering has progressed to multifunctional formulations that deliver both therapeutic and diagnostic components to target sites, leading to the hybrid system often described as nanotheranostics^{248,272-274}. With advances made in unmasking biomarkers for disease states, another layer of complexity is currently being explored with nanotheranostics in which an additional targeting ligand (used for better accumulation at the target site) is added to the same physical entity. The goal of this study is to design a nanoparticle formulation that, as a single entity, will be able to target, carry payload, and monitor response to therapy.

We designed a tunable nanophotonic formulation that has superior resolution with increased signal-to-noise ratio and improved penetration depths compared with existing optical imaging agents. From a detailed study of the PEI interactions and conformation on RENPs using a small-molecule counter-ion such as Yb acetate, we established that the ~1 nm PEI nanocoating was most likely present as a collapsed-chain conformation. A collapsed PEI chain conformation around RENPs was critical toward enhancing the availability of the amine functional groups for functionalization (e.g., targeting peptides and antibodies) and the increased loading of genetic cargo. We also modified the surface charge to reduce toxicity even further in using Yb-acetate, leading to RENPs@PEI-Yb30, which showed little or no cellular toxicity, even at concentrations as high as 625 µg/mL, with no change in cellular distribution. The absence of cellular toxicity commonly associated with highly positively charged nanocarriers was attributed to the reduced

surface-charge effects of our RENPs@PEI that formed tightly bonded aggregates of 2 to 4 nanoparticles. Furthermore, the use of Yb-acetate modification also expanded the functions of the RENPs for potential applications in photothermal therapy or as photoacoustic imaging probes due to its increased optical absorption at selected wavelengths. We also show that RENPs@PEI are well-tolerated in mice and is completely cleared, such that the bright emissions from the RENPs@PEI enabled the successful detection of lung lesions at superior resolution and enabled the differentiation of signal from organs of clearance such as the liver using an established preclinical lung metastases model of breast cancer. The RENPs@PEI formulation was also used to deliver genetic cargo (FILIP1L oligo) to FILIP1L over-expressing cells more efficiently than FILIP1L oligo alone. Most importantly, this study exploits not only the surface modification of RENPs for genetic cargo but also the SWIR emission of RENPs that will allow for deep-tissue imaging and gene-therapy monitoring at target sites.

The added challenges faced with nanotheranostics in clinical translation are the long-term assessment of toxicity, high efficacy at target sites, and reduced distribution in healthy tissues. The ability to deliver therapeutic payload with targeted precision and monitor the real-time delivery of the therapeutic cargo will be beneficial in understanding on-target accumulation levels and also assessing off-target side-effects for enabling informed therapeutic decision-making in the clinic.

5.5. Methods

5.5.1. Chemicals

Lanthanide oxides (99.99%; Y_2O_3 , Yb_2O_3 , and Er_2O_3), trifluoroacetic acid (99%), sodium trifluoroacetate (98.0%; CF_3COONa), 1-octadecene (97%; ODE), oleylamine (70%; OM), oleic acid (90%; OA), cyclohexane (99.5%), chloroform (99.99%), polyethylenimine (PEI, $M_w = 25$

000 g/mol), and ytterbium(III) acetate tetrahydrate were purchased from Sigma-Aldrich (Saint Louis, MO). All chemicals were used as obtained without any further purification.

5.5.2. Trifluoroacetate Precursor Preparation

The precursors composed of lanthanide trifluoroacetates ($\text{Ln}(\text{CF}_3\text{COO})_3$) dissolved in OM at a ratio of Y:Yb:Er = 0.78/0.2/0.02 were prepared by first dissolving the lanthanide oxides in their stoichiometric ratios in a solution of trifluoroacetic acid and water at 1:1 %v/%v in a glass bottle. To ensure the complete solubilization of the oxides, the solution was placed on a hot plate at 90 °C for about 1 week. Subsequently, the temperature was increased to ~120 °C to vaporize the solvent mixture of water and trifluoroacetic acid. The dried precursors composed of $\text{Ln}(\text{CF}_3\text{COO})_3$ solids were next dissolved in OM at 120 °C until a transparent solution was obtained.

5.5.3. Synthesis of Rare-Earth-Doped Nanoparticles

The rare-earth-doped nanoparticles composed of a rare earth doped $\beta\text{-NaY}_{0.78}\text{F}_4\text{:Yb}_{0.20}\text{Er}_{0.02}$ core nanoparticle surrounded by a layer of an undoped $\beta\text{-NaYF}_4$ shell were synthesized according to a method proposed in our previous work 21,31. In brief, 2 mL of $\text{Ln}-(\text{CF}_3\text{COO})_3\text{OM}$ solution (0.5 M) and 0.204 g of CF_3COONa were dissolved in 3.2 mL of ODE and 2.5 mL of OA at 120 °C for 30 min until a clear solution was formed. Under vigorous mixing, the mixture was next heated to ~330–340 °C at a ramp rate of ~20 °C/min for ~1 h in an Ar environment. Next, a precursor shell solution (without the rare-earth dopants) containing 0.204 g of CF_3COONa , 2 mL of $\text{Y}(\text{CF}_3\text{COO})_3\text{OM}$ solution (0.5 M), and 3 mL of OA was added drop-wise to enable the formation of core-shell heterostructures. The resultant solution was then cooled to room temperature after additional stirring for 30 min in Ar. The as-synthesized RENPs were washed 3 times in ethanol (~40 mL) by centrifugation at 7750 g for 10 min before resuspension of the particles in water for freeze-drying (VirTis BenchTop Pro with Omnitronics, England, 4 Pa operating pressure and

condenser temperature of $-62\text{ }^{\circ}\text{C}$) to obtain RENPs in the powder form (yield: $\sim 120\text{ mg}$) for further characterization.

5.5.4. Synthesis of PEI-Coated RENPs

Typically, 30 mg of RENPs were dispersed in 1 mL of chloroform followed by the addition of 5 mL of PEI (20 mg/mL ethanol solution). The mixture was stirred for 72 h at $25\text{ }^{\circ}\text{C}$, and the RENPs@PEI were subsequently separated by centrifugation at 7750g for 10 min, at which point the clear supernatant containing excess PEI was discarded and the pellet was redispersed with ethanol. After further washing of the particles with ethanol (three times total), any unbound PEI was removed using the dialysis method with regenerated cellulose dialysis tubing (Spectra Por 34/22 mm, 50 000 MWCO, Cole-Parmer) for 72 h. The aqueous suspension of RENPs@PEI was freeze-dried (VirTis BenchTop Pro with Omnitronics, England, 4 Pa operating pressure and condenser temperature of $-62\text{ }^{\circ}\text{C}$) to obtain the particles in powder form for further characterization.

5.5.5. Synthesis of Yb³⁺ Impregnated RENPs

PEI-coated RENPs ($\sim 100\text{ mg}$, RENPs@PEI) were dispersed in an aqueous solution of ytterbium(III) acetate tetrahydrate (10 or 30 μmol) in 100 mL of water. The solution was stirred for 24 h and separated by centrifugation at 7750g for 15 min. After further washing of the particles with ethanol (three times), any Yb that was not absorbed was removed using the dialysis method with regenerated cellulose dialysis tubings. The aqueous suspension of RENPs@PEI was freeze-dried (VirTis BenchTop Pro with Omnitronics, England, 4 Pa operating pressure and condenser temperature of $-62\text{ }^{\circ}\text{C}$) to obtain the particles in powder form for further characterization.

5.5.6. Material Characterization

5.5.6.1. Size, Morphology, and Crystal Structure

The XRD profiles of powders were measured using a D8 Eco Advance powder diffractometer (Bruker AXS Inc., Madison, WI) equipped with a Cu K α source having a wavelength of 1.54 Å (step size of 0.02°, step duration of 0.5 s, working voltage of 40 kV, and working current of 25 mA). The 2 θ scan range is from 20 to 80°. The estimated grain sizes were calculated using the Scherrer equation and the width of the characteristic peaks for a given crystal phase. The hexagonal-phase diffractogram pattern (JCPDS no. 00-028-1192) was used as a reference for the samples.

The sizes and morphologies of the powders were measured using a field emission scanning electron microscope (JSM-7600F, JEOL Ltd., Japan) equipped with a secondary electron detector using the following parameters: voltage of 5 kV, current of 6 A, and working distance of 8 mm. Particle size distribution were evaluated from the SEM micrographs using ImageJ.

5.5.6.2. Surface Chemical Functional Groups and Characteristics

The hydrodynamic diameter and ζ potential of the samples (5 mg/mL in deionized water) were determined by DLS (NanoBrook Omni, Brookhaven Instruments Corp., Long Island, NY) with a 632 nm wavelength laser and a scattering angle of 90° in aqueous solution. The chemical functional groups of the as-prepared powders were evaluated from the FTIR spectra that were measured using the Bruker infrared spectrophotometer (Bruker Vertex 70, Bruker Optics) coupled with the attenuated total reflection module that is equipped with a diamond crystal from 4000 to 400 cm⁻¹ with a step size of 4 cm⁻¹ and is averaged over 256 scans.

To determine the amount of organic molecules or polymers coated around the inorganic nanoparticles, thermogravimetric analysis (TGA) was performed using a thermogravimetric

analyzer (TGA Q50, TA Instruments, New Castle, DE) with a mass flow rate of 40 mL/min and a heating rate of 20 °C/min from 25 to 1000 °C in a nitrogen environment.

5.5.6.3. Optical Properties

The absorption spectra of a fixed amount of powders (~150 mg) that were pressed into a pellet of ~2–3 mm thick (i.e., fixed path length) were measured using a fiber-based spectrometer that connects the deuterium halogen balanced light source (AVANTES AvaLight-DHS, 239 μW, 200 to 2500 nm, Netherlands, Europe) to an 80 mm integrating sphere (AvaSphere, sample port diameter of 15 mm) via a fused silica optical fiber (2 m, numerical aperture of 0.22, and core diameter of 600 μm). The detector port is next connected via another fused silica optical fiber (1 m, numerical aperture of 0.22, and core diameter of 400 μm) to a visible Ocean Optics spectrometer (USB4000, Ocean Optics Inc., Newark, NJ). The scan measurements are completed from 400–1050 nm with step size of 2 nm and an integration time of 100 ms per scan.

Steady-state emission spectra were measured upon excitation with a 975 nm continuous wave laser (CNI MDL-III-975, Changchun New Industries Optoelectronics Tech. Co. Ltd.) using a FLS980 fluorescence spectrometer (Edinburgh Instruments Ltd.) equipped with a visible detector (Hamamatsu R928P) and near-infrared detector (Hamamatsu H1033A-75). For both visible and infrared emission measurements, a step size of 2 nm with a dwell time of 0.2 s is used for the laser power of 20 mW, having a spot size of 19.63 mm². The powder samples (~20 mg) were packed in demountable Spectrosil far UV quartz Type 20 cells (Starna Cells, Inc., Atascadero, CA) with a fixed 0.5 mm path length for emission collection. The integrated areas of the steady spectra for the green (i.e., 500–600 nm), red (i.e., 600–700 nm), and infrared (i.e., 1450–1650 nm) emission regions were determined using the integration function on OriginLab Pro. To measure the time-resolved luminescence spectrum, the excitation source is modulated using an electronic pulse modulator to obtain excitation pulse at pulse duration of 10 μs with a repetition

rate of 10 Hz. To estimate the decay constants, especially decay time (τ), the decay curves were fitted to a double-exponential equation:

$$I(t) = A_1 \times \exp\left(-\frac{t}{\tau_1}\right) + A_2 \times \exp\left(-\frac{t}{\tau_2}\right) \quad (1)$$

where $I(t)$ is the decaying intensity for the 1530 nm emission, A_1 and A_2 are the exponential prefactors, and τ_1 and τ_2 are the fitted decay times. The average decay time constant, τ_{ave} , can be determined using:

$$\tau_{ave} = \frac{A_1\tau_1^2 + A_2\tau_2^2}{A_1\tau_1 + A_2\tau_2} \quad (2)$$

5.5.7. Cellular Toxicity and Intracellular Distribution Studies

5.5.7.1. MTT Cell-Proliferation Assay

Toxicity to cells was determined as a function of reduction in the proliferation and viability of cells. Briefly, MDA-MB-231 cells were grown in Dulbecco's modified Eagle media (DMEM; Life Technologies) supplemented with 10% v/v fetal bovine serum and 1% v/v penicillin–streptomycin (Life Technologies). The cells were cultured in a humidity-controlled chamber at 37 °C in 5% CO₂. MDA-MB-231 cells were seeded at a density of 5000 cells per well in 96-well plates. Following seeding, the cells were incubated at 37 °C in 5% CO₂ overnight. Cells were treated with the varying doses of nanoparticles (0–625 µg/mL) in supplemented DMEM media and proliferation assessed at varying time-points (24–72 hr). An MTT assay (Thermo Scientific) was performed per the manufacturer's instructions. Cells treated with nanoparticles were supplemented at the end point with 100 µL of fresh media and 10 µL of MTT solution. After incubation for 4 h at 37 °C and 5% CO₂, the media and MTT solution were aspirated, and sodium dodecyl sulfate in 0.01 M hydrochloric acid was added to dissolve the formazan crystals (in the MTT solution) and incubated for an additional 4 h. Colorimetric readings at 570 nm were

recorded using a microplate reader. Background absorbance was subtracted from non-treated control cell samples.

5.5.7.2. Localization of RENPs@PEI Nanoparticles on Cells

MDA-MB-231 and MCF-7 cells were incubated overnight with RENPs@PEI, RENPs@PEI-Yb10, and RENPs@PEI-Yb30 solutions, at a concentration of 125 $\mu\text{g}/\text{mL}$ in supplemented DMEM media, to allow for particle uptake. Prelabeled cells were trypsinized and reseeded in an 8-well Permax slide LabTek chamber slide at a cell density of 20 000 cells per well for imaging. Following overnight incubation cells in slides were washed and fixed with 4% paraformaldehyde and counterstained with Prolong Gold Antifade with 4'-6-diamidino-2-phenylindole. Imaging was performed using an in-house line scanning SWIR confocal microscope with a 40 \times objective and 609 nm emission filter.

5.5.8. Biodistribution and Toxicity of RENPs *in vivo*

5.5.8.1. *In vivo* Imaging Studies

Imaging studies were conducted using female homozygous nude mice (Taconic, Hudson, NY). All animal studies were approved by the Institutional Review Board for the Animal Care and Facilities Committee of Rutgers University and performed in accordance with institutional guidelines on animal handling.

5.5.8.2. Whole-Animal SWIR Imaging

A small-animal SWIR imaging system was assembled in-house. Mice were fully anesthetized using 2% isoflurane (Butler-Schein, Dublin, OH) and were continuously scanned with a collimated 980 nm laser (1.7 W). SWIR emission was detected with an InGaAs camera (Sensors Unlimited, Princeton, NJ) equipped with a pair of 1020 nm long-pass filters, a band-pass 1538/82 nm filter (Semrock, Rochester, NY), and a 25 mm focal length SWIR lens (StingRay Optics, Keene, NH). The system is capable of real-time animal imaging with an exposure time of 33

microseconds per frame. Images were acquired as video files and processed for quantitative analysis using custom Matlab scripts. Animals injected with 200 μ L of RENPs@PEI intravenously were imaged at 20 fps.

5.5.8.3. Shortwave Infrared Image Analysis

SWIR emission from animals was collected before and after the injection of nanoparticles in the form of a video file in the .bin format. A white-light image of the animal for both time points was taken and labeled according to the condition. The .bin file conversion of the Matlab file was used to process the video files to extract the maximum pixel values from each frame of the video, and the result was saved as a .tiff image file. Image processing was done through the manual selection of regions of interest (ROI). ROIs corresponding to the desired organ were selected using anatomical landmarks present in background images. These ROIs were then applied to the associated infrared image, and the mean SWIR signal intensity for the region was calculated. These values were then used to perform statistical analysis to compare SWIR signals from each ROI between tumor-bearing and healthy control groups.

5.5.9. Biodistribution, Clearance, and Toxicology Studies

Athymic nude mice were injected with 6.25 mg/kg of RENPs@PEI. SWIR imaging was performed as described above to visualize the accumulation of nanoparticles in various organs. For clearance studies, the primary organs of clearance (liver, lung, kidney, and spleen) were harvested at 0 h, 1 day, 3 days, and 7 days post-injection and imaged *ex vivo* using the SWIR imaging system. *Ex vivo* analysis of organs of clearance was performed by fixing organs in 10% neutral-buffered formalin overnight followed by incubation in 70% ethanol prior to processing. Tissues were then embedded in paraffin and 5 μ m sections prepared. Tissue sections were deparaffinized, rehydrated, and stained with hematoxylin and eosin.

5.5.10. Resolution of Tumor lesions Using RENPs *in vivo*

5.5.10.1. Resolution of the Lowest Cell Cluster *in vitro*

Briefly, MDA-MB-231 cells were incubated with RENPs@PEI nanoparticles for 18h at 37 °C with 5% CO₂. Subsequently, treated cells were trypsinized and centrifuged at 1500g for 5 min. The cell pellet was washed once with PBS and, following centrifugation, analyzed by SWIR imaging, in which SWIR emissions were detected with the setup discussed above.

5.5.10.2. Detection of Lung Metastatic Lesions *in vivo*

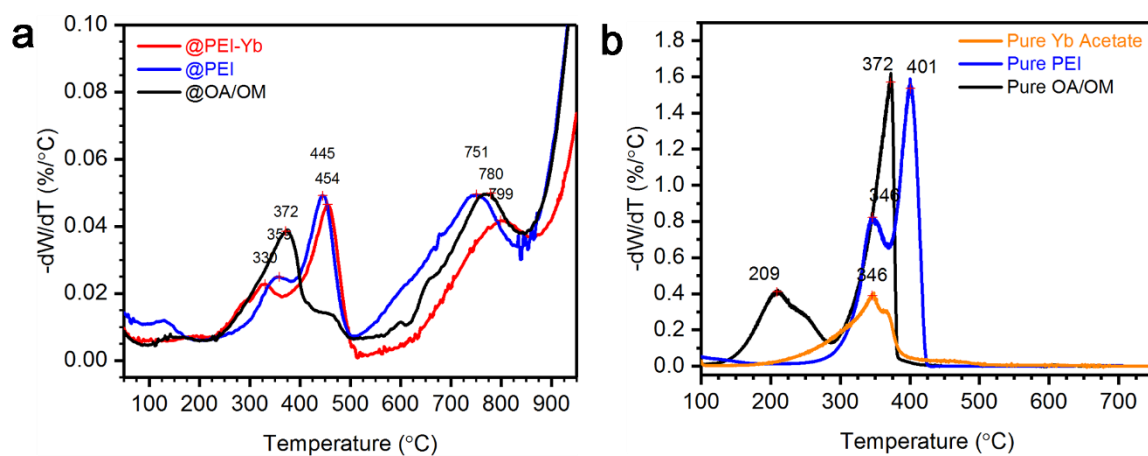
Female homozygous athymic nude mice were obtained from Taconic Laboratories (Hudson, NY) at 3–4 weeks of age and were injected via tail vein with MDA-MB-231 cells in an established model of lung metastasis. Animals were treated with a bolus intravenous injection of RENPs@PEI at a dose of 6.25 milligrams per kilogram of body weight and imaged using the SWIR imaging system described above to determine the ability of the nanoprobe to resolve tumor lesions. The animals were sacrificed, and their organs were excised and imaged via SWIR imaging *ex vivo* to determine particle biodistribution and localization to lesion sites.

5.5.11. Gene-Therapy Applications of RENPs: In Situ Hybridization of Oligonucleotides Conjugated to RENPs@PEI

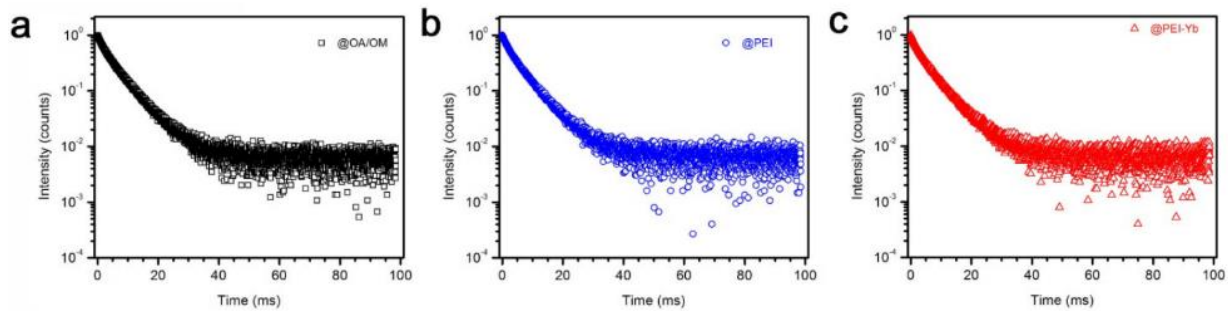
ES2 cells were grown in Labtek 8-well chamber slides and treated with doxycycline (100 ng/mL) for 4 h. Cells were fixed with 4% paraformaldehyde for 10 min at room temperature and permeabilized with 70% ethanol. Hybridization was performed using a Stellaris RNA Fish reagent kit. Briefly, permeabilized cells were incubated in wash buffer A containing formamide for 5 min followed by treatment with either DNA alone or RENPs@PEI-conjugated DNA in hybridization buffer containing formamide. Treated cells were incubated at 37 °C overnight in a humidified chamber. The DNA probe was FILIP1L oligonucleotide expressing 6-FAM with

excitation at 492 nm and emission at 517 nm. Following incubation, cells were washed and counter-stained with Hoechst for nuclear staining.

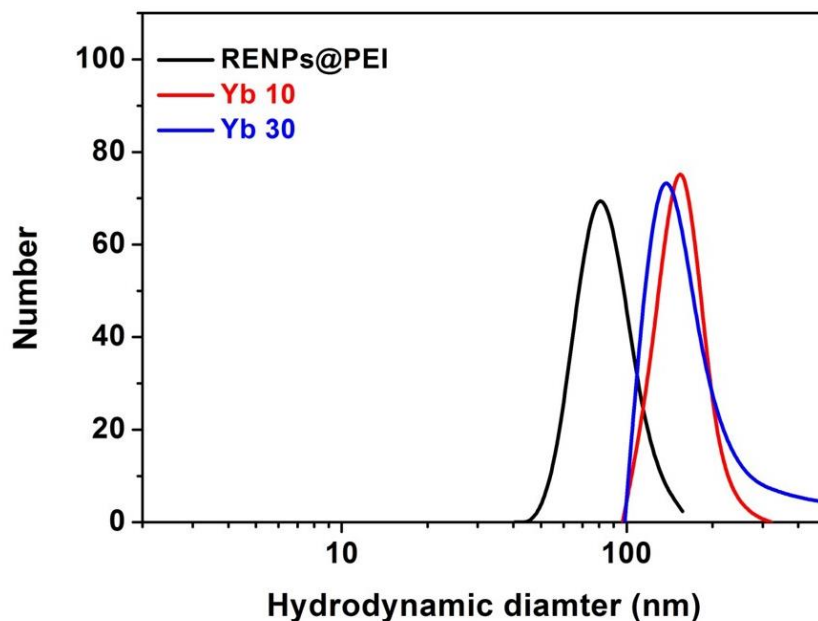
5.6. Supplementary Figures



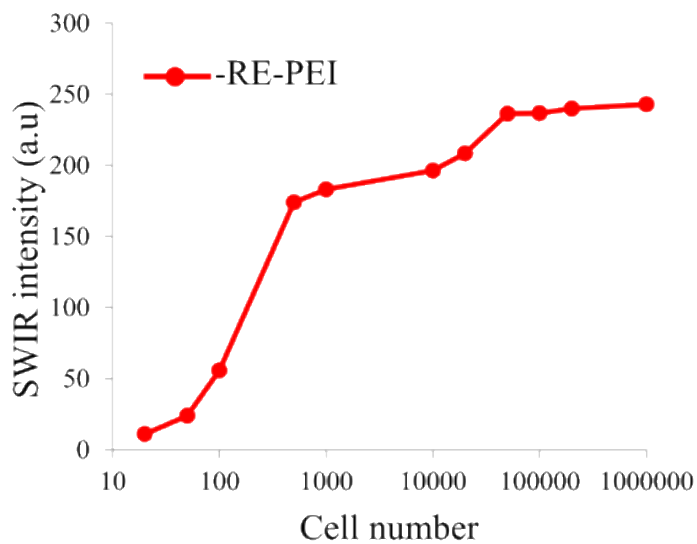
Supplementary Figure 5.1 - Inflection points calculated from the first derivative weight loss of the TGA measurement data for (a) various as-synthesized and surface-modified RENPs and (b) pure solvent or polymers. This is used to identify the characteristic decomposition temperature of various organic species in a N₂ environment.



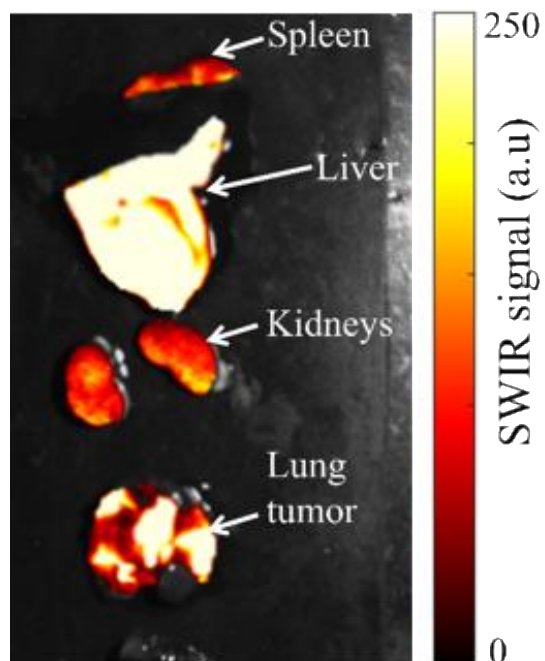
Supplementary Figure 5.2 - Time resolved lifetime measurements of the IR emission ($^4I_{13/2} \rightarrow ^4I_{15/2}$) for as synthesized and surface-modified RENPS, which is used to characterized the effective energy transfer interactions between Yb-Er or Er-Er with quenching transitions, if any.



Supplementary Figure 5.3 - Hydrodynamic diameter of PEI coated particles, RENPs@PEI was lower than that of Yb acetate impregnated RENPs, such as RENPs@PEI-Yb10 (Yb 10) and RENPs@PEI-Yb30 (Yb 30), suggesting that smaller agglomerates and more tightly bonded clusters of RENPs@PEI were present in solution. These tightly bonded clusters were most likely formed by hydrogen bonding between the high densities of primary amines available on the RENPs@PEI surfaces due to the collapsed chain conformation of PEI. With the reduction of available amine groups due to the impregnation of Yb acetate, the extent of hydrogen bonding between the RENPs@PEI-Yb particles would be much lower, leading to larger clusters that are not as tightly bonded.



Supplementary Figure 5.4 - RENP@PEI show increased resolution of smaller cell clusters, where a cluster of ~50 cells could reliably be detected using our SWIR imaging system.



Supplementary Figure 5.5 - *Ex vivo* SWIR imaging of organs of accumulation and clearance shows accumulation of particles mainly in the liver (implicating the reticuloendothelial system as a possible route of clearance) and in the lung tumors.

Pure OA		Pure OM		Pure PEI		RENP@OA/OM		RENP@PEI		RENP@PEI-Yb	
Wavenumber (cm ⁻¹)	Assignment	Wave number (cm ⁻¹)	Assignment	Wavenumber (cm ⁻¹)	Assignment	Wavenumber (cm ⁻¹)	Assignment	Wavenumber (cm ⁻¹)	Assignment	Wavenumber (cm ⁻¹)	Assignment
		3364	RNH ₂ , N-H stretch	3275	RNH ₂ , N-H stretch	3343	O-H or N-H stretch	3287	N-H stretch(H bond)	3418	N-H stretch
3003	C=C stretch	3005	+NH ₃ stretch			2968	C=C stretch				
2922	C-H stretch	2922	C-H stretch	2933	C-H stretch	2926	C-H stretch	2922	C-H stretch	2926	C-H stretch
2853	C-H stretch	2853	C-H stretch	2810	C-H stretch	2856	C-H stretch	2853	C-H stretch	2855	C-H stretch
2669	O-H stretch of COOH										
				2121	R ₂ NH ₂ ⁺ , R ₃ NH ⁺						
1709	C=O stretch of COOH					1651	COO ⁻ stretch or CONH	1699	COO ⁻ stretch or CONH	1680	COO ⁻ stretch or CONH
		1585	RNH ₂ , N-H bending	1589	RNH ₂ , N-H bending	1553	RNH ₂ , N-H bending	1562	RNH ₂ , N-H bending	1558	RNH ₂ , N-H bending
1462	COO ⁻ stretch	1464	+NH ₃ bending	1456	+NH ₃ bending	1466	COO ⁻ stretch & +NH ₃ bending	1464	+NH ₃ bending	1462	+NH ₃ bending
1412	COO ⁻ stretch					1408	COO ⁻ stretch	1416	COO ⁻ stretch	1414	COO ⁻ stretch
		1377, 1342, 1313	C-H bending	1352	C-H bending	1379, 1340, 1304	C-H bending				
1283, 1246	C-C stretch			1296	C-H bending			1279, 1204	C-C stretch	1205	C-C stretch
1119, 1088	C-C stretch	1157, 1070	C-C stretch	1109, 1045	C-C stretch	1161, 1128, 1107	C-C stretch			1101	C-C stretch

Supplementary Table 5.1 - Assignment of the FTIR absorption peaks with the characteristic vibration modes (e.g., stretching or bending) of chemical functional groups available on the molecules such as oleic acid (OA), oleylamine (OM) and polyethyleneimine (PEI).

CHAPTER 6

CONCLUSIONS AND FUTURE DIRECTIONS

6.1 Conclusions

Cancer, a molecularly dynamic disease, when metastasized to secondary organs can lead to poor survival rates and recurrence. Due to the vast variation among (inter-tumor) and within (intra-tumor) patients there is a dire need to develop molecularly precise diagnostic strategies capable of early stage detection. In this work, we used the biocompatible and disease targeting features of RE nanoparticles to develop an *in vivo* imaging platform to image challenging disease states in a preclinical setting. The dissertation lays the groundwork for addressing current problems in cancer imaging: 1. Non-invasive detection of micro-lesions via development of targeted nanoparticles to specific molecular subtype; 2. Detection of lesions in challenging metastatic sites earlier than current conventional imaging systems; 3. Identification of molecular phenotype of tumors using multi-colored nanoparticles and 4. Validation of alternative polymer coating to facilitate multi-functional nanoparticle system capable of imaging and gene delivery.

6.1.1. CXCR-4 targeted, Short Wave Infrared (SWIR) emitting nanoprobes for enhanced deep tissue imaging and micro metastatic cancer lesion detection

Metastasis in breast cancer is difficult to treat in cases with the presence of micro-metastatic cell populations that possess variable phenotype compared to parent tumor. Chapter 2 of this dissertation focuses on modifying the ReANCs to actively target and discern micro-metastatic lesions *in vivo*. The albumin coating for these nanoparticles allows for loading ligands targeted to specific cellular receptors. We hypothesized that the targeted nanoparticles will lead to the development of a non-invasive imaging tool capable of discerning deep tissue micro-lesions based on their molecular phenotype. Breast cancer cells with higher receptor expression show increased localization of the targeted nanoparticles both *in vitro* and *in vivo*. The increased uptake

of targeted nanoparticles led to the increase of SWIR signal from receptor positive tumors in mice. The most significant observation of this study is that targeted nanoparticles were able to detect 18.9 mm³ micro lesions at ~1 cm deep. This increased accumulation at the lesion can be beneficial for early detection and potential clinical translation to monitor tumor progression.

6.1.2. Surveillance nanotechnology for multi-organ cancer metastases

The dynamics of cancer metastasis progression and response to therapy remain poorly understood due to limitations of conventional imaging modalities. In chapter 3 of this dissertation, we focused on analyzing the use of ReANCs as a non-invasive optical tool to resolve multi-organ metastasis specifically in challenging spaces like the bone marrow. Via passive accumulation, optimally sized ReANCs were able to home to lesions in the bone space as studied using *in vivo* orthotopic and experimental metastasis models of breast cancer. The ReANCs showed increased localization to the bone lesions 5 weeks post inoculation, compared to healthy control animals, whereas, conventional imaging modalities like MRI and CT did not reveal any bone deformities even at the end point of week 9. Most notably, ReANCs were able to discern bone lesions two weeks earlier than contrast-enhanced MRI.

Intrinsic to the nanoprobe detection of multi-organ metastases is the design of multivariate targeting mechanisms. In our study of multi-organ metastasis, the use of both the active and passive targeting approach was key to detect lesions in both bone and adrenal spaces.

Unfunctionalized ReANCs detected the bone lesions effectively by accumulation via EPR effect.

In comparison, adrenal lesions showed poor localization of ReANCs while having pronounced localization of CXCR4 targeted fReANCs resolving tumor as small as 8mm³. With this study, we have demonstrated the application potential of this imaging modality in several *in vivo* breast cancer models.

6.1.3. Cancer-specific Short-wave infrared emitting multi-colored nanoprobes for *in vivo* imaging

In addition to metastasis, another critical limitation in the development of effective targeted therapies is intratumor heterogeneity. Understanding the presence and extent of each cancer subtype can streamline development of personalized therapies and reduce risk of cancer relapse. In chapter 4, we have developed a proof of concept multi-color imaging platform by engineering biomarker specific nanoprobes to discern corresponding cellular subsets. We used the distinct SWIR spectra of three different biomarker-specific nanoprobes for macroscopic *in vivo* imaging. Additionally, we incorporated conventional fluorophores in the nanoprobes enabling imaging in the visible region for *in vitro* and *ex vivo* validation. In this study, we demonstrate that functionalized nanoprobes target biomarker specific MCF7 (overexpressing CXCR4) and 4175 (overexpressing Cav-1) tumors *in vivo* showing increased accumulation as compared to unfunctionalized counterparts. Additionally, in a bilateral tumor model, we showed the ability to exclusively target the AMD-3100 tagged functionalized probes to MCF7 tumors and daidzein tagged probes to 4175 tumors. The combined findings indicate the promise for the multi-colored imaging biomarker platform to detect tumor populations with distinct biomarker expression.

6.1.4. Surface-Modified Shortwave-Infrared-Emitting Nanophotonic Reporters for Gene-Therapy Applications

The efficiency of nanoparticles as biological delivery agents has paved way for the use of nanoparticles for delivery of therapeutic drugs and diagnostic contrast agents. Furthermore, with more discoveries being made about biomarkers associated with lesions, addition of targeting ligand will increase localization at target site and reduce off target effects. In chapter 5, we explore a modification of our nanoparticles system with ability to target lesions and carry payloads. With new surface coatings of PEI, PEI-Yb30 and PEI0-Yb10, we showed that the nanoparticles showed limited toxicity in cells. We also observed that the RE@PEI nanoparticles

are well tolerated in mice with similar clearance patterns as ReANCs. Additionally, in a lung metastases model of breast cancer we saw that the RENPs@PEI enabled the successful detection of lung lesions at superior resolution. The genetic cargo delivery ability of RE@PEI system was tested in FILIP1L overexpressing cells to demonstrate increased efficiency of delivery of FILIP1L oligo when conjugated with the nanoparticles. Of note, this study exploits not only the surface modification of RENPs for genetic cargo but also the SWIR emission of RENPs that will allow for deep-tissue imaging and gene-therapy monitoring at target sites.

6.2. Future Directions

6.2.2. Theranostic particles

Molecularly tailored imaging techniques²⁷⁵ paired with a therapeutic will benefit by providing additional crucial information on pharmacokinetics at lesion site and reduce the unwanted side effects that could occur due to accumulation in off-target sites. The effective delivery mechanism of nanoparticles based on physical and chemical attributes coupled with its multi-functional capabilities allow for design modification, facilitating delivery of both therapeutic moiety and diagnostic agent at target site. The nanoparticle design for effective therapeutic delivery can take advantage of the tumor microenvironment rich in proteases and incorporate drugs to be covalently linked using protease cleavable linkers, or design nanoparticles that can initiate photo ablation of tumors. The major challenge that will remain in the successful development of theranostic nanoparticles will be the balance between targeting ligand density for sufficient accumulation to ensure increased signal from target site while loading drug that will have a high therapeutic index for desired pharmacological effects.

Zevon et al. have previously explored loading of therapeutic agents on albumin nanocomposites. Curcumin, riluzole and a combination of both drugs were effectively loaded on albumin nanoparticles and the therapeutic effect on cancer cells was studied *in vitro*¹³⁸. Hence, physical

adsorption can be used for effective conjugation of drugs with loading concentrations modified to induce optimal cytotoxicity in cancer cells. Furthermore, chapters 2, 3 and 4 explore the modification of optical contrast agent bearing ReANCs with targeting ligands to show improved localization and retention at disease site. Utilizing the drug binding pockets of the albumin coating in ReANCs to add targeted ligands and therapeutic agents will be beneficial for targeted effect at lesion site. Future studies could focus on the use of doxorubicin along with corresponding targeting ligands as theranostics in breast or ovarian cancer. Balancing loading of therapeutic moiety and ligand on nanoparticles to achieve optimal specificity along with cytotoxic effects will be crucial in initial experiments. Once synthesized, the multifunctional system will have to be tested for localization and effect on tumor size in an *in vivo* model. The tumor size can be monitored via SWIR emission and validated with other imaging modalities like MRI or BLI.

The ability to deliver therapeutic payload with targeted precision and monitor the real-time delivery of the therapeutic cargo will be beneficial in understanding on-target accumulation levels and assessing off-target side effects for enabling informed therapeutic decision-making, which will be beneficial for effective clinical translation.

6.2.3. Nanoparticle guided immune surveillance

Immunotherapy, used to boost the body's natural response to cancer, is the new treatment paradigm used to developing cures for multiple cancer types. Several types of immunotherapy are being explored including: (i) PD1, PDL1 and CTLA4 as checkpoint inhibitors, (ii) adoptive cell transfer where cytotoxic T cells responding to tumors are extracted from patients, expanded *ex vivo* and induced back into the patients for better results and (iii) monoclonal antibodies used to mark tumors for enhanced recognition by the immune system. Although enhanced immune response has been observed with multiple cancers, there are still limited number of patients who see prolonged clinical benefits while vast majority of others remain clinically unresponsive.

Hence, there is a critical need to dynamically monitor the immune cell recruitment at tumor site and modify the treatment in real time.

The ReANC based imaging platform has displayed abilities of detecting smaller cell clusters *in vitro* and micro lesions *in vivo*. Leveraging the optical properties of ReANCs to detect minute cell clusters and the versatile targeting abilities would be crucial to identify immune dynamics at lesion site. Preliminary experiments in this project were done to explore the ability of ReANCs to target and track immune cells. ReANCs were functionalized with PD1/PDL1 small molecular inhibitor and used to treat splenocytes extracted from immunocompetent C57B6 mice. Functionalized ReANCs showed ~27% increase in uptake compared with unfunctionalized ReANCs as determined by flow cytometry analysis. The mouse splenocytes were pre-labelled with fReANCs and injected intraperitoneally into the animal, where the progression of the immune cells was observed through whole body SWIR imaging over 24 hrs. SWIR signal was detected *in vivo* to show the progression of the cells and eventual homing to the spleen *ex vivo*. (Figure 6.1).

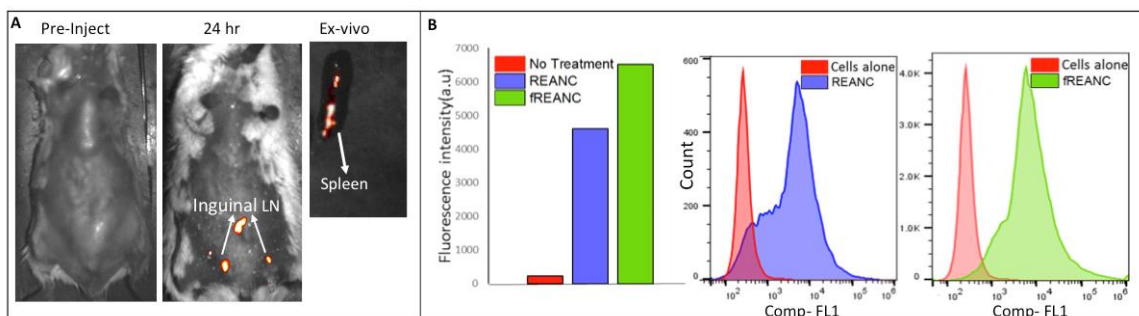


Figure 6.1- PD1-targeted REANCs illuminate T-cells *in vivo* and *ex vivo*. Tracking of ReANC labeled mouse splenocytes in lymph nodes in a syngeneic mouse following i.p injection. (A) SWIR imaging at 24 h revealed signal from cells homing to inguinal lymph nodes. *Ex vivo*, imaging shows SWIR signal from the spleen. (B) FACS data shows enhanced uptake of PD-1 targeted REANCs by splenocytes vis-à-vis REANCs and controls.

Future studies can focus on developing targeted ReANCs to CD8 T cells, to evaluate T cell recruitment at lesion site, using a CD8 peptide. The *in vitro* experiments could focus on T cells extracted from splenocytes of immunocompetent mice, to validate targeting ability of ReANCs. *In vivo* studies should focus on developing syngeneic mouse tumor models and monitor immune response to chemotherapy treatments. Additionally, using the multispectral aspect of ReANCs different populations of T cells like CD4 and Tregs can be evaluated to understand their individual and cumulative recruitment effect to tumors (**Figure 6.2**). Use of a non-invasive precision targeted system will be very beneficial in the field of immune-oncology not only to analyze effective immune response in patients, but also in examining efficacy of novel drugs in inducing an immune response in a preclinical setting.

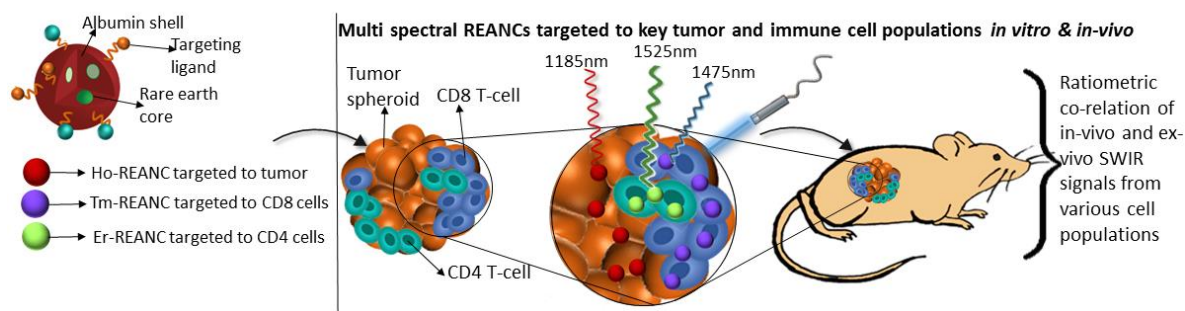


Figure 6.2: Workflow for the use of Rare earth probes for immune response monitoring: In future work rare earth based nanoparticles will be functionalized and administered *in vivo* to label distinct immune cell components within the tumor microenvironment. When illuminated, these probes will provide a composite snapshot of the immune microenvironment in real time.

APPENDIX

NIR - Near Infrared

SWIR - Short Wave Infrared

RENPs - Rare Earth nanoparticles

ReANCs - Rare Earth Albumin Nanocomposites

PEI - Polyethylenimine

BC - Breast Cancer

ER- Estrogen hormone receptor

PR - Progesterone Receptor

HER2 - Human Epidermal Growth Factor Receptor

FDA - Food and Drug Administration

TNBC - Triple Negative Breast Cancer

MRI - Magnetic resonance imaging

PET - Positron emission tomography

SPECT - Single-photon emission computed tomography

CT - Computed tomography

CE-MRI - Contrast-Enhanced MRI

IR - Infrared

OCT - Optical Coherence Tomography

DOT - Optical Tomography

FITC - Fluorescein

ICG - Indocyanine Green

NPs - Nanoparticles

UV - Ultraviolet

InGaAs - Indium Gallium Arsenide

PD - pharmacodynamics

PK – Pharmacokinetics

RES - Reticulo-endothelial system

VEGF-A - Vascular Endothelial Growth Factor

EPR - Enhanced Penetration and Retention

BBB - Blood Brain Barrier

PEG - Polyethylene Glycol

SWNTs - Single walled carbon nanotubes

ADMET - Absorption, Distribution, Metabolism and Elimination along with Toxicological issues

HSA - Human serum albumin

FcRn - Fc receptor

SPARC - Secreted Protein, Acidic and Rich in Cysteine

PEI – Polyethylenimine

fReANCs - functionalized ReANCs

DLS - Dynamic Light Scattering

SEM - Scanning electron microscopy

I.P- Intraperitoneal

CXCR4 - C-X-C chemokine receptor type4

BCA - Bicinchoninic Acid assay

ICP/MS - Inductively Coupled Plasma-Mass Spectrometry

BLI - Bioluminescence Imaging

H&E - Hematoxylin and Eosin

ADAM17 - ADAM metalloproteinase domain 17

JAM-A - Junctional adhesion molecule-A

EGFR - Epidermal growth factor receptor

MMP-3 -Matrix Metalloproteinase-3

EpCAM - Epithelial Cell Adhesion molecule

DMEM - Dulbecco's modified eagle medium

FA - Folic Acid

EDC - 1-ethyl-3-(3-dimethylaminopropyl) carbodiimide

CAV-1 - Caveolin-1

ROI - Regions Of Interest

OA - Oleic acid

OM - Oleylamine

IACUC - Institutional Animal Care and Use Committee

IEP - Isoelectric Point

FTIR – Fourier-transform infrared Spectroscopy

FILIP1L - Filamin A interacting protein 1 like

DOX – Doxycycline

FAM – Carboxyfluorescein

TGA - Thermogravimetric analysis

CHAPTER 7

REFERENCES

- 1 Cancer Facts - All Cancers- <http://gco.iarc.fr/today/data/factsheets/cancers/39-All-cancers-fact-sheet.pdf>. *Globocan* (2018).
- 2 National Cancer Institute - <https://www.cancer.gov/about-cancer/understanding/statistics>. (2018).
- 3 Pollack, E. S., Nomura, A. M., Heilbrun, L. K., Stemmermann, G. N. & Green, S. B. Prospective study of alcohol consumption and cancer. *N Engl J Med* **310**, 617-621, doi:10.1056/NEJM198403083101003 (1984).
- 4 Allen, N. E. *et al.* Moderate alcohol intake and cancer incidence in women. *J Natl Cancer Inst* **101**, 296-305, doi:10.1093/jnci/djn514 (2009).
- 5 Flegal, K. M., Kit, B. K., Orpana, H. & Graubard, B. I. Association of all-cause mortality with overweight and obesity using standard body mass index categories: a systematic review and meta-analysis. *JAMA* **309**, 71-82, doi:10.1001/jama.2012.113905 (2013).
- 6 Kitahara, C. M. *et al.* Association between class III obesity (BMI of 40-59 kg/m²) and mortality: a pooled analysis of 20 prospective studies. *PLoS Med* **11**, e1001673, doi:10.1371/journal.pmed.1001673 (2014).
- 7 National Cancer Institute - "What is cancer?". (2018).
- 8 Poste, G. & Fidler, I. J. The pathogenesis of cancer metastasis. *Nature* **283**, 139-146 (1980).
- 9 Talmadge, J. E. & Fidler, I. J. AACR centennial series: the biology of cancer metastasis: historical perspective. *Cancer Res* **70**, 5649-5669, doi:10.1158/0008-5472.CAN-10-1040 (2010).
- 10 Paget, S. The distribution of secondary growths in cancer of the breast. 1889. *Cancer Metastasis Rev* **8**, 98-101 (1989).
- 11 Fidler, I. J. & Poste, G. The "seed and soil" hypothesis revisited. *Lancet Oncol* **9**, 808, doi:10.1016/S1470-2045(08)70201-8 (2008).
- 12 Allison, K. H. & Sledge, G. W. Heterogeneity and cancer. *Oncology (Williston Park)* **28**, 772-778 (2014).
- 13 Fisher, R., Pusztai, L. & Swanton, C. Cancer heterogeneity: implications for targeted therapeutics. *Br J Cancer* **108**, 479-485, doi:10.1038/bjc.2012.581 (2013).
- 14 Dagogo-Jack, I. & Shaw, A. T. Tumour heterogeneity and resistance to cancer therapies. *Nat Rev Clin Oncol* **15**, 81-94, doi:10.1038/nrclinonc.2017.166 (2018).
- 15 MSKCC. What is tumor heterogeneity?- <https://www.mskcc.org/blog/what-tumor-heterogeneity>. (2014).
- 16 Esposito, A., Criscitiello, C., Locatelli, M., Milano, M. & Curigliano, G. Liquid biopsies for solid tumors: Understanding tumor heterogeneity and real time monitoring of early resistance to targeted therapies. *Pharmacol Ther* **157**, 120-124, doi:10.1016/j.pharmthera.2015.11.007 (2016).
- 17 Khoo, B. L. *et al.* Liquid biopsy and therapeutic response: Circulating tumor cell cultures for evaluation of anticancer treatment. *Sci Adv* **2**, e1600274, doi:10.1126/sciadv.1600274 (2016).
- 18 Levitin, H. M., Yuan, J. & Sims, P. A. Single-Cell Transcriptomic Analysis of Tumor Heterogeneity. *Trends Cancer* **4**, 264-268, doi:10.1016/j.trecan.2018.02.003 (2018).

- 19 Gerlinger, M. *et al.* Intratumor heterogeneity and branched evolution revealed by multiregion sequencing. *N Engl J Med* **366**, 883-892, doi:10.1056/NEJMoa1113205 (2012).
- 20 Joung, J. G. *et al.* Genomic Characterization and Comparison of Multi-Regional and Pooled Tumor Biopsy Specimens. *PLoS One* **11**, e0152574, doi:10.1371/journal.pone.0152574 (2016).
- 21 http://www.breastcancer.org/symptoms/understand_bc/statistics.
- 22 Ellsworth, R. E., Blackburn, H. L., Shriver, C. D., Soon-Shiong, P. & Ellsworth, D. L. Molecular heterogeneity in breast cancer: State of the science and implications for patient care. *Semin Cell Dev Biol* **64**, 65-72, doi:10.1016/j.semcdb.2016.08.025 (2017).
- 23 clinic, M. Breast cancer types: <https://www.mayoclinic.org/diseases-conditions/breast-cancer/in-depth/breast-cancer/art-20045654>. (2018).
- 24 Nemoto, T. *et al.* Management and survival of female breast cancer: results of a national survey by the American College of Surgeons. *Cancer-Am Cancer Soc* **45**, 2917-2924 (1980).
- 25 Stages of breast cancer.
- 26 Dawood, S., Broglio, K., Ensor, J., Hortobagyi, G. N. & Giordano, S. H. Survival differences among women with de novo stage IV and relapsed breast cancer. *Ann Oncol* **21**, 2169-2174, doi:10.1093/annonc/mdq220 (2010).
- 27 Dawood, S. *et al.* Differences in Survival Among Women With Stage III Inflammatory and Noninflammatory Locally Advanced Breast Cancer Appear Early A Large Population-Based Study. *Cancer-Am Cancer Soc* **117**, 1819-1826, doi:10.1002/cncr.25682 (2011).
- 28 Manders, K. *et al.* Clinical management of women with metastatic breast cancer: a descriptive study according to age group. *Bmc Cancer* **6**, doi:Artn 179 10.1186/1471-2407-6-179 (2006).
- 29 Plunkett, T. A., Smith, P. & Rubens, R. D. Risk of complications from bone metastases in breast cancer: implications for management. *Eur J Cancer* **36**, 476-482, doi:Doi 10.1016/S0959-8049(99)00331-7 (2000).
- 30 Goldhirsch, A. *et al.* Strategies for subtypes--dealing with the diversity of breast cancer: highlights of the St. Gallen International Expert Consensus on the Primary Therapy of Early Breast Cancer 2011. *Ann Oncol* **22**, 1736-1747, doi:10.1093/annonc/mdr304 (2011).
- 31 Cancer Genome Atlas, N. Comprehensive molecular portraits of human breast tumours. *Nature* **490**, 61-70, doi:10.1038/nature11412 (2012).
- 32 Molecular Subtypes of Breast Cancer
:<https://www.breastcancer.org/symptoms/types/molecular-subtypes> (2016).
- 33 Cheang, M. C. *et al.* Ki67 index, HER2 status, and prognosis of patients with luminal B breast cancer. *J Natl Cancer Inst* **101**, 736-750, doi:10.1093/jnci/djp082 (2009).
- 34 Vallejos, C. S. *et al.* Breast cancer classification according to immunohistochemistry markers: subtypes and association with clinicopathologic variables in a peruvian hospital database. *Clin Breast Cancer* **10**, 294-300, doi:10.3816/CBC.2010.n.038 (2010).
- 35 American Cancer society: <https://www.cancer.org/cancer/breast-cancer/treatment/hormone-therapy-for-breast-cancer.html#references>. (2017).
- 36 Osborne, C. K. Tamoxifen in the treatment of breast cancer. *N Engl J Med* **339**, 1609-1618, doi:10.1056/NEJM199811263392207 (1998).

- 37 Davies, C. *et al.* Long-term effects of continuing adjuvant tamoxifen to 10 years versus stopping at 5 years after diagnosis of oestrogen receptor-positive breast cancer: ATLAS, a randomised trial. *Lancet* **381**, 805-816, doi:10.1016/S0140-6736(12)61963-1 (2013).
- 38 Howell, A. *et al.* Fulvestrant versus anastrozole for the treatment of advanced breast carcinoma: a prospectively planned combined survival analysis of two multicenter trials. *Cancer-Am Cancer Soc* **104**, 236-239, doi:10.1002/cncr.21163 (2005).
- 39 Robertson, J. F. *et al.* Fulvestrant versus anastrozole for the treatment of advanced breast carcinoma in postmenopausal women: a prospective combined analysis of two multicenter trials. *Cancer-Am Cancer Soc* **98**, 229-238, doi:10.1002/cncr.11468 (2003).
- 40 Slamon, D. J. *et al.* Human breast cancer: correlation of relapse and survival with amplification of the HER-2/neu oncogene. *Science* **235**, 177-182 (1987).
- 41 Mitri, Z., Constantine, T. & O'Regan, R. The HER2 Receptor in Breast Cancer: Pathophysiology, Clinical Use, and New Advances in Therapy. *Chemother Res Pract* **2012**, 743193, doi:10.1155/2012/743193 (2012).
- 42 Atri, M. New technologies and directed agents for applications of cancer imaging. *J Clin Oncol* **24**, 3299-3308, doi:10.1200/JCO.2006.06.6159 (2006).
- 43 Naumova, A. V., Modo, M., Moore, A., Murry, C. E. & Frank, J. A. Clinical imaging in regenerative medicine. *Nat Biotechnol* **32**, 804-818, doi:10.1038/nbt.2993 (2014).
- 44 Hillman, B. J. Introduction to the special issue on medical imaging in oncology. *J Clin Oncol* **24**, 3223-3224, doi:10.1200/JCO.2006.06.6076 (2006).
- 45 Fass, L. Imaging and cancer: a review. *Mol Oncol* **2**, 115-152, doi:10.1016/j.molonc.2008.04.001 (2008).
- 46 Kumar, S., Mohan, A. & Guleria, R. Biomarkers in cancer screening, research and detection: present and future: a review. *Biomarkers* **11**, 385-405, doi:10.1080/13547500600775011 (2006).
- 47 Smith, J. J., Sorensen, A. G. & Thrall, J. H. Biomarkers in imaging: realizing radiology's future. *Radiology* **227**, 633-638, doi:10.1148/radiol.2273020518 (2003).
- 48 Reynolds, J. S. *et al.* Imaging of spontaneous canine mammary tumors using fluorescent contrast agents. *Photochem Photobiol* **70**, 87-94 (1999).
- 49 Yang, M. *et al.* Whole-body optical imaging of green fluorescent protein-expressing tumors and metastases. *Proc Natl Acad Sci U S A* **97**, 1206-1211 (2000).
- 50 Weissleder, R. & Ntziachristos, V. Shedding light onto live molecular targets. *Nat Med* **9**, 123-128, doi:10.1038/nm0103-123 (2003).
- 51 Muldoon, T. J. *et al.* Subcellular-resolution molecular imaging within living tissue by fiber microendoscopy. *Opt Express* **15**, 16413-16423 (2007).
- 52 Sheth, R. A., Upadhyay, R., Weissleder, R. & Mahmood, U. Real-time multichannel imaging framework for endoscopy, catheters, and fixed geometry intraoperative systems. *Mol Imaging* **6**, 147-155 (2007).
- 53 Pierce, M. C., Strasswimmer, J., Park, B. H., Cense, B. & de Boer, J. F. Advances in optical coherence tomography imaging for dermatology. *J Invest Dermatol* **123**, 458-463, doi:10.1111/j.0022-202X.2004.23404.x (2004).
- 54 Dzik-Jurasz, A. S. Molecular imaging in vivo: an introduction. *Br J Radiol* **76 Spec No 2**, S98-109, doi:10.1259/bjr/25833499 (2003).
- 55 Dhawan, A. P., D'Alessandro, B. & Fu, X. Optical imaging modalities for biomedical applications. *IEEE Rev Biomed Eng* **3**, 69-92, doi:10.1109/RBME.2010.2081975 (2010).
- 56 Pierce, M. C., Javier, D. J. & Richards-Kortum, R. Optical contrast agents and imaging systems for detection and diagnosis of cancer. *Int J Cancer* **123**, 1979-1990, doi:10.1002/ijc.23858 (2008).

- 57 Doubrovin, M., Serganova, I., Mayer-Kuckuk, P., Ponomarev, V. & Blasberg, R. G. Multimodality in vivo molecular-genetic imaging. *Bioconjug Chem* **15**, 1376-1388, doi:10.1021/bc0498572 (2004).
- 58 Mather, S. Molecular imaging with bioconjugates in mouse models of cancer. *Bioconjug Chem* **20**, 631-643, doi:10.1021/bc800401x (2009).
- 59 Hilger, I. *et al.* Near-infrared fluorescence imaging of HER-2 protein over-expression in tumour cells. *Eur Radiol* **14**, 1124-1129, doi:10.1007/s00330-004-2257-9 (2004).
- 60 Solomon, M., Liu, Y., Berezin, M. Y. & Achilefu, S. Optical imaging in cancer research: basic principles, tumor detection, and therapeutic monitoring. *Med Princ Pract* **20**, 397-415, doi:10.1159/000327655 (2011).
- 61 Hsu, E. R. *et al.* A far-red fluorescent contrast agent to image epidermal growth factor receptor expression. *Photochem Photobiol* **79**, 272-279 (2004).
- 62 Chang, S. K., Rizvi, I., Solban, N. & Hasan, T. In vivo optical molecular imaging of vascular endothelial growth factor for monitoring cancer treatment. *Clin Cancer Res* **14**, 4146-4153, doi:10.1158/1078-0432.CCR-07-4536 (2008).
- 63 Hoetker, M. S. *et al.* Molecular in vivo imaging of gastric cancer in a human-murine xenograft model: targeting epidermal growth factor receptor. *Gastrointest Endosc* **76**, 612-620, doi:10.1016/j.gie.2012.05.013 (2012).
- 64 Choi, H. S. *et al.* Renal clearance of quantum dots. *Nat Biotechnol* **25**, 1165-1170, doi:10.1038/nbt1340 (2007).
- 65 Nitin, N. *et al.* Optical molecular imaging of epidermal growth factor receptor expression to improve detection of oral neoplasia. *Neoplasia* **11**, 542-551 (2009).
- 66 Cheng, Z., Wu, Y., Xiong, Z., Gambhir, S. S. & Chen, X. Near-infrared fluorescent RGD peptides for optical imaging of integrin alphavbeta3 expression in living mice. *Bioconjug Chem* **16**, 1433-1441, doi:10.1021/bc0501698 (2005).
- 67 Derfus, A. M., Chan, W. C. W. & Bhatia, S. N. Probing the Cytotoxicity Of Semiconductor Quantum Dots. *Nano Lett* **4**, 11-18, doi:10.1021/nl0347334 (2004).
- 68 Jacques, S. L. Optical properties of biological tissues: a review. *Phys Med Biol* **58**, R37-61, doi:10.1088/0031-9155/58/11/R37 (2013).
- 69 PETTY, J. A. C. A. C. C. The Near Infrared Absorption Spectrum of Liquid Water. *JOURNAL OF THE OPTICAL SOCIETY OF AMERICA* **41** (1951).
- 70 Hale, G. M. & Querry, M. R. Optical Constants of Water in the 200-nm to 200-microm Wavelength Region. *Appl Opt* **12**, 555-563, doi:10.1364/AO.12.000555 (1973).
- 71 Naczynski, D. J. *et al.* Rare-earth-doped biological composites as in vivo shortwave infrared reporters. *Nature communications* **4**, 2199, doi:10.1038/ncomms3199 (2013).
- 72 S.Luryi, A. K., J.C. Bean. New infrared detector on a silicon chip. *IEEE transactions on Electron Devices* **31**, 1135-1139, doi:10.1109/T-ED.1984.21676 (1984).
- 73 Marc P. Hansen, D. S. M. Overview of SWIR detectors, cameras, and applications. *SPIE* **6939**, doi:10.1117/12.777776 (2008).
- 74 Langer, R. Drug delivery and targeting. *Nature* **392**, 5-10 (1998).
- 75 Ferrari, M. Cancer nanotechnology: opportunities and challenges. *Nat Rev Cancer* **5**, 161-171, doi:10.1038/nrc1566 (2005).
- 76 Davis, M. E., Chen, Z. G. & Shin, D. M. Nanoparticle therapeutics: an emerging treatment modality for cancer. *Nat Rev Drug Discov* **7**, 771-782, doi:10.1038/nrd2614 (2008).
- 77 Allen, T. M. Ligand-targeted therapeutics in anticancer therapy. *Nat Rev Cancer* **2**, 750-763, doi:10.1038/nrc903 (2002).
- 78 Jain, R. K. The next frontier of molecular medicine: delivery of therapeutics. *Nat Med* **4**, 655-657 (1998).

- 79 Peer, D. *et al.* Nanocarriers as an emerging platform for cancer therapy. *Nat Nanotechnol* **2**, 751-760, doi:10.1038/nnano.2007.387 (2007).
- 80 Maeda, H., Greish, K. & Fang, J. in *Polymer Therapeutics II* (eds Ronit Satchi-Fainaro & Ruth Duncan) 103-121 (Springer Berlin Heidelberg, 2006).
- 81 Alexis, F., Pridgen, E., Molnar, L. K. & Farokhzad, O. C. Factors affecting the clearance and biodistribution of polymeric nanoparticles. *Mol Pharm* **5**, 505-515, doi:10.1021/mp800051m (2008).
- 82 Ilium, L. *et al.* Blood clearance and organ deposition of intravenously administered colloidal particles. The effects of particle size, nature and shape. *International Journal of Pharmaceutics* **12**, 135-146, doi:[https://doi.org/10.1016/0378-5173\(82\)90113-2](https://doi.org/10.1016/0378-5173(82)90113-2) (1982).
- 83 Carmeliet, P. & Jain, R. K. Molecular mechanisms and clinical applications of angiogenesis. *Nature* **473**, 298-307, doi:10.1038/nature10144 (2011).
- 84 Hoshyar, N., Gray, S., Han, H. & Bao, G. The effect of nanoparticle size on in vivo pharmacokinetics and cellular interaction. *Nanomedicine (Lond)* **11**, 673-692, doi:10.2217/nnm.16.5 (2016).
- 85 Fang, J., Nakamura, H. & Maeda, H. The EPR effect: Unique features of tumor blood vessels for drug delivery, factors involved, and limitations and augmentation of the effect. *Adv Drug Deliv Rev* **63**, 136-151, doi:10.1016/j.addr.2010.04.009 (2011).
- 86 Jain, R. K. & Stylianopoulos, T. Delivering nanomedicine to solid tumors. *Nat Rev Clin Oncol* **7**, 653-664, doi:10.1038/nrclinonc.2010.139 (2010).
- 87 Nafee, N., Schneider, M., Schaefer, U. F. & Lehr, C. M. Relevance of the colloidal stability of chitosan/PLGA nanoparticles on their cytotoxicity profile. *Int J Pharm* **381**, 130-139, doi:10.1016/j.ijpharm.2009.04.049 (2009).
- 88 Frohlich, E. The role of surface charge in cellular uptake and cytotoxicity of medical nanoparticles. *Int J Nanomedicine* **7**, 5577-5591, doi:10.2147/IJN.S36111 (2012).
- 89 Chirio, D. *et al.* Positive-charged solid lipid nanoparticles as paclitaxel drug delivery system in glioblastoma treatment. *Eur J Pharm Biopharm* **88**, 746-758, doi:10.1016/j.ejpb.2014.10.017 (2014).
- 90 Bertrand, N., Wu, J., Xu, X., Kamaly, N. & Farokhzad, O. C. Cancer nanotechnology: the impact of passive and active targeting in the era of modern cancer biology. *Adv Drug Deliv Rev* **66**, 2-25, doi:10.1016/j.addr.2013.11.009 (2014).
- 91 Elias, D. R., Poloukhine, A., Popik, V. & Tsourkas, A. Effect of ligand density, receptor density, and nanoparticle size on cell targeting. *Nanomedicine* **9**, 194-201, doi:10.1016/j.nano.2012.05.015 (2013).
- 92 Friedman, A. D., Claypool, S. E. & Liu, R. The smart targeting of nanoparticles. *Curr Pharm Des* **19**, 6315-6329 (2013).
- 93 Mammen, M., Choi, S. K. & Whitesides, G. M. Polyvalent Interactions in Biological Systems: Implications for Design and Use of Multivalent Ligands and Inhibitors. *Angew Chem Int Ed Engl* **37**, 2754-2794, doi:10.1002/(SICI)1521-3773(19981102)37:20<2754::AID-ANIE2754>3.0.CO;2-3 (1998).
- 94 Mukherjee, S., Ghosh, R. N. & Maxfield, F. R. Endocytosis. *Physiol Rev* **77**, 759-803, doi:10.1152/physrev.1997.77.3.759 (1997).
- 95 Stefanick, J. F., Ashley, J. D., Kiziltepe, T. & Bilgicer, B. A systematic analysis of peptide linker length and liposomal polyethylene glycol coating on cellular uptake of peptide-targeted liposomes. *ACS Nano* **7**, 2935-2947, doi:10.1021/nn305663e (2013).
- 96 Adams, G. P. *et al.* High affinity restricts the localization and tumor penetration of single-chain fv antibody molecules. *Cancer Res* **61**, 4750-4755 (2001).

- 97 Daniels, T. R., Delgado, T., Rodriguez, J. A., Helguera, G. & Penichet, M. L. The transferrin receptor part I: Biology and targeting with cytotoxic antibodies for the treatment of cancer. *Clin Immunol* **121**, 144-158, doi:10.1016/j.clim.2006.06.010 (2006).
- 98 Gabizon, A., Shmeeda, H., Horowitz, A. T. & Zalipsky, S. Tumor cell targeting of liposome-entrapped drugs with phospholipid-anchored folic acid-PEG conjugates. *Adv Drug Deliv Rev* **56**, 1177-1192, doi:10.1016/j.addr.2004.01.011 (2004).
- 99 Stupack, D. G. & Cheresch, D. A. Integrins and angiogenesis. *Curr Top Dev Biol* **64**, 207-238, doi:10.1016/S0070-2153(04)64009-9 (2004).
- 100 Hermanson, G. T. Bioconjugate Techniques, 3rd Edition. *Bioconjugate Techniques, 3rd Edition*, 1-1146 (2013).
- 101 Sung, J. C., Pulliam, B. L. & Edwards, D. A. Nanoparticles for drug delivery to the lungs. *Trends Biotechnol* **25**, 563-570, doi:10.1016/j.tibtech.2007.09.005 (2007).
- 102 Roger, E., Lagarce, F., Garcion, E. & Benoit, J. P. Biopharmaceutical parameters to consider in order to alter the fate of nanocarriers after oral delivery. *Nanomedicine (Lond)* **5**, 287-306, doi:10.2217/nnm.09.110 (2010).
- 103 Ensign, L. M., Cone, R. & Hanes, J. Oral drug delivery with polymeric nanoparticles: the gastrointestinal mucus barriers. *Adv Drug Deliv Rev* **64**, 557-570, doi:10.1016/j.addr.2011.12.009 (2012).
- 104 Klibanov, A. L., Maruyama, K., Torchilin, V. P. & Huang, L. Amphipathic polyethyleneglycols effectively prolong the circulation time of liposomes. *FEBS Lett* **268**, 235-237 (1990).
- 105 Allen, T. M., Hansen, C., Martin, F., Redemann, C. & Yau-Young, A. Liposomes containing synthetic lipid derivatives of poly(ethylene glycol) show prolonged circulation half-lives in vivo. *Biochim Biophys Acta* **1066**, 29-36 (1991).
- 106 Bareford, L. M. & Swaan, P. W. Endocytic mechanisms for targeted drug delivery. *Adv Drug Deliv Rev* **59**, 748-758, doi:10.1016/j.addr.2007.06.008 (2007).
- 107 Rejman, J., Oberle, V., Zuhorn, I. S. & Hoekstra, D. Size-dependent internalization of particles via the pathways of clathrin- and caveolae-mediated endocytosis. *Biochem J* **377**, 159-169, doi:10.1042/BJ20031253 (2004).
- 108 Welsher, K. *et al.* A route to brightly fluorescent carbon nanotubes for near-infrared imaging in mice. *Nat Nanotechnol* **4**, 773-780, doi:10.1038/nnano.2009.294 (2009).
- 109 Robinson, J. T. *et al.* High Performance In Vivo Near-IR (>1 μm) Imaging and Photothermal Cancer Therapy with Carbon Nanotubes. *Nano Res* **3**, 779-793, doi:10.1007/s12274-010-0045-1 (2010).
- 110 Rogach, A. L., Eychmuller, A., Hickey, S. G. & Kershaw, S. V. Infrared-emitting colloidal nanocrystals: synthesis, assembly, spectroscopy, and applications. *Small* **3**, 536-557, doi:10.1002/sml.200600625 (2007).
- 111 Naczynski, D. J. Rare-earth-doped biological composites as in vivo shortwave infrared reporters. *Nature Commun.* **4**, doi:10.1038/ncomms3199 (2013).
- 112 Naczynski, D. J., Tan, M. C., Riman, R. E. & Moghe, P. V. Rare Earth Nanoprobes for Functional Biomolecular Imaging and Theranostics. *J Mater Chem B* **2**, 2958-2973, doi:10.1039/C4TB00094C (2014).
- 113 Wang, Q., Tan, M. C., Zhuo, R., Kumar, G. A. & Riman, R. E. A solvothermal route to size- and phase-controlled highly luminescent NaYF₄:Yb,Er up-conversion nanocrystals. *J Nanosci Nanotechnol* **10**, 1685-1692 (2010).
- 114 Boyer, J. C., Vetrone, F., Cuccia, L. A. & Capobianco, J. A. Synthesis of colloidal upconverting NaYF₄ nanocrystals doped with Er³⁺, Yb³⁺ and Tm³⁺, Yb³⁺ via thermal

- decomposition of lanthanide trifluoroacetate precursors. *J Am Chem Soc* **128**, 7444-7445, doi:10.1021/ja061848b (2006).
- 115 Elzoghby, A. O., Samy, W. M. & Elgindy, N. A. Albumin-based nanoparticles as potential controlled release drug delivery systems. *J Control Release* **157**, 168-182, doi:10.1016/j.jconrel.2011.07.031 (2012).
- 116 Kratz, F. Albumin as a drug carrier: design of prodrugs, drug conjugates and nanoparticles. *J Control Release* **132**, 171-183, doi:10.1016/j.jconrel.2008.05.010 (2008).
- 117 Peters, T. All about albumin: biochemistry, genetics, and medical applications. *San Diego, Calif: Academics* (1996).
- 118 Schnitzer, J. E. gp60 is an albumin-binding glycoprotein expressed by continuous endothelium involved in albumin transcytosis. *Am J Physiol* **262**, H246-254, doi:10.1152/ajpheart.1992.262.1.H246 (1992).
- 119 Tirupathi, C., Finnegan, A. & Malik, A. B. Isolation and characterization of a cell surface albumin-binding protein from vascular endothelial cells. *Proc Natl Acad Sci U S A* **93**, 250-254 (1996).
- 120 Liu, Z. & Chen, X. Simple bioconjugate chemistry serves great clinical advances: albumin as a versatile platform for diagnosis and precision therapy. *Chem Soc Rev* **45**, 1432-1456, doi:10.1039/c5cs00158g (2016).
- 121 Desai, N. *et al.* Increased antitumor activity, intratumor paclitaxel concentrations, and endothelial cell transport of cremophor-free, albumin-bound paclitaxel, ABI-007, compared with cremophor-based paclitaxel. *Clin Cancer Res* **12**, 1317-1324, doi:10.1158/1078-0432.CCR-05-1634 (2006).
- 122 Desai, N., Trieu, V., Damascelli, B. & Soon-Shiong, P. SPARC Expression Correlates with Tumor Response to Albumin-Bound Paclitaxel in Head and Neck Cancer Patients. *Transl Oncol* **2**, 59-64 (2009).
- 123 Legigan, T. *et al.* Synthesis and antitumor efficacy of a beta-glucuronidase-responsive albumin-binding prodrug of doxorubicin. *J Med Chem* **55**, 4516-4520, doi:10.1021/jm300348r (2012).
- 124 Naczynski, D. J. *et al.* Albumin Nanoshell Encapsulation of Near-Infrared-Excitable Rare-Earth Nanoparticles Enhances Biocompatibility and Enables Targeted Cell Imaging. *Small* **6**, 1631-1640, doi:DOI 10.1002/smll.200902403 (2010).
- 125 Naczynski, D. J. *et al.* Rare-earth-doped biological composites as in vivo shortwave infrared reporters. *Nat Commun* **4**, doi:Artn 2199 10.1038/Ncomms3199 (2013).
- 126 Clemons, M., Danson, S., Hamilton, T. & Goss, P. Locoregionally recurrent breast cancer: incidence, risk factors and survival. *Cancer Treat Rev* **27**, 67-82, doi:10.1053/ctrv.2000.0204 (2001).
- 127 Weigelt, B., Peterse, J. L. & van 't Veer, L. J. Breast cancer metastasis: markers and models. *Nat Rev Cancer* **5**, 591-602, doi:10.1038/nrc1670 (2005).
- 128 Seemann, M. D. Whole-body PET/MRI: the future in oncological imaging. *Technology in cancer research & treatment* **4**, 577-582 (2005).
- 129 Antoch, G. & Bockisch, A. Combined PET/MRI: a new dimension in whole-body oncology imaging? *Eur J Nucl Med Mol Imaging* **36 Suppl 1**, S113-120, doi:10.1007/s00259-008-0951-6 (2009).
- 130 Hwang, J. Y. *et al.* Multimodality imaging in vivo for preclinical assessment of tumor-targeted doxorubicin nanoparticles. *PLoS One* **7**, e34463, doi:10.1371/journal.pone.0034463 (2012).

- 131 Resch-Genger, U., Grabolle, M., Cavaliere-Jaricot, S., Nitschke, R. & Nann, T. Quantum dots versus organic dyes as fluorescent labels. *Nat Methods* **5**, 763-775, doi:nmeth.1248 [pii]
10.1038/nmeth.1248 (2008).
- 132 He, H., Xie, C. & Ren, J. Nonbleaching fluorescence of gold nanoparticles and its applications in cancer cell imaging. *Anal Chem* **80**, 5951-5957, doi:10.1021/ac8005796 (2008).
- 133 Diao, S., Hong, Guosong, Antaris, Alexander, Blackburn, Jeffrey, Cheng, Kai, Cheng, Zhen, Dai, Hongjie. Biological imaging without autofluorescence in the second near-infrared window. *Nano Research* **8**, 3027-3034, doi:10.1007/s12274-015-0808-9 (2015).
- 134 Villa, I. *et al.* 1.3 μ m emitting SrF₂:Nd³⁺ nanoparticles for high contrast in vivo imaging in the second biological window. *Nano Research* **8**, 649-665, doi:10.1007/s12274-014-0549-1 (2015).
- 135 Riman, R. E., Kumar, G. A., Atakan, V., Brennan, J. G. & Ballato, J. Engineered solution synthesis of rare-earth nanomaterials and their optical properties. *Proc. SPIE-Int. Soc. Opt. Eng.* **6707**, 670707/670701-670707/670711, doi:10.1117/12.740828 (2007).
- 136 Riman, R. E., Tan, M. C. & Gangadharan, K. A. Near Infrared-Emitting ER and Yb/Er doped CeF₃ Nanoparticulates with no visible upconversion. (2012).
- 137 Smith, A. M., Mancini, M. C. & Nie, S. Bioimaging: second window for in vivo imaging. *Nat Nanotechnol* **4**, 710-711, doi:10.1038/nnano.2009.326 (2009).
- 138 Cui, M. *et al.* Multifunctional albumin nanoparticles as combination drug carriers for intra-tumoral chemotherapy. *Adv Healthc Mater* **2**, 1236-1245, doi:10.1002/adhm.201200467 (2013).
- 139 Hendrix, C. W. *et al.* Pharmacokinetics and safety of AMD-3100, a novel antagonist of the CXCR-4 chemokine receptor, in human volunteers. *Antimicrobial agents and chemotherapy* **44**, 1667-1673 (2000).
- 140 Le Bon, B. *et al.* AMD3100 conjugates as components of targeted nonviral gene delivery systems: synthesis and in vitro transfection efficiency of CXCR4-expressing cells. *Bioconjug Chem* **15**, 413-423, doi:10.1021/bc034220o (2004).
- 141 Hinton, C. V., Avraham, S. & Avraham, H. K. Role of the CXCR4/CXCL12 signaling axis in breast cancer metastasis to the brain. *Clin Exp Metastasis* **27**, 97-105, doi:10.1007/s10585-008-9210-2 (2010).
- 142 Muller, A. *et al.* Involvement of chemokine receptors in breast cancer metastasis. *Nature* **410**, 50-56, doi:10.1038/35065016 (2001).
- 143 Zlotnik, A. Involvement of chemokine receptors in organ-specific metastasis. *Contributions to microbiology* **13**, 191-199, doi:10.1159/000092973 (2006).
- 144 Nimmagadda, S. *et al.* Molecular imaging of CXCR4 receptor expression in human cancer xenografts with [64Cu]AMD3100 positron emission tomography. *Cancer Res* **70**, 3935-3944, doi:10.1158/0008-5472.CAN-09-4396 (2010).
- 145 Kratz, F. Albumin as a drug carrier: Design of prodrugs, drug conjugates and nanoparticles. *J Control Release* **132**, 171-183, doi:DOI 10.1016/j.jconrel.2008.05.010 (2008).
- 146 Paal, K., Muller, J. & Hegedus, L. High affinity binding of paclitaxel to human serum albumin. *Eur J Biochem* **268**, 2187-2191 (2001).
- 147 Kang, Y. *et al.* A multigenic program mediating breast cancer metastasis to bone. *Cancer Cell* **3**, 537-549 (2003).

- 148 Sun, Y. *et al.* CXCL12-CXCR4 axis promotes the natural selection of breast cancer cell metastasis. *Tumour biology : the journal of the International Society for Oncodevelopmental Biology and Medicine* **35**, 7765-7773, doi:10.1007/s13277-014-1816-1 (2014).
- 149 Ganapathy, V. *et al.* Targeting the Transforming Growth Factor-beta pathway inhibits human basal-like breast cancer metastasis. *Molecular cancer* **9**, 122, doi:10.1186/1476-4598-9-122 (2010).
- 150 Minn, A. J. *et al.* Genes that mediate breast cancer metastasis to lung. *Nature* **436**, 518-524, doi:10.1038/nature03799 (2005).
- 151 Minn, A. J. *et al.* Distinct organ-specific metastatic potential of individual breast cancer cells and primary tumors. *J Clin Invest* **115**, 44-55, doi:10.1172/JCI22320 (2005).
- 152 Kelly, K. A. *et al.* Targeted nanoparticles for imaging incipient pancreatic ductal adenocarcinoma. *Plos Medicine* **5**, 657-668, doi:ARTN e85
DOI 10.1371/journal.pmed.0050085 (2008).
- 153 Xiao, Z. Y. *et al.* Engineering of Targeted Nanoparticles for Cancer Therapy Using Internalizing Aptamers Isolated by Cell-Uptake Selection. *Acs Nano* **6**, 696-704, doi:Doi 10.1021/Nn204165v (2012).
- 154 Anhorn, M. G., Wagner, S., Kreuter, J., Langer, K. & von Briesen, H. Specific targeting of HER2 overexpressing breast cancer cells with doxorubicin-loaded trastuzumab-modified human serum albumin nanoparticles. *Bioconjug Chem* **19**, 2321-2331, doi:10.1021/bc8002452 (2008).
- 155 Bartlett, D. W., Su, H., Hildebrandt, I. J., Weber, W. A. & Davis, M. E. Impact of tumor-specific targeting on the biodistribution and efficacy of siRNA nanoparticles measured by multimodality in vivo imaging. *Proc Natl Acad Sci U S A* **104**, 15549-15554, doi:10.1073/pnas.0707461104 (2007).
- 156 Kang, M. J., Park, S. H., Kang, M. H., Park, M. J. & Choi, Y. W. Folic acid-tethered Pep-1 peptide-conjugated liposomal nanocarrier for enhanced intracellular drug delivery to cancer cells: conformational characterization and in vitro cellular uptake evaluation. *Int J Nanomedicine* **8**, 1155-1165, doi:10.2147/IJN.S39491 (2013).
- 157 Low, K., Wacker, M., Wagner, S., Langer, K. & von Briesen, H. Targeted human serum albumin nanoparticles for specific uptake in EGFR-Expressing colon carcinoma cells. *Nanomed-Nanotechnol* **7**, 454-463, doi:DOI 10.1016/j.nano.2010.12.003 (2011).
- 158 Ming, X., Carver, K. & Wu, L. Albumin-based nanoconjugates for targeted delivery of therapeutic oligonucleotides. *Biomaterials* **34**, 7939-7949, doi:10.1016/j.biomaterials.2013.06.066 (2013).
- 159 Vlashi, E., Kelderhouse, L. E., Sturgis, J. E. & Low, P. S. Effect of folate-targeted nanoparticle size on their rates of penetration into solid tumors. *Acs Nano* **7**, 8573-8582, doi:10.1021/nn402644g (2013).
- 160 Wang, Z. *et al.* The use of a tumor metastasis targeting peptide to deliver doxorubicin-containing liposomes to highly metastatic cancer. *Biomaterials* **33**, 8451-8460, doi:10.1016/j.biomaterials.2012.08.031 (2012).
- 161 Kratz, F. & Elsadek, B. Clinical impact of serum proteins on drug delivery. *J Control Release* **161**, 429-445, doi:10.1016/j.jconrel.2011.11.028 (2012).
- 162 Hellebust, A. & Richards-Kortum, R. Advances in molecular imaging: targeted optical contrast agents for cancer diagnostics. *Nanomedicine (Lond)* **7**, 429-445, doi:10.2217/nnm.12.12 (2012).

- 163 Chinnathambi, S., Chen, S., Ganesan, S. & Hanagata, N. Silicon quantum dots for biological applications. *Adv Healthc Mater* **3**, 10-29, doi:10.1002/adhm.201300157 (2014).
- 164 Biju, V., Itoh, T., Anas, A., Sujith, A. & Ishikawa, M. Semiconductor quantum dots and metal nanoparticles: syntheses, optical properties, and biological applications. *Anal Bioanal Chem* **391**, 2469-2495, doi:10.1007/s00216-008-2185-7 (2008).
- 165 Jayakumar, M. K., Idris, N. M., Huang, K. & Zhang, Y. A paradigm shift in the excitation wavelength of upconversion nanoparticles. *Nanoscale* **6**, 8441-8443, doi:10.1039/c4nr02422b (2014).
- 166 Wang, Y. F. *et al.* Nd(3+)-sensitized upconversion nanophosphors: efficient in vivo bioimaging probes with minimized heating effect. *ACS nano* **7**, 7200-7206, doi:10.1021/nn402601d (2013).
- 167 Haro-Gonzalez, P. *et al.* Quantum dot-based thermal spectroscopy and imaging of optically trapped microspheres and single cells. *Small* **9**, 2162-2170, doi:10.1002/sml.201201740 (2013).
- 168 Maestro, L. M. *et al.* Heating efficiency of multi-walled carbon nanotubes in the first and second biological windows. *Nanoscale* **5**, 7882-7889, doi:10.1039/c3nr01398g (2013).
- 169 Kummar, S., Gutierrez, M., Doroshow, J. H. & Murgu, A. J. Drug development in oncology: classical cytotoxics and molecularly targeted agents. *British journal of clinical pharmacology* **62**, 15-26, doi:10.1111/j.1365-2125.2006.02713.x (2006).
- 170 Allen, T. M. Ligand-targeted therapeutics in anticancer therapy. *Nature Reviews Cancer* **2**, 750-763, doi:10.1038/Nrc903 (2002).
- 171 Horm, T. M. & Schroeder, J. A. MUC1 and metastatic cancer: expression, function and therapeutic targeting. *Cell adhesion & migration* **7**, 187-198, doi:10.4161/cam.23131 (2013).
- 172 Kennecke, H. *et al.* Metastatic behavior of breast cancer subtypes. *J Clin Oncol* **28**, 3271-3277, doi:10.1200/JCO.2009.25.9820 (2010).
- 173 Chaffer, C. L. & Weinberg, R. A. A perspective on cancer cell metastasis. *Science* **331**, doi:10.1126/science.1203543 (2011).
- 174 Dawood, S. Differences in survival among women with stage III inflammatory and noninflammatory locally advanced breast cancer appear early: a large population-based study. *Cancer-Am Cancer Soc* **117**, doi:10.1002/cncr.25682 (2011).
- 175 Plunkett, T. A., Smith, P. & Rubens, R. D. Risk of complications from bone metastases in breast cancer. Implications for management. *Eur. J. Cancer* **36**, doi:10.1016/S0959-8049(99)00331-7 (2000).
- 176 Ganapathy, V. Luminal breast cancer metastasis is dependent on estrogen signaling. *Clin. Exp. Metastasis* **29**, doi:10.1007/s10585-012-9466-4 (2012).
- 177 Ganapathy, V. Targeting the transforming growth factor-beta pathway inhibits human basal-like breast cancer metastasis. *Mol. Cancer* **9**, doi:10.1186/1476-4598-9-122 (2010).
- 178 Setyawati, M. I., Tay, C. Y., Docter, D., Stauber, R. H. & Leong, D. T. Understanding and exploiting nanoparticles' intimacy with the blood vessel and blood. *Chem Soc Rev* **44**, 8174-8199, doi:10.1039/c5cs00499c (2015).
- 179 Cleaver, O. & Melton, D. A. Endothelial signaling during development. *Nat. Med.* **9**, doi:10.1038/nm0603-661 (2003).
- 180 Barua, S. & Mitragotri, S. Challenges associated with penetration of nanoparticles across cell and tissue barriers: a review of current status and future prospects. *Nano Today* **9**, doi:10.1016/j.nantod.2014.04.008 (2014).

- 181 Blanco, E., Shen, H. & Ferrari, M. Principles of nanoparticle design for overcoming
biological barriers to drug delivery. *Nat. Biotechnol.* **33**, doi:10.1038/nbt.3330 (2015).
- 182 Smith, A. M., Mancini, M. C. & Nie, S. Bioimaging: second window for in vivo imaging.
Nat. Nanotech. **4**, doi:10.1038/nnano.2009.326 (2009).
- 183 Sordillo, L. A., Pu, Y., Pratavieira, S., Budansky, Y. & Alfano, R. R. Deep optical imaging of
tissue using the second and third near-infrared spectral windows. *J. Biomed. Opt.* **19**,
doi:10.1117/1.JBO.19.5.056004 (2014).
- 184 Saders, B., Al-Baroudi, L., Tan, M. C. & Riman, R. E. Rare-earth doped particles with
tunable infrared emissions for biomedical imaging. *Opt. Mater. Express* **3**,
doi:10.1364/OME.3.000566 (2013).
- 185 Tan, M. C., Connolly, J. & Riman, R. E. Optical efficiency of short wave infrared emitting
phosphors. *J. Phys. Chem. C* **115**, doi:10.1021/jp203735n (2011).
- 186 Kang, Y. A multigenic program mediating breast cancer metastasis to bone. *Cancer Cell*
3, doi:10.1016/S1535-6108(03)00132-6 (2003).
- 187 Zevon, M. *et al.* CXCR-4 Targeted, Short Wave Infrared (SWIR) Emitting Nanoprobes for
Enhanced Deep Tissue Imaging and Micrometastatic Cancer Lesion Detection. *Small* **11**,
6347-6357, doi:10.1002/smll.201502202 (2015).
- 188 Zhao, X., He, S. & Tan, M. C. Design of infrared-emitting rare earth doped nanoparticles
and nanostructured composites. *J. Mater. Chem. C* **4**, doi:10.1039/C6TC02373H (2016).
- 189 Sheng, Y., Liao, L., Thakor, N. V. & Tan, M. C. Nanoparticles for molecular imaging. *J.*
Biomed. Nanotechnol. **10**, doi:10.1166/jbn.2014.1937 (2014).
- 190 Hendrix, C. W. Pharmacokinetics and safety of AMD-3100, a novel antagonist of the
CXCR-4 chemokine receptor, in human volunteers. *Antimicrob. Agents Chemother.* **44**,
doi:10.1128/AAC.44.6.1667-1673.2000 (2000).
- 191 Clercq, E. The bicyclam AMD3100 story. *Nat. Rev. Drug Discov.* **2**, doi:10.1038/nrd1134
(2003).
- 192 Baglioni, M. Binding of the doxorubicin-lactosaminated human albumin conjugate to
HCC cells is mediated by the drug moieties. *Dig. Liver Dis.* **40**,
doi:10.1016/j.dld.2008.05.014 (2008).
- 193 Kratz, F. Albumin as a drug carrier: design of prodrugs, drug conjugates and
nanoparticles. *J. Control Release* **132**, doi:10.1016/j.jconrel.2008.05.010 (2008).
- 194 Ulmert, D., Solnes, L. & Thorek, D. Contemporary approaches for imaging skeletal
metastasis. *Bone Res.* **3**, doi:10.1038/boneres.2015.24 (2015).
- 195 Minn, A. J. Genes that mediate breast cancer metastasis to lung. *Nature* **436**,
doi:10.1038/nature03799 (2005).
- 196 Minn, A. J. Distinct organ-specific metastatic potential of individual breast cancer cells
and primary tumors. *J. Clin. Investig.* **115**, doi:10.1172/JCI22320 (2005).
- 197 Toy, R., Peiris, P. M., Ghaghada, K. B. & Karathanasis, E. Shaping cancer nanomedicine:
the effect of particle shape on the in vivo journey of nanoparticles. *Nanomedicine* **9**,
doi:10.2217/nnm.13.191 (2014).
- 198 Berman, A. T., Thukral, A. D., Hwang, W. T., Solin, L. J. & Vapiwala, N. Incidence and
patterns of distant metastases for patients with early-stage breast cancer after breast
conservation treatment. *Clin. Breast Cancer* **13**, doi:10.1016/j.clbc.2012.11.001 (2013).
- 199 Sethi, N. & Kang, Y. Notch signalling in cancer progression and bone metastasis. *Br. J.*
Cancer **105**, doi:10.1038/bjc.2011.497 (2011).
- 200 Hazan, R. B., Phillips, G. R., Qiao, R. F., Norton, L. & Aaronson, S. A. Exogenous
expression of N-cadherin in breast cancer cells induces cell migration, invasion, and
metastasis. *J. Cell Biol.* **148**, doi:10.1083/jcb.148.4.779 (2000).

- 201 Gligorijevic, B. Intravital imaging and photoswitching in tumor invasion and
intravasation microenvironments. *Micros Today* **18**, doi:10.1017/S1551929510991220
(2010).
- 202 Hult, J. The use of fluorescent proteins for intravital imaging of cancer cell invasion.
Methods Mol. Biol. **872**, doi:10.1007/978-1-61779-797-2_2 (2012).
- 203 Kedrin, D. Intravital imaging of metastatic behavior through a mammary imaging
window. *Nat. Methods* **5**, doi:10.1038/nmeth.1269 (2008).
- 204 Fein, M. R. & Egeblad, M. Caught in the act: revealing the metastatic process by live
imaging. *Dis. Model. Mech.* **6**, doi:10.1242/dmm.009282 (2013).
- 205 Lunov, O. Differential uptake of functionalized polystyrene nanoparticles by human
macrophages and a monocytic cell line. *ACS Nano* **5**, doi:10.1021/nn2000756 (2011).
- 206 Suva, L. J., Griffin, R. J. & Makhoul, I. Mechanisms of bone metastases of breast cancer.
Endocr. Relat. Cancer **16**, doi:10.1677/ERC-09-0012 (2009).
- 207 Murugan, K. Parameters and characteristics governing cellular internalization and trans-
barrier trafficking of nanostructures. *Int. J. Nanomed.* **10** (2015).
- 208 Bertrand, N., Wu, J., Xu, X., Kamaly, N. & Farokhzad, O. C. Cancer nanotechnology: the
impact of passive and active targeting in the era of modern cancer biology. *Adv. Drug
Deliv. Rev.* **66**, doi:10.1016/j.addr.2013.11.009 (2014).
- 209 Kettiger, H., Schipanski, A., Wick, P. & Huwyler, J. Engineered nanomaterial uptake and
tissue distribution: from cell to organism. *Int. J. Nanomed.* **8** (2013).
- 210 Kang, Y. & Pantel, K. Tumor cell dissemination: emerging biological insights from animal
models and cancer patients. *Cancer Cell* **23**, doi:10.1016/j.ccr.2013.04.017 (2013).
- 211 van Saders, B., Al-Baroudi, L., Tan, M. C. & Riman, R. E. Rare-earth doped particles with
tunable infrared emissions for biomedical imaging. *Opt. Mater. Express* **3**, 566-573
(2013).
- 212 Cui, M. *et al.* Multifunctional Albumin Nanoparticles As Combination Drug Carriers for
Intra-Tumoral Chemotherapy. *Advanced healthcare materials*,
doi:10.1002/adhm.201200467 (2013).
- 213 Kantamneni, H. *et al.* Surveillance nanotechnology for multi-organ cancer metastases.
Nat Biomed Eng **1**, 993-1003, doi:10.1038/s41551-017-0167-9 (2017).
- 214 Sharma, S., Singh, M. & Sharma, P. L. Ameliorative effect of daidzein: a caveolin-1
inhibitor in vascular endothelium dysfunction induced by ovariectomy. *Indian J Exp Biol*
50, 28-34 (2012).
- 215 Layne, J., Majkova, Z., Smart, E. J., Toborek, M. & Hennig, B. Caveolae: a regulatory
platform for nutritional modulation of inflammatory diseases. *J Nutr Biochem* **22**, 807-
811, doi:10.1016/j.jnutbio.2010.09.013 (2011).
- 216 Rosenkilde, M. M. *et al.* Molecular mechanism of AMD3100 antagonism in the CXCR4
receptor: transfer of binding site to the CXCR3 receptor. *J Biol Chem* **279**, 3033-3041,
doi:10.1074/jbc.M309546200 (2004).
- 217 Kawaguchi, A. *et al.* Inhibition of the SDF-1alpha-CXCR4 axis by the CXCR4 antagonist
AMD3100 suppresses the migration of cultured cells from ATL patients and murine
lymphoblastoid cells from HTLV-I Tax transgenic mice. *Blood* **114**, 2961-2968,
doi:10.1182/blood-2008-11-189308 (2009).
- 218 Shen, Z., Li, Y., Kohama, K., Oneill, B. & Bi, J. Improved drug targeting of cancer cells by
utilizing actively targetable folic acid-conjugated albumin nanospheres. *Pharmacol Res*
63, 51-58, doi:10.1016/j.phrs.2010.10.012 (2011).

- 219 Yang, H. *et al.* Multifunctional core/shell nanoparticles cross-linked polyetherimide-folic acid as efficient Notch-1 siRNA carrier for targeted killing of breast cancer. *Sci Rep* **4**, 7072, doi:10.1038/srep07072 (2014).
- 220 Siwowska, K., Schmid, R. M., Cohrs, S., Schibli, R. & Muller, C. Folate Receptor-Positive Gynecological Cancer Cells: In Vitro and In Vivo Characterization. *Pharmaceuticals (Basel)* **10**, doi:10.3390/ph10030072 (2017).
- 221 Hamilton, G. & Rath, B. A short update on cancer chemoresistance. *Wien Med Wochenschr* **164**, 456-460, doi:10.1007/s10354-014-0311-z (2014).
- 222 Maeda, H. & Khatami, M. Analyses of repeated failures in cancer therapy for solid tumors: poor tumor-selective drug delivery, low therapeutic efficacy and unsustainable costs. *Clin Transl Med* **7**, 11, doi:10.1186/s40169-018-0185-6 (2018).
- 223 Babbs, C. F. Predicting success or failure of immunotherapy for cancer: insights from a clinically applicable mathematical model. *Am J Cancer Res* **2**, 204-213 (2012).
- 224 Zhao, Z. *et al.* Surface-Modified Shortwave-Infrared-Emitting Nanophotonic Reporters for Gene-Therapy Applications. (2018).
- 225 Hu, F. *et al.* Supermultiplexed optical imaging and barcoding with engineered polyynes. *Nat Methods* **15**, 194-200, doi:10.1038/nmeth.4578 (2018).
- 226 Takai, A. *et al.* Expanded palette of Nano-lanterns for real-time multicolor luminescence imaging. *Proc Natl Acad Sci U S A* **112**, 4352-4356, doi:10.1073/pnas.1418468112 (2015).
- 227 Yap, T. A., Sandhu, S. K., Workman, P. & de Bono, J. S. Envisioning the future of early anticancer drug development. *Nat Rev Cancer* **10**, 514-523, doi:10.1038/nrc2870 (2010).
- 228 Kosaka, N., Ogawa, M., Sato, N., Choyke, P. L. & Kobayashi, H. In vivo real-time, multicolor, quantum dot lymphatic imaging. *J Invest Dermatol* **129**, 2818-2822, doi:10.1038/jid.2009.161 (2009).
- 229 Longmire, M., Kosaka, N., Ogawa, M., Choyke, P. L. & Kobayashi, H. Multicolor in vivo targeted imaging to guide real-time surgery of HER2-positive micrometastases in a two-tumor coincident model of ovarian cancer. *Cancer Sci* **100**, 1099-1104, doi:10.1111/j.1349-7006.2009.01133.x (2009).
- 230 Thurber, G. M., Figueiredo, J. L. & Weissleder, R. Multicolor fluorescent intravital live microscopy (FILM) for surgical tumor resection in a mouse xenograft model. *PLoS One* **4**, e8053, doi:10.1371/journal.pone.0008053 (2009).
- 231 Yamamoto, N., Tsuchiya, H. & Hoffman, R. M. Tumor imaging with multicolor fluorescent protein expression. *Int J Clin Oncol* **16**, 84-91, doi:10.1007/s10147-011-0201-y (2011).
- 232 Yang, M., Jiang, P. & Hoffman, R. M. Whole-body subcellular multicolor imaging of tumor-host interaction and drug response in real time. *Cancer Res* **67**, 5195-5200, doi:10.1158/0008-5472.CAN-06-4590 (2007).
- 233 Alizadeh, A. A. *et al.* Toward understanding and exploiting tumor heterogeneity. *Nat Med* **21**, 846-853, doi:10.1038/nm.3915 (2015).
- 234 Gentles, A. J. *et al.* The prognostic landscape of genes and infiltrating immune cells across human cancers. *Nat Med* **21**, 938-945, doi:10.1038/nm.3909 (2015).
- 235 Natrajan, R. *et al.* Microenvironmental Heterogeneity Parallels Breast Cancer Progression: A Histology-Genomic Integration Analysis. *PLoS Med* **13**, e1001961, doi:10.1371/journal.pmed.1001961 (2016).
- 236 Yuan, Y. Spatial Heterogeneity in the Tumor Microenvironment. *Cold Spring Harb Perspect Med* **6**, doi:10.1101/cshperspect.a026583 (2016).
- 237 Higgins, L. M. *et al.* Multiscale optical imaging of rare-earth-doped nanocomposites in a small animal model. *J Biomed Opt* **23**, 1-4, doi:10.1117/1.JBO.23.3.030505 (2018).

- 238 Kumar, A. *et al.* Innovative pharmaceutical development based on unique properties of nanoscale delivery formulation. *Nanoscale* **5**, 8307-8325, doi:10.1039/c3nr01525d (2013).
- 239 Chen, H., Zhang, W., Zhu, G., Xie, J. & Chen, X. Rethinking cancer nanotheranostics. *Nat Rev Mater* **2**, doi:10.1038/natrevmats.2017.24 (2017).
- 240 Zelikin, A. N., Ehrhardt, C. & Healy, A. M. Materials and methods for delivery of biological drugs. *Nat Chem* **8**, 997-1007, doi:10.1038/nchem.2629 (2016).
- 241 Conde, J. *et al.* Revisiting 30 years of biofunctionalization and surface chemistry of inorganic nanoparticles for nanomedicine. *Front Chem* **2**, 48, doi:10.3389/fchem.2014.00048 (2014).
- 242 Lai, W. F., Rogach, A. L. & Wong, W. T. Molecular design of upconversion nanoparticles for gene delivery. *Chem Sci* **8**, 7339-7358, doi:10.1039/c7sc02956j (2017).
- 243 Svenson, S. What nanomedicine in the clinic right now really forms nanoparticles? *Wiley interdisciplinary reviews. Nanomedicine and nanobiotechnology* **6**, 125-135, doi:10.1002/wnan.1257 (2014).
- 244 Ma, X., Zhao, Y. & Liang, X. J. Theranostic nanoparticles engineered for clinic and pharmaceuticals. *Acc Chem Res* **44**, 1114-1122, doi:10.1021/ar2000056 (2011).
- 245 Anselmo, A. C. & Mitragotri, S. Nanoparticles in the clinic. *Bioeng Transl Med* **1**, 10-29, doi:10.1002/btm2.10003 (2016).
- 246 Yang, J. *et al.* Ultrasmall and photostable nanotheranostic agents based on carbon quantum dots passivated with polyamine-containing organosilane molecules. *Nanoscale* **9**, 15441-15452, doi:10.1039/c7nr05613c (2017).
- 247 Ma, Y. *et al.* Zero-dimensional to three-dimensional nanojoining: current status and potential applications. *RSC Advances* **6**, 75916-75936, doi:10.1039/C6RA15897H (2016).
- 248 Drude, N., Tienken, L. & Mottaghy, F. M. Theranostic and nanotheranostic probes in nuclear medicine. *Methods* **130**, 14-22, doi:10.1016/j.ymeth.2017.07.004 (2017).
- 249 Belyanina, I. *et al.* Targeted Magnetic Nanotheranostics of Cancer. *Molecules* **22**, doi:10.3390/molecules22060975 (2017).
- 250 Zhang, B. *et al.* Engineering Quantum Dots with Different Emission Wavelengths and Specific Fluorescence Lifetimes for Spectrally and Temporally Multiplexed Imaging of Cells. *Nanotheranostics* **1**, 131-140, doi:10.7150/ntno.18989 (2017).
- 251 Nigam Joshi, P. *et al.* Multifunctional inulin tethered silver-graphene quantum dots nanotheranostic module for pancreatic cancer therapy. *Mater Sci Eng C Mater Biol Appl* **78**, 1203-1211, doi:10.1016/j.msec.2017.03.176 (2017).
- 252 Zhao, X., He, S. & Tan, M. C. Advancements in infrared imaging platforms: complementary imaging systems and contrast agents. *Journal of Materials Chemistry B* **5**, 4266-4275, doi:10.1039/C7TB00123A (2017).
- 253 van Saders, B., Al-Baroudi, L., Tan, M. C. & Riman, R. E. Rare-earth doped particles with tunable infrared emissions for biomedical imaging. *Optical Materials Express* **3**, 566-573, doi:10.1364/OME.3.000566 (2013).
- 254 Tan, M. C., Kumar, G. A. & Riman, R. E. Near infrared-emitting Er- and Yb-Er- doped CeF₃ nanoparticles with no visible upconversion. *Opt Express* **17**, 15904-15910, doi:10.1364/OE.17.015904 (2009).
- 255 Teng, B. *et al.* Upconversion nanoparticles loaded with eIF4E siRNA and platinum(IV) prodrug to sensitize platinum based chemotherapy for laryngeal cancer and bioimaging. *Journal of Materials Chemistry B* **5**, 307-317, doi:10.1039/C6TB02360F (2017).
- 256 Lai, W. F. In vivo nucleic acid delivery with PEI and its derivatives: current status and perspectives. *Expert Rev Med Devices* **8**, 173-185, doi:10.1586/erd.10.83 (2011).

- 257 Demeneix, B. & Behr, J. P. Polyethylenimine (PEI). *Adv Genet* **53**, 217-230 (2005).
- 258 Lin, M. *et al.* Facial Layer-by-Layer Engineering of Upconversion Nanoparticles for Gene Delivery: Near-Infrared-Initiated Fluorescence Resonance Energy Transfer Tracking and Overcoming Drug Resistance in Ovarian Cancer. *ACS Appl Mater Interfaces* **9**, 7941-7949, doi:10.1021/acsami.6b15321 (2017).
- 259 Choi, Y. J., Kang, S. J., Kim, Y. J., Lim, Y. B. & Chung, H. W. Comparative studies on the genotoxicity and cytotoxicity of polymeric gene carriers polyethylenimine (PEI) and polyamidoamine (PAMAM) dendrimer in Jurkat T-cells. *Drug Chem Toxicol* **33**, 357-366, doi:10.3109/01480540903493507 (2010).
- 260 Brunot, C. *et al.* Cytotoxicity of polyethyleneimine (PEI), precursor base layer of polyelectrolyte multilayer films. *Biomaterials* **28**, 632-640, doi:10.1016/j.biomaterials.2006.09.026 (2007).
- 261 Zhao, L. *et al.* Stem cell labeling using polyethylenimine conjugated (alpha-NaYbF₄:Tm³⁺)/CaF₂ upconversion nanoparticles. *Theranostics* **3**, 249-257, doi:10.7150/thno.5432 (2013).
- 262 Jin, J. *et al.* Polymer-coated NaYF₄:Yb(3)(+), Er(3)(+) upconversion nanoparticles for charge-dependent cellular imaging. *ACS Nano* **5**, 7838-7847, doi:10.1021/nn201896m (2011).
- 263 Calarco, A. *et al.* The genotoxicity of PEI-based nanoparticles is reduced by acetylation of polyethylenimine amines in human primary cells. *Toxicol Lett* **218**, 10-17, doi:10.1016/j.toxlet.2012.12.019 (2013).
- 264 Sheng, Y. *et al.* Size and Shell Effects on the Photoacoustic and Luminescence Properties of Dual Modal Rare-Earth-Doped Nanoparticles for Infrared Photoacoustic Imaging. *ACS Biomaterials Science & Engineering* **2**, 809-817, doi:10.1021/acsbiomaterials.6b00012 (2016).
- 265 Sheng, Y., Liao, L. D., Thakor, N. & Tan, M. C. Rare-Earth doped particles as dual-modality contrast agent for minimally-invasive luminescence and dual-wavelength photoacoustic imaging. *Sci Rep* **4**, 6562, doi:10.1038/srep06562 (2014).
- 266 Curtis, K. A. *et al.* Unusual Salt and pH Induced Changes in Polyethylenimine Solutions. *PLoS One* **11**, e0158147, doi:10.1371/journal.pone.0158147 (2016).
- 267 Israel, L. L. *et al.* Acute in vivo toxicity mitigation of PEI-coated maghemite nanoparticles using controlled oxidation and surface modifications toward siRNA delivery. *ACS Appl Mater Interfaces* **7**, 15240-15255, doi:10.1021/acsami.5b02743 (2015).
- 268 LDS, Y. Organic Spectroscopy. *Infrared Spectroscopy* (2005).
- 269 Higgins, L. M. *et al.* Line-scanning confocal microscopy for high-resolution imaging of upconverting rare-earth-based contrast agents. *J Biomed Opt* **20**, 110506, doi:10.1117/1.JBO.20.11.110506 (2015).
- 270 Kwon, M. *et al.* Filamin A interacting protein 1-like inhibits WNT signaling and MMP expression to suppress cancer cell invasion and metastasis. *Int J Cancer* **135**, 48-60, doi:10.1002/ijc.28662 (2014).
- 271 Kwon, M. *et al.* Reduced expression of FILIP1L, a novel WNT pathway inhibitor, is associated with poor survival, progression and chemoresistance in ovarian cancer. *Oncotarget* **7**, 77052-77070, doi:10.18632/oncotarget.12784 (2016).
- 272 Stark, M. & Cheng, R. H. Surface modulatable nanocapsids for targeting and tracking toward nanotheranostic delivery. *Pharm Pat Anal* **5**, 307-317, doi:10.4155/ppa-2016-0021 (2016).

- 273 Jagtap, P., Sritharan, V. & Gupta, S. Nanotheranostic approaches for management of bloodstream bacterial infections. *Nanomedicine* **13**, 329-341, doi:10.1016/j.nano.2016.09.005 (2017).
- 274 Ding, H. L., Zhang, Y. X. & Li, G. H. Recent research progress on magnetic nanocomposites with silica shell structures: preparation and nanotheranostic applications. *Recent Pat Nanotechnol* **8**, 117-128 (2014).
- 275 Li, C. A targeted approach to cancer imaging and therapy. *Nature materials* **13**, 110-115, doi:10.1038/nmat3877 (2014).